Determination of Orbital Parameters of Kepler Binary Stars Using Time-delay Method on 1646 Pulsating δ Scuti Stars

GF. AYANE

orcid.org/0000-0002-3566-3723

Thesis submitted for the degree *Philosophiae Doctor in Physics*
at the North-West University

Promoter: Prof. Thebe Medupe

Co-promoter: Dr. Luis Balona

Graduation July 2018

Student number: 24427527

NWU®
NORTH-WEST UNIVERSITY
NOORDWES-UNIVERSITEIT
UNIBESITI YA BOKONE-BOPHIRIMA

Declaration

I, Getinet Feleke Ayane, declare that this thesis titled, "Determination of Orbital Parameters of *Kepler* Binary Stars Using Time-Delay Method on 1646 Pulsating δ Scuti Stars" and the work presented in it are my original work and has not been submitted for any other degree or professional qualification at this University or any other institution. Where other sources of information have been used, and where the work has been done in collaboration with others, I have acknowledged all.

Signed:

Date:

Abstract

A binary system is a pair of stars that are held together in closed orbits around their common centre of gravity, under the influence of their mutual gravitation. The night sky presents a variety of double stars, ranging from wide, optical pairs to close binary systems. Close binary stars are magnificent laboratories in astrophysics. They affect each other's structure and evolution. Multiplicity is one fundamental property of stars. Binary systems are as common as single stars in the universe and about half of the stars in our galaxy are members of so-called binary star systems. Similar independent proportions of triple, quadruple and quintuple systems have been reported in the literature. The study of binary stars is fundamental to our understanding of stellar structure and evolution and also allows physical stellar parameters to be determined. Multiple systems are of particular interest. For example, in triple systems, masses and orbital parameters of the constituent stars can tell about the unclear process of the formation of systems of multiple stars. The orbital parameter of a triple star system can also inform about the final contraction of the interstellar cloud that formed the system, given that the dynamical evolution of the system leaves the initial configuration relatively unchanged.

The main purpose of this thesis is to use the high quality data observed by the *Kepler* space telescope to identify binary stars from the samples that have δ Sct pulsation and to determine their orbital parameters (projected semi-major axis, $a \sin i$, eccentricity, e, angle of periastron, ω, time of periastron passage, $T_{\rm per}$, orbital period, P, and the two ancillary parameters:- semi-amplitude of radial velocity curve, K, and mass function, $f(m)$). The parameters of binary systems are generally obtained from astrometric, spectroscopic or photometric observations, and in favourable cases by a combination of two or even all three, of these methods. Time-delay is a periodic arrival time of light from a binary system caused by the

periodic distance variation while the star orbits around its binary companion. The time-delay method allows the determination of orbital parameters directly with high precision which avoids the need for spectroscopy. In this thesis we used the time-delay method and we attempted to achieve the following objectives. The first objective was to identify the most important pulsation frequencies. Possible binary stars and their orbital periods were then identified. To achieve this, we searched for peaks in the 'binarogram', which is a plot of the time-delay as a function of orbital frequency. Once a star has been identified as a possible binary from the binarogram, we inspected a graph of time-delay as a function of time, as given by the 10 pulsation frequencies of highest amplitude. Since the presence of close pulsation frequencies distorts the time-delay, only a few of these will produce meaningful time-delay variations. The best time-delay curves were selected and fitted with a truncated Fourier series and distortions removed using a low-degree polynomial. These were averaged to produce the final time-delay variation. A code was developed to determine the best orbital parameters using non-linear least squares.

The data for this analysis was downloaded from the *Mikulski Archive for Space Telescopes* (MAST) in FITS format. Data from the full *4-yr Kepler* mission were used. These data were examined and 1646 candidate δ Sct stars were identified. These stars were observed in long-cadence mode which nominally allows only variations with frequencies less than about 24 cycles per day to be distinguished. Many δ Sct stars have pulsations of higher frequency. Fortunately, the slightly non-uniform time sampling allows pulsation frequencies higher than this nominal Nyquist limit to be determined with some confidence, provided their amplitudes are sufficiently high.

Of the 1646 δ Sct stars examined, we detected 131 binary stars and 9 stars which appear to be triple or multiple systems.

Acknowledgements

I owe my gratitude to all the people who have made this thesis possible and because of whom my graduate experience has been one that I will cherish forever. This thesis could not have been written without them.

First and foremost I would like to thank my supervisor, Professor Thebe Medupe for giving me an invaluable opportunity to work. Thebe always gave me technical advice, guidance and suggestions, not only on my research work but also on how to live in a different environment. It has been a pleasure to work with and learn from such an individual.

Suggestions, ideas and continuous follow-up on my research also came from my co-supervisor, Dr. Luis Balona, whom I also thank for the unique opportunity, to work on the extremely interesting project that become one of the most successful topics of the *Kepler* mission. I would also like to thank him for his support and patience, and for responding to my emails and questions very rapidly. I have been very fortunate.

Research without fund is unthinkable. I thank Professor Eno Ebenso for making life easier by getting me different funds. It was really a great support.

I would also like to thank my colleagues Dr. Abedigamba and Mr. Getachew who have contributed on LaTex related issues and Dr. Andry Rajoelimanana for discussions we had on various ideas related to programming. I am greatly indebted to colleagues who have made life fun: Dr. Bruno, Mr. Shobo, Dr. Amare and Dr. Nahom. I am so glad to have met them and I will continue to treasure their friendship.

I would also like to acknowledge the support I got from the Physics Department,

Mafikeng Campus. I was allowed easy access to printing and scanning and even participated in social activities with staff members. I always felt like a staff member. It means a lot to me.

Special thanks goes to the NASA team behind *Kepler* Spacecraft, and the *Kepler* Asteroseismic Science Consortium, KASC, for providing many young researchers the opportunity to work with such special data.

I am grateful to my home institution Kotebe University College (KUC) for allowing me to stay as a staff member and waiting for me until I finish my PhD. This has been a source of psychological support throughout my study. I am also happy for the fact that Entoto Observatory invited me to be an adjunct staff member while I was studying.

I owe my deepest thanks to my family - my mother and my sisters. Words cannot express the gratitude I owe them. I always refresh myself, get energized and move forward when I remember their love.

Lastly, thank you all and thank God!

Abbreviations

KASC	**K**epler **A**steroseismic **S**cience **C**onsortium
MAST	**M**ulti-mission **M**ikulski **A**rchive at **S**pace **T**elescope
KIC	**K**epler **I**nput **C**atalogue
CCD	**C**harge **C**oupled **D**evice
TESS	**T**ransiting **E**xoplanet **S**atellite **S**urvey
JWST	**J**ames **W**ebb **S**pace **T**elescope
DFT	**D**iscrete **F**ourier **T**ransform
FFT	**F**ast **F**ourier **T**ransform
SC	**S**hort **C**adence
LC	**L**ong **C**adence
MOST	**M**icrovariability and **OS**cillations of stars
NASA	**N**ational **A**eronautics and **S**pace **A**dministration
FITS	**F**lexible **I**mage **T**ransport **S**ystem
PA	**P**hotometric **A**nalysis
PDC	**P**re-search **D**ata **C**onditioning
CAL	**CAL**ibration
SAP	**S**imple **A**perture **P**hotometry
PNN	**P**robabilistic **N**eural **N**etwork
CoRoT	**Co**nvection, **Ro**tation and planetary **T**ransits
FM	**F**requency **M**odulation
PM	**P**hase **M**odulation
AU	**A**stronomical **U**nit
BEER	**BE**aming, **E**llipsoidal, and **R**eflection periodic modulations
SPB	**S**lowly **P**ulsating **B**-type
HADS	**H**igh-**A**mplitude **D**elta **S**cuti

Physical Constants

Speed of light	$c =$	$173.144632674 AU/day$
Mass of the sun	$M_\odot =$	$1.989 \times 10^{30} kg$
Gravitational constant	$G =$	$6.67408 \times 10^{-11} m^3 kg^{-1} s^{-2}$
Astronomical unit	$AU =$	$1.495 \times 10^{8} km$

List of symbols

Symbol	Description	Units
ω	angle of periastron passage	rad
$a \sin i$	projected semi-major axis	AU
$T_{\rm per}$	time of periastron passage	days
P	orbital period	days
τ	time-delay	days
$f(m)$	mass function	solar mass
ν	true anomaly	rad
K	semi-amplitude of radial velocity	km/s
γ	radial velocity of center of mass	km/s
Vr	radial velocity	km/s
E	eccentric anomaly	rad
M	mean anomaly	rad
i	angle of orbital inclination	rad
e	eccentricity	

Contents

List of Figures

List of Tables

Chapter 1

Introduction

To calculate the basic physical parameters of stars accurately, binary stars are among the most important objects in stellar astrophysics. Space based observations provided by space missions like *Kepler* are one of the best ways to study binary systems. With the study of red giants and solar-like pulsators, the *Kepler* mission data brought a big change. Since its launch in March 2009 until the end of the primary mission in May 2013, *Kepler* obtained high-precision broadband photometry of about 150,000 stars. With their regular sampling, time span of longer observation, and micromagnitude precision, the *Kepler* data are revolutionising asteroseismic studies. In addition to providing precision time series photometry from space, *Kepler* gives the possibility of determining the orbital parameters of pulsating stars that are members of a binary system. What ever careful photometric measurements can be done from ground based observations, day-night cycles and the weather limit observation cycles, and scintillation of the atmosphere also affects the precision. This is one of the reasons that in the future photometry using the Transiting Exoplanet Satellite Survey (TESS) and James Webb Space Telescope (JWST) will be in space. However, observations from the ground are still compulsory. Photometry from *Kepler* is white-light only and its field of view is also fixed. Multi-colour observations, spectral classification of many stars and full abundance analyses still require dedicated ground-based observations.

Our list of targets are from the groups of δ Sct stars. For many reasons, the δ Sct stars are important astrophysically. These stars are the best targets for asteroseimology, where the structure of their interior can be studied from their pulsations

and the high amplitude stars can serve as standard candles to measure cosmic distances. They are one of the most abundant pulsating variables in our Galaxy. Many δ Sct stars pulsate with higher frequencies than nominal Nyquist frequency of long cadence mode, but because of the slightly unequal time spacing, higher frequencies can be detected if the amplitude is sufficiently high. Balona (unpublished) has classified a list of over 20000 *Kepler* stars brighter than 12 magnitude by inspecting the periodogram and the light curve of each star. There are 1679 δ Sct stars in this list. These are the stars which form the basis of this study.

According to the Newtonian mechanics of point masses, the orbit of the binary system and the physical properties of the individual stars can be determined from the observational data. The orbit can also be described using Kepler's third law as the position and velocity of a star are functions of time. Fundamental parameters of a binary star orbit can be determined from the radial velocity curve of a companion, or by using the time-delay method shown in this thesis. The time-delay method allows for the determination of orbital parameters directly with great precision, which avoids the need for spectroscopy. For best results in time-delay, we need the shortest possible pulsating period and stable pulsations. The calculation of the binarogram for the range 0 - 0.1 d^{-1} takes less than one minute. This makes the time-delay method most effective in detecting binaries. This implies the possibility of using binarograms for different combinations of pulsation frequencies in a relatively short time. Solar-like oscillations have short periods, but their amplitudes are too low. γ Dor and SPB stars, on the other hand, have periods which are too long. Unfortunately, there are too few Beta Cep stars in the *Kepler* data. sdB stars and pulsating white dwarfs have periods that are too unstable. However, δ Sct stars are the best options since they are numerous and also have short periods. On the other hand, their pulsation periods may sometimes be unstable. Many δ Sct stars have close frequencies which cause interference with the time-delay. This, in fact, is one of the greatest difficulties in using δ Sct stars in the time-delay method.

In general, the following steps were used to determine the orbital prameters of δ Sct stars using the time-delay method. (i) The frequencies of the 10 modes of highest amplitude were determined using the periodogram. (ii) Frequencies which

are too close are removed since these would cause interference. (iii) The binarogram was calculated for each of the remaining frequencies. Those stars in which the binarogram did not show the same orbital frequency peak were rejected. (iv) The remaining stars were further analysed by plotting the time-delay curves determined from each pulsation frequency. Only stars in which at least two frequencies show consistent time-delay as a function of time were accepted. (v) Since most of the time-delay curves are distorted owing to close frequencies, these need to be corrected by fitting a combination of truncated Fourier series and polynomials by least squares. (vi) The corrected time-delay curves were averaged and a non-linear least squares solution was applied to determine the orbital parameters.

An important aspect of this thesis is to take the high quality data observed by the *Kepler* space telescope, identify the binary stars from the samples that have δ Sct pulsation and finally to determine their orbital parameters. The structure of the thesis is as follows. The first chapter provides a literature review on binary stars, *Kepler* telescope and its observations, binary system orbits, radial velocity and time-delay methods. Chapter 2 is dedicated to explaining how we identified binary stars using binarograms. In Chapter 3, the time-delay variations as a function of time are presented, together with the least squares fits applied to the *Kepler* data. Chapter 4 contains the main results and discussions. Finally, conclusions on the whole thesis are presented in Chapter 5.

1.1 Multiple Star Systems

One fundamental property of stars is their multiplicity. There are many triple systems, and not a few are quadruples. Many of the purely spectroscopic binaries are triple or other multiple systems and one in twenty of the known visual binaries has at least one additional member, either visible or identified by a spectrograph. Many systems are quadruple or even more complex, as mentioned by Aitken (1964). Triple systems, whether visual or spectroscopic, consist of a close binary pair and a relatively distant companion. Zurhellen (1907), Schlesinger (1915), and Paddock (1915) reported how the presence of a third body system can be revealed in radial

velocity curves. There are many ways of identifying triple star systems. These include: resolving a bound star system visually (Tokovinin et al. 2006; Rucinski et al. 2007; Raghavan et al. 2010), looking for the presence of three different stellar spectra (Zucker et al. 1995; D'Angelo et al. 2006) or using radial velocity techniques (Carter et al. 2011a). For centuries, long-term monitoring of binary eclipses (Irwin 1952; Steffen et al. 2011; Gies et al. 2012; Borkovits et al. 2013) has been a dominant way of identifying triple stars. A relatively rare method is the direct observation of eclipses of the three bodies (Derekas et al. 2011).

In triple systems, masses and orbital parameters of the constituent stars can give information about the unclear process of the formation of systems of multiple stars (Boss 1991, 1995; Bodenheimer et al. 2000; Sterzik et al. 2003; Bate 2009; Reipurth & Mikkola 2012). The orbital parameters of a triple star system can also inform us about the final contraction of the interstellar cloud that formed the system, given that the dynamical evolution of the system leaves the initial configuration relatively unchanged (Boss 1991; Bate 2009; Reipurth & Mikkola 2012). Most importantly, understanding the relative ratio of the number of binaries versus triples and quadruples is very important in predicting what other unseen stars in any particular system may be present (Tokovinin et al. 2006; Pribulla & Rucinski 2006; Raghavan et al. 2010).

To be stable over a long time scale, multiple stars need to follow a certain hierarchical structure in general. The structure can be a star and a binary orbiting around each other in triple systems or two binaries orbiting around each other in quadruple systems. Therefore, most multiple systems can be described as binaries with several levels. Quadruple stars for example can be ordered in two ways. One option is that the two pairs can orbit the common centre of gravity, or alternatively, a double star is orbited by a distant third star, and then even more distantly a fourth star circles the whole group. The status of currently known quadruple systems is referred to by Graczyk et al. (2011), Cagaš & Pejcha (2012), Lehmann et al. (2012) and Lohr et al. (2012).

As a good example, we can see the geometry (Fig.1.1) of quadruple system V994

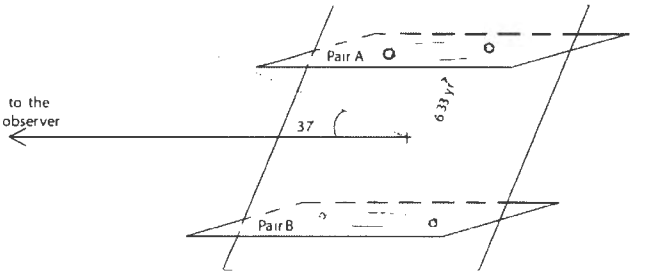

Figure 1.1: The V994 Her system and its schematic sketch. The celestial plane and the orbital planes of both A and B pairs are almost perpendicular (i.e. edge-on to the observer, 84° and 86°, respectively). Image: Zasche & Uhlař (2013).

Her which consists of two bound eclipsing binaries orbiting each other. This system is one of the most interesting groups of multiple star systems studied so far (Perryman et al. 1997; Mason et al. 2001; Lee et al. 2008; Zasche & Uhlař 2013).

A third body can have an effect on eccentricity (Kozai 1962; Mazeh & Shaham 1979; Mazeh 1990) and on tidal friction created (Kiseleva et al. 1998; Eggleton & Kisseleva-Eggleton 2006; Eggleton 2006; Fabrycky & Tremaine 2007) which results in a hierarchical multiple system (Reipurth & Mikkola 2012). Being tight or tightest binary with a tertiary companion further contributes to the evolution toward an increasingly hierarchical configuration (Law et al. 2010; Dhital et al. 2010). The contribution of apsidal motion is also reported by Bozkurt & Değirmenci (2007) and nodal precession by Mayor & Mazeh (1987) and Mazeh (2008).

It is common practice to find exoplanets using eclipse timing and transit timing (Schwarz et al. 2011). Using transit timing, multiple planetary systems were studied by Steffen et al. (2012), Fabrycky et al. (2012) and Ford et al. (2012). The discovery of planet *Kepler*-16b by Doyle et al. (2011) and the two planets *Kepler*-34b and *Kepler*-35b by Welsh et al. (2012) are also results of the transit method. *Kepler* data has also been a vital source of multiple star studies. Gies et al. (2012) reported timing variations studies in 41 *Kepler* eclipsing binaries and Rappaport et al. (2013) published a list of 39 candidate third-body *Kepler* systems

using eclipse times. Conroy et al. (2014) found a third body rate of $\sim$ 20 percent.

1.2 Binary Stars

A binary system is a pair of stars that are held together in closed orbits around their common centre of gravity, under the influence of their mutual gravitation. Binary systems have been studied for centuries. ζ Ursae Majoris (Mizar) was the first binary to be discovered by Jean Baptiste Riccioli in 1650. Goodricke (1783) also identified Algol as one of the first eclipsing binary star systems. However, Herschel (1802) is the one who first introduced and used the term 'binary star' from his observations, to designate a union of two stars that are formed together in one system by the laws of attraction.

The name 'binary star' is usually used for a pair of stars which can be seen close together through a telescope. Closeness of binary star systems can be due to two reasons. One is that the systems may actually be close together in space, forming a system in which their mutual gravitational attraction might be the reason for their orbital motion. The second reason is that the two stars may be at greatly differing distances from each other, but nearly in the same direction as viewed from the earth. Thus the stars may be in contact, or may be separated by thousands of astronomical units. In general, the two members of a binary star have different brightness. The brighter star is called the *primary* and the fainter is called the *companion*. Fig.1.2 shows the orbits of two stars with a higher mass star A and a lower mass star B. The stars share a common focus which is the centre of mass or barycenter of the system and orbit around this point. The radius vector joining the two stars always cuts through the barycenter.

The night sky presents a variety of double stars, ranging from wide, optical pairs to close binary systems. According to recent observations among young stars in many nearby star forming regions, an excess binary population exists (Ghez et al. 1993; Leinert et al. 1993; Simon et al. 1993; Duchêne et al. 2007). This large number of young doubles, in comparison to field stars in the solar neighbourhood, is reported by Duquennoy & Mayor (1991). This anti-correlates with the property

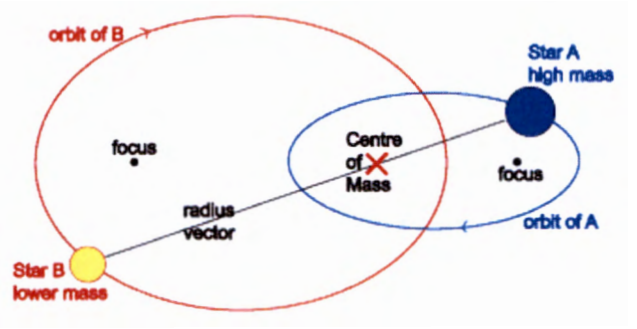

Figure 1.2: A sketch showing two stars A and B in a binary system orbiting about their centre of mass (Image credit: www.atnf.csiro.au).

of stellar density as demonstrated by Prosser et al. (1994), Petr et al. (1998) and Patience et al. (2002) and Beck et al. (2003). This shows that the denser clusters in which most stars form, contain a lower fraction of bound multiple systems that are comparable to the fraction found among field stars.

The study of binary stars is fundamental to our understanding of stellar structure and evolution, because of the information it provides. Binaries are very important in determining fundamental physical stellar parameters. In particular, eclipsing binaries are the main sources of stellar fundamental parameters such as mass and radius. With the invention of speckle interferometry, double-star observation underwent a revolution in the 1970s. The launch of the Hipparcos satellite in 1989 also brought a new era of double-star discovery. The other interesting aspect is that planetary bodies (exoplanets) can exist in binary star systems (Lowrance et al. 2002).

1.3 Proportion of Binary and Multiple Star Systems

Binary systems are as common as single stars in the universe, and since they are numerous, it is important to study their nature. Argyle (2004) suggested that the number of binary systems we can find depends on the separation of the components. There is a huge range of binary star periods which can extend up to 100,000

years or more, as mentioned by Argyle (2004). The periods of many of the binaries lie between 100 and 1000 years and can be easily observed with small telescopes.

Observations show that even higher multiplicity systems exist. The catalogue of multiple stars (Tokovinin 1997) reported 626 triples, 141 quadruples, 28 quintuples and ten sextuples. Fitzpatrick (2012) also stated that half of the stars in our galaxy are members of so-called binary star systems. As reported by Karttunen et al. (2003), less than half of all stars are single stars like the Sun and more than 50 percent belong to systems containing two or more members. The estimated binary fraction varies from $\sim (40-60)$ percent for $M \sim 1M\odot$ stars (Duquennoy & Mayor 1991; Raghavan et al. 2010) to almost 100 percent for more massive A/B and O-stars (Mason et al. 1998; Kobulnicky & Fryer 2007; Kouwenhoven et al. 2007; Mason et al. 2009; Sana et al. 2012; Chini et al. 2012). However, in Sana et al. (2011) and Mahy et al. (2013) a substantially lower binary fraction for massive stars is claimed. Prša et al. (2011) reported that the average occurrence rate of eclipsing binaries across *Kepler* field is 1.2 percent.

The spectroscopy and imaging studies by Tokovinin (1997) and Tokovinin et al. (2006) show that of the multiple star systems they studied, 40 percent were binaries with periods less than 10 days and 96 percent of these had a wide tertiary companion. From the General Catalogue of Radial Velocities, Wilson (1953) and Jaschek & Jaschek (1957) reported that the fraction of spectroscopic binaries among the main sequence stars ranges between 20 and 30 percent. Petrie (1960) used a different approach on these spectroscopic binaries and estimated the fraction to be over 50 percent. Further fractions of spectroscopic binaries in galactic clusters can be referred from Abt and co-workers (Abt & Hunter 1962; Abt & Snowden 1964; Abt 1965; Geary & Abt 1970). The proportion seems to work even when we go down to specific types of stars. For instance $60-70$ percent of Am stars are spectroscopic binaries (Abt & Levy 1985; Carquillat & Prieur 2007; Smalley et al. 2014). De Loore & Doom (1992) postulated that about 30 percent of the main sequence stars are binaries, while about 60 percent of the early type stars are binaries with mass ratio larger than 0.2.

Carroll & Ostlie (1996) mentioned that at least half of all 'stars' in the sky are actually multiple systems. Similarly, according to Lada (2006), about 50 percent of visible stars are members of binary or multiple systems. As a general remark, De Loore & Doom (1992) concluded that 50 percent of the stars observed in the solar neighbourhood are binary (or multiple star) systems. Further studies of proportions of triple, quadruple and quintuple systems were also reported in other papers (Worley 1967; Heintz 1969).

1.4 The Origin of Binary Stars

Haghighipour (2010) mentioned that studies of large samples of binaries in a wide variety of star-forming regions are key to unravelling the nature of binary formation mechanisms and the impact of environment on evolution, distribution and multiplicity fraction. Studying the isolated formation of binaries does not provide a complete result of the processes since most star formation occurs in localized star forming regions and results in clusters (Clarke et al. 2000; Horton et al. 2001). According to Benacquista (2013), stars in binary systems do not evolve in isolation. Batten (1973) also argues that duplicity is not an isolated phenomenon, but rather a special case of multiplicity. This means that the existence of large numbers of multiple systems is a relevant phenomenon.

A general principle regarding the origin of binary systems is that any theory must explain the observed proportion of multiple systems, even though binary systems might be produced in more than one way. Different hypotheses on the origin of binary stars have been suggested. According to the first hypothesis, two stars can be gravitationally bound due to a chance encounter. For this situation to happen, triple encounter or influence of a local interstellar medium is required. This restriction greatly reduces the probability of capture. Ambartsumian (1956) suggested that since there must be equilibrium between the newly formed pairs and those which dissociate as a result of encounters, the observed frequency of wide visual pairs is far too large to be accounted for by the capture hypothesis.

The formation of a double star by fission of a single rapidly rotating star is the

second hypothesis of origin of binary stars. However, this hypothesis is criticized for the fact that it applies only to incompressible fluids and it does not consider the existence of wide pairs. Ambartsumian (1956) mentioned that any rapidly rotating single star has very little angular momentum within it to form a binary system. The reason is that the orbital angular momentum of any binary system is much greater than the rotational angular momentum of its components. There are also studies in favour of the fission theory. Ostriker (1970) believed that criticisms on the fission hypothesis are due to misunderstanding of the nature of binaries. Steinitz & Pyper (1970) discovered correlation between the rotational velocities of the components of wide visual binaries, which they suggested could be a result of fission. The fact that some kinds of binaries have been formed through fission cannot be entirely ruled out, but it seems unlikely that this hypothesis can explain the formation of all binaries. Chandrasekhar (1944), Ambartsumian (1956) and Yabushita (1966) studied the possibility of encounters of binary systems to form a binary pair, but they concluded that through the whole main-sequence lifetime, no great changes are expected to result in the separation of the system.

The third hypothesis suggests that binary systems can be formed due to condensation of the interstellar cloud about neighbouring nuclei. Huang (1957) proposed a theory which supports this idea. However, the major drawback which still exists is that the formation of one condensation in a pre-stellar medium tends to inhibit the formation of any nearby ones.

The fourth hypothesis, which seems to be the extension of the separate condensation hypothesis, is that stars form within clusters in small groups containing up to some tens of members (Worrall 1967; van Albada 1968; Szebehely 1969). The small groups formed are unstable and disintegrate into multiple systems centred on a 'close' binary. In this context, 'close' means a separation of about 10 A.U. The number of stars left in the final multiple system depends on the number in the original group. This hypothesis relates the formation of binary and multiple systems. The ratio of multiple to binary systems predicted by this hypothesis depends on the number of members in the original group from which the multiple systems are supposed to form.

There still exist views on the origin of binary systems which are different from the four hypotheses mentioned so far. Bleksley (1934) and Blaauw & van Albada (1967) proposed that binary systems are produced in more than one way. Their study explains the number of binaries as a function of the semi-major axis of their orbit in many clusters and associations of early-type stars. This concept actually eliminates the need to find a way to turn close binaries into wide ones, or vice versa. Again it remains a fact that neither of the two modes of formation of binary systems can be ruled out. To explain the origin and evolution of binary stars, information on the masses, the mass ratios, the absolute magnitudes, and the spectral characteristics of the components in the systems is important (Aitken 1964). Some current theories of star formation propose that multiple stars or stars and planets are preferential results of gravitating proto-stellar material. Studies of sensitive infrared and millimetre wave photometry on molecular clouds have shown that many of the objects found in these clouds are double or multiple.

Our understanding of the processes behind the formation and evolution of stars has greatly improved recently due to the use of powerful computer simulations. Binary star origin related to the process of fragmentation, where multiple proto-stellar cores were created during the collapse of a molecular cloud, has also been suggested. The distribution of mass ratios in binary stars also explains the processes involved in their formation (Clarke 2001; Tohline 2002; Bonnell et al. 2003). Bate & Bonnell (1997) made simulations to produce isolated binary systems, and found that the mass ratio with which a binary forms is correlated with the separation of the two components, and hence the orbital period of the system. Their result shows that long period binaries are expected to have small mass ratios whereas short period binaries should have components of more equal mass. Similarly, mass ratio distribution was measured for short period binaries by Mazeh et al. (2003) and long period binaries by Duquennoy & Mayor (1991). Another simulation result by Bate et al. (2002) showed the collapse of an entire molecular cloud into a cluster, and additionally found that fragmentation does not produce binaries with separation less than about 10 AU. Instead, these close systems form through dynamical interactions, which preferentially create binaries with components of the same masses. Further reviews on the origins of binary and multiple star systems are explained

in detail by van den Heuvel and co-workers (van den Heuvel 1983; Bhattacharya & van den Heuvel 1991; Eggleton 2006; Tauris & van den Heuvel 2006; van den Heuvel 2011).

1.5 Classification of Binary Stars

There are different techniques for observing binary stars. Their classification based on these techniques can be useful. It is also logical to look for some form of classification that can divide the whole group into smaller sub-classes. An easier and better way to classify binary stars is based on the method of observation which is shown below.

- *Spectroscopic binaries*: These are stars so close together that they appear to be single in telescopes. Their spectra show a regular variation due to the Doppler shift as the stars approach and recede from the observer. There are two subgroups of spectroscopic binaries, the single-lined spectroscopic binary (SB1) in which the spectrum of only the luminous star is observed, and the double-lined spectroscopic binary (SB2) where two distinct spectra can be detected because luminosities of both stars are comparable. Most spectroscopic binaries have short orbital periods so that a changing Doppler shift can be measured easily. Using Doppler shift absorption lines, the line-of-sight velocity (radial velocity) of the binary system can be measured spectroscopically. The radial velocity is negative when the star is moving towards the observer and the spectra will be blue-shifted. When a star is moving away from the observer, the spectra will be red-shifted and the radial velocity will be positive. We will apply a similar concept to this for negative and positive time delay in this thesis. Measuring radial velocity can yield many important parameters of the binary orbit.

- *Eclipsing binaries*: These are binaries where one star passes in front of the other, as seen from the earth, and blocks the light from the eclipsed component so that the light coming from the system varies periodically. Such sys-

tems can be identified by regular variation of the amount of light received at the telescope. The variation of apparent magnitude of the eclipsing variable as a function of time is called a *light curve*. Based on the shape of the light curve, eclipsing binaries are divided into three classes: Algol, β Lyrae and W Ursae Majoris. Eclipsing binary systems also provide the best method to determine masses, radii and luminosities of stars (Andersen 1991). Masses and radii determined from eclipsing binaries are important in refining stellar evolution models (Schroder et al. 1997; Guinan et al. 2000; Torres & Ribas 2002).

- *Visual binaries*: These are binaries which can be resolved by a telescope and can thus be recognized visually as a double star if the orbital period is not prohibitively long. By taking appropriate and repeated observations, the changes in relative position of the stars can be seen while they are in motion in their orbits. From their mutual centre of mass, the systems provide important information about their angular separation. If the distance of the binary is also known, the linear separation of the stars can also be determined.

- *Astrometric binaries*: These are stars which look single in all telescopes but their double nature is known by the effect that a second invisible companion star has the proper motion or the transverse motion of the star against the background of fainter stars in the same field. Because Newton's first law requires that a constant velocity must be maintained by a mass unless a force is acting on it, an oscillatory motion of the system implies the existence of another component. On such systems of binaries, one of the members is significantly brighter than the other, so that the second component is hidden.

- *Spectrum binaries*: These binaries are stars that show two spectral lines but radial velocity changes are not observable because the components are widely separated from each other where the orbital period becomes long. Because the stars in the binary system are continuously in motion with respect to their center of mass, there must necessarily be periodic shifts in

wavelength of every spectral line of the stars.

- *Optical binaries*: These are stars which appear to be close together in the sky while they are in fact at very different distances. These systems are not actually binaries and because of their physical separation the stars are not gravitationally bound systems. They are simply two stars which lie along the same line of sight when observed from earth.

The classifications shown above are based only on the methods of observation, but there have been other techniques suggested. This classification which is based on method of observation, for example, is not unique. For instance, all eclipsing binaries are at least potentially spectroscopic binaries. Unresolved visual binaries can also be observed spectroscopically. Some systems can be observed in three different ways. In general, a given binary can be placed in more than one of the classifications listed above.

Depending on the position of the component stars in the Hertzsprung-Russell diagram, a different scheme of classification has been suggested (Sahade 1960). Kopal (1955) also proposed a classification based on another criterion, where the presence of a companion star sets an upper limit to the size that the star can reach. Classification according to Kopal divides all binaries into three categories: *contact*, *detached* and *semi-detached* systems. The advantage of Kopal's system is that it employs information on radii and masses of the stars to classify the binary system. Plavec (1964) suggested the combination of Kopal's classification and a scheme which is based on the Hertzsprung-Russell diagram, and it was considered to be the best classification. Binary stars can still be classified differently on the basis of their mutual separation, considering how 'close' or 'wide' they are from each other. In 'close' binaries the separation ranges from about one AU down to the radius of the stars and the orbital period ranges from a few hours to a few years. In 'wide' binaries the separation between the components is tens or hundreds of astronomical units and their orbital periods range from tens to thousands of years. In conclusion, it seems that a general or comprehensive system of classification of

binary systems might not be possible even if classifications which exist so far are fairly adequate to study binary systems.

1.6 δ Scuti Stars

If pulsating variables have spectral type A – F with pulsation periods between 18 min - 8 hr and light amplitudes ranging from thousandths of magnitude to some tenths, we call them δ Scuti stars. These stars have masses in the range of 1.5 - 2.5 $M\odot$. They have higher density than large amplitude pulsating variables such as classical Cepheids from their position on the H-R diagram.

The δ Sct stars are located on an extension of the Cepheid instability strip to the main sequence and show multiple frequency pulsations ranging from 5 to 50 cycles per day. Zwintz et al. (2014) pointed out that in addition to main sequence and more evolved sub-giants, δ Sct pulsations have also been detected in pre-main sequence stars, providing important information for early stellar evolution of the stars. The driving mechanism in these stars is κ *mechanism* (Breger 2000) in the He II partial ionization zone. They pulsate in radial or non radial modes, low-order, low-degree pressure (p) or mixed pressure (p) and gravity (g) type modes. The simplest form of pulsation is radial pulsation which is a simple, spherically symmetric 'in-and-out' expansion and contraction. Another form of pulsation is non-radial pulsation, where the star changes shape, not volume. For Cepheid variables, RR Lyrae stars, δ Sct stars, β Cep stars and for most of the pulsating variables seen in Fig.1.3 the driving mechanism is connected with the opacity. In those zones of the star where the gases are partially ionized, part of the work done on the gases as they are compressed produces further ionization rather than raising the temperature of the gas. With a smaller temperature raise, the increase in density with compression produces a corresponding increase in the Kramers opacity. Similarly, during expansion, the temperature does not decrease as much as expected since the ions now recombine with electrons and release energy. Again, the density term in Kramers law dominates, and the opacity decreases with decreasing density during the expansion. This layer of the star can thus absorb heat during compression, be

pushed outward to release the heat during expansion, and fall back down again to begin another cycle. *Partial ionization zones* are the pistons that drive the oscillations of stars; they modulate the flow of energy through the layers of the star and are the direct cause of stellar pulsation (Carroll & Ostlie 1996).

Pulsating stars are not generally found uniformly over the HR diagram. Instead, most pulsating stars occupy a narrow, vertical band of the HR diagram, both above and below the main sequence. This region in which stars pulsate is called the *instability strip* (Fig.1.3). The main instability regions are the Cepheid strip, including its intersection with the main sequence (dashed line), the region of the coolest stars (Miras and their relatives), and the region of the Beta Cepheid and SPB stars. There are also instability regions along the white dwarf cooling track (dotted line) at the bottom of the diagram, including the nuclei of planetary nebulae (PNNV) and pulsating white dwarfs (DOV, DBV and DAV). Further reviews and descriptions of basic properties of δ Sct stars are given by Breger (2000) and Percy (2007).

Both ground and space based observations of δ Sct stars show they pulsate in many radial and non-radial modes covering a wide range in frequencies. Much of the driving mechanism in the cooler δ Sct stars is a convective blocking mechanism. There are a large number of observed frequencies in some δ Sct stars and in a few of these stars the spherical harmonic degree of many of these modes are known. Pulsating main sequence or giant A-F stars of solar composition ('classical' δ Sct stars) have been particularly well studied, since they give good prospects for asteroseismology. This is because many independent pulsation modes have been detected, they are bright, numerous and also they are easy to observe.

The high-amplitude δ Sct stars (HADS) are intermediate between δ Sct stars and classical Cepheids. Most of the time, HADS are slow-rotating and pulsate radially with peak-to-peak amplitudes exceeding 0.3 mag in V. Many other δ Sct stars are faster rotating with many low-amplitude radial and non-radial modes. The best candidate for asteroseismology is a star which is rotating very slowly (or not rotating) and one that is at near zero-age main sequence stage. In determination of

the large and small separations, slow rotation minimizes confusion by rotational splitting. It may be due to these cases that no entirely satisfactory asteroseismic solution has emerged for any δ Sct stars.

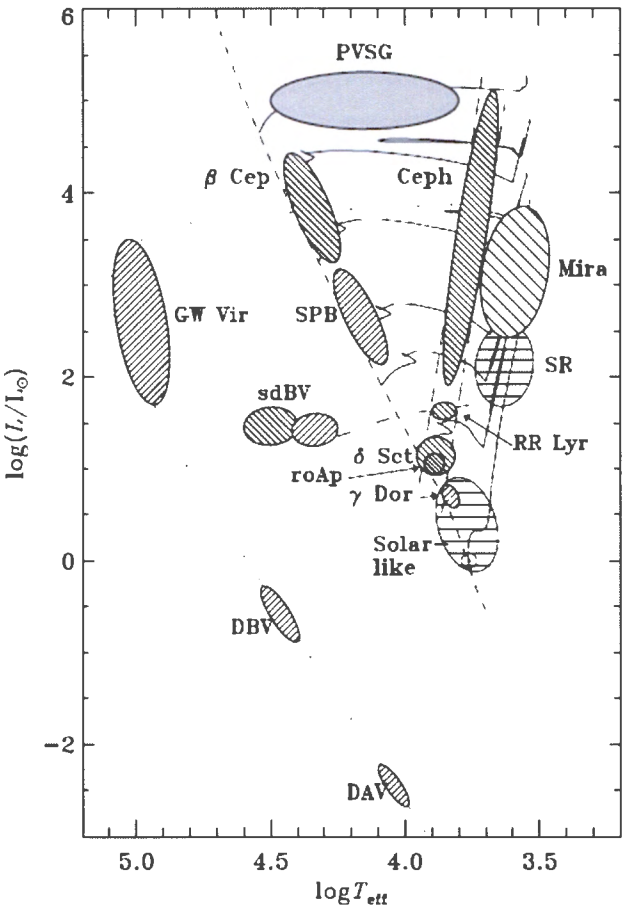

Figure 1.3: A pulsation HR diagram showing instability strips of various classes of pulsating stars for which asteroseismology is possible (Aerts et al. 2010).

1.6.1 Effect of Pulsation on Binarity

Thousands of stars are now known to be variable. Pulsation is only one mechanism responsible for variability. A pulsating star is a type of star in which brightness variations are caused by changes in the area and temperature of the star's surface layers. Astronomers use the word pulsation for vibration or oscillation of a star. The Milky Way Galaxy is estimated to contain several million pulsating stars. Considering that our Galaxy consists of several hundred billion stars, this implies that the stellar pulsation must be a transient phenomenon (Carroll & Ostlie 1996). A pulsating star in a binary system acts as a clock. If the star is one member of a binary system, its distance will vary as it orbits the barycentre, which results in a variable phase of pulsation (Shibahashi & Kurtz 2012; Murphy et al. 2014).

The simplest form of pulsation is radial pulsation, which is a simple, spherically symmetric 'in-and-out' expansion and contraction. Another form of pulsation is non-radial pulsation, where the star changes shape, not volume. The two main non-radial modes are pressure modes, in which the motion is primarily radial and the restoring force is pressure and the other modes are gravity modes, in which the restoring force is buoyancy or gravity. The radial oscillation of a pulsating star is the result of sound waves resonating in the interior of the star. Such a mechanism can exist in a star as a result of the thermodynamic effect of partial ionization zones. A driving mechanism for the changes in luminosity of many types of pulsating variables located in the instability strip is called the κ mechanism. δ Sct, Classical Cepheids, WW Virginis and RR Lyrae are among the group of pulsating stars. Excellent overviews of pulsating stars in multiple systems is given by Lampens (2006) and Pigulski (2006).

In a binary system, determination of orbital elements can be affected by the pulsation of one of the component stars, or by the presence of an undetected third body. For example, Soydugan et al. (2006a) reported results of relationships between pulsational and orbital periods. The study includes a compilation of orbital periods and pulsational periods gathered from the literature, and a discussion of their possible relationship as a function of stellar radius and mass. This resulted in the

preparation of a list of potential candidates for pulsating variables in close binary systems in a catalogue prepared by Soydugan et al. (2006b). Originally, Tsvetkov & Petrova (1993) investigated the idea of pulsational and orbital period.

Different observations have been conducted for a search of δ Sct stars in close binary systems (Mkrtichian et al. 2002; Kim et al. 2002). Additional reports on the general properties of close binary systems and pulsating components are given by Pigulski & Michalska (2007), Turcu et al. (2008), Liakos & Niarchos (2009) and Dvorak (2009). However, despite their benefits, pulsating binaries can be difficult to analyse since signals of two different origins must be disentangled. As we will see later in the *Kepler* observations for δ Sct binaries, the periodic flux variations caused by stellar pulsations are far more prominent than the binary signal. A better solution is obtained by treating binary and pulsation signals separately and using an iterative method to solve the problem (Debosscher et al. 2013; Maceroni et al. 2013, 2014). In our case we have used periodograms and 'binarograms' to deal with pulsations and orbital period respectively. The iterative method of determining the orbital parameters is described in Section 1.8.3.

1.6.2 Periodogram

Any time series can be expressed as a combination of *sine* or *cosine* waves with differing frequencies and amplitudes. The plot of amplitude as a function of frequency is called a *periodogram*. A periodogram is used to identify the dominant periods (or frequencies) of a time series of data to identify any intrinsic periodic signals. This can be a helpful tool for identifying the dominant cyclical behaviour in a time series, particularly when the cycles are not related to the commonly encountered seasonality. For example, Fig.1.4 shows the periodograms of the two δ Sct *Kepler* stars KIC 4936524 and KIC 5200544.

A periodogram is similar to a Fourier Transform, but is optimized for uneven time-sampled data and for different shapes in periodic signals. In astronomy, unevenly sampled data is particularly common, where a target might rise and set over several nights, day-time changes, due to weather conditions or data gaps that naturally

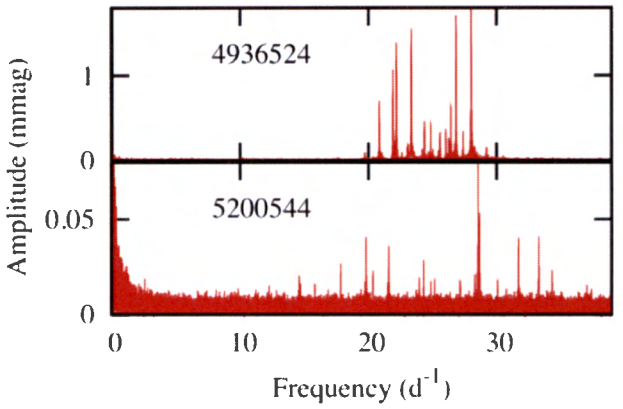

Figure 1.4: Periodograms of δ Sct *Kepler* stars KIC 4936524 and KIC 5200544 (Balona et al. 2013).

arise (for example, the time taken for the data to be sent to Earth from the *Kepler* spacecraft).

The classical periodogram was defined originally in 1898 by Schuster and it is called a *Schuster periodogram*. If the data are regularly spaced in time, the Schuster periodogram is a simple method and a basic tool for evaluating the power spectra (Terebizh 1992). In most cases, it is also adequate for frequency analysis. If data is sampled at equal time intervals, one can also use the discrete Fourier transform (DFT); and the Fast Fourier transform (FFT) is an efficient algorithm to compute the DFT and its inverse. However, there are few cases where the FFT can be applied directly to time series in astronomy, although it is widely used in imaging and signal processing. If the data are nearly equally spaced, one can interpolate to a grid of evenly spaced times and then use FFT methods.

Another method of data analysis is the *Lomb-Scargle Periodogram*. This periodogram was introduced by Lomb (1976) and further improved by Ferraz-Mello (1981) and Scargle (1982). It is defined differently from the classical periodogram. It is slow and in most cases offers no significant advantage over the Schuster periodogram. The methods discussed so far are suitable for pulse shapes which are

approximately sinusoidal. If the shape of the pulse is quite different from sinusoidal, power is shared by many Fourier harmonics and these methods perform poorly. In such a case one can use the phase dispersion minimization method. Given frequency values, one bins the light curve into 10 phase bins for example and calculates the scatter within each bin. The value that minimizes the sum of the variances in the phase bins is the best fitting frequency. If the number of bins is properly chosen, this method can give good results even when the pulse shape is far from sinusoidal.

In pulsational frequency analysis, it is the patterns in the frequencies that lead to astrophysical inference (Unno et al. 1989; Aerts et al. 2010). For the *Kepler* data, we used a Fortran program to calculate the Lomb-Scargle periodogram of a pulsating star in the binary system. This is shown in detail in Chapter 2.

1.7 The *Kepler* Space Telescope

1.7.1 Overview of *Kepler*

Kepler is NASA's tenth 'Discovery' mission, an Earth-trailing heliocentric orbit. It was designed to survey our region of the Milky Way galaxy to detect potentially hundreds of Earth-size planets orbiting in or near the habitable zone of Sun-like stars (FGKM dwarfs). The *Kepler* space telescope was launched on 6 March 2009 and ended its primary mission on 11 May 2013 after a second reaction wheel failed and pointing could no longer be kept stable. Because the earth's atmosphere is a turbulent mix of gases in constant motion which brings distortion to telescope images, searching Earth-size planets orbiting other stars is almost impossible with ground-based telescopes. Planets are detected using the transit method as they pass in front of their stars.

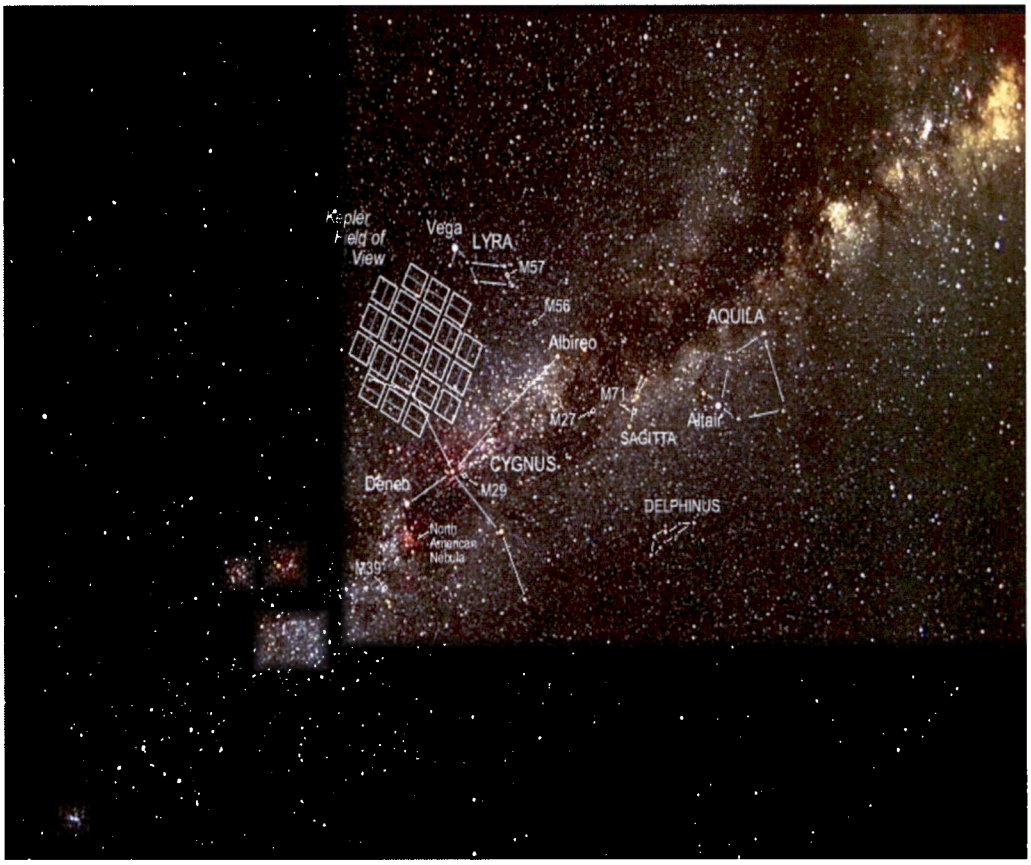

Figure 1.5: *Kepler* field of view (Image credit: www.nasa.gov).

Kepler was kept continuously pointing towards the same field in a region of the sky in the constellation of Cygnus and Lyra centred on galactic coordinates $l = 76.32°$, $b = +13.5°$ (RA = 19h 22m 40s, DEC = $+44°$ 30' 00). Fig.1.5 shows the field of view of the *Kepler* Spacecraft. *Kepler* observed over 150,000 stars over a time span of four years. One of the main successes of *Kepler* lies in its unprecedented near-micromagnitude photometric precision. The *Kepler* spacecraft is in a 372.5-days period, heliocentric Earth-trailing orbit, that can maintain a stable trajectory that keeps the spacecraft within telecommunications capability. Fig.1.6 shows the orbit of the *Kepler* satellite around the sun. This orbit is oriented to avoid the high-radiation risks associated with an Earth orbit, but it is subject to energetic particles from solar flares and cosmic rays.

Once every three months the spacecraft was pointed towards Earth to download the data stored, and approximately every 90 day the *Kepler* space craft rotated 90 degrees around one of its axes to orient the solar panels and sun shields towards the Sun. Therefore, the data came in so-called Quarters of 90 days. The quarters are denoted by Qn, and Short Cadence (SC) data are further subdivided into three one-month segments, denoted Qnm. This shows that the data contains gaps corresponding to both the quarterly rolls and monthly downlink times. The first 10 days of science data obtained during the initial commissioning time is referred to as Q0. After this comes the first operational data set, Q1. Subsequent quarters are referred to as Q2, Q3, etc. During the whole operation time, *Kepler* collected data in eighteen quarters. Thus the length of *Kepler* time series from Q0 to Q17 is about 1450 days.

Kepler's early science results, mission and data characteristics have been presented by different authors. Description of the mission design was given by Koch et al. (2010), an overview of the processing pipeline by Jenkins et al. (2010a), science operations by Haas et al. (2010) and target selection by Batalha et al. (2010). The first use of data for asteroseismology was presented by Chaplin et al. (2010). Characteristics of the long cadence were given by Jenkins et al. (2010b), characteristics of the short cadence by Gilliland et al. (2010), findings of the first *Kepler* planets by Borucki et al. (2010) and Dunham et al. (2010), instrument performance by

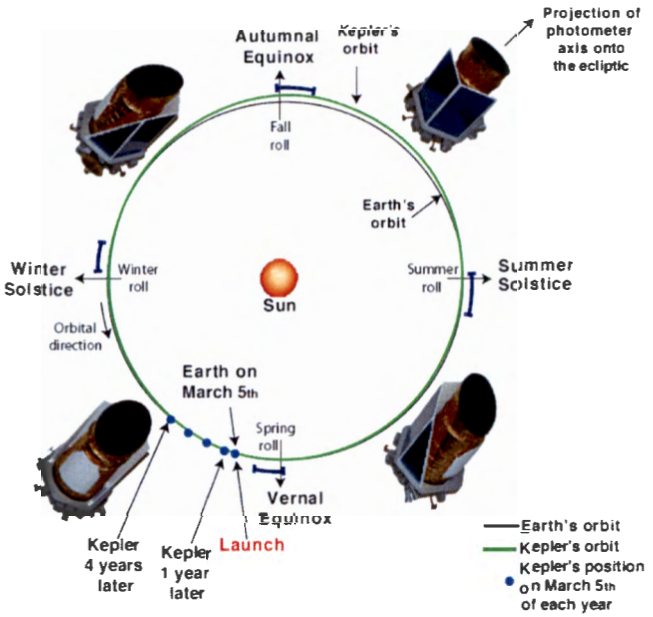

Figure 1.6: Orbit of *Kepler* around the Sun (Image credit: www.nasa.gov).

Caldwell et al. (2010), and *Kepler* point spread function by Bryson et al. (2010).

1.7.2 Scientific Goals and Objectives

The primary goal of the *Kepler* Space Mission (Koch et al. 2010; Borucki et al. 2010) was to survey our region of the Milky Way galaxy to detect potentially hundreds of Earth-size or larger planets in or near the habitable zone of sun-like stars and determine how many of the billions of stars in our galaxy have such planets. The outcome of the mission will allow scientists to put our solar system within the continuum of planetary systems in the galaxy.

The scientific objective of the *Kepler* Mission was to explore the structure and diversity of extrasolar planetary systems. This was to be achieved through observation of very large samples of stars. These samples allow us to: determine the percentage of terrestrial and larger planets that are in or near the habitable zone of a wide variety of stellar spectral types of stars, determine the distribution of

sizes and shapes of the orbits of these planets: and estimate the number of planets in multiple-star systems. The samples of the stars further help us to determine the variety of orbit sizes and planet reflection properties, and the sizes, masses and densities of short-period giant planets, to identify additional members of each photometrically discovered planetary system using different techniques, and to determine the properties of those stars that harbour planetary systems.

Asteroseismology was secondary to the main goal of the mission, however it has contributed vital information about host stars which can be used for planet characterization. From the original transit method, transit depths give only the ratio of the planet and the host star radii. However, asteroseismology allows further analysis of the interior of the star, and according to Stello et al. (2009), it can also give us the radii of solar-like pulsators.

Kepler has been successful in advancing studies of stellar astrophysics due to its high-precision photometry from space at a level of a few micromagnitudes. At this level of precision, it is possible to observe additional interesting properties of stars which cannot be seen from ground- based observations. One example is the finding which shows that most δ Sct stars have unexpectedly low frequencies attributed to γ Doradus pulsations (Grigahcène et al. 2010).

Prior to the launch of *Kepler*, the *MOST* satellite (Walker et al. 2003) and the *CoRoT* satellite (Baglin et al. 2006; Auvergne et al. 2009) provided precise photometry from space. However, because of their Earth orbits, the noise levels were often very high and the data needed extensive correction before they could be used. *Kepler's* heliocentric orbit and larger telescope aperture allowed for a very low noise level and even more precise photometry. Because the satellites probed different regions of the Milky Way, the large numbers of targets from the satellites allowed for population studies as pioneered by Miglio et al. (2009). In general, even though the main goal of *Kepler* was to search for transit exoplanets, the unparalleled quality of the measurements allowed for numerous breakthroughs in the field of stellar astrophysics through asteroseismology. This seismic analysis of data is organized in the *Kepler* Asteroseismic Science Consortium, KASC, cur-

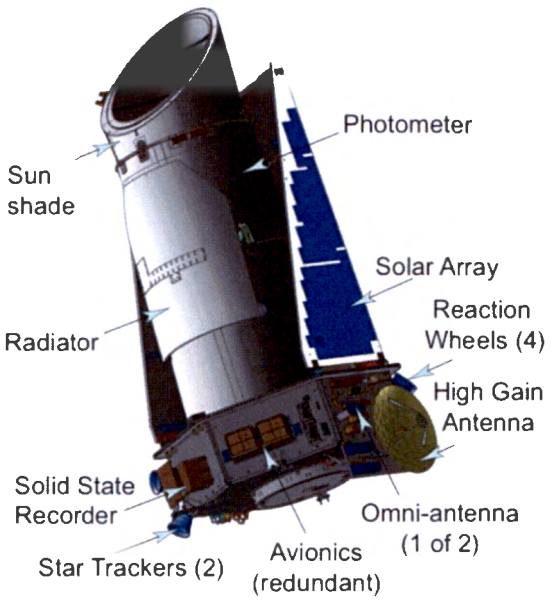

Figure 1.7: *Kepler* spacecraft (Image credit: www.nasa.gov).

rently one of the largest consortia in astronomy.

1.7.3 *Kepler* Instrument

The *Kepler* Instrument (Fig.1.7) is a photometer with 0.95-meter aperture Schmidt type telescope and 1.4-meter primary mirror. The spacecraft is in a heliocentric Earth-trailing orbit allowing continuous coverage of its 115.6 square degrees field of view. The photometer camera has an array of 42 CCDs arranged in 21 modules with 2200 $\times$ 1024 pixels, where each pixel covers 4 arcsec. The 42 CCDs had four-fold symmetrical pattern on the sky so that after each quarterly roll the telescope still covers the same area of the sky and the same stars stay visible during the mission. *Kepler* spacecraft has a very wide field of view for an astronomical telescope of about 15° in diameter.

The *Kepler* point-spread function has an average of 95 percent encircled energy

width of 4 pixels diameter. An average of 47 percent of the flux is also recorded in the central pixel for a star centered on a pixel. Out of about half-million targets in the field of view brighter than 16th magnitude, only about 30 percent have been targeted.

Sampling Rate

Kepler observations were taken at regular intervals according to the clock on-board the spacecraft and obtained in two different sampling rates: in long-cadence (LC) mode with integration time of 29.43 minutes and short-cadence mode with integration time of 58.8 seconds. Most photometry observed by *Kepler* consists of almost uninterrupted long-cadence (LC) observations. These cadences give the data an excellent option for asteroseismic investigations. All the data in this thesis are taken only from the long cadence mode. Characteristics of LC data are further described in detail by Jenkins et al. (2010b) and SC data descriptions have been presented by Gilliland et al. (2010).

Nyquist frequency is the highest frequency which can be resolved in a power spectrum. It is the inverse of twice the time step for equally spaced sampling. Since frequency resolution depends on the length of the dataset, it is critical to know how close together the values of two pulsation frequencies are. Therefore, increasing the number of orbits further sharpens the peaks and resolution will also be better. In equally spaced data, there can be an infinity of frequencies that fit the data equally well and true frequency is not uniquely identified. This shows that in the case of sampling with a uniform cadence, external physical constraints are necessary to select the frequency range that is appropriate for pulsating stars. Murphy et al. (2013b) showed how the correction of the times of observations of *Kepler* data to the Solar System barycentre generates a time-dependent Nyquist frequency. This completely removes all Nyquist alias ambiguities in the amplitude spectrum.

The highest frequency that can be detected in LC mode (the Nyquist frequency) is about $\nu_{Ny} \approx 24.27 d^{-1}$. Many astrophysical objects, e.g. solar-like oscillations, δ Sct, roAp and sdB stars, etc. pulsate at higher frequencies. A higher sampling rate

is very expensive in terms of resources and thus SC mode is normally limited to a few thousand stars in each quarter. If a source varies periodically with frequency ν, then the periodogram of the LC data will show peaks at alias frequencies given by $|\nu + 2n\nu_{Ny}|$, where n is a positive or negative integer. The peak of highest amplitude will be at $n = 0$ or at the smallest value of n within the measured frequency range. However, if the data is sampled at exact time intervals, the alias peaks will have the same amplitude. Fortunately, the time sampling in the *Kepler* light curves is not quite equally spaced, allowing the true frequency to be selected according to the peak of highest amplitude.

It should also be noted that a low-frequency signal is sampled more often over its cycle than a high-frequency signal. For example, a signal with a period of 1 d is sampled with about 24 data points in LC mode, whereas a signal with a period of 0.5 d is sampled with only 12 data points over its cycle. During the duration of an exposure, the intensity of the signal is integrated, which means that even if the 1 d and 0.5 d signals have exactly the same amplitude, the 0.5 d signal will be measured with a slightly lower amplitude. For a Fourier peak with true amplitude A_0 , it can be shown that the observed amplitude, A, is described by the equation

$$A = \frac{\sin \pi/n}{\pi/n} A_0, \tag{1.1}$$

for n points per cycle (Murphy 2012).

The SC exposure time implies that because of integration of more exposures to make the LC data, there are 30 times more SC points than LC points in a quarter. For SC data, this results in bringing an increased sampling rate for resolving short time-scale events such as flares. The Nyquist frequencey of LC data can also be a limiting factor in analysis of short data sets. Therefore, another consideration related to different cadences in *Kepler* data is their different Nyquist frequencies. There are many stars that pulsate with frequencies higher than the Nyquist frequency. For example, Solar-like oscillations and pulsations in roAp occur only at frequencies much higher than the LC Nyquist frequency. But δ Sct stars can have frequencies on both sides of this Nyquist frequency since δ Sct pulsators have frequency ranges of 5 to 50 d^{-1}.

Gaps in the Data

Because of its heliocentric orbit, *Kepler* data may be considered nearly continuous at its normal micromagnitude precision. Some of the gaps were scheduled while some were unplanned. Every quarter (four times per orbit), the spacecraft rolled 90 degrees to maximize electric power production and thermal control by making its solar panels face the sun. This caused short gaps in the observed light curve and made the stars fall on different CCD modules, which deviated in sensitivity and lead to observed flux which is variable. In addition to the gap created due to the downlink that took place at each quarterly roll, there is also another gap due to two more downlinks occurring at approximately 30-d intervals in the middle of each quarter which divides the data into three 'months' per quarter. These two events represent the most frequent gaps in *Kepler* data corresponding to both the quarterly rolls and monthly downlink times. In the previous sections, we have seen that *Kepler* data are available in two cadences, the long cadence (LC) and short cadence (SC). Both cadences are stored on-board and downlinking every 30-d introduces gaps up to $\sim 24\,h$ in length during which data was not taken by the photometer.

Other gaps also occurred on *Kepler* data. For example one gap is due to an occasional safe-mode event. This happened when Q8 started and this gave about 18 d of data outage counting from the end of Q7. The other gap is due to fine pointing loss. This happened due to the regular event of 'reaction wheel angular momentum desaturation'. Desaturation is necessary since the solar radiation torque causes angular momentum to build up in the reaction wheels. Christiansen et al. (2012) explained that the telescope went into coarse point mode and fine pointing control was not maintained for a few hours. Desaturation occurred approximately every three days and the events were flagged in the fits files obtained at MAST. Large gaps in *Kepler* data have two main consequences. One case is that Earth-like planet transits that are rare events might be missed. The other is that data for frequency determination, which is useful for the calculation, can be lost. The largest gap (one Quarter; $\sim$ 93 d) in *Kepler* data was due to the failure of Module 3. Module 3, which consisted of two CCDs, unfortunately failed during its early mission. Due

to this failure, for three quarters of the year, only a small fraction ($\sim 4/21$) of the field of view was observable.

Apart from the above cases, for some targets, random flux discontinuities were observed since the first flight data as shown in Jenkins et al. (2010b). These discontinuities were not the same as discontinuities introduced into many of the target light curves as a result of spacecraft activities and anomalies (monthly downlinks, safe modes) and commanded altitude adjustments. The random flux discontinuities might be due to the impact of cosmic rays or other energetic particles on CCD pixels, or abrupt decreases in sensitivity.

Filtering Data

Kepler data processing and calibration pipeline convert raw data numbers recorded on the spacecraft into calibrated pixels and corrected and time-stamped photometric light curves in three different software modules. The software modules are Calibration (CAL), Photometric Analysis (PA) and Pre-Search Data Conditioning (PDC). Calibration is a program that converts raw data numbers for each observation (cadence) into calibrated pixels. Raw data include photometric (target with background observation) pixels and also additional pixels that are used to eliminate smear, bias and other instrumental artefacts. For the case of PA, timestamps are assigned, then background signals are removed and photocenters are computed. Next, PA performs optimal aperture photometry using the aperture definitions determined during target management. A calibrated light curve with the generated error will be the final result. The science data acquired are processed in the *Kepler* science processing Pipeline (Jenkins et al. 2010a; Middour et al. 2010). The task of PDC is to find systematic error corrections to the light curves derived by PA. This software module corrects instrumental signatures including thermal effects, pointing drift, velocity aberration and cosmic rays.

Two forms of *Kepler* data were available. The Pre-search Data Conditioned (PDC) and the Simple Aperture Photometry (SAP). The *Kepler* SAP photometric data contains discontinuities, outliers, drifts, jumps, systematic trends and other instrumental signatures. There is a zero-point difference between data in different

quarters and the instrumental drift varies from quarter to quarter. PDC can be considered as a more processed version of SAP. PDC data have fewer jumps, drifts, and outliers which therefore gives cleaner light curves and Fourier spectra. Therefore, PDC can be considered as 'corrected' flux. The PDC flux uses the best fit that simultaneously removes systematic effects while reducing the signal distortion and noise injection. Stumpe et al. (2012) presented further explanations on the fitting procedures. The above fact also tells us that noise in the periodogram can be vastly reduced by analysing the PDC data instead of SAP data. In this thesis, the PDC flux has been used.

As shown in Klaus et al. (2010a,b), the standard PDC task for LC and SC science data processing was a single module output for a duration of one quarter or one month. Corrected flux light curves (with harmonic content) for LC and SC targets were then exported periodically to the MAST. PDC is designed to remove discontinuities as discussed above, but it is still possible that residual long-term instrumental effects were present at a low level. Balona et al. (2015) performed a simple simulation where they applied their own correction to the SAP data of a few stars which appeared to be the least variable among 20000 *Kepler* stars. The simulation result showed that frequencies higher than about 0.08 d^{-1} were not affected by the crude correction procedure so that frequencies higher than 0.08 d^{-1} were easily recovered. To correct the SAP data, Balona et al. (2015) fitted and removed low degree polynomials to each individual quarter.

1.8 Binary Star Orbits

True orbits can be all shapes and sizes from circular to elongated ellipse orbits. Orbital inclination varies from $0°$ in which the orbit is face on, to $90°$. The actual motion of the components of the binary are about the center of mass (also known as the *barycenter*). It is possible to show that this motion is also elliptical and obeys a version of *Kepler's* third law. When we can only observe one star in the binary system, the orbital shape of the barycentric orbits is important. If we can see both stars and can identify the motion of the barycenter, then we can identify

the individual masses of the stars.

In most cases, the motion is described by the fainter star relative to the brighter star that is located near the focus of the ellipse. This can be calculated from *Kepler's* third law where we have to know the geometry of an ellipse. Analysis of the orbital parameters of binary star systems gives important information about a variety of stellar characteristics. The methods used to analyse the orbital data vary somewhat depending on the distance of the observer, geometry of the system and the relative masses and luminosities of the components (Carroll & Ostlie 1996). In the following sections, we will review different mechanisms of determining orbital parameters and then derive time delay as a function of the orbital parameters. We will also discuss ways of finding differential correction to the elements.

1.8.1 Methods of Determining the Orbital Elements

Six quantities are needed to describe the orbit of a binary system. These are the projected semi-major axis $a \sin i$, eccentricity e, angle of periastron ω, time of periastron passage $T_{\rm per}$, orbital period P and the zero point of velocity (velocity of the barycenter with respect to the observer γ). Other useful ancillary quantities are the semi-amplitude of the radial-velocity curve, K and the mass function, $f(m)$. Stars with $K > 300$ km/s are likely not to be binaries and K cannot exceed the upper limit for orbital velocity at the surface of the star. For δ Sct stars which have masses in the range $1.2 < M_{\odot} < 2.2$, and radii in the range $1.5 < R_{\odot} < 4$ solar radii, this velocity cannot exceed about 300 km/s. The angle of periastron is the angle between the ascending node and the periastron (the point in the orbit where the stars are closest together). The ascending node is a point where the orbiting star would be moving away from the earth. The time of periastron passage on the other hand is the time at which the orbit of a star goes through its periastron.

Five of these parameters (with the exception of zero point of velocity) and the ancillary quantities are also orbital elements which this thesis aimed to find. In practice, it is usually convenient to determine the orbital period separately from the other elements, although in theory it is possible to determine it with the other

elements. In our case, we determined the orbital period separately first as it is shown in Chapter 2. Sometimes the orbital period P is also regarded as an extra orbital element since it can be calculated from *Kepler's* third law.

The determination of the elements can be carried out in two general ways, using a graphical method (not used any more) or an analytical method which is usually based on the principle of least squares. According to Batten (1973), any method of solution, whether graphical or least squares, must be iterative. Wyse & Kron (1939) and Kopal (1947) developed methods of finding differential corrections to graphically determined elements. For the least squares method, the principles can be applied only when the observational errors are distributed according to the normal law, and also when the equations of condition are linear in the unknowns. Such kinds of restriction to linear equations of condition imply that the least squares solution must be used for differential corrections to values of the orbital elements already approximately known. However, there are some conditions in which least squares solutions can break down. A spectroscopic binary with an orbit of small eccentricity is a known example.

In circular orbits, the elements ω and $T_{\rm per}$ do not have significance, and when the eccentricity is very small the two elements become practically indeterminate by graphical or geometrical methods. Since the coefficients for the differential corrections will be nearly equal, it is impossible to find corrections to both elements from the same least squares solution if approximate values are assumed. As proposed by Wilsing (1893), Russell (1902), Zurhellen (1907), Plummer (1908) and Paddock (1915), an analytical method gives better results for such kind of orbits. This means that the normal equations of Lehmann-Filhés (1894) fail because the coefficients of the corrections $\Delta\omega$ and $\Delta Tper$ are almost proportional to each other and the equations become indeterminate. To consider such kinds of situations, Sterne (1941) suggested an alternative method of solution which is particularly important for orbits which are nearly circular.

Since observational errors exist, spectroscopic binaries with eccentricities close to zero should be assigned circular orbits as proposed by Lucy & Sweeney (1971).

Their argument was based on statistical considerations to test the reality of an observed orbit being nearly circular regardless of the orbital period. Skuljan et al. (2004) however, did not agree with such reasoning. There are many further descriptions of the determination of orbits of binary stars. For example, van den Bos (1962) gave good explanations of visual binaries. Similarly, Kopal (1959) and Petrie (1962) explained descriptions of orbit determination of eclipsing and spectroscopic binaries respectively. Many authors applied either geometrical or analytical methods to determine the orbit of a binary system in their work. Lehmann-Filhés (1894) introduced a geometrical method to determine the orbital elements of a binary system from the geometrical nature of the radial velocity curve, like properties of the curve at minima and maxima. This method also considers another geometrical condition that the area of the velocity curve must be equal for the portions of the curve above and below the V-axis where V is velocity of the center of mass of the binary system. Using the method of least squares, differential corrections to the preliminary elements can also be used in order to improve the final solution of the orbit.

Russell (1902) presented an analytical method to change the observed radial velocity to a Fourier series, and the orbital elements are obtained by comparing this series with the corresponding analytical expression of the radial velocity. Compared to the method of Lehmann-Filhés (1894), this one is longer and more laborious, specially when the eccentricity is much greater than 0.4.

Similar to the method of Russell (1902), Singh (1984) presented a method of expanding radial velocity as a Fourier (trigonometric) series. To determine preliminary elements by a least square correction, this technique gives a standard set of velocity curves for given values of eccentricity, and the longitude of periastron. Karami & Teimoorinia (2007) reported a new method of non-linear least squares velocity curve analysis for spectroscopic binary stars. The method is faster than the Lehmann-Filhés (1894) method, and it can also be applied for orbits of all eccentricities and inclination angles. They also proved that their method works well by applying in to a wide range of binaries (Karami & Mohebi 2007a,b; Karami et al. 2008; Karami & Mohebi 2009). A Non-linear regression method was pro-

posed by Karami & Mohebi (2007a) which can be used to determine the orbital parameters of spectroscopic binary stars. To analyse orbital elements of a binary system, a software application called Spectroscopic Binary Solver (SBS) was introduced by Johnson (2004) which is a different style from methods discussed before. In recent times, there are still varieties of techniques to describe orbits of a binary system. Ghaderi et al. (2012) applied the Probabilistic Neural Network (PNN) technique to obtain the orbital parameters of spectroscopic binary stars, and this is also applicable to all eccentricity types. This method was also tested previously by Bazarghan et al. (2008). Repeatability is one good criterion for the reliability of orbital elements when the systems are observed at different epochs. However, for spectroscopic binaries for example, independent determinations of orbital elements at different epochs have been made only for a few systems. Batten (1968) demonstrated that some of them showed suspected changes in the 'orbital elements,' most of which could not be considered as real changes in the binary system.

The BEER algorithm is also a different approach for binary star detection, especially for short period binaries (Faigler & Mazeh 2011; Tal-Or et al. 2015). Faigler & Mazeh (2011) introduced the BEER algorithm to find non-eclipsing short-period beaming binaries. There are three photometric effects caused by a short-period companion, namely the BEaming, Ellipsoidal, and Reflection periodic modulations. According to Loeb & Gaudi (2003), *Kepler's* photometric precision would be sufficient to detect short period companions. For instance, for binaries with typical RV semi-amplitudes of 10 - 100 km s^{-1}, the beaming amplitudes are in the range of 10^{-3} - 10^{-4} mag. From such result Zucker et al. (2007) proposed that *Kepler* and CoRoT can also detect hundreds of non-eclipsing binaries of this type, and create a new observational category of systems, beaming binaries. The beaming effect can be caused by the modification of the angular distribution of the radiated energy (stellar aberration). The source of ellipsoidal variation is tidal interactions between the two components of the binary. Reflection variation, originates from the brightness difference between the day side and the night side of each component.

Observing beaming binaries can have advantages compared to the eclipsing binaries because systems with edge-on inclinations can be detected. Furthermore, intrinsically rare systems such as brown dwarf and massive planetary companions to main-sequence stars can also be detected (Halbwachs et al. 2000; Faigler et al. 2013). Because of the three photometric effects mentioned above, several studies were effective in detecting the weak beaming effect caused by a transiting brown dwarf or even a transiting massive planet in *Kepler* and *CoRoT* light curves (Mazeh & Faigler 2010; Shporer et al. 2011; Jackson et al. 2012; Mislis et al. 2012; Mazeh et al. 2012). In fact, as soon as the first *Kepler* light curves became available, many studies reported the beaming effect of a few eclipsing binaries detected by *Kepler* (van Kerkwijk et al. 2010; Carter et al. 2011b).

1.8.2 Binary Star Orbit and Orbital Elements

The motion of the stars in a binary system can be considered in two ways relative to their common centre of mass or relative to each other. The barycentric orbit is an orbit of each body relative to the common centre of mass or the barycentre. Using *Kepler's* equation, the orbit of a star in a system can be calculated and the position and velocity of the star are functions of time. The gravitational force (which is the central force and also a conservative force) plays the most important role in the motion of stars in a binary system. Theoretically, time-delay is expressed as a function of time t and the orbital elements ($a \sin i$, P, e, ω and $T_{\rm per}$). Hence, these orbital elements can be obtained from the observed time-delay as the best-fitting set of parameters.

Let us consider the spectroscopic binary system shown in Fig.1.8, where only one component enables radial velocity measurements to be made (SB1 type binary). Each star in the system describes an elliptic orbit around the center of gravity, G. S is the position of one of the stars in its orbit with respect to G. L is the ascending node and we assume that the direction of motion is from A towards P.

Let a sphere be drawn with the center of gravity located at G. The straight line joining the earth to G cuts the sphere at K. The plane of the great circle where K

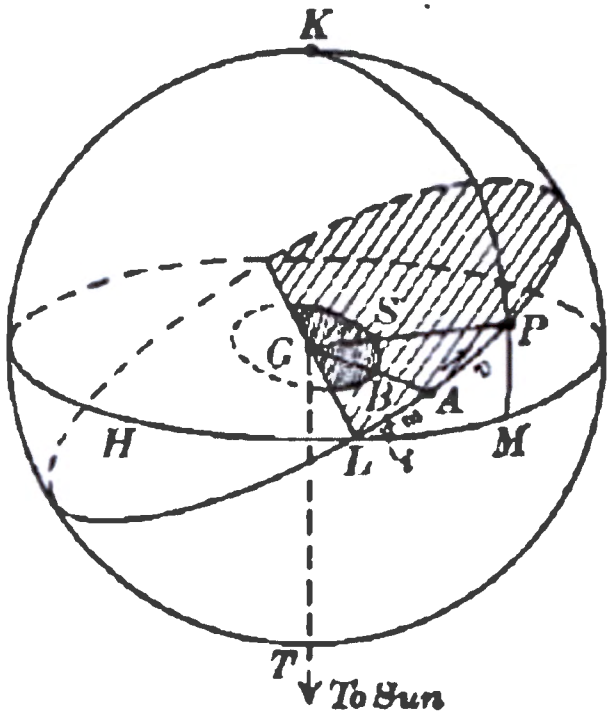

Figure 1.8: A representation of the orbit in space which is inclined at an angle i with respect to the observer (direction GT). The sphere centred on G is a construction which makes it easier to visualize directions and angles (Smart & Green 1977).

is its pole, represents the plane of the apparent orbit and KG is the line of sight. The great circle passing through L and P defines the plane of the true orbit of the companion star with respect to G. The straight line passing through G and L, which is the intersection of the two planes considered, is the *line of nodes*. B is the point on the true orbit at which the companion star is nearest the primary star. This point is called *periastron*. The other extreme point on the major axis is called *apastron*.

Let z denote the distance of S from the plane of HLM, having a positive value when S is on the same side of this plane as K, and let r be the distance between the centre of gravity and the star when its true anomaly is ν.

Therefore, the distance, z, of the star in the direction of an observer along the line of sight varies according to

$$z = r \sin(\nu + \omega) \sin i, \tag{1.2}$$

where i is inclination of the orbit, ν is true anomaly and ω is angle of periastron. In a binary system, the orbital plane is inclined to the equator of the celestial sphere by the angle i, which ranges from 0 to π. The star has orbital motion in the direction of increasing position angle, if $0 \leq i < \pi/2$. When $\pi/2 < i \leq \pi$, the star moves in the direction of decreasing position angle.

The distance r is given by:

$$r = \frac{a(1 - e^2)}{1 + e \cos \nu}, \tag{1.3}$$

where a is the semi-major axis and e is eccentricity.

The orbit of a binary star can be determined from the variation of its radial velocity as shown in Equation (1.4) where V_r is the radial velocity of the secondary star located at S with respect to the sun, γ is the systemic velocity or the radial velocity of the center of mass of the binary system with respect to the sun, $\frac{dz}{dt}$ is the radial velocity of star S relative to the center of mass G of the system.

$$V_r = \gamma + \frac{dz}{dt}, \tag{1.4}$$

$$\frac{dz}{dt} = \frac{d}{dt}[r \sin(\upsilon + \omega) \sin i] \tag{1.5}$$

$$= \frac{dr}{dt} \sin(\upsilon + \omega) \sin i + r \cos(\upsilon + \omega) \sin i \frac{d\upsilon}{dt}, \tag{1.6}$$

$$\frac{d}{dt}[r\sin(\upsilon+\omega)] = \sin(\upsilon+\omega)\frac{dr}{dt} + r\cos(\upsilon+\omega)\frac{d\upsilon}{dt} \tag{1.7}$$

$$\frac{dr}{dt} = \frac{d}{dt}[\frac{a(1-e^2)}{1+e\cos\upsilon}] \tag{1.8}$$

$$= [\frac{ae(1-e^2)\sin\upsilon}{(1+e\cos\upsilon)^2}]\frac{d\upsilon}{dt} \tag{1.9}$$

$$= [\frac{r^2 e\sin\upsilon}{a(1-e^2)}]\frac{d\upsilon}{dt} \tag{1.10}$$

$$= \frac{2\pi ae\sin\upsilon}{P(1-e^2)^{1/2}} \tag{1.11}$$

$$r\frac{d\upsilon}{dt} = \frac{r^2}{r}\frac{d\upsilon}{dt} \tag{1.12}$$

$$= \frac{2\pi a^2(1-e^2)^{1/2}(1+e\cos\upsilon)}{Pa(1-e^2)} \tag{1.13}$$

$$= \frac{2\pi a(1+e\cos\upsilon)}{P(1-e^2)^{1/2}}. \tag{1.14}$$

Therefore,

$$\frac{dz}{dt} = \frac{2\pi a\sin i}{P(1-e^2)^{1/2}}[e\sin\upsilon\sin(\upsilon+\omega) + (1+e\cos\upsilon)\cos(\upsilon+\omega)] \tag{1.15}$$

$$= \frac{2\pi a\sin i}{P(1-e^2)^{1/2}}[\cos(\upsilon+\omega)+e\cos\omega]. \tag{1.16}$$

If we denote the constant terms as

$$K = \frac{2\pi a\sin i}{P(1-e^2)^{1/2}}, \tag{1.17}$$

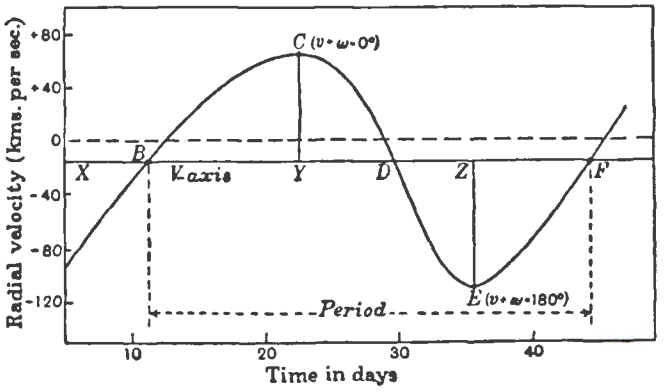

Figure 1.9: Radial velocity curve of a binary star HR 8800 with a period of 33.3 days (Smart & Green 1977).

then,

$$V_r = \gamma + K[\cos(v + \omega) + e\cos\omega]. \tag{1.18}$$

Equation (1.18) describes the radial velocity variations of one star orbiting with respect to G.. Fig.1.9 is the radial velocity curve and it gives the relation between the radial velocity V_r in km/s and the time t in days.

The radial velocity V_r reaches a maximum value when $\cos(v + \omega) = 1$, i.e., $v + \omega = 0^0$ when the star is entering the plane of the sky, and it reaches a minimum value when $\cos(v + \omega) = -1$, i.e. $v + \omega = 180^0$ when the star is exiting the plane of the sky.

When measured with respect to γ, maximum V_r is given by:

$$\alpha = V_r - \gamma = K(1 + e\cos\omega), \tag{1.19}$$

while minimum V_r is given by:

$$\beta = \gamma - V_r = K(1 - e\cos\omega) \tag{1.20}$$

From equations 19 and 20 we get

$$K = \frac{(\alpha + \beta)}{2}, \tag{1.21}$$

and

$$e\cos\omega = \frac{(\alpha-\beta)}{(\alpha+\beta)}. \tag{1.22}$$

Thus, the measured values of α and β can be used to determine the values of K and $e\cos\omega$.

Lehmann-Filhés Method

This method is one of the commonly used methods to derive orbital elements from the velocity curve. γ can be determined from the fact that the area BCD above this axis (γ) shown in Fig.1.9 is equal to area DEF below it. Let us measure these areas relative to γ:

$$Area\,BCD = \int_{z_B}^{z_D} \frac{dz}{dt}dt = z_D - z_B \tag{1.23}$$

$$Area\,DEF = \int_{z_D}^{z_F} \frac{dz}{dt}dt = z_F - z_D \tag{1.24}$$

But $z_F = z_B$ which shows that the two areas are equal i.e., Area BCD = Area DEF. γ therefore can be found either from planimetry or mathematical integration software. Points where

$$V_r - \gamma = K[\cos(\upsilon+\omega) + e\cos\omega] = 0 \tag{1.25}$$

have, $\cos(\upsilon+\omega) = -e\cos\omega$.

Hence,

$$\cos(\upsilon+\omega) = -e\cos\omega = \frac{-(\alpha-\beta)}{(\alpha+\beta)}. \tag{1.26}$$

We can now determine two areas A_1 and A_2 where A_1 = area CYD and A_2 = area DZE shown on the radial velocity curve. If we integrate the velocity curve relative to the points of inflection, which correspond to the nodal passage of the star:

$$A_1 = \int_{z_C}^{z_D} \frac{dz}{dt}dt = z_D - z_C = z - 0 = z \tag{1.27}$$

Similarly,

$$A_2 = \int_{z_D}^{z_E} \frac{dz}{dt} dt = z_E - z_D = 0 - z = -z \tag{1.28}$$

which shows that the two areas are equal, i.e. Area A_1 = Area A_2 = Δ_1.

At point D, $\cos(\upsilon + \omega) = -e\cos\omega$. Let υ_1 and r_1 be true anomaly and radius vector values at point D respectively. Using Equation 1.26 we get,

$$\cos(\upsilon_1 + \omega) = -e\cos\omega = \frac{-(\alpha - \beta)}{(\alpha + \beta)}. \tag{1.29}$$

which then gives:

$$\sin(\upsilon_1 + \omega) = [1 - \cos^2(\upsilon_1 + \omega)]^{1/2} \tag{1.30}$$

$$= [1 - \frac{(\alpha^2 - 2\alpha\beta + \beta^2)}{(\alpha + \beta)^2}]^{1/2} \tag{1.31}$$

$$= [\frac{4\alpha\beta}{(\alpha + \beta)^2}]^{1/2} \tag{1.32}$$

$$= \frac{2\sqrt{\alpha\beta}}{(\alpha + \beta)}. \tag{1.33}$$

A positive sign applies since point D lies between the ascending and descending nodes where z reaches a maximum positive value, i.e.,

$$z_2 = r_1 \sin(\upsilon_1 + \omega)\sin i = \Delta_1 \tag{1.34}$$

Let υ_2 and r_2 respectively be true anomaly and radius vector values at point F. A minimum negative value for z is reached at point F,

$$z_F = r_2 \sin(\upsilon_2 + \omega)\sin i = \Delta_2 \tag{1.35}$$

and

$$sin\,(\upsilon_2+\omega)=\frac{-2\sqrt{\alpha\beta}}{(\alpha+\beta)} \tag{1.36}$$

$$\begin{aligned}\Delta_1 &= \int_{z_1}^{z_2}\frac{dz}{dt}dt = z_2-z_1=z_2-0=z_2\\ &= r_1\sin(\upsilon_1+\omega)\sin i \end{aligned}\tag{1.37}$$

$$\begin{aligned}\Delta_2 &= \int_{z_4}^{z_1}\frac{dz}{dt}dt = z_1-z4=0-z_4=-z_4\\ &= -r_2\sin(\upsilon_2+\omega)\sin i. \end{aligned}\tag{1.38}$$

From Equations (1.33) and (1.36), $\sin(\upsilon_2+\omega)=-\sin(\upsilon_1+\omega)$.

Hence,

$$\frac{\Delta_1}{\Delta_2}=\frac{r_1\sin(\upsilon_1+\omega)\sin i}{-r_2\sin(\upsilon_2+\omega)\sin i}=\frac{r_1}{r_2}. \tag{1.39}$$

This is when we take both Δ_1 and Δ_2 as positive. Using Equation (1.3) radius vector at point D is given as:

$$r_1=\frac{a\left(1-e^2\right)}{(1+e\cos\upsilon_1)} \tag{1.40}$$

and

$$r_2=\frac{a\left(1-e^2\right)}{(1+e\cos\upsilon_2)} \tag{1.41}$$

Therefore, we can write Equation (1.39) as follows:

$$\frac{\Delta_1}{\Delta_2} = \frac{r_1}{r_2} \tag{1.42}$$

$$= \frac{(1 + e\cos\upsilon_2)}{(1 + e\cos\upsilon_1)} \tag{1.43}$$

$$= \frac{1 + e\cos[(\upsilon_2 + \omega) - \omega]}{1 + e\cos[(\upsilon_1 + \omega) - \omega]} \tag{1.44}$$

$$= \frac{1 + e\cos(\upsilon_2 + \omega)\cos\omega + e\sin(\upsilon_2 + \omega)\sin\omega}{1 + e\cos(\upsilon_1 + \omega)\cos\omega + e\sin(\upsilon_1 + \omega)\sin\omega} \tag{1.45}$$

$$= \frac{2\alpha\beta - \sqrt{\alpha\beta}\,(\alpha + \beta)\,e\sin\omega}{2\alpha\beta + \sqrt{\alpha\beta}\,(\alpha + \beta)\,e\sin\omega}. \tag{1.46}$$

Which then gives:

$$e\sin\omega = \frac{2\sqrt{\alpha\beta}}{(\alpha + \beta)}\left(\frac{\Delta_2 - \Delta_1}{\Delta_2 + \Delta_1}\right). \tag{1.47}$$

Therefore, using Equations 1.22 and 1.47 we can determine e and ω. Time of periastron passage $T_{\rm per}$ occurs for $\upsilon = 0$, in other words for:

$$V_r = \gamma + K\,(1 + e)\cos\omega \tag{1.48}$$

V_r can be determined since K, e, ω and γ are known. The possible ambiguity in where $T_{\rm per}$ falls in the velocity curve is resolved by noting that $(\upsilon + \omega) = 0^0$ at point B and $(\upsilon + \omega) = 180^0$ at point F in Fig.1.9.

The orbital period P can be found by curve fitting to the radial velocity data, typically by Fourier analysis or other similar techniques. The semi-amplitude of the velocity curve is

$$K = \frac{2\pi a\sin i}{P\,(1 - e^2)^{1/2}} = \frac{(\alpha + \beta)}{2} \tag{1.49}$$

Therefore,

$$a \sin i = \frac{P\,(\alpha + \beta)\,\left(1 - e^2\right)^{1/2}}{4\pi} \tag{1.50}$$

When the period is expressed in days (1 day = 86400 seconds) and α and β are given in Km/s, we get:

$$a \sin i = \frac{21600 P(\alpha + \beta)(1 - e^2)^{1/2}}{\pi} \tag{1.51}$$

Equation (1.51) gives the value of $a \sin i$ in kilometers. Unless the inclination i can be determined by other means, the semi-major axis a with respect to the center of gravity of the system cannot be determined.

Mass function

The masses of stars are the most useful factors in determining their evolution and the binary mass function is one important concept which helps to constrain the masses of the components in a binary system. When only one spectrum is detectable, the information concerning the masses of the stars is contained in the value of the mass function. If the system is a double-lined spectroscopic binary, we can determine the mass function for each component. Let a_1 denote the semi-major axis of one orbit, with respect to the center of gravity of the system, and a_2 the semi-major axis of the other orbit. Semi-amplitudes of the radial velocity curves can then be written as follows:

$$K_1 = \frac{2\pi a_1 \sin i}{P\sqrt{1 - e^2}} \tag{1.52}$$

$$K_2 = \frac{2\pi a_2 \sin i}{P\sqrt{1 - e^2}} \tag{1.53}$$

Therefore, we can re-arrange these two equations and write again as follows:

$$a_1 \sin i = \frac{\sqrt{1 - e^2}}{2\pi} K_1 P \tag{1.54}$$

$$a_2 \sin i = \frac{\sqrt{1-e^2}}{2\pi} K_2 P \tag{1.55}$$

Since we know that

$$m_1 a_1 = m_2 a_2 \tag{1.56}$$

and

$$GM = 4\pi^2 a^3 / P^2 \tag{1.57}$$

we make substitutions:

$$m_2 = m_1 (\frac{a_1}{a_2}) \tag{1.58}$$

$$= m_1 (\frac{a_1 \sin i}{a_2 \sin i}) \tag{1.59}$$

$$= m_1 (\frac{K_1}{K_2}) \tag{1.60}$$

Thus, the ratio of the masses can be derived. However, individual masses cannot be found unless i can be derived by other means.

Therefore,

$$G m_1 (1 + \frac{K_1}{K_2}) = \frac{4\pi^2}{P^2} (a_1 \sin i + a_2 \sin i)^3 / \sin^3 i \tag{1.61}$$

$$m_1 \sin^3 i = \frac{4\pi^2}{P^2} \frac{K_2}{G(K_1 + K_2)} (\frac{\sqrt{1-e^2}}{2\pi} P)^3 (K_1 + K_2)^3 \tag{1.62}$$

$$= \frac{P}{2\pi G} (1-e^2)^{3/2} (K_1 + K_2)^2 K_2 \tag{1.63}$$

This gives an upper limit for m_1 unless i is known. Interchanging 1 and 2 in Equation (1.60), we can also find an upper limit for m_2. If we can measure K_1, using Equation (1.57) to determine K_2, the mass function can be determined and we get the following:

$$m_2 \sin^3 i = \frac{PK_1^3}{2\pi G}(1-e^2)^{3/2}(\frac{m_1+m_2}{m_2})^2 \tag{1.64}$$

and so

$$f(m) = \frac{m_2^3 \sin^3 i}{(m_1+m_2)^2} = \frac{PK_1^3}{2\pi G}(1-e^2)^{3/2} \tag{1.65}$$

where $f(m)$ is known as the *mass function*. The right-hand side of the equation contains only measurable quantities where G is the gravitational constant. Besides $\sin i$, the terms in the middle contain the main quantities of interest, the masses of the two components, m_1 and m_2. Thus, the mass functions directly relate the two masses to observable quantities. For a double-lined spectroscopic binary, where the radial velocity amplitudes of both components can be measured, these relations can be used to determine mass ratio and we can also determine $m_1 \sin^3 i$ and $m_2 \sin^3 i$. The mass function when we consider time-delay is given in the next section.

Determining the inclination angle i is often difficult, but in cases where this is possible (e.g., for an eclipsing binary with $i \approx 90^\circ$ or for a visual binary), one obtains the masses of both components. In fact, this is one of the most important methods for determining stellar masses, including those of compact objects, such as black holes.

1.8.3 Time-delay as a Function of Orbital Elements

Using distance to the barycentre, z_0, Equation (1.2) can be written as

$$z = r \sin i \sin(\nu + \omega) + z_0. \tag{1.66}$$

Time-delay τ and distance z of the star from the plane of the sky are related as

$$\tau = \frac{z}{c} \tag{1.67}$$

where c is speed of light. Distance z and phase ϕ are also defined as follows:

$$z = \frac{-c\phi}{2\pi f} \tag{1.68}$$

Using Equations (1.2, 1.3 and 1.68) we can write for phase ϕ as follows:

$$\phi = \frac{-2\pi f}{c} a(1-e^2)\sin i \frac{\sin(\nu+\omega)}{1+e\cos\nu} \tag{1.69}$$

Therefore, we can write distance z as:

$$z = \frac{a\sin i(1-e^2)\sin(\nu+\omega)}{1+e\cos\nu} \tag{1.70}$$

From Equations (1.69 and 1.70) we can write for time-delay τ as follows:

$$\tau = \frac{a\sin i}{c}\frac{(1-e^2)\sin(\nu+\omega)}{1+e\cos\nu} + \tau_0 \tag{1.71}$$

where τ_0 is an arbitrary offset.

Time-delay is defined so that it is negative when the star is nearer to the observer than the barycentre. A negative delay indicates an early arrival time.

Equation (1.71) gives us expression for time-delay τ in terms of true anomaly ν. However, it is also possible and better to express τ in terms of the eccentric anomaly, E, rather than true anomaly to avoid writing the expression in fractional form. We know that

$$r\sin\nu = b\sin E \tag{1.72}$$

but

$$b = a\sqrt{1-e^2} \tag{1.73}$$

where b is semi-minor axis.

$$r\sin\nu = a\sqrt{1-e^2}\sin E \tag{1.74}$$

$$r\cos\nu = a(\cos E - e) \tag{1.75}$$

When we expand Equation (1.66), we can get the following:

$$z = (r\sin i)(\sin\nu\cos\omega) + (r\sin i)(\cos\nu\sin\omega) + z_0, \tag{1.76}$$

$$z = (r\sin\nu)(\sin i\cos\omega) + (r\cos\nu)(\sin i\sin\omega) + z_0, \tag{1.77}$$

$$\begin{aligned} z &= (a\sin i)(\sqrt{1-e^2})\cos\omega\sin E \\ &+ (a\sin i)(\sin\omega)(\cos E - e) + z_0. \end{aligned} \tag{1.78}$$

Using Equations (1.67 and 1.78) we find the following,

$$\tau = \frac{a\sin i}{c}\sqrt{1-e^2}\cos\omega\sin E + \frac{a\sin i}{c}\sin\omega(\cos E - e) + \tau_0 \tag{1.79}$$

Let

$$A = \frac{a\sin i}{c}. \tag{1.80}$$

Then,

$$\tau = A\sqrt{1-e^2}\cos\omega\sin E + A\sin\omega\cos E - Ae\sin\omega + \tau_0. \tag{1.81}$$

Let's again assign the constants in Equation (1.81) as follows:

$$a_1 = -Ae\sin\omega + \tau_0, \tag{1.82}$$

$$a_2 = A\sqrt{1-e^2}\cos\omega, \tag{1.83}$$

$$a_3 = A\sin\omega, \tag{1.84}$$

Therefore, we can write Equation (1.81) in a simpler form as follows:

$$\tau = a_1 + a_2\sin E + a_3\cos E, \tag{1.85}$$

where a_1, a_2 and a_3 are coefficients which contain the orbital parameters. From *Kepler's* equation, eccentric anomaly, E and mean anomaly, M are related as follows:

$$E - e \sin E = M, \tag{1.86}$$

where

$$M = \frac{2\pi}{P}(t - Tper). \tag{1.87}$$

Therefore,

$$E - e \sin E = \frac{2\pi}{P}(t - Tper). \tag{1.88}$$

where P is orbital period and $T_{\rm per}$ is time of periastron passage. For any given time, t, we can calculate E and use it to calculate τ in Equation (1.85).

If the eccentricity is smaller than the expected error, it is better to assume that the orbit is circular (e = 0), in which case

$$\tau = \tau_0 + A \cos\phi \sin\frac{2\pi}{P}t + A \sin\phi \cos\frac{2\pi}{P}t, \tag{1.89}$$

$$= a_1 + a_2 \sin\frac{2\pi}{P}t + a_3 \cos\frac{2\pi}{P}t. \tag{1.90}$$

The solution to the elements proceeds as before, except that we will not have values of e, ω and $T_{\rm per}$. We also use least squares to solve for a_1, a_2, a_3 and their standared deviations from which the parameters can be derived.

Time-delay velocities (radial velocities) of some of the *Kepler* stars can also be calculated by taking the time derivative of distance z as

$$\frac{\partial z}{\partial t} = Ac(\sqrt{1 - e^2} \cos\omega \cos E - e \sin\omega \sin E)\frac{\partial E}{\partial t}. \tag{1.91}$$

From Equation (1.88) we can write

$$\frac{\partial E}{\partial t}(1 - e\cos E) = \frac{2\pi}{P}. \tag{1.92}$$

Hence

$$V_r = (\sqrt{1-e^2}\cos\omega\cos E - e\sin\omega\sin E)\frac{2\pi}{P}\frac{Ac}{1-e\cos E}. \tag{1.93}$$

From Equation (1.93) radial velocity curve can be constructed and the spectroscopic radial velocity amplitude is

$$K = \frac{2\pi}{P}\frac{Ac}{\sqrt{1-e^2}}. \tag{1.94}$$

The mass function we calculated with the time-delay method we used is calculated in detail as follows.

If a is measured in AU, then the value of A (time-delay) expressed in days is

$$A = 0.0057755183a\sin i. \tag{1.95}$$

where the values of c and AU considered (in mks units) are $c = 2.99792458 \times 10^8$ m s^{-1} and 1 AU$= 1.49597871 \times 10^{11}$m respectively. If P is also in days, the semi-amplitude of radial velocity in km s^{-1} is

$$K = \frac{2\pi}{86400 \times P}\frac{1.49597871 \times 10^{11}a\sin i}{\sqrt{1-e^2}}, \tag{1.96}$$

$$= 1.73145684028 \times 10^6\frac{2\pi}{P}\frac{Ac}{\sqrt{1-e^2}}. \tag{1.97}$$

If the masses of two stars in a binary are m_1 and m_2, the mass function is given as

$$f(m) = f(m_1.m_2) = \frac{4\pi^2}{G}\frac{(a\sin i)^3}{P^2} = \frac{(m_2\sin i)^3}{(m_1+m_2)^2} \tag{1.98}$$

In mks system of units

$$f(m_1, m_2) = \frac{4\pi^2}{6.67384 \times 10^{-11}} \frac{(1.49597871 \times 10^{11} a \sin i)^3}{(86400.0 \times P)^2}, \quad (1.99)$$

$$= 2.652972204970216 \times 10^{35} \frac{(a \sin i)^3}{P^2}. \quad (1.100)$$

If the mass function is expressed in solar masses, we must devide by the solar mass $M\odot = 1.9891 \times 10^{30}$ kg. Hence

$$f(m_1, m_2) = 133375.50676035474 \frac{(a \sin i)^3}{P^2}. \quad (1.101)$$

Equation 1.86 is called a *transcendental* equation. The equation does not have a closed-form solution for E given M. The mean anomaly increases at a constant rate with time. It indicates where the star would be if it moved in a circular orbit of radius a. For circular orbits all three anomalies ν , E, and M are always equal. Equation (1.86) is usually solved using numerical techniques. Since *Kepler's* equation cannot be solved algebraically, the solution of E can be treated using iteration methods which we also applied in the Fortran program developed. The procedure is as follows. A very good estimate of orbital period can be obtained from the binarogram, but we need to guess values of e and $T_{\rm per}$ in order to calculate E for each observation. Therefore, we can use the best values of e and $T_{\rm per}$ as input to the non-linear least squares routine to get corrections and standard deviations for the orbital parameters. We can find the standard deviation $sigma$ for many values of e and $T_{\rm per}$. The values which give the smallest value of σ are the most probable values. The search for minimum σ is limited to $0 \leq e < 1$ and $0 \leq T_{\rm per} < P$. A way to proceed is to first do a coarse search with quite large steps, δe, in e and δT in $T_{\rm per}$ and obtain first approximations for e and $T_{\rm per}$. A better suggestion is $\delta e = 0.1$ and $\delta T_{\rm per} = 0.1 \times P$. This means that we only get the value of e accurate to 0.1 and $T_{\rm per}$ accurate to $0.1 \times P$. A better approximation can be obtained by searching around these values using smaller step sizes. It is possible to continue in this way until the value of σ no longer decreases, at which point we have found the best solution for e and $T_{\rm per}$. We are trying to get values which are close enough to the true values to be able to use non-linear least squares. The code

developed will search through all possible values of e and $T_{\rm per}$ and pick out those which best fit the data. We used these procedures and concepts to develop the code which calculates orbital elements.

Preliminary Elements From Time-delay

There are different methods to get initial elements for a binary star orbit (Rabe 1951; Docobo 1985). However, there is no single method which can handle all cases equally well or which can give the final solution in one step. If time-delay τ is given as a function of time, we can fit observations to Equation 1.85 by least squares method and get constants a_1, a_2 and a_3 by selecting all possible values of e and $T_{\rm per}$. From best values of a_1, a_2 and a_3, we can calculate first approximations for A and ω as follows. From Equation 1.83 we write

$$\frac{a_2}{\sqrt{1-e^2}} = A\cos\omega = \alpha_2, \tag{1.102}$$

$$\cos\omega = \frac{\alpha_2}{A}, \tag{1.103}$$

$$A = \sqrt{\alpha_2^2 + a_3^2}, \tag{1.104}$$

From Equation 1.84

$$\sin\omega = \frac{a_3}{A}, \tag{1.105}$$

Equation 1.82 also gives

$$\tau_0 = a_1 + Ae\sin\omega. \tag{1.106}$$

Since we now have good starting values of all the orbital parameters A, e, ω, $T_{\rm per}$ and P, we can calculate corrections using the partial derivatives calculated. These parameters just found should actually be very close to the true values. We can use these parameters to solve for the corrections, and, at the same time, get the standard deviation of each parameter. Therefore, the next step is to calculate the corrections required to these starting values using non-linear least squares. In order to solve for the corrections, we need to find partial derivatives of time delay as a function of

the five parameters ($\partial\tau/\partial A$, $\partial\tau/\partial e$, $\partial\tau/\partial\omega$, $\partial\tau/\partial Tper$, $\partial\tau/\partial P$). These partial derivatives were solved in this study, and the values of the derivatives are shown in Appendix B. These values were used in the program written in this thesis.

Initial elements should be corrected by means of a least squares fit (van den Bos 1937; Heintz 1967). This procedure is an iterative one as a rule. If orbit is too uncertain for all elements to be corrected simultaneously, one or several elements have to be fixed. This can be done by limiting the number of elements to be corrected in one step. From the covariance matrix, it is possible to know which elements are weakly determined and whether there is a strong coupling between two elements. In addition to this, approximate values for the errors of the individual elements can be calculated.

Differential Corrections to the Elements

Using the iterative least squares method known as differential corrections, the best values of the orbital elements can be determined. It is generally advisable to determine the differential corrections to the preliminary elements by the method of least squares, whatever method may be used in finding the preliminary orbit. Schlesinger (1910) reported the least squares method, which allows for the differential corrections to be a set of preliminary orbital elements. The method has great accuracy and it is also suitable. Sterne (1941) presented two forms of least square solutions, where both forms differentially correct the preliminary elements. One of the forms is particularly applicable for orbits having very small eccentricities. The second form is a modified version of the method of Schlesinger (1910), where the date of periastron passage is replaced by the date at which the mean longitude is zero. This second form is suitable for all orbits except for those with very small eccentricities. Schlesinger (1915) clearly described the advantage of applying the method of least squares using spectroscopic binary stars as an example. According to Schlesinger (1915), the main advantage of the method of least squares is to enable us to vary all of the unknowns simultaneously, instead of one or two at a time. It also eliminates any personal bias or arbitrary steps from the computations and greater accuracy shows the reliability of the results. A shorter approach on

least squares method is also proposed by Curtiss (1916).

As a general example, the above concepts of differential corrections can be applied to orbital analysis of spectroscopic binaries. Orbital parameters of a binary system can be derived from a set of radial velocities of any spectroscopic binary system. Radial velocity analysis is based on the well known radial velocity equation (Equation 1.18): $Vr = \gamma + K[\cos(\nu + \omega) + e\cos\omega]$ where ν is a function of $T_{\rm per}$ and P.

Therefore, the radial velocity at any time is a function of the six parameters: Vrad (γ, K, e, ω, $T_{\rm per}$, P). Equation 1.18 was introduced by Lehmann-Filhés (1894) and, as discussed in the previous sections, the orbital elements were determined using the geometrical method of calculating the areas of radial velocity curves. The six orbital elements (γ, K, e, ω, $T_{\rm per}$, P) can be obtained from the radial velocity observations. A small change in any of the orbital elements of Equation 1.18 also leads to a change in the value of the radial velocity. Therefore, using Taylor's expansion and ignoring terms higher than the first, Equation 1.18 can be written as shown in Equation 1.107. The partial derivatives are tedious and were first shown by Lehmann-Filhés (1894) as indicated in Equation 1.108.

$$\Delta V = \frac{\partial F}{\partial \gamma}\Delta\gamma + \frac{\partial F}{\partial K}\Delta K + \frac{\partial F}{\partial e}\Delta e + \frac{\partial F}{\partial \omega}\Delta\omega + \frac{\partial F}{\partial Tper}\Delta Tper + \frac{\partial F}{\partial P}\Delta P \quad (1.107)$$

$$\begin{aligned}
\Delta V &= \Delta\gamma \\
&+ [\cos(\nu+\omega) + e\cos\omega]\Delta K \\
&+ K[\cos\omega - \frac{\sin(\nu+\omega)\sin\nu(2+e\cos\nu)}{(1-e^2)}]\Delta e \\
&- K[\sin(\nu+\omega) + e\sin\omega]\Delta\omega \\
&+ K[\sin(\nu+\omega)(1+e\cos\nu)^2\frac{2\pi}{P(1-e^2)^{3/2}}]\Delta T \\
&+ K[\sin(\nu+\omega)(1+e\cos\nu)^2\frac{2\pi(t-Tper)}{P^2(1-e^2)^{3/2}}]\Delta P \qquad (1.108)
\end{aligned}$$

The coefficients (the differential correction terms) can be calculated from the preliminary estimation of the orbital elements. The difference between the actual observed radial velocity and the radial velocity calculated using initial estimation for the orbital parameters is, $\Delta Vr = Vr - Vr0$. Since it is possible to calculate the partial derivatives at each time, t, this would become a least squares type of problem where we can determine the coefficients. The coefficients in this case are $\Delta\gamma$, ΔK, Δe, $\Delta\omega$, $\Delta Tper$ and ΔP. Once we have these values, it is possible to obtain better estimates of the initial approximate values. If the approximate parameters are γ, K, e, etc, the improved values are $\gamma + \Delta\gamma$, $K + \Delta K$, $e + \Delta e$, etc. Thus, it is possible to use these new values and repeat the procedure until all the $\Delta\gamma$, ΔK, Δe, etc are close to zero. One can get n simultaneous equations for n observations with six unknown differential correction terms. The least squares solution can be represented in terms of the matrix equation and the coefficients of

the matrix give corrections to the parameters. Since the longitude of periastron ω and the time of periastron passage $T_{\rm per}$ become indeterminate when eccentricity approaches zero, the solution becomes more unstable for a system with low eccentricity as usual. It is also known that the method proposed by Lehmann-Filhés (1894) provides a reasonable result for a system with eccentricity $e > 0.15$. In this case it can be a good choice to use the method suggested by Sterne (1941) where the date of periastron passage is replaced by the date at which the mean longitude is zero, which is the time of ascending-node passage.

Similarly, we applied this technique of differential corrections to the elements on time-delay as follows. The time-delay analysis is based on the time-delay equation (Equation 1.79) derived before. Therefore, the time-delay at any time is a function of the parameters $\tau(A.e.\omega, T_{per}, P)$. Any small changes in orbital elements brings a change in the time-delay. Suppose we wish to determine the corrections (δA, δe, $\delta\omega$, $\delta T_{\rm per}$ and δP) to the approximate parameters. Ignoring terms higher than the first, and using Taylor's expansion time-delay equation. Equation 1.79 can be written as shown in Equation 1.109. Therefore, using these partial derivatives mentioned in Appendix B, Equation 1.109 can be expressed as shown in Equation 1.110.

$$\delta\tau = \frac{\partial\tau}{\partial\tau_0}\delta\tau_0 + \frac{\partial\tau}{\partial A}\delta A + \frac{\partial\tau}{\partial e}\delta e + \frac{\partial\tau}{\partial\omega}\delta\omega + \frac{\partial\tau}{\partial Tper}\delta Tper + \frac{\partial\tau}{\partial P}\delta P \quad (1.109)$$

$$\begin{aligned}
\delta\tau &= 1 \\
&+ [\sqrt{1-e^2}\cos\omega\sin E + \sin\omega\cos E - e\sin\omega]\delta A \\
&+ [(A\cos\omega)(\sin E)[\frac{-e}{\sqrt{1-e^2}} + \frac{\sqrt{1-e^2}\cos E}{(1-e\cos E)}] - A\sin\omega[\frac{\sin^2 E}{1-e\cos E} + 1]]\delta e \\
&+ [-A\sqrt{1-e^2}\sin E\sin\omega + A\cos\omega\cos E - Ae\cos\omega]\delta\omega \\
&+ [\frac{-2\pi}{P}\frac{1}{(1-e\cos E)}[A\sqrt{1-e^2}(\cos\omega)(\cos E) - A\sin\omega(\sin E)]]\delta Tper \\
&+ [[A\sqrt{1-e^2}(\cos\omega)(\cos E) - A\sin\omega(\sin E)]\frac{-2\pi(t-T_{per})}{P^2(1-e\cos E)}]\delta P. \quad (1.110)
\end{aligned}$$

This means

$$\tau_{obs} - \tau_c = \delta\tau_0 + x_1\delta A + x_2\delta e + x_3\delta\omega + x_4\delta T_{\rm per} + x_5\delta P. \quad (1.111)$$

This is a multivariate least squares problem. For each observed value of τ, τ_{obs}, we can determine the calculated value of τ, τ_{cal} , using the approximate parameters as well as the values x_1, x_2, x_3, x_4, x_5, which are the partial derivatives. Therefore, we can determine the corrections by least squares fitting.

Error Analysis

As described in the previous sections, we obtained the standard deviations of the five parameters, $a\sin i, e, \omega, T_{\rm per}$ and P from the covariance matrix of the least

squares solution to the corrections. However, we do not have standard deviations for the derived parameters K and $f(m_1, m_2)$.
From propagation of errors,

$$\sigma_K^2 = \left(\frac{\partial K}{\partial P}\right)^2 \sigma_P^2 + \left(\frac{\partial K}{\partial A}\right)^2 \sigma_A^2 + \left(\frac{\partial K}{\partial e}\right)^2 \sigma_e^2. \tag{1.112}$$

We have also

$$\ln K = -\ln P + \ln(a \sin i) - \frac{1}{2}\ln(1 - e^2) + const. \tag{1.113}$$

Therefore,

$$\frac{\partial K}{\partial P} = -K\frac{1}{P}, \tag{1.114}$$

$$\frac{\partial K}{\partial A} = K\frac{1}{A}, \tag{1.115}$$

$$\frac{\partial K}{\partial e} = K\frac{e}{1 - e^2}. \tag{1.116}$$

Which gives

$$\sigma_K^2 = \left(\frac{K}{P}\right)^2 \sigma_P^2 + \left(\frac{K}{A}\right)^2 \sigma_A^2 + \left(\frac{Ke}{1 - e^2}\right)^2 \sigma_e^2 \tag{1.117}$$

Hence

$$\sigma_K = \sqrt{\left(\frac{K}{P}\right)^2 \sigma_P^2 + \left(\frac{K}{A}\right)^2 \sigma_A^2 + \left(\frac{Ke}{1 - e^2}\right)^2 \sigma_e^2}. \tag{1.118}$$

The standared deviation in the mass function is

$$\sigma_f^2 = \left(\frac{\partial f}{\partial a \sin i}\right)^2 \sigma_a^2 + \left(\frac{\partial f}{\partial P}\right)^2 \sigma_P^2 \tag{1.119}$$

From Equation 1.101 we have $f(m_1, m_2) = 133375.50676035474 \frac{(a \sin i)^3}{P^2}$.

So that

$$\ln f = 3 \ln(a \sin i) - 2 \ln P + constant. \tag{1.120}$$

Therefore,

$$\frac{\partial f}{\partial a \sin i} = \frac{3f}{a \sin i}, \tag{1.121}$$

$$\frac{\partial f}{\partial P} = -\frac{2f}{P}. \tag{1.122}$$

Which gives

$$\sigma_f^2 = \left(\frac{3f}{a \sin i}\right)^2 \sigma_a^2 + \left(\frac{2f}{P}\right)^2 \sigma_P^2, \tag{1.123}$$

Thus

$$\sigma_f = \sqrt{\left(\frac{3f}{a \sin i}\right)^2 \sigma_a^2 + \left(\frac{2f}{P}\right)^2 \sigma_P^2}. \tag{1.124}$$

For a circular orbit, we need to find the standard deviation of A and ϕ in

$$\tau = \tau_0 + A \cos\phi \sin \frac{2\pi}{P} t + A \sin\phi \cos \frac{2\pi}{P} t, \tag{1.125}$$

$$= a_1 + a_2 \sin \frac{2\pi}{P} t + a_3 \cos \frac{2\pi}{P} t. \tag{1.126}$$

given that $A^2 = a_2^2 + a_3^2$ and $\phi = \arctan(a_3/a_2)$. The least squares solution provides standared deviations of the coefficients a_1, a_2, a_3.

We have

$$2A\frac{\partial A}{\partial a_2} = 2a_2, \frac{\partial A}{\partial a_2} = \frac{a_2}{A}, 2A\frac{\partial A}{\partial a_3} = 2a_3, \frac{\partial A}{\partial a_3} = \frac{a_3}{A} \tag{1.127}$$

Hence by propagation of errors

$$\sigma_A^2 = \frac{a_2^2\sigma_2^2 + a_3^2\sigma_3^2}{A^2}. \tag{1.128}$$

Therefore,

$$\sigma_A = \frac{1}{A}\sqrt{a_2^2\sigma_2^2 + a_3^2\sigma_3^2}. \tag{1.129}$$

Also

$$\sec^2\phi\frac{\partial\phi}{\partial a_2} = \frac{1}{a_3}, \tag{1.130}$$

$$\sec^2\phi\frac{\partial\phi}{\partial a_3} = -\frac{a_2}{a_3^2}, \tag{1.131}$$

$$\frac{\partial\phi}{\partial a_2} = \frac{\cos^2\phi}{a_3} \tag{1.132}$$

$$\frac{\partial\phi}{\partial a_3} = -\frac{a_2\cos^2\phi}{a_3^2} \tag{1.133}$$

We also note that $\sec^2\phi = 1 + \tan^2\phi = 1 + a_2^2/a_3^2$.
Hence

$$\sec^2\phi = \frac{a_2^2 + a_3^2}{a_3^2} = \frac{A^2}{a_3^2}, \tag{1.134}$$

$$\cos^2\phi = \frac{a_3^2}{A^2} \tag{1.135}$$

and

$$\frac{\partial \phi}{\partial a_2} = \frac{a_3}{A^2}, \frac{\partial \phi}{\partial a_3} = -\frac{a_2}{A^2} \tag{1.136}$$

By propagation of errors

$$\sigma_\phi^2 = \left(\frac{\partial \phi}{\partial a_2}\right)^2 \sigma_2^2 + \left(\frac{\partial \phi}{\partial a_3}\right)^2 \sigma_3^2, \tag{1.137}$$

$$= \frac{a_3^2}{A^4}\sigma_2^2 + \frac{a_2^2}{A^4}\sigma_3^2, \tag{1.138}$$

Hence

$$\sigma_\phi = \frac{1}{A^2}\sqrt{a_3^2\sigma_2^2 + a_2^2\sigma_3^2}. \tag{1.139}$$

1.9 The Time-delay Method

1.9.1 Introduction

The time-delay method traces back to Ole Roemer who made the first real measurement of the speed of light by timing eclipses of Jupiter's moon *Io*. The satellite is eclipsed by Jupiter once every orbit, as seen from the Earth. By timing these eclipses over many years, Roemer noticed that the light from the Jupiter system has to travel an extra distance represented by the diameter of the Earth's orbit. This causes a delay in the timing of the eclipses. As the earth in its orbit moved toward Jupiter, the time interval between successive eclipses became steadily shorter and became steadily longer as the Earth moved away from Jupiter. The time difference is due to the finite speed of light which means that light from the Jupiter system has to travel farther to reach the Earth when the two planets are on opposite sides of the Sun than when they are closer together.

In a binary system, which is also pulsating, the orbital motion of the star leads to a periodic variation in the distance travelled by light emitted from the star and arriving on earth. This is called the path length of the light. This is the light time effect and brings a time-delay that varies and results in the pulsation phase that also varies. A description equivalent to this is a variation in pulsation frequency which is periodic and results from the Doppler effect. In a study of variation of the apparent period, Woltjer (1922) introduced the time-delay method. This was applied to an eclipsing binary where this system is in orbit around a third star. Irwin (1952) discussed this idea further. To obtain the radial velocity curve in a pulsar, Hulse & Taylor (1975) also applied the method. By timing the arrival of radio signals from a rapidly spinning pulsar, the most convincing evidence so far for a planetary system outside our solar system was found. The method became famous after Wolszczan & Frail (1992) used it for the discovery of the millisecond pulsar PSR1257+12 which has a planetary system around it.

The time-delay method allows the determination of orbital parameters directly with high precision, thus avoiding the need for spectroscopy. Therefore, modelling the time-delays might be preferred over the radial velocity curve. For many stars, obtaining the required radial velocity curves from ground-based observations is not possible. In recent times, it has been possible to get precision time series photometry from space missions like *CoRot* and *Kepler*. In addition, such space missions offer the chance to calculate orbital elements of a star which is pulsating and is part of a binary syatem. For example, the method was applied by Telting et al. (2012) on KIC 11558725, a pulsating sdB star having a companion which is a white dwarf, and by Murphy et al. (2013a) to find a binary companion of KIC 11754974.

Using modern high-precision photometry from the ground by Zasche & Uhlař (2013) and from space by Rappaport et al. (2013) and Conroy et al. (2014), the time-delay method was used to identify third bodies in eclipsing binary systems. Spectroscopic orbital parameters were also presented for 'heartbeat' stars by Smullen & Kobulnicky (2015) which support the idea that photometric data are sufficient to derive reliable orbital parameters for these stars.

In most cases the method is applicable to δ Sct *Kepler* stars, but these stars have a variable amplitude of close frequencies which can be similar in amplitude with pulsation frequencies. These close frequencies obscure or distort any effect due to time- delay variations. Therefore, methods which consider time-delay effects should be designed to avoid such problems, in order to get the appropriate orbital period. Balona (2014a) focuses on such issues. Taking *Kepler* A stars as an example, Balona (2011) also showed that about 20 percent of A stars have dominant low frequencies which are visible in the periodogram. In most A-type stars, these low frequencies ($0.2 < \nu < 5.0\,d^{-1}$) have typical amplitudes of about 40 ppm where the low frequency is assumed to be due to rotational modulation caused by star spots or co-rotating structures. Considering *Kepler* A stars again, Balona (2014b) further explained that low frequencies in δ Sct stars show the presence of δ Sct pulsations. In fact, a high amplitude with a large number of combination frequencies is also shown in δ Sct star KIC 11754974 (Murphy et al. 2013a). Such a relation between frequency and amplitude is also a topic of discussion on other types of *Kepler* pulsating stars (Balona 2013). Balona & Nemec (2012) proposed high amplitude as a selection effect on taking SX Phe samples among *Kepler* δ Scuti stars.

In general, time-delay is a new technique that avoids the need for time-consuming spectroscopic observations to determine the orbital parameters of binary star systems. It allows the orbital solution to be obtained from the light curve alone. The time-delay method to detect binary companions has a different range of applications from the usual radial velocity observations. For example, since $a \sin i$ and time-delay are proportional, the time-delay method is best to identify binaries at bigger distances from the centre of mass. This implies that long orbital period systems can be studied with this method. On the other hand, for short-period binaries the usual radial velocity method is preferable. The time-delay method has some limitations. One limitation is that it requires lengthy time series and high precision photometry. The method is also not suitable for detecting planets having a mass less than the mass of Jupiter, although the detection of low mass systems might be possible if the systems have very high frequencies like pulsars.

1.9.2 Using Phase and Frequency Modulation to Search for Binarity

It is known that if a star is a member of a binary system, its distance varies while it is in orbit with respect to the barycentre. If one member of this system pulsates, the variation in distance brings variation in phase of pulsation. Such changes can be used to derive orbital information of a binary system. For example, using data transformed to the frequency domain, Shibahashi & Kurtz (2012) applied the method called frequency modulation (FM) on artificial data and KIC4150611. Murphy et al. (2014) also applied the method on entire *Kepler* light curves using a direct analysis of phase variation with the method known as phase modulation (PM). More recently, Murphy & Shibahashi (2015) improved the phase modulation method for finding orbital parameters from light arrival time-delays directly without converting time-delays to radial velocities by numerical differentiation. This method was applied to KIC 8264492, KIC 10990452 and KIC 9651065 and the orbital parameters were obtained for each system. Figure 1.10 shows an example of the time-delay method by Murphy & Shibahashi (2015) applied to KIC 9651065.

The PM method is an important way to convert pulsational phase modulation into light arrival time-delays. From Fig.1.10, it can be seen that the projected size of the orbit is obtained from the time-delay difference between the maximum and the minimum. Deviation of the curve from a sinusoid also indicates that the orbit is eccentric. The pulsating star is nearest to us when the time-delay curve reaches its minima, while the star is furthest from us when the curve reaches its maxima. The sharp minima and blunt maxima further show that periapsis is at the near side of the orbit. The asymmetry of the time-delay curve, which is shown by the fast rise and slow fall was explained by the fact that the star passes the periapsis after reaching the nearest point to us. Time-delay curves, therefore, are excellent tools in giving information about the orbit of a binary system. The best-fitting time-delay curve obtained which matches with the observed time-delay is shown in Fig.1.11.

The FM method shows the appearance of a frequency multiplet in the Fourier

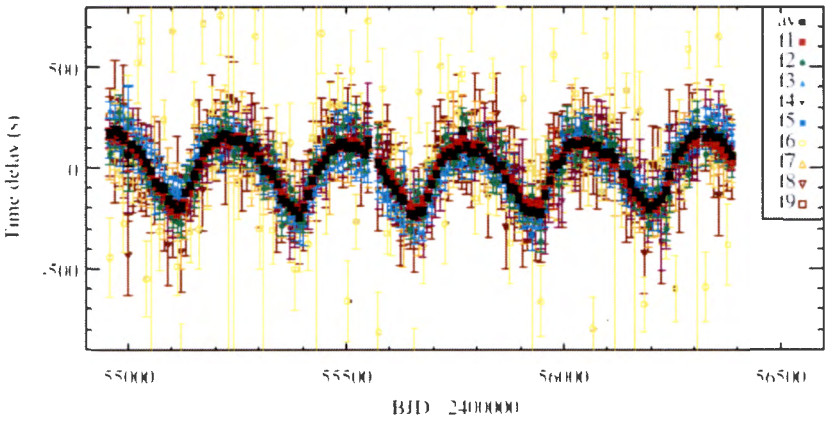

Figure 1.10: An example of a time-delay diagram applied to KIC 9651065 using nine different pulsation modes. The time-delay varies periodically with the binary orbital period (Murphy & Shibahashi 2015).

transform of the light curve of a pulsating star due to the light-time effect in a binary system. The members of the multiplet are then separated by the orbital frequency of the orbiting star. All the orbital information then be derived from the amplitudes and phases of the components of the frequency multiplet. Fig.1.12 shows a case for KIC 4150611 where the highest amplitude peak at 20.243260 d^{-1} has another pulsation mode frequency nearby. The triplet is shown as the second-highest peak at 22.619577 d^{-1} .

This FM method described by Shibahashi & Kurtz (2012) is especially applicable when the observational time span of the data is long compared to the binary orbital period. However, since the frequency splitting due to the binary motion becomes comparable to the frequency resolution, the FM method is not necessarily appropriate for wider binary systems.

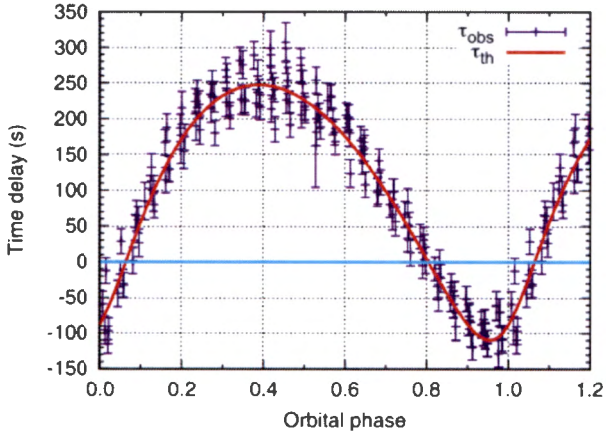

Figure 1.11: A phase plot of data presented in Fig.1.10 (Murphy & Shibahashi 2015).

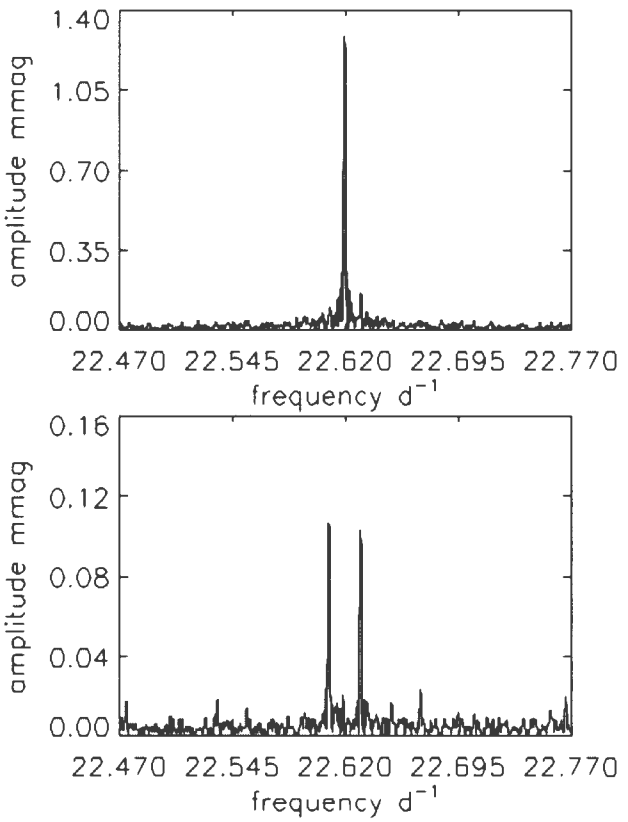

Figure 1.12: Amplitude spectrum (top panel) for KIC 4150611 where data is centred on the peak at 22.619577 d $^{-1}$. The bottom panel is an amplitude spectrum showing the two sidelobes split from the central peak by exactly the orbital frequency (Shibahashi & Kurtz 2012).

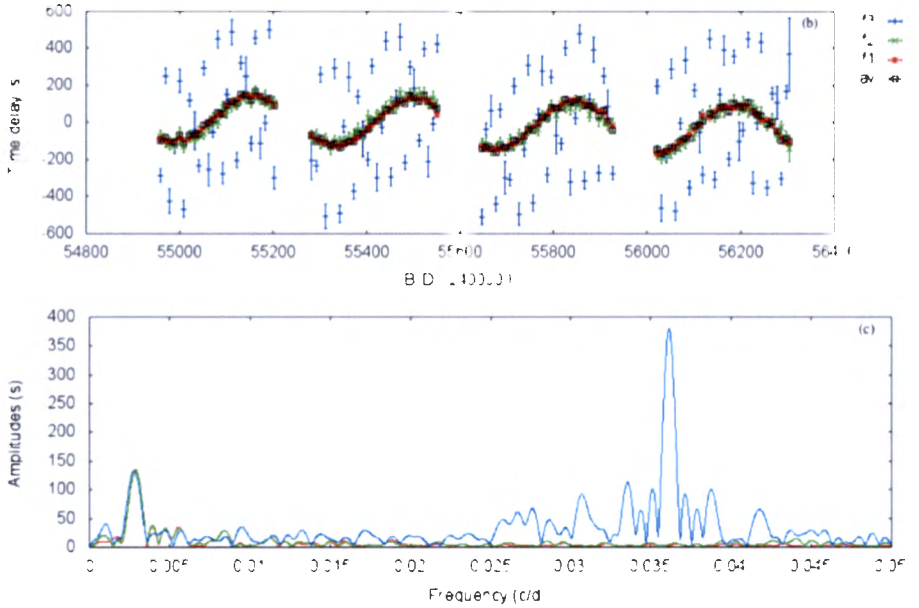

Figure 1.13: Time-delay as a function of time (top panel) of KIC 11754974 and its Fourier transform (lower panel). The time-delay contains information on the orbital period and the frequency of one of the stars is equal to the separation of the two pulsation frequencies (Murphy et al. 2014).

On the other hand, the PM method results in a series of time-delay measurements where binarity is apparent as a periodic modulation whose amplitude gives the projected light travel time across the orbit. The orbital parameters can be obtained from Fourier analysis of this time-delay curve. For example, Fig.1.13 illustrates this for the star KIC 11754974 where the top panel shows time-delay containing information on the orbital period and the lower panel is a Fourier transform of the time-delay. One can also find the radial-velocity curve by differentiating the time-delay curve.

Compared to the FM method, the PM method has the advantage of giving the variation in the light-travel time at short intervals (PM sampling segments must be short). However, FM gives better results for short period binaries. The short time

interval in PM makes it suitable for long-period binaries and it gives a more detectable signal for low-frequency pulsations compared to FM. Murphy et al. (2014) explained that their method of PM permits companions to be located in orbit at least as long as the 1400-d *Kepler* data sets and companions can be found around very low amplitude pulsators of about 20 μmag, regardless of orbital period. They further suggested that by extrapolating the results, planetary companions could also be discovered around mmag amplitude pulsators.

1.9.3 Binarogram

Balona et al. (2015) also applied the time-delay method to Am star KIC 3429637 observed by *Kepler* to calculate orbital elements. Balona (2014a) described a time-delay method where orbital parameters for a system of pulsating binary star are calculated. The method was checked using simulations. In addition to the simulations, the method was also tested on the following two real stars whose orbital parameters were already determined: KIC 4150611 by Shibahashi & Kurtz (2012) and KIC 11754974 by Murphy et al. (2013a). The method differs from previous methods because it provides a direct periodogram of the orbital frequency, which Balona (2014a) called a 'binarogram'. The application of this method by Balona (2014a) to 34 *Kepler* δ Sct stars also resulted in the detection of five binary stars. Koen (2014) used a similar method to find binary stars from photometry.

According to Balona (2014a), the first requirement in using the time-delay method to obtain orbital elements is that the data of the photometry must be precise. The data also is expected to be sampled well and observations spanning a very long time. Pulsation frequency and length in time series can result in a better resolution of the orbital period. One of the stars should act like a clock when there is no variation in frequency. This is a requirement which is critical. Best time resolutions can be obtained when the frequency of pulsation is high as in pulsars. Other compact objects like sdB stars and white dwarfs that are pulsating are also candidates for this method. The roAp stars can also be good candidates but their frequency variability and low amplitudes limit their usefulness. Because they are stochastically driven and also have low amplitudes, solar-like oscillations are not

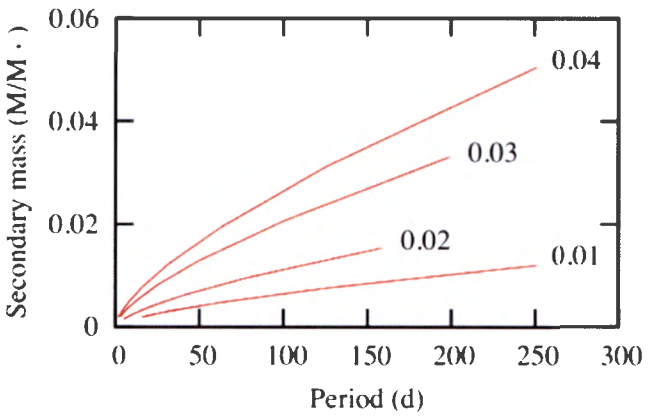

Figure 1.14: The mass of the secondary as a function of orbital period for companions of typical δ Sct star. The numbers on the different curves are $a \sin i$ values (Balona 2014a).

good candidates for this method.

In obtaining orbital parameters, the time-delay method with its sensitivity domain and radial velocities approach is not the same as previous methods even though the first derivative in time-delay gives radial velocity. For example, the time-delay method provides the semi-major axis, $a \sin i$ directly. Using data taken from *Kepler* observations, Balona (2014a) further explained that when $a \sin i \approx 0.01$ AU, which corresponds to a time-delay amplitude of about 5s, the method would be limited. This means that if the time travelled by light from the secondary star to the center of mass of the system is less that 5 s, the two systems cannot be resolved and what we observe will be a noise. This implies that for δ Sct stars, 0.002 $M_\odot$ is the minimum detectable mass of the secondary, where this limit corresponds to the orbital period of about 20 days. When the orbital period increases to about one year, 0.02 $M_\odot$ will be the minimum mass of the secondary that can be detected. For example, Fig.1.14 describes the dependence of mass of a companion star to a δ Scuti star with mass range 1.5 - 2.0 $M/M_\odot$ on period of the orbit for various $a \sin i$ values. The companion star has an orbital period of about 250 days for a mass of $M = 0.01\ M_\odot$, when the peak value of the binarogram is $a \sin i = 0.01$ AU.

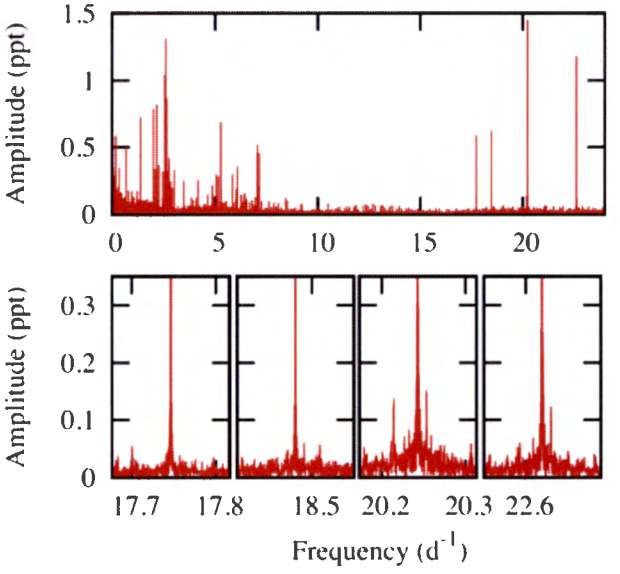

Figure 1.15: Periodogram of KIC 4150611. The full frequency and amplitude range are shown in the top panel. Further details around four of the peaks at 17.75, 18.48, 20.24 and 22.62 d^{-1} are shown in the bottom panel (Balona 2014a).

Rapid identification of star systems that have detectable variations in time-delay is the main purpose of a binarogram. In this thesis, the binarogram is also used for the same purpose. The value of $a \sin i$ and orbital period can be calculated from the binarogram. The peaks of the binarogram represent the orbital frequencies. One peak is usually visible, however, in multiple systems, two orbital frequencies can be observed. If there is time-delay variation of orbital frequency, a plot of $a \sin i$ versus orbital frequency will be a maximum. As an example, Fig.1.16 shows the binarogram of KIC 4150611 for seven frequencies which are in δ Sct range as given by Balona (2014a). The periodogram of the same star (KIC 4150611) is shown in Fig.1.15. Four prominent peaks can be observed at 20.24, 22.62, 18.48 and 17.75 d^{-1}. In the bottom panel, details nearby each of the four peaks are shown.

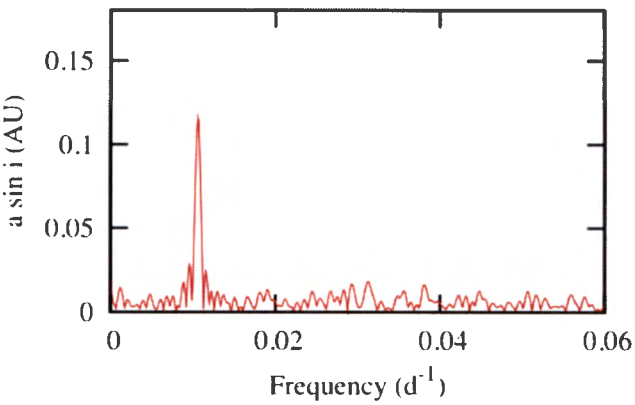

Figure 1.16: An example of a binarogram plot of KIC 4150611. Seven frequencies are used and in the range 0-0.06 d^{-1}, there is only one peak visible that corresponds to the orbital period (Balona 2014a).

Chapter 2

Identifying Binary Stars and Determining the Orbital Period Using the Binarogram

Users can search for *Kepler* data or light curves in different ways. Common methods are based on position, time of observation, target name or *Kepler* Identification Number (*Kepler*-ID). Light curves can also be obtained from *Mikulski Archive for Space Telescopes* (MAST). In this chapter we will discuss how one gets the specific data products archived at MAST and the procedure we followed to get data and extract the data from the FITS file. There are different ways of identifying binary star systems. In this chapter we will also discuss our own method of identifying binary systems using the method called binarogram. Finally the list of identified binary systems will be given.

2.1 Obtaining *Kepler* Light Curves

Kepler Data

The *Kepler* data has been made public and can be retrieved from MAST which serves as NASA's primary archive for ultraviolet and optical space-based data. *Kepler* data are decompressed and sorted as long and short cadence with pixel type

(target, background or collateral). Then the data is converted to the FITS (Flexible Image Transport System) format to comply with astronomical data standards. A variety of data products are archived for direct download from the public site in the following form for all users: processed Light curves derived by Photometric Analysis (PA) and corrected by Pre-search Data Conditioning (PDC), Full-frame images output from all 84 channels on the detector array, and Target pixel images, the individual pixel masks collected for each observation during a quarter and calibrated by Calibration CAL.

In *Kepler* data, light curve files are produced for each target using simple aperture photometry. A light curve file contains time series data. At any time, there will be more than 160,000 long cadence targets and up to 512 short cadence targets being observed. Data observed by the *Kepler* photometer are recorded on orbit, downlinked, archived, processed and calibrated through the *Kepler* Science Pipeline. Its primary focus is on scientifically related data sets in the optical, ultraviolet, and near-infrared parts of the spectrum. The archived data contains the raw and calibrated pixel values, background pixels, calibrated and corrected light curves, and related ancillary engineering data. For this research, we first selected 1646 δ Sct stars identified by Balona (unpublished) from MAST where all our data belongs to long cadence sampling rate. The data are in FITS file format and these FITS files contain only tables and we need a special reader to access these tables. A simpler way to get the data is to use a script. We used a Fortran program to extract the required data from a FITS file into an easy and usable four column file (barycentric Julian date, photometry corrected by our program, photometry using PDC (*Kepler's* own correction), photometry using SAP (uncorrected simple aperture photometry)). Fig.2.1 shows examples of *Kepler* light curves for two of the binary stars we identified (KIC 1294670 and KIC 2168333). The corresponding corrected light curve of these two stars using PDC is given in Fig.2.2.

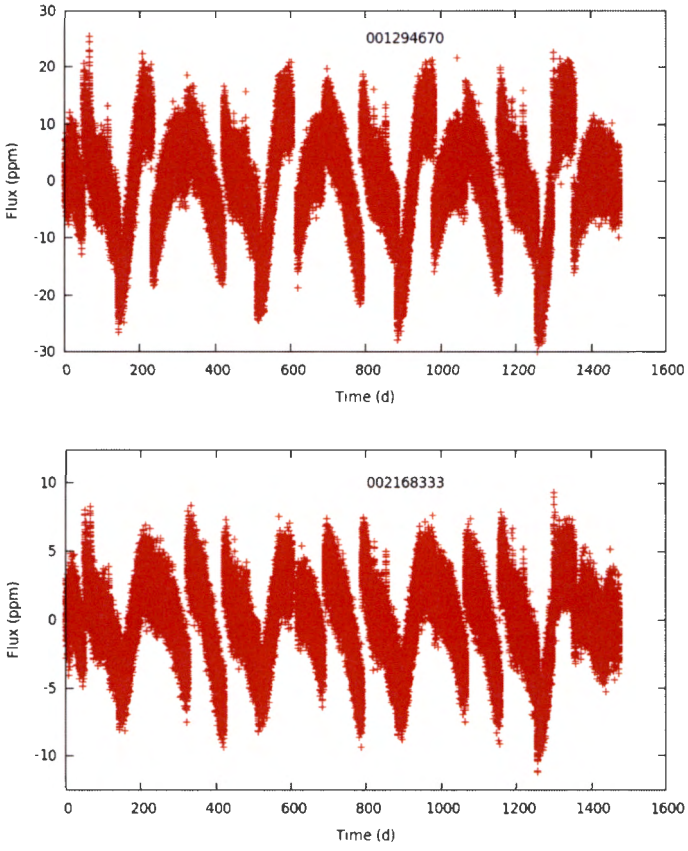

Figure 2.1: *Kepler* light curve for the two sample binary stars we identified: KIC 1294670 (top panel) and KIC 2168333 (bottom panel) using raw (uncorrected) SAP data. Mostly, the gaps are due to quarterly rolls and monthly downlinks.

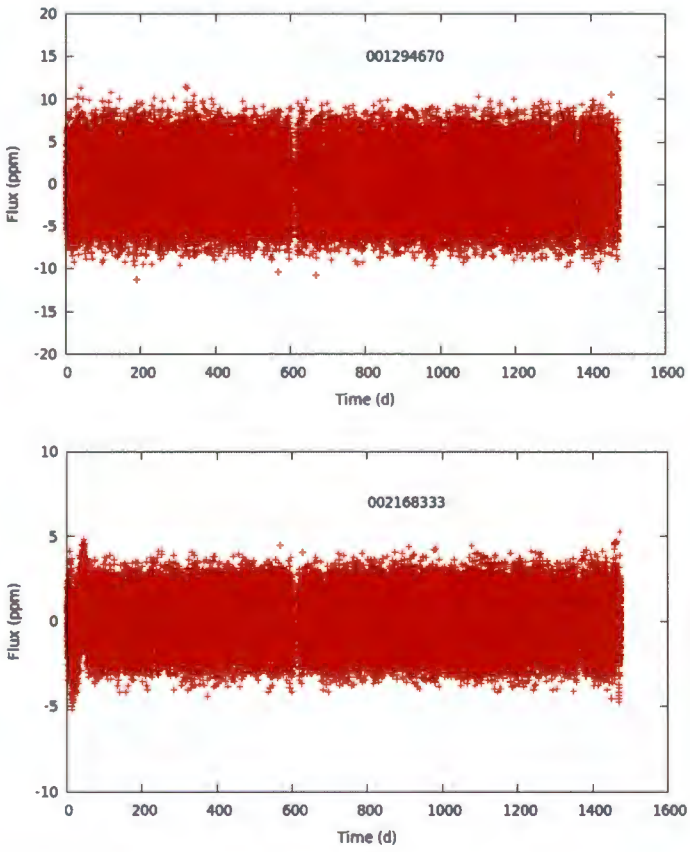

Figure 2.2: Corrected *Kepler* light curve for the two sample binary stars we identified: KIC 1294670 (top panel) and KIC 2168333 (bottom panel) using PDC (*Kepler's* own correction).

The next step in the research was to search for the pulsation frequencies in a star. To perform this task, we used the Fortran program to calculate the Lomb-Scargle periodogram of a pulsating star in the binary system. The photometric input data we used for the periodogram was the Pre-search Data Conditioning (PDC) where signatures in the light curves that are correlated with systematic error sources from the telescope and spacecraft, such as pointing drift, focus changes, and thermal transients are corrected. We limited the frequencies needed to be used for the periodogram in the range between 0 to 48 d^{-1} and the number of frequencies to be extracted was 50. The search from 0 to 48 d^{-1} extends beyond the nominal Nyquist frequency of 24 d^{-1}. The reason for this is to use the non-uniform data spacing to identify peaks at frequencies higher than 24 d^{-1}. Running the program gives frequencies, amplitudes and phases and their errors. The program also removes everything except about 10 of the frequencies of highest amplitude, avoids frequencies which are very close to each other and uses only frequencies in the range 10-30 d^{-1}. Another related assumption we made was that pulsation frequency must be constant. The next task was to use these pulsation frequencies and identify binary stars using a binarogram. This is discussed in the next section.

Before applying to the real *Kepler* data, a program was developed which creates a simulated data file (a synthetic 'delta Scuti'star) for a pulsating star in a binary orbit. The simulated data gives time, photometry without error and with standard error. This allows one to simulate real data more closely. From the simulation, we can learn the effect of fictitious peaks which are the result of frequencies close to each other. This happens if we do not include both frequencies in calculating the binarogram. Fig.2.3 shows the periodogram plot for the synthetic light curve and the corresponding binarogram for the data is shown in Fig.2.4. The pulsation frequencies produced are 12.3813, 14.3703 and 15.6727 d^{-1}. Using these artificial data, it is also possible to recover the time-delay using another program developed to obtain time-delay as a function of time.

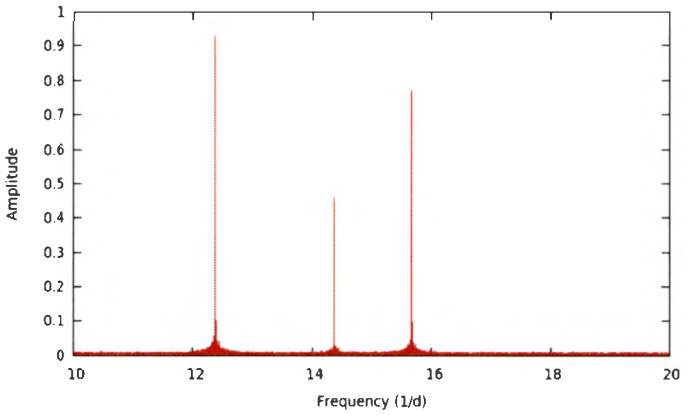

Figure 2.3: Periodogram of the synthetic data.

2.2 Identifying Binary Stars Using Binarogram

Mathematically, the way in which a binarogram works is given below. The distance z of a star along the line of sight varies according to the following equation:

$$z = a \sin i \frac{(1 - e^2) \sin(\nu + \omega)}{1 + e \cos \nu} \tag{2.1}$$

where $a \sin i$ is the projected semi-major axis, e is the eccentricity of the orbit, ν is the true anomaly and ω is the angle of periastron. For circular orbit, the time-delay ($\tau = z/c$) is,

$$\tau = \frac{a \sin i}{c} \sin(\Omega t + \omega) = \alpha_1 \sin \Omega t + \alpha_2 \cos \Omega t \tag{2.2}$$

where $\Omega = 2\pi / P_{orb}$ is the orbital angular frequency, P_{orb} is the orbital period and α_1 and α_2 are coefficients given as,

$$\alpha_1 = \frac{a \sin i}{c} \cos \omega, \alpha_2 = \frac{a \sin i}{c} \sin \omega \tag{2.3}$$

For a multiperiodic pulsating star, at time t the observed brightness variation y, can be written as follows as a Fourier series that is truncated:

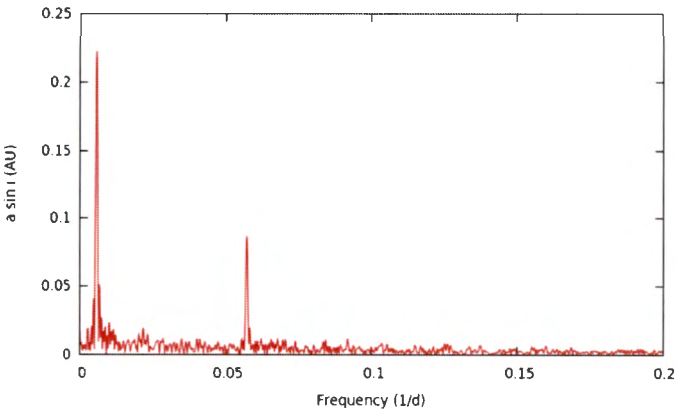

Figure 2.4: Binarogram of the synthetic data.

$$y = a_1 + \sum_{j=1}^{q} [a_{2j} \sin \omega_j (t + \tau) + a_{2j+1} \cos \omega_j (t + \tau)] \tag{2.4}$$

where $\omega_j = 2\pi f_j$. If we assume pulsation frequencies, f_j and orbital period, P_{orb} is already known, this indicates that y will be a function of the two coefficients, $y = y(\alpha_1, \alpha_2)$. If we further assume that we know estimates of $\alpha_1$and α_2, the corrections to these estimated values are,

$$\Delta y = \frac{\partial y}{\partial \alpha_1} \Delta \alpha_1 + \frac{\partial y}{\partial \alpha_2} \Delta \alpha_2 \tag{2.5}$$

where calculated and observed brightness variations are expressed by Δy. This expression is a type of least squares that is linear. Therefore, the corrections Δ_{α_1} and Δ_{α_2} can be solved. The partial derivatives can be given by

$$\frac{\partial y}{\partial \alpha_1} = u \sin k\Omega t, \frac{\partial y}{\partial \alpha_2} = u \cos k\Omega t, \tag{2.6}$$

and

$$\frac{\partial y}{\partial \tau} = u = \sum_{j=1}^{q} \omega_j [a_{2j} \cos \omega_j (t + \tau) - a_{2j+1} \sin \omega_j (t + \tau)]. \tag{2.7}$$

If we are trying to find a periodic time-delay with frequency f_{orb}, we choose a value for f_{orb} to use the least squares to solve the above problem. The calculation gives α_1 and α_2 and the values of $a \sin i$ are obtained. The procedure can be repeated by choosing another value of f_{orb} until the corrections are small enough. When there is variation in time-delay for that frequency in the data, f_{orb} as a function of $a \sin i$ will be at a maximum. This is what we call a binarogram.

For our case, we used a Fortran program which calculates the binarogram of a pulsating star. We used the following inputs and assumptions in the program. First of all, since at least one member of the binary system is a pulsating star, we need to know the most important pulsation frequencies. These frequencies are calculated using the periodogram program as discussed previously. It is important to use pulsation frequencies of the highest amplitude (to maximimize the signal-to-noise ratio) and as free from neighbouring frequencies as possible. We selected frequencies in which there are no neighbouring peaks closer than 0.1 d^{-1} with amplitudes in excess of 0.1 of the peak amplitude. Frequencies were selected within the range 5 - 100 d^{-1}. In calculating the binarogram we used an orbital frequency step of 0.001 d^{-1} and a range 0 to 0.10 d^{-1}.

The program reads the data and pulsation frequencies. It then automatically selects and improves the frequencies and calculates up to three binarograms. These last three binarogram files contain pulsation frequencies and amplitudes used in constructing the corresponding binarogram which is ready to be examined by plotting.

The binarogram is only a guide to which stars may be binaries. Because δ Sct stars have many frequencies, they are not perfect clocks. If a star is a binary, the binarogram will certainly have a peak at the orbital frequency. However, a peak in the binarogram does not neccessarily imply that the star is indeed a binary. Such fictitous peaks are a result of intereference between close frequencies. In a true binary, all pulsation frequencies should result in the same peak in the binaoragram. Therefore, true binaries are easily identified by the fact that two or more pulsation frequencies give rise to the same peak. In this way, true binaries are quickly identified. The resulting list of stars obtained in this way can then be further analysed by

detailed examination of the time-delay as a function of time for different pulsation frequencies, as will be discussed in Chapter 3 of this thesis.

The binarogram is affected by close pulsation frequencies, which means that a peak need not necessarily be due to a binary. It can be a result of interference by a neighbouring pulsation frequency as already mentioned. To eliminate such possibilities, the program calculates up to three binarograms for each star. Each of the three binarograms uses a different set of pulsation frequencies. If the peak is due to interference, it will not be seen in all three binarograms. If it is a real peak due to binary motion, then the peak will be present in all the binarograms.

To get the approximate orbital period, we need to select those stars which we think are binaries and obtain the orbital frequency of the binarogram peak. This does not have to be obtained very accurately. We used gnuplot, in which the cursor is placed at the peak and the peak frequency is read. The orbital period will be the inverse of this frequency. To explain this, one of our binary systems, KIC 1294670, is used as an example as shown in Fig.2.5. When we put the cursor at the peak point, the orbital frequency value is 0.00273224 d^{-1}. Therefore, the orbital period will be 366 days. Fig.2.6 shows a case of a *Kepler* star KIC 1434660 where the peak is not seen in all the three binarograms which indicates that the system is not binary. The same procedure was applied for the rest of the binary stars identified and their corresponding binarogram plots are also shown from Fig.2.7 to Fig.2.30. The horizontal axis is orbital frequency and the vertical axis represents semi-major axis of the orbits.

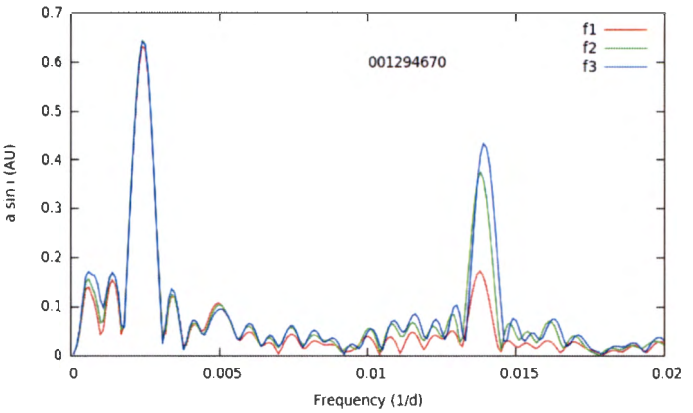

Figure 2.5: Binarogram of KIC 1294670 showing peak value at orbital frequency of 0.00273224 d^{-1} for three pulsation frequencies (f_1 = 12.6228 d^{-1}, f_2= 14.9703 d^{-1} and f_3 = 16.7269 d^{-1}).

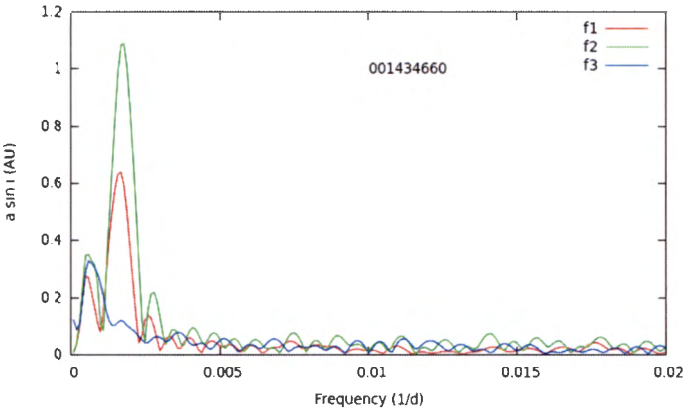

Figure 2.6: Binarogram of KIC 1434660 where the three binarograms do not match (the peak is not visible in all the binarograms) showing that the system is not binary.

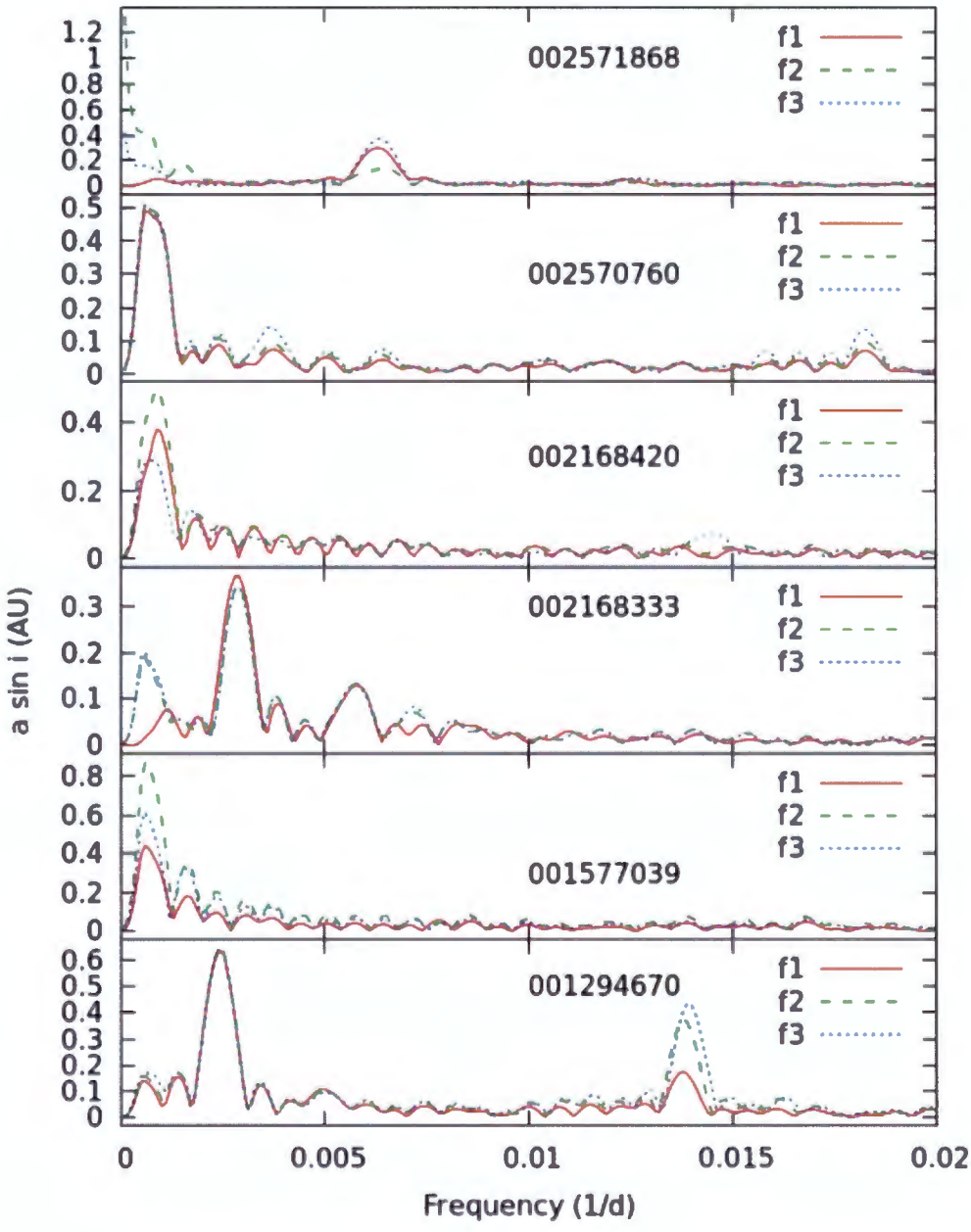

Figure 2.7: Binarograms for stars with KIC numbers indicated. The three curves corresponded to time-delay solutions with three different pulsation frequencies.

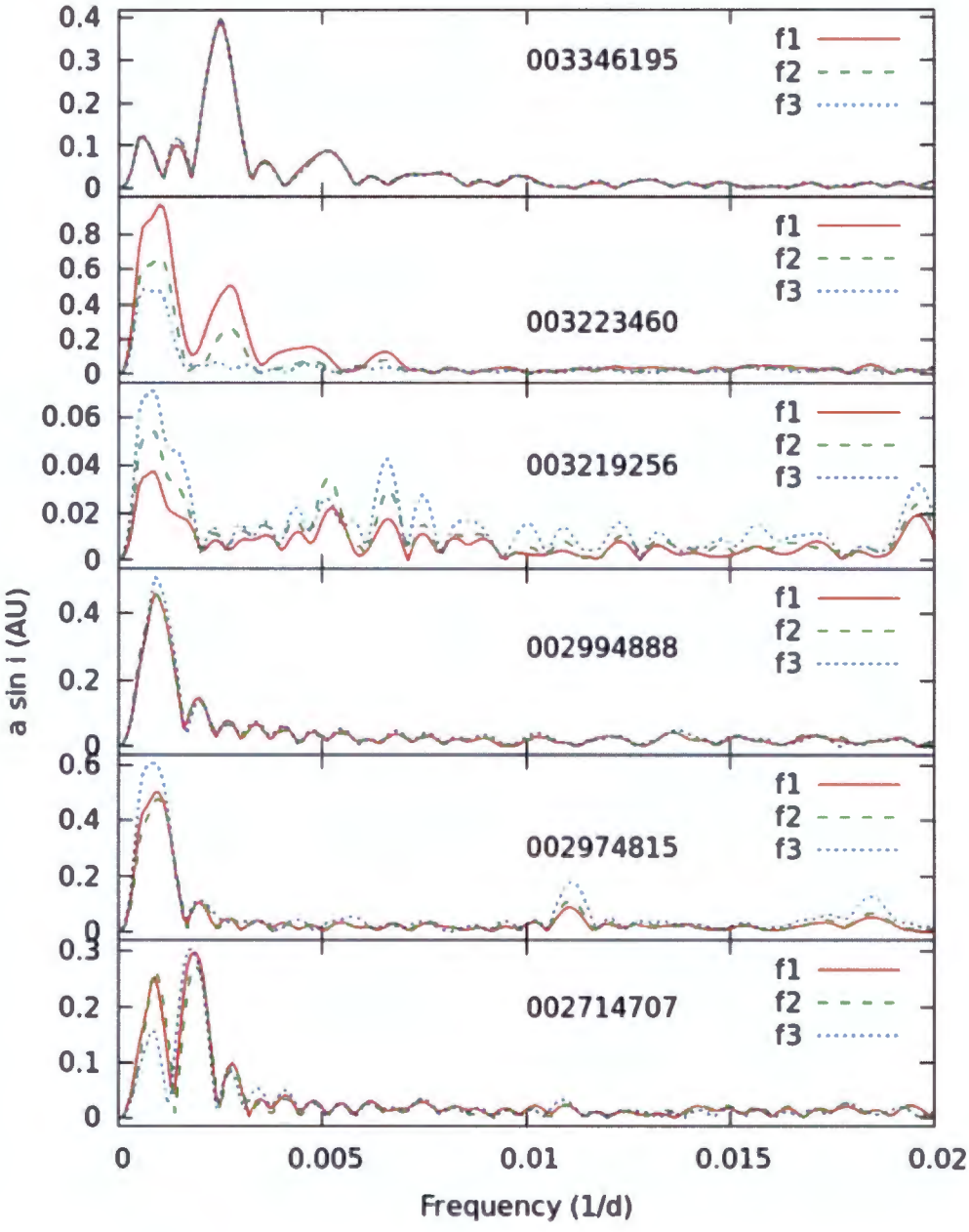

Figure 2.8: The same as Fig.2.7, in this case for KIC numbers 003346195, 003223460, 003219256, 002994888, 002974815 and 002714707.

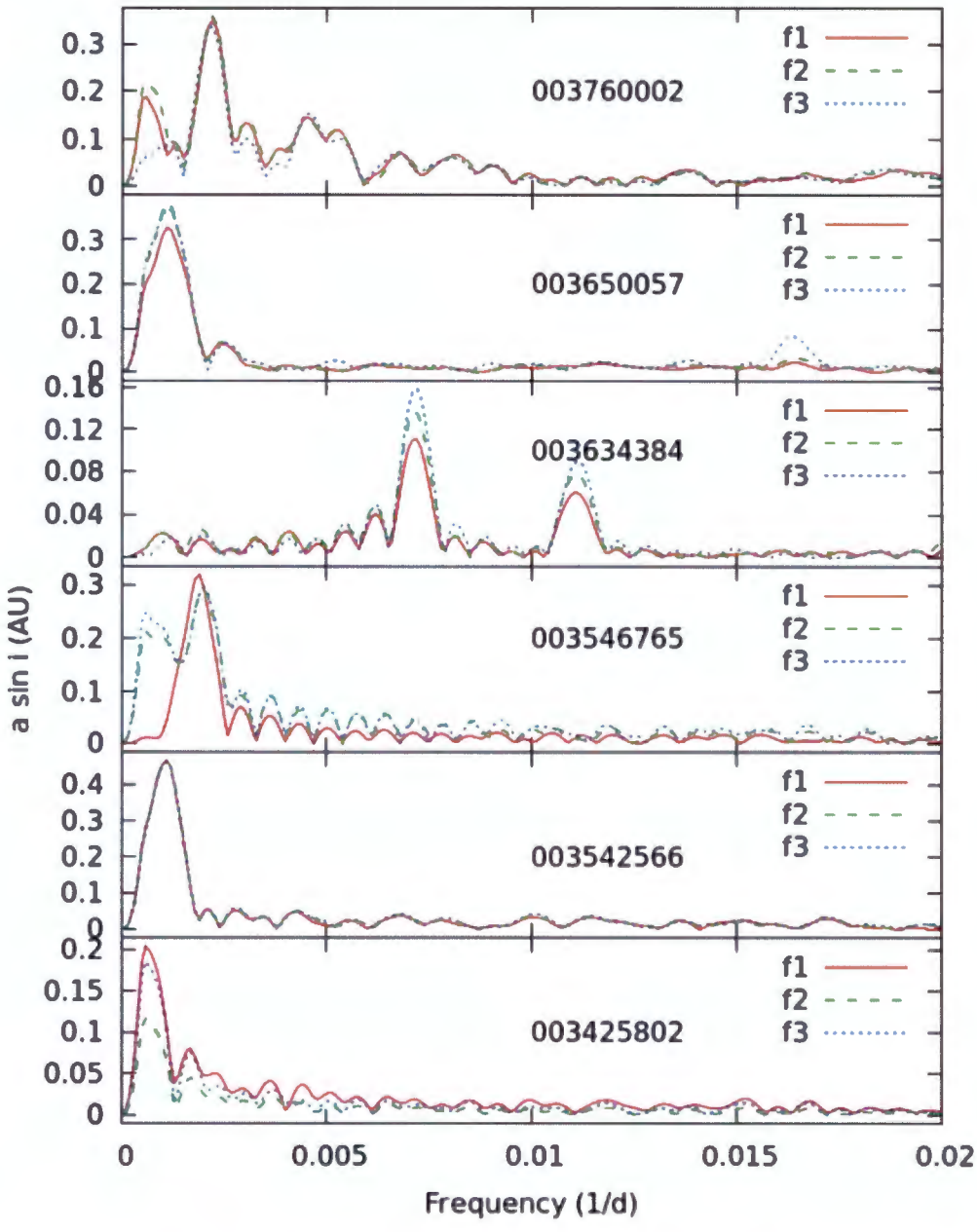

Figure 2.9: The same as Fig.2.7, in this case for KIC numbers 003760002, 003650057, 003634384, 003546765, 003542566 and 003425802.

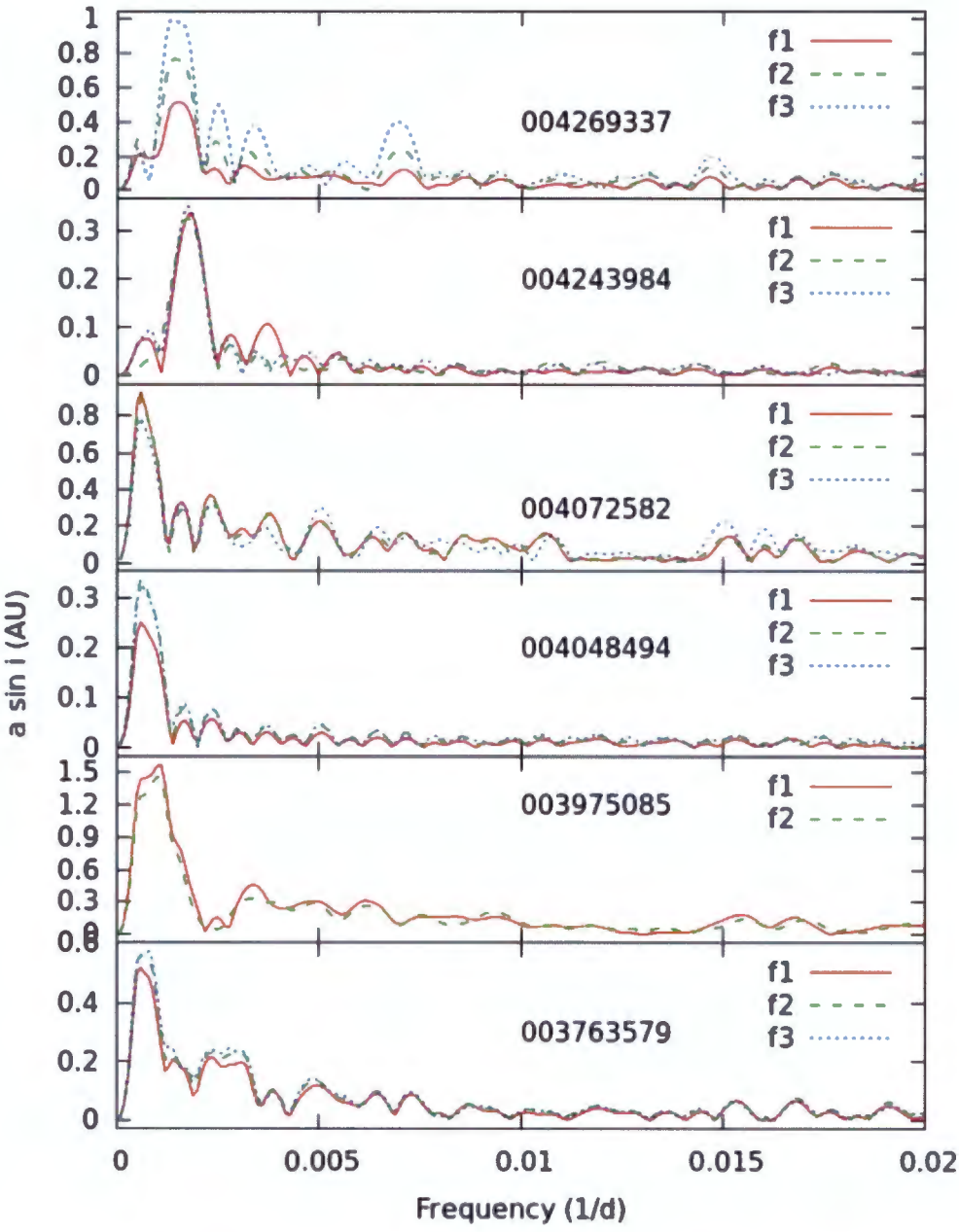

Figure 2.10: The same as Fig.2.7, in this case for KIC numbers 004269337, 004243984, 004072582, 004048494, 003975085 and 003763579.

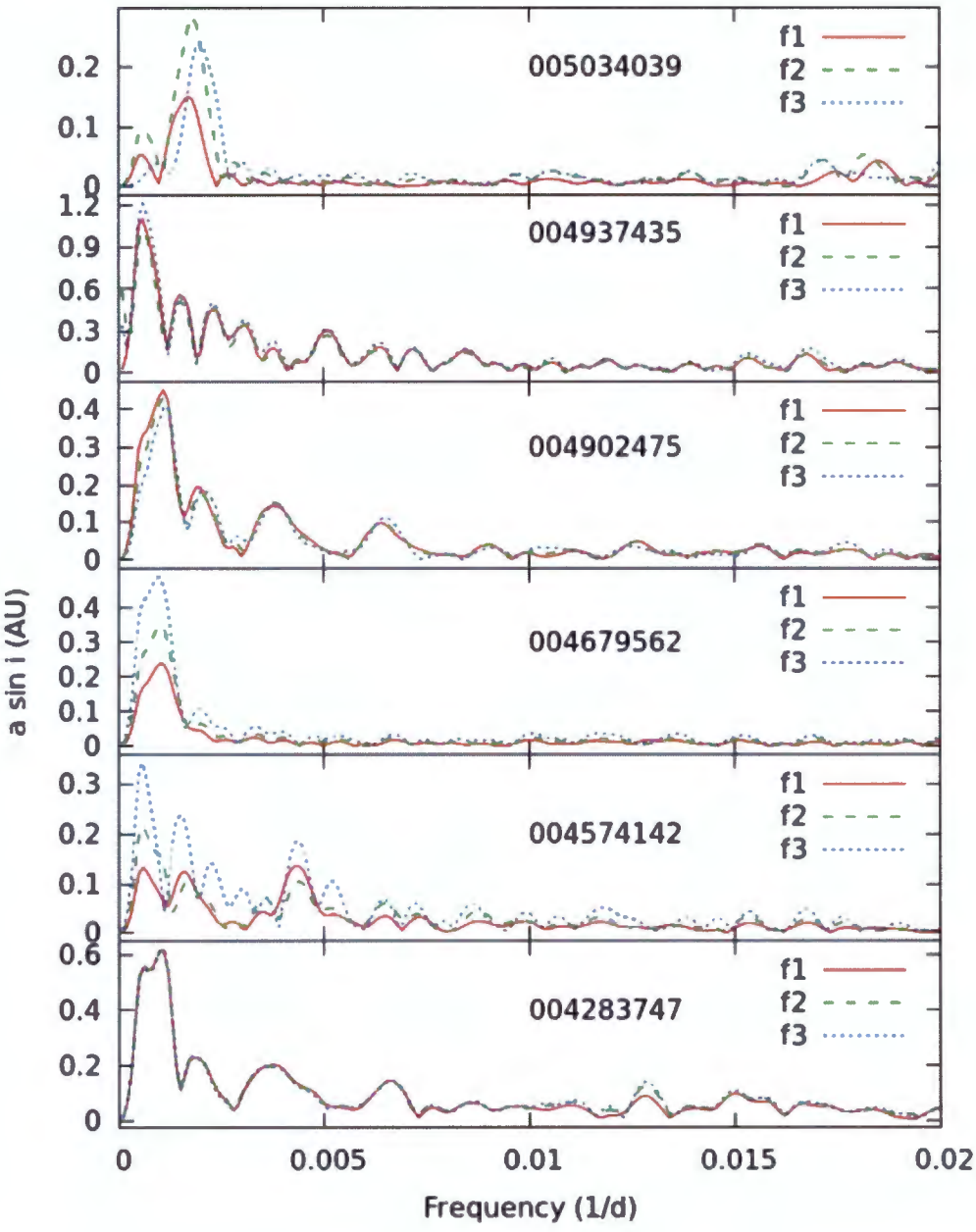

Figure 2.11: The same as Fig.2.7, in this case for KIC numbers 005034039, 004937435, 004902475, 004679562, 004574142 and 004283747.

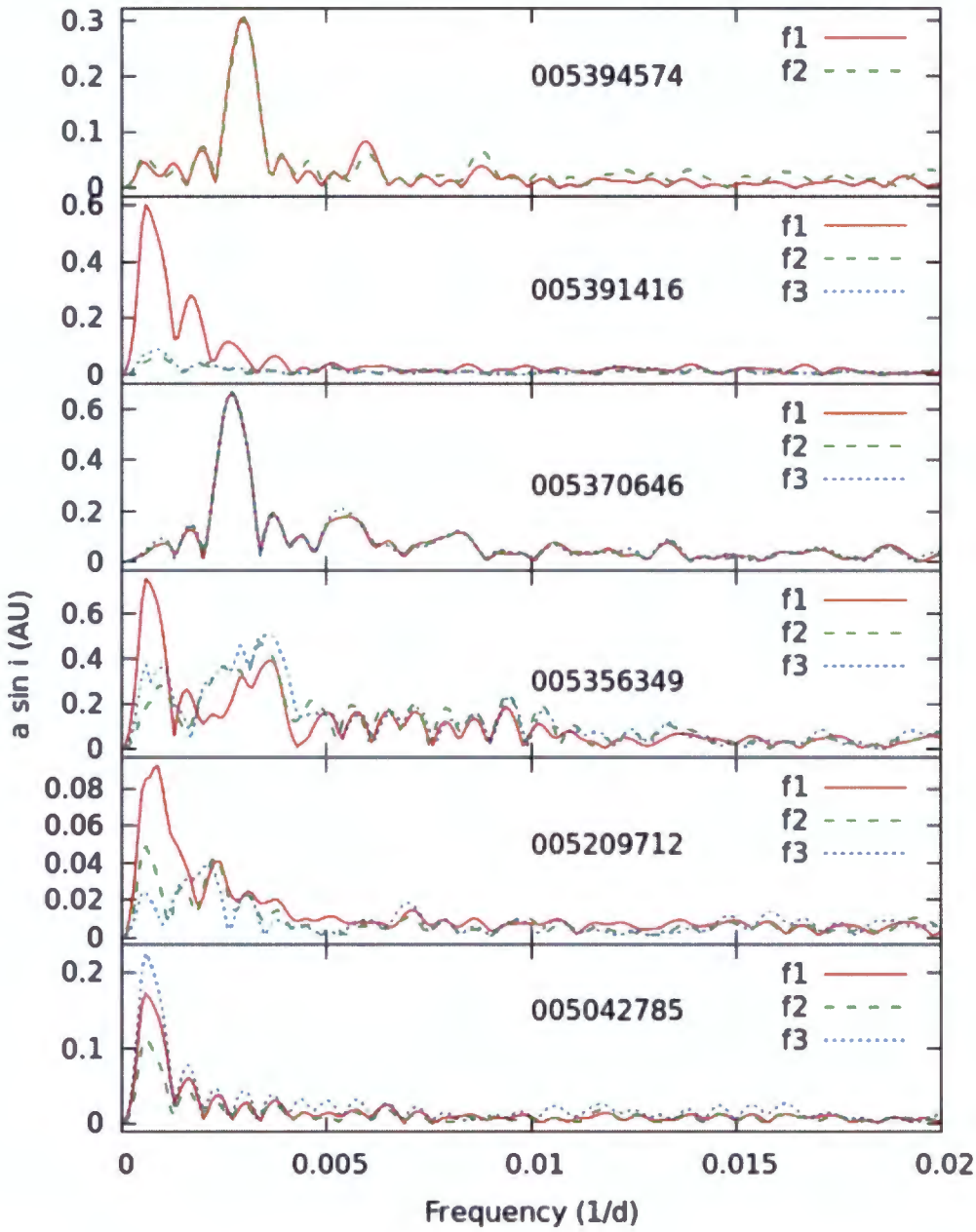

Figure 2.12: The same as Fig.2.7, in this case for KIC numbers 005394574, 005391416, 005370646, 005356349, 005209712 and 005042785.

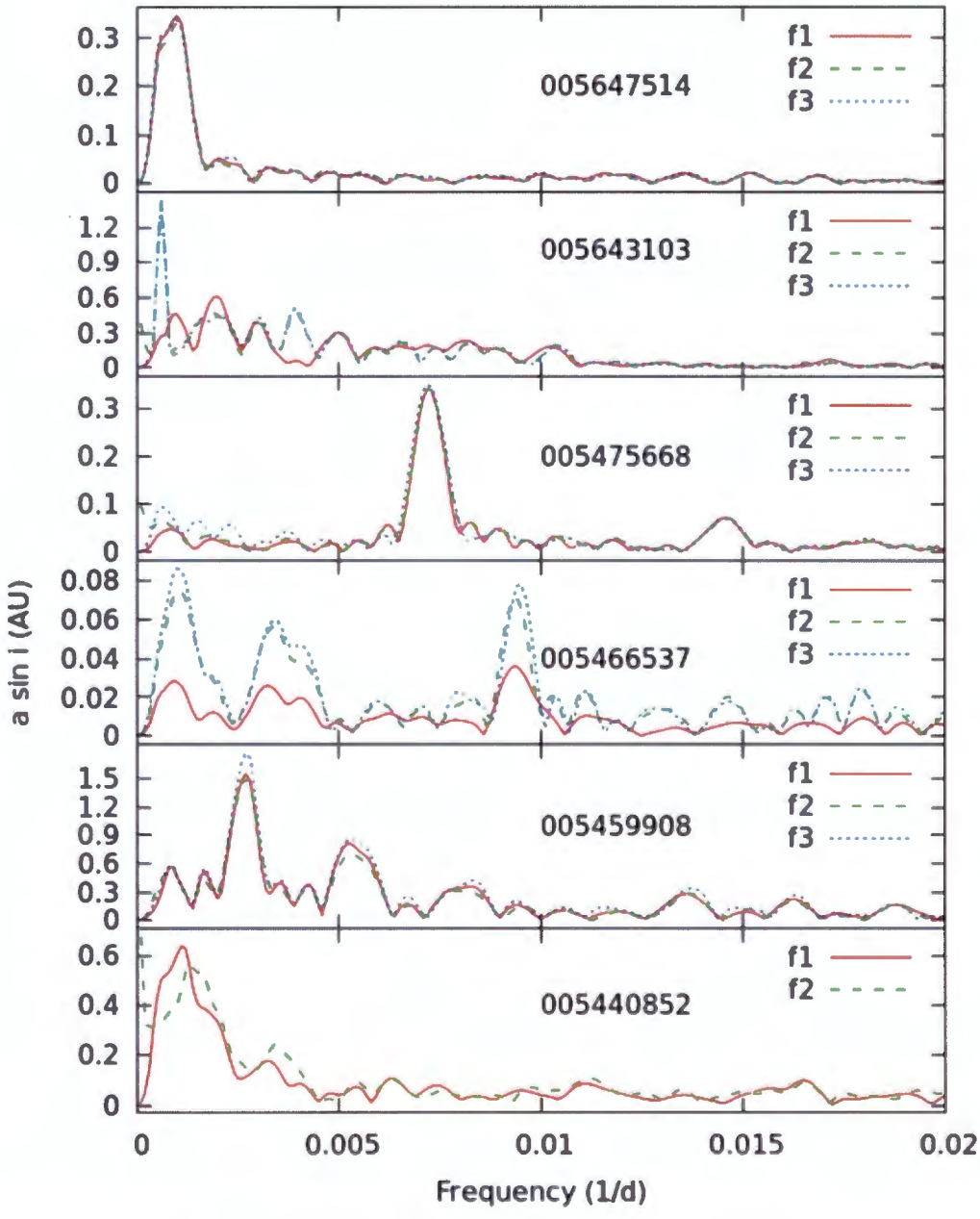

Figure 2.13: The same as Fig.2.7, in this case for KIC numbers 005647514, 005643103, 005475668, 005466537, 005459908 and 005440852.

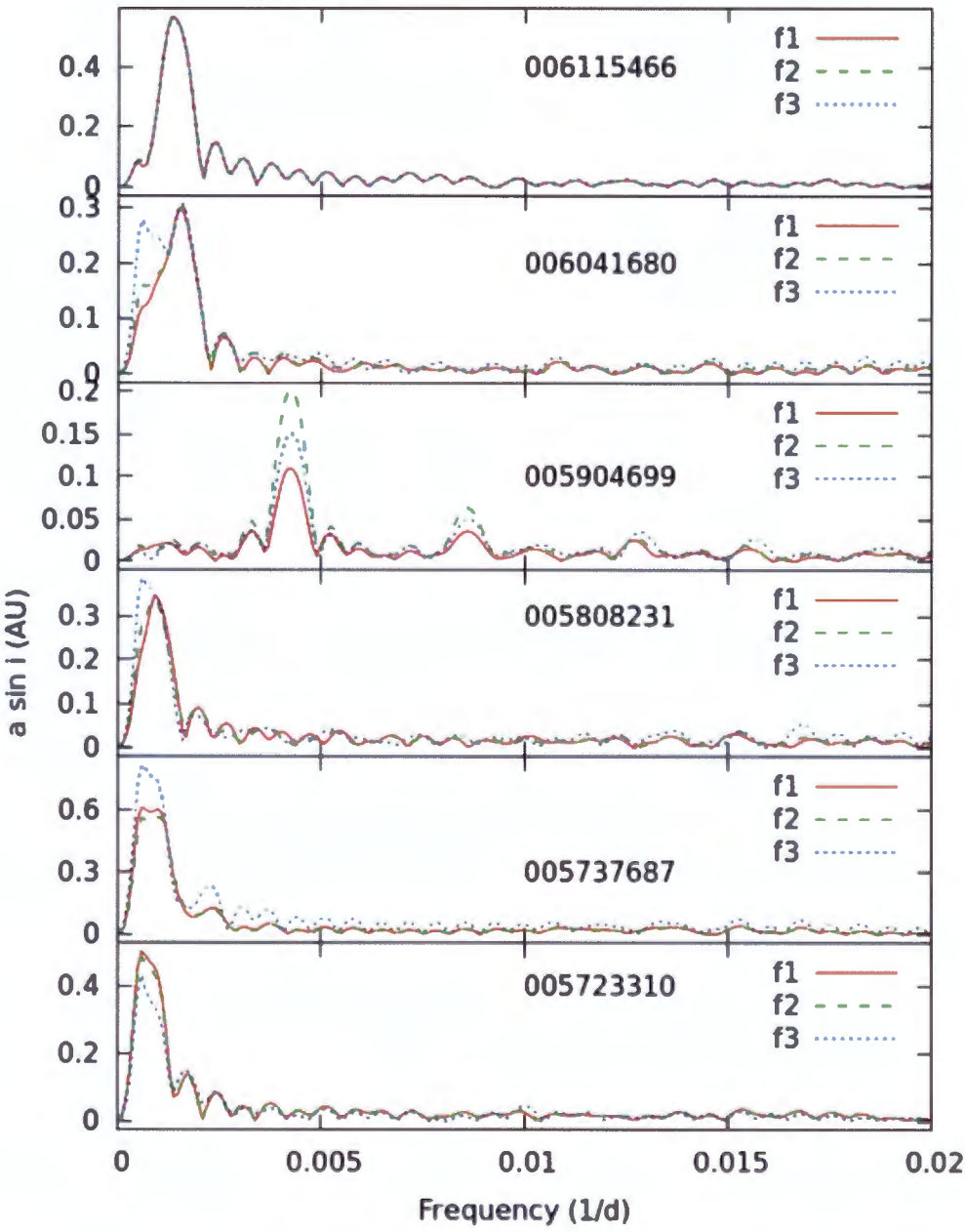

Figure 2.14: The same as Fig.2.7, in this case for KIC numbers 006115466, 006041680, 005904699, 005808231, 005737687 and 005723310.

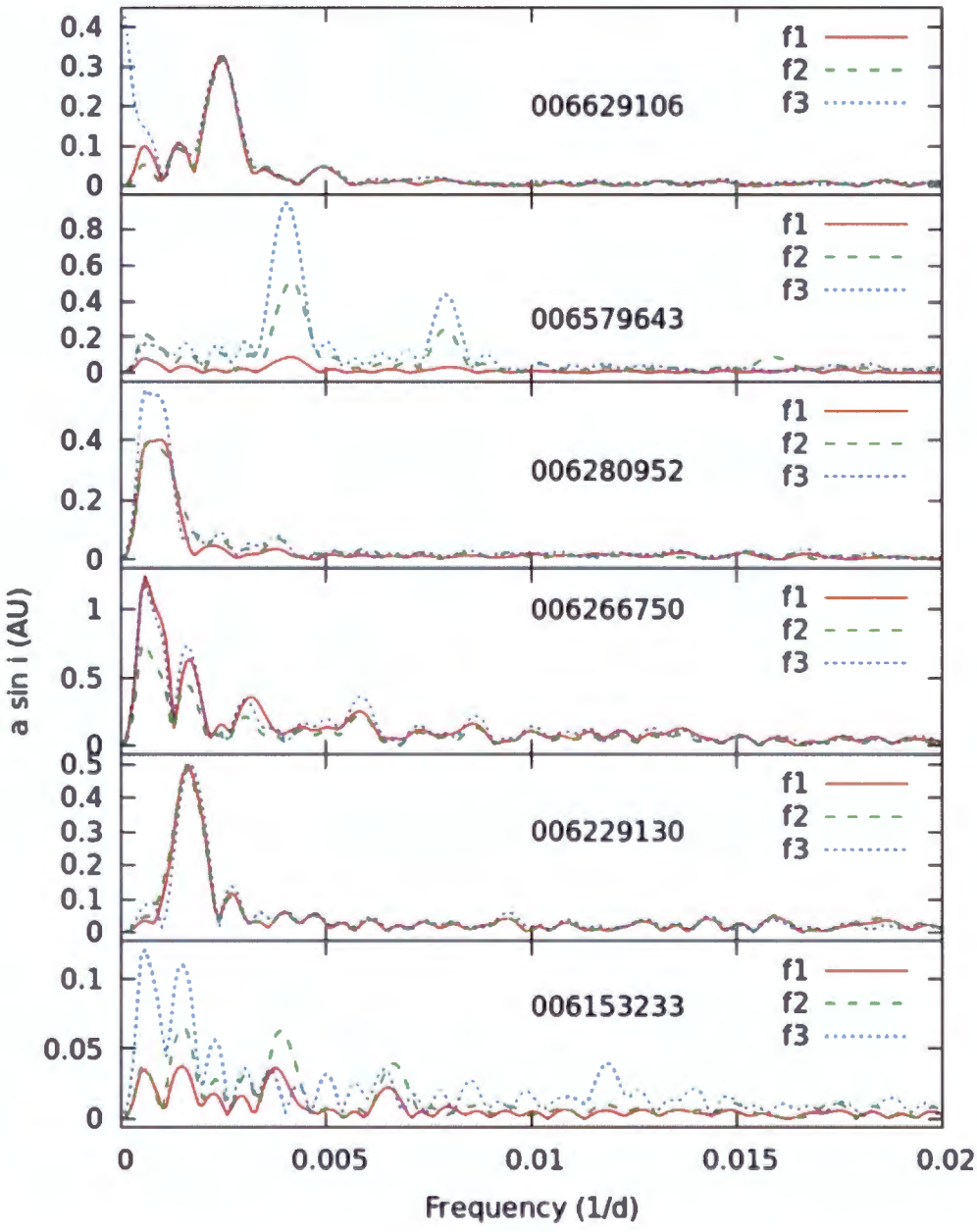

Figure 2.15: The same as Fig.2.7, in this case for KIC numbers 006629106, 006579643, 006280952, 006266750, 006229130 and 006153233.

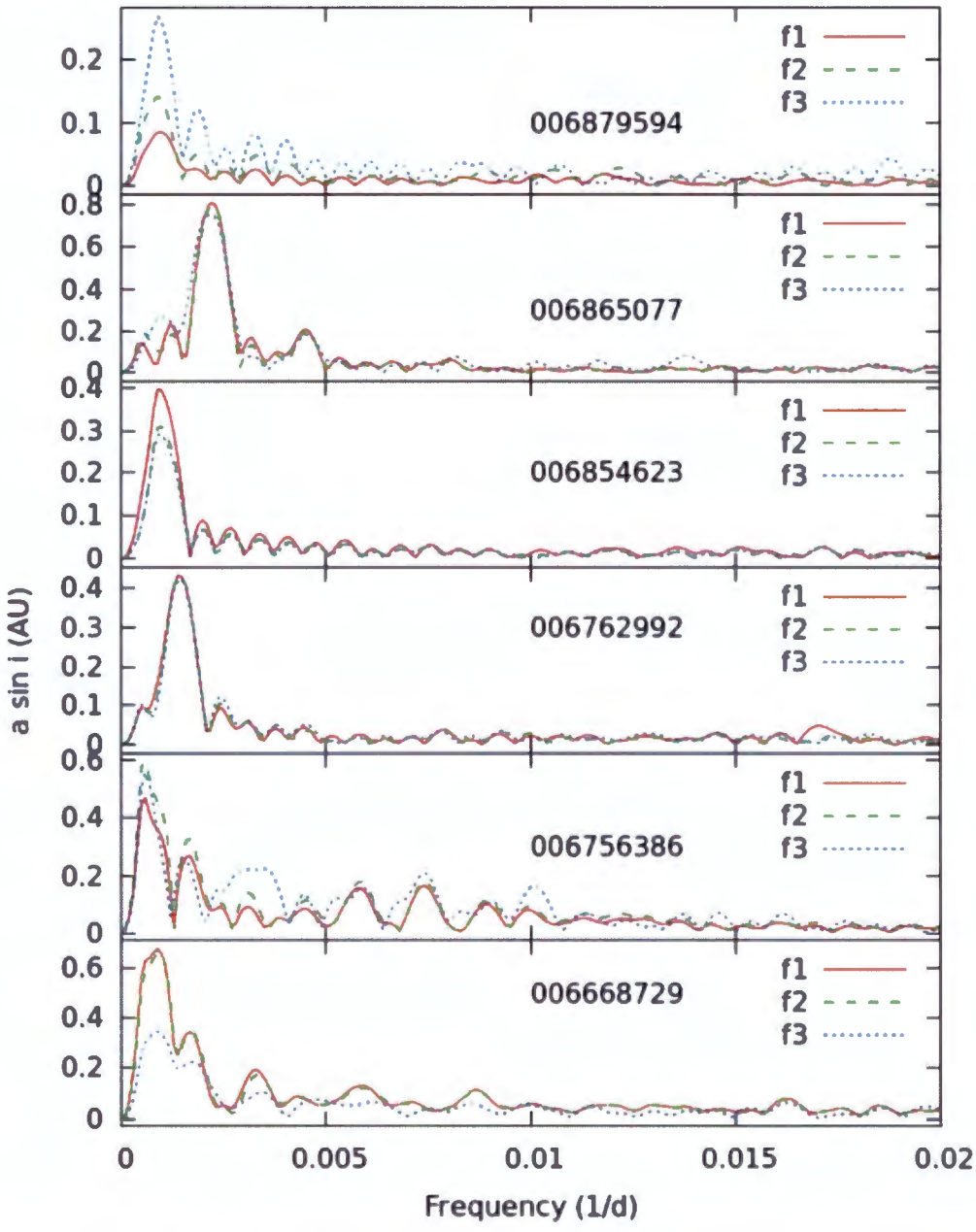

Figure 2.16: The same as Fig.2.7, in this case for KIC numbers 006879594, 006865077, 006854623, 006762992, 006756386 and 006668729.

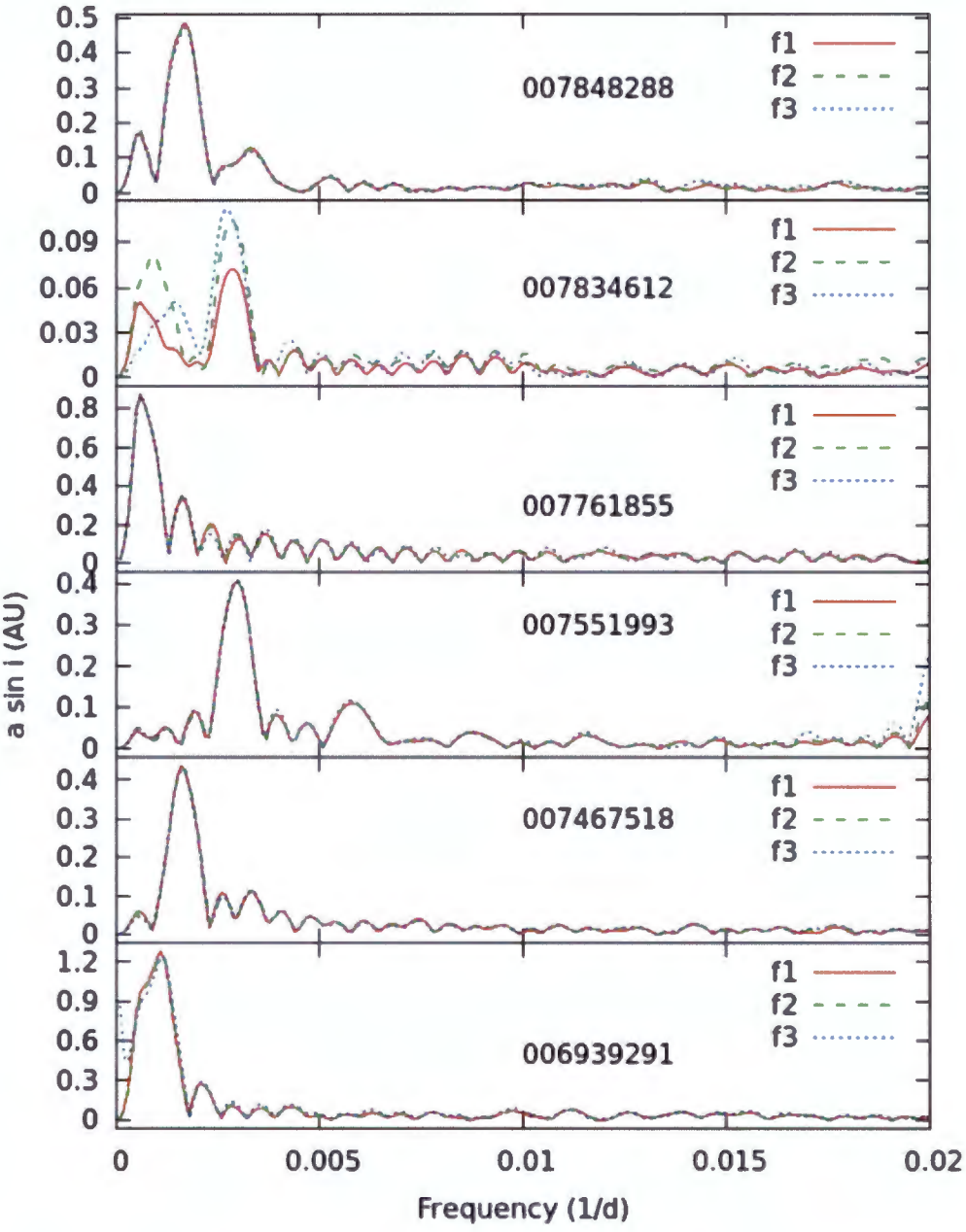

Figure 2.17: The same as Fig.2.7, in this case for KIC numbers 007848288, 007834612, 007761855, 007551993, 007467518 and 006939291.

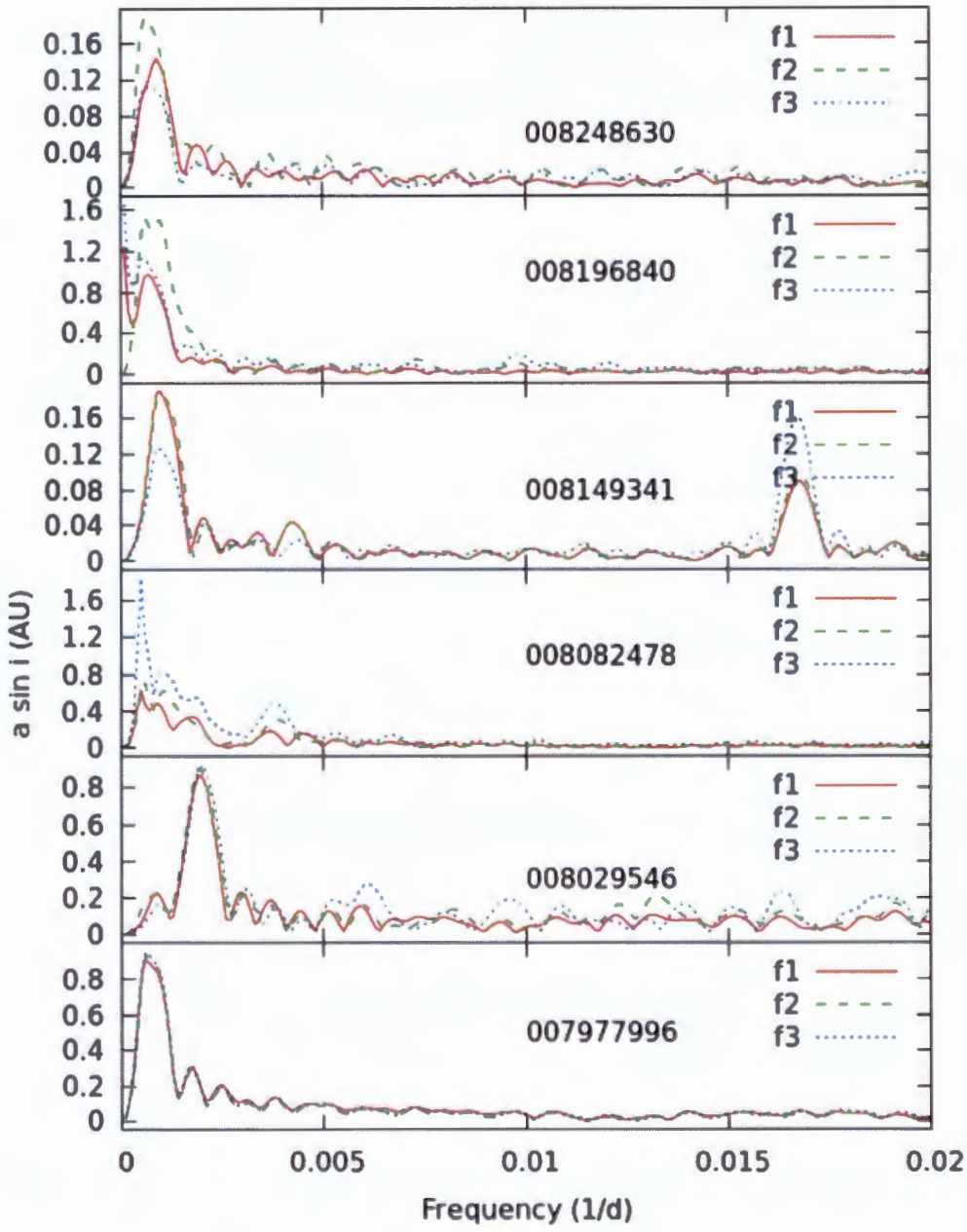

Figure 2.18: The same as Fig.2.7, in this case for KIC numbers 008248630, 008196840, 008149341, 008082478, 008029546 and 007977996.

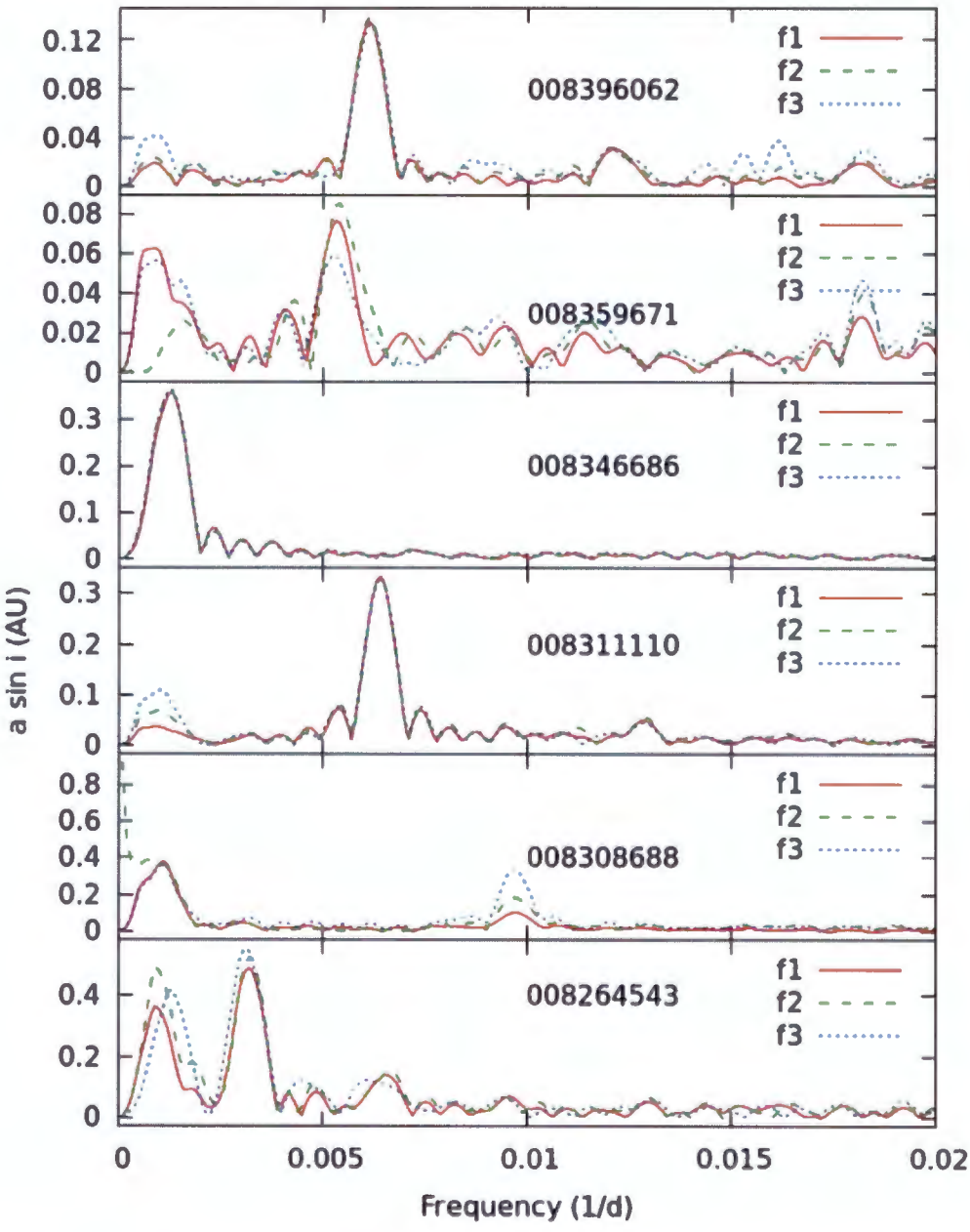

Figure 2.19: The same as Fig.2.7, in this case for KIC numbers 008396062, 008359671, 008346686, 008311110, 008308688 and 008264543.

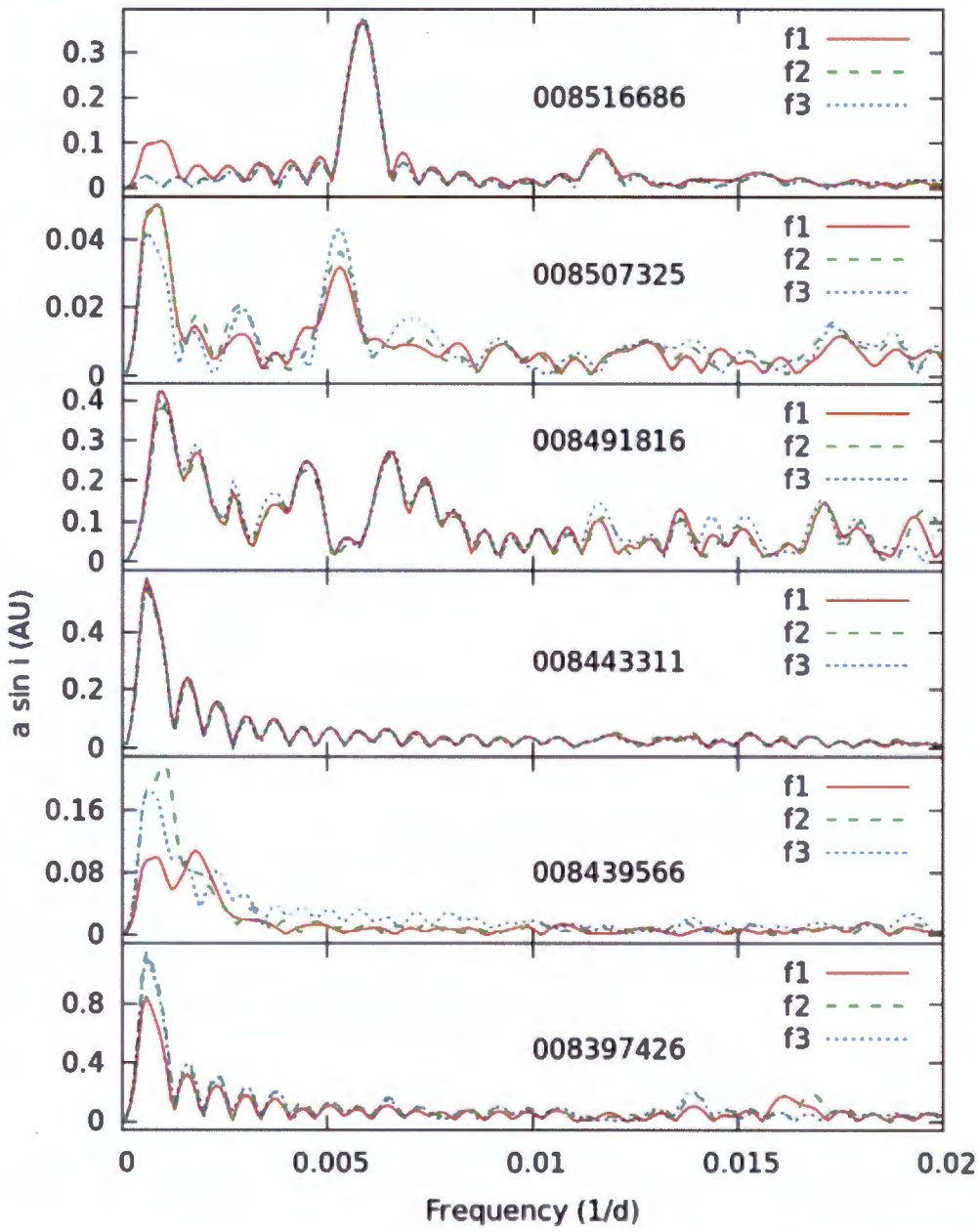

Figure 2.20: The same as Fig.2.7, in this case for KIC numbers 008516686, 008507325, 008491816, 008443311, 008439566and 008397426.

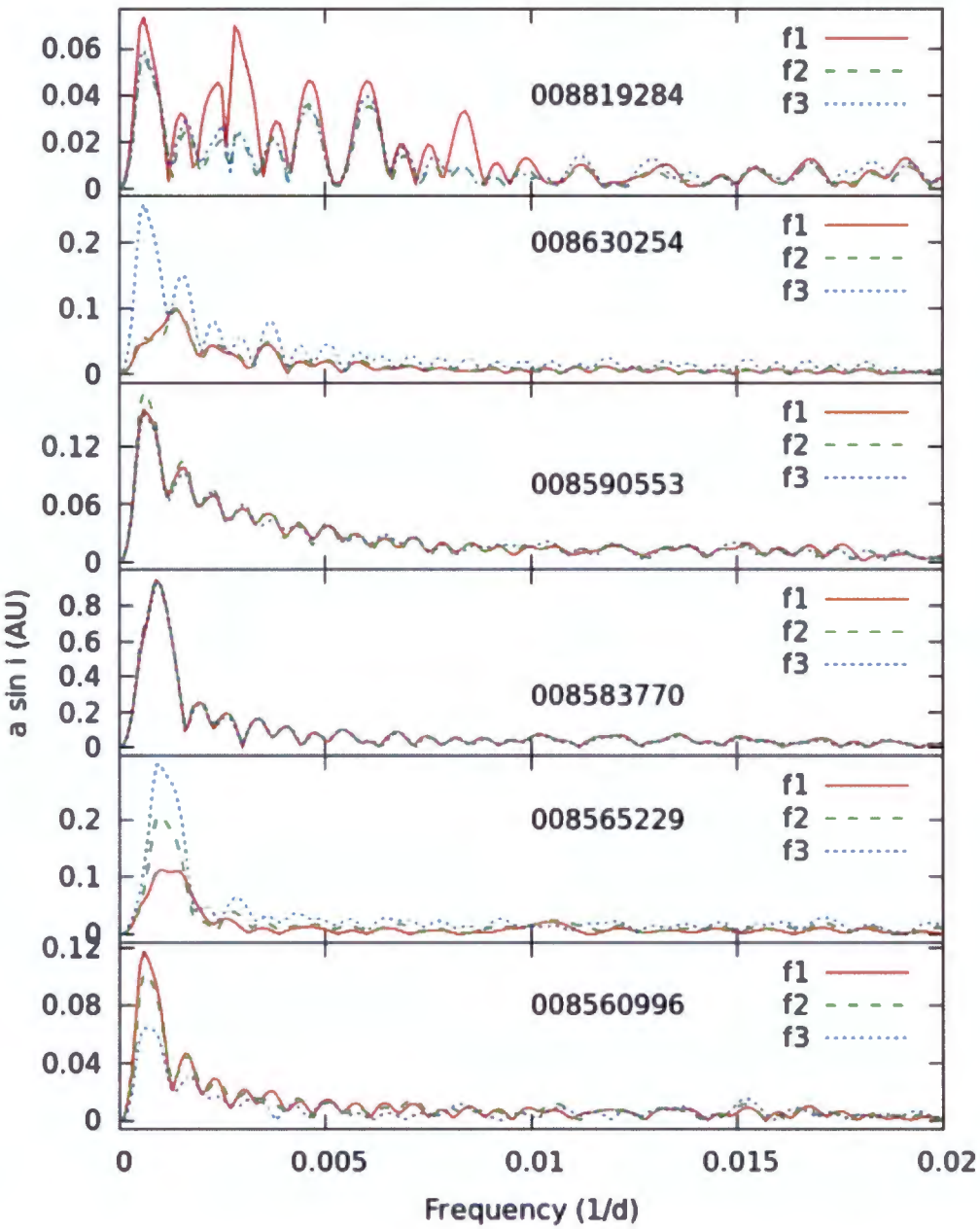

Figure 2.21: The same as Fig.2.7, in this case for KIC numbers 008819284, 008630254, 008590553, 008583770, 008565229 and 008560996.

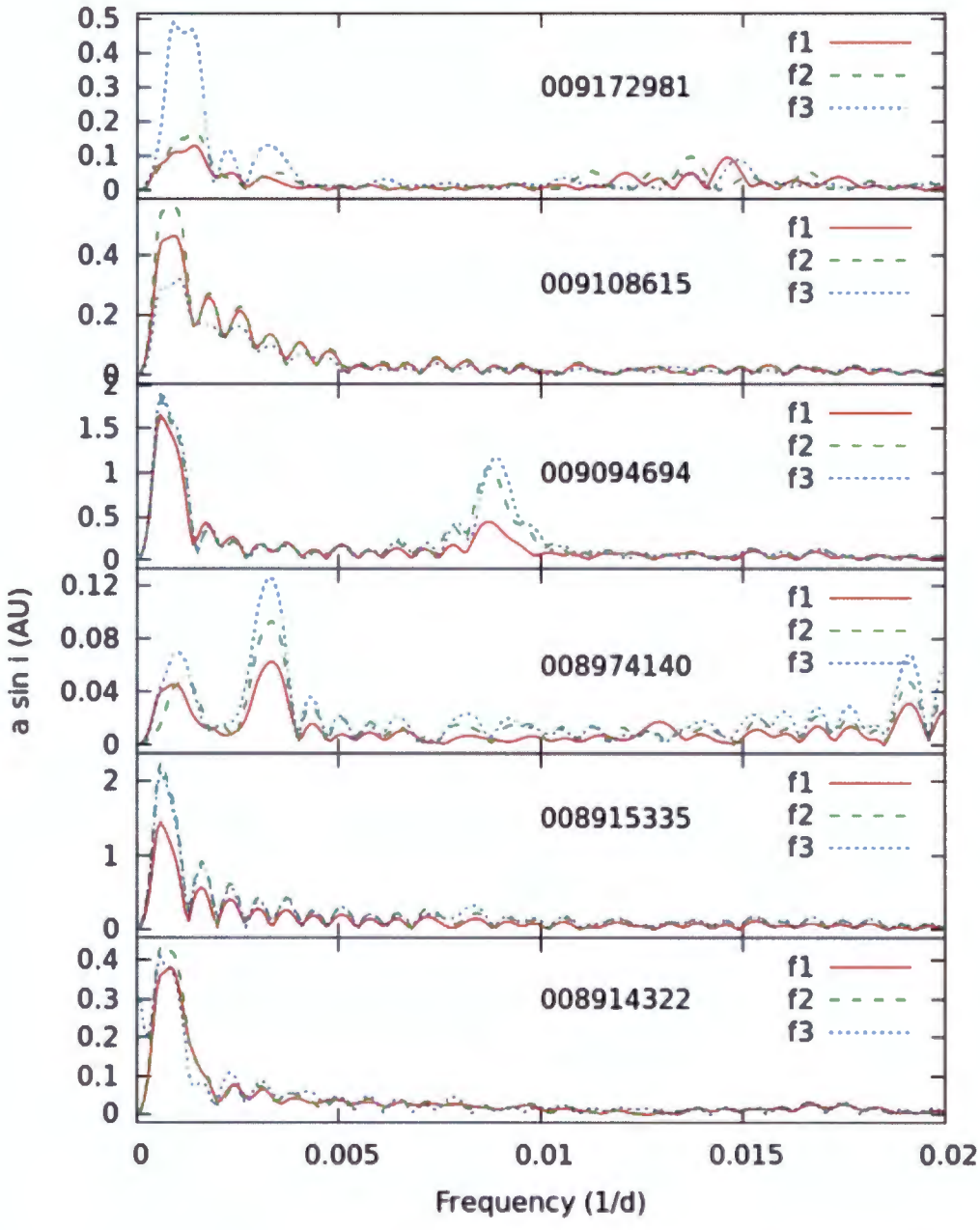

Figure 2.22: The same as Fig.2.7, in this case for KIC numbers 009172891, 009108615, 009094694, 008974140, 008915335 and 008914322.

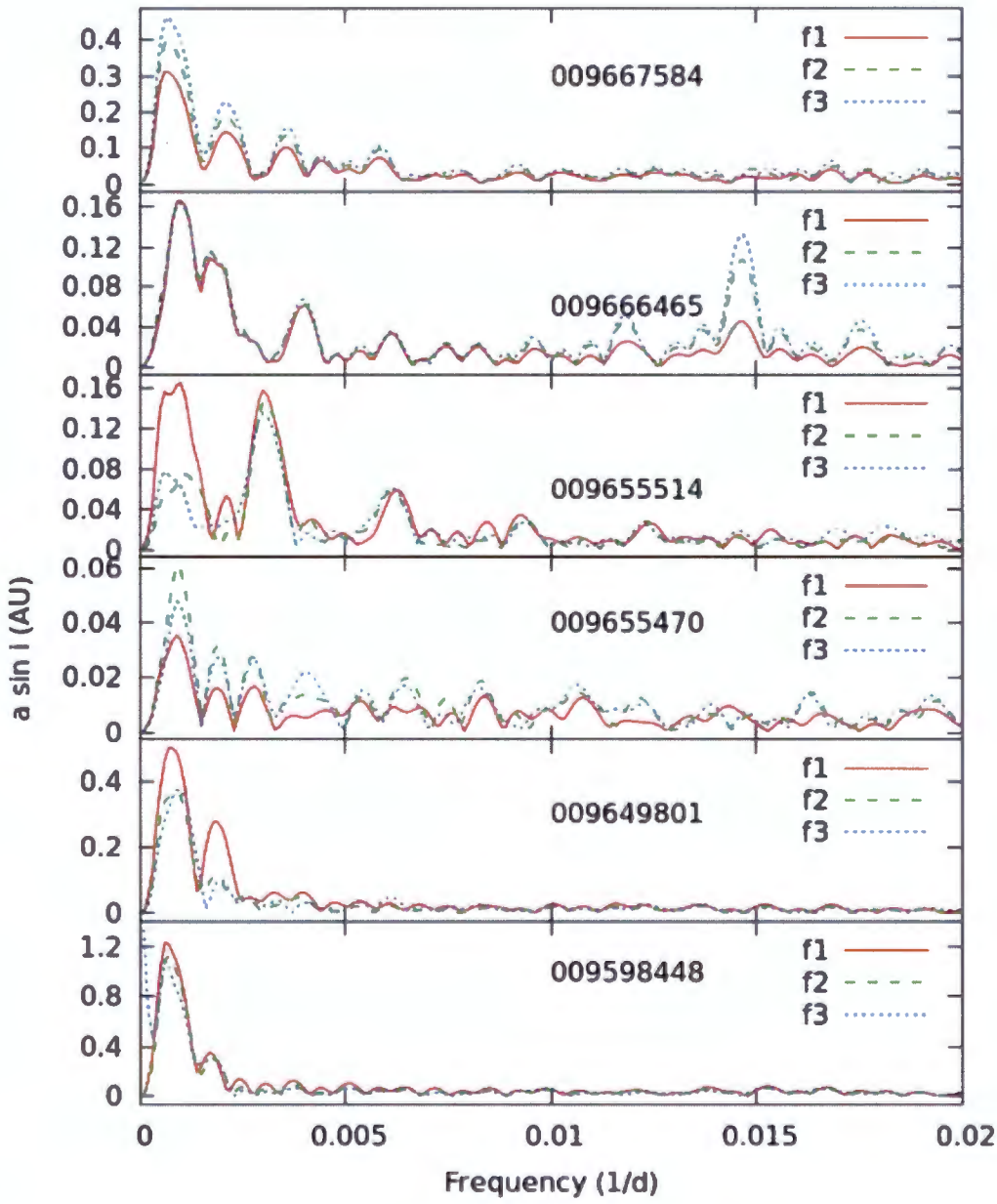

Figure 2.24: The same as Fig.2.7, in this case for KIC numbers 009667584, 009666465, 009655514, 009655470, 009649801 and 009598448.

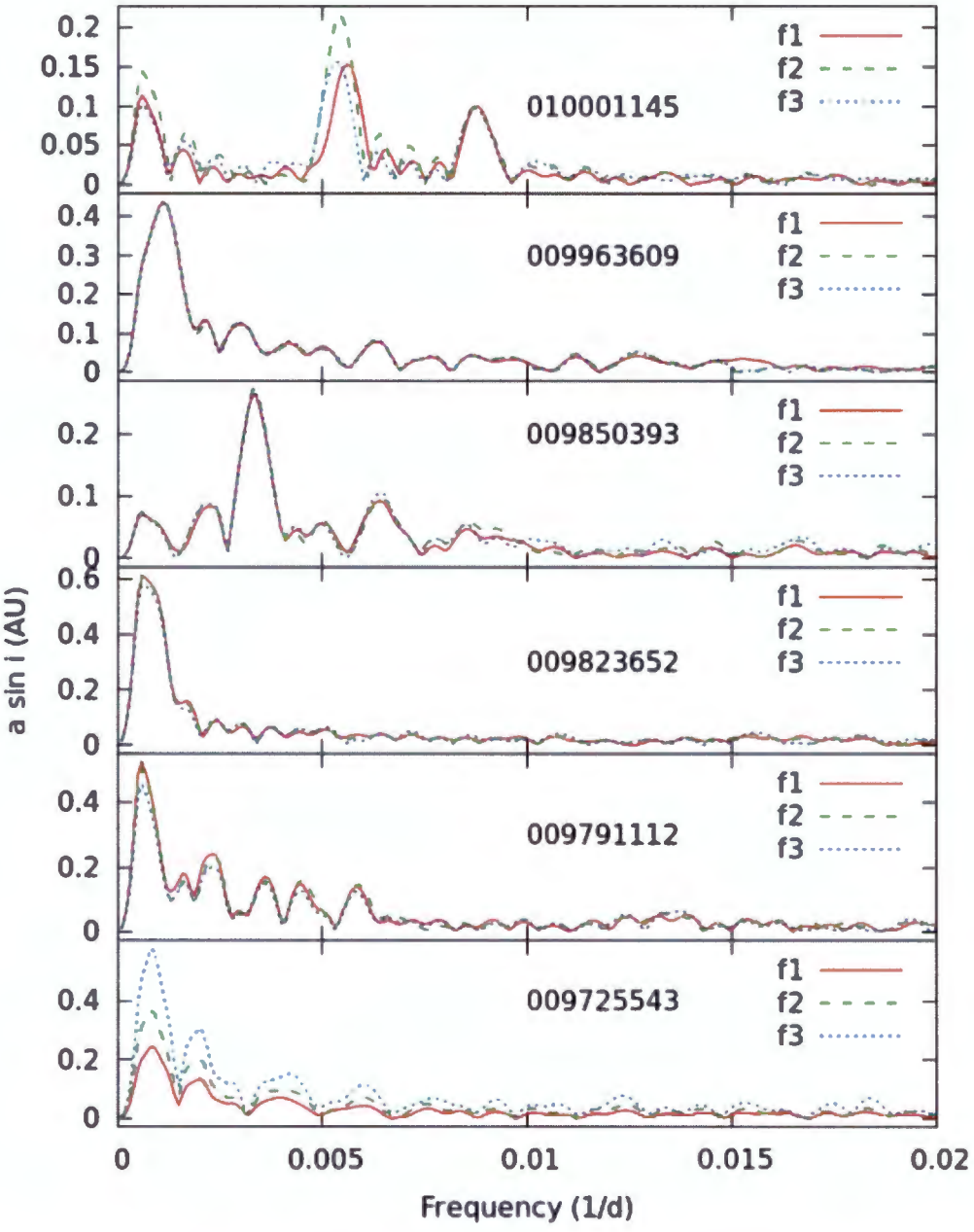

Figure 2.25: The same as Fig.2.7, in this case for KIC numbers 010001145, 009963609, 009850393, 009823652, 009791112 and 009725543.

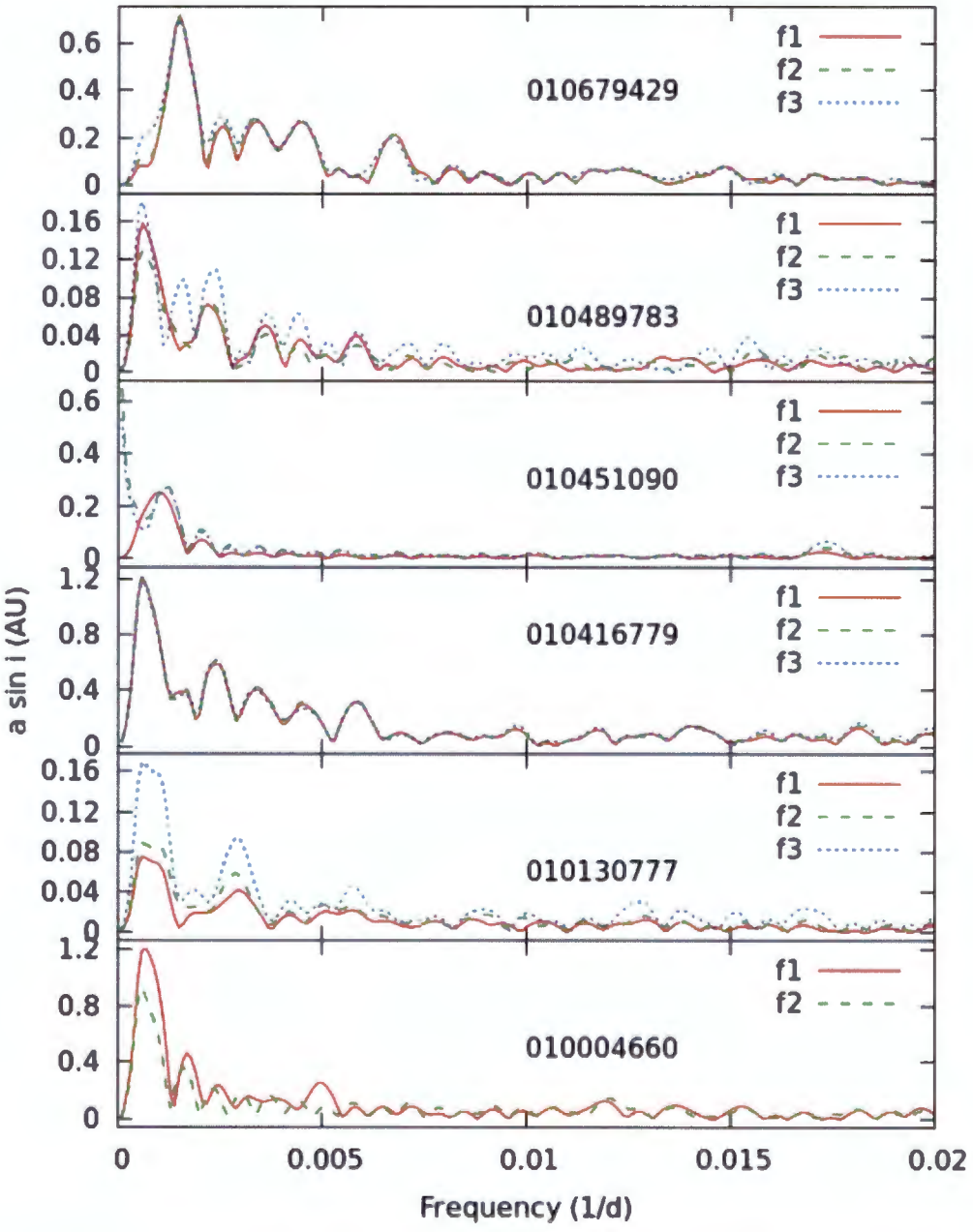

Figure 2.26: The same as Fig.2.7, in this case for KIC numbers 010679429, 010489783, 010451090, 010416779, 010130777 and 010004660.

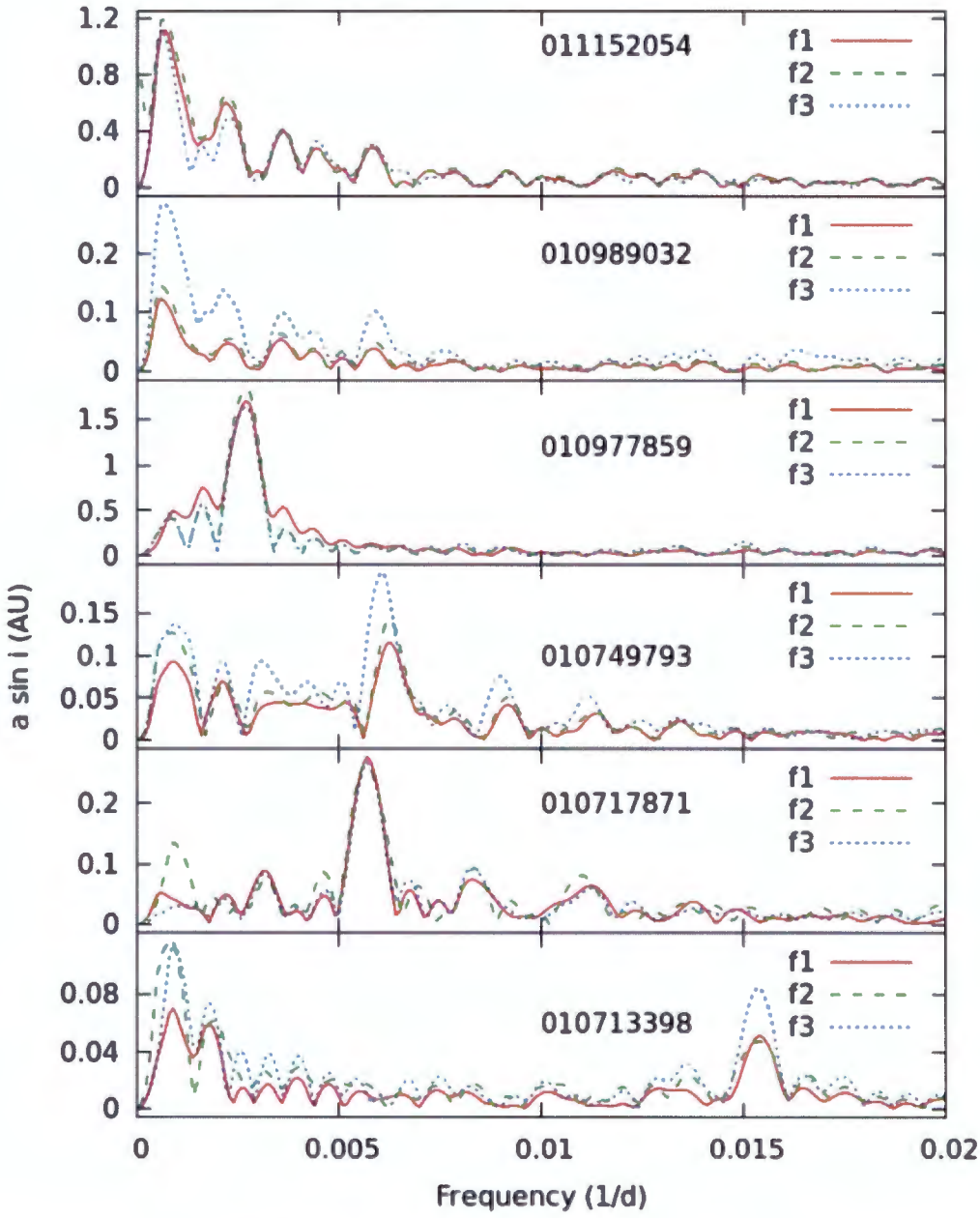

Figure 2.27: The same as Fig.2.7, in this case for KIC numbers 011152054, 010989032, 010977859, 010749793, 010717871 and 010713398.

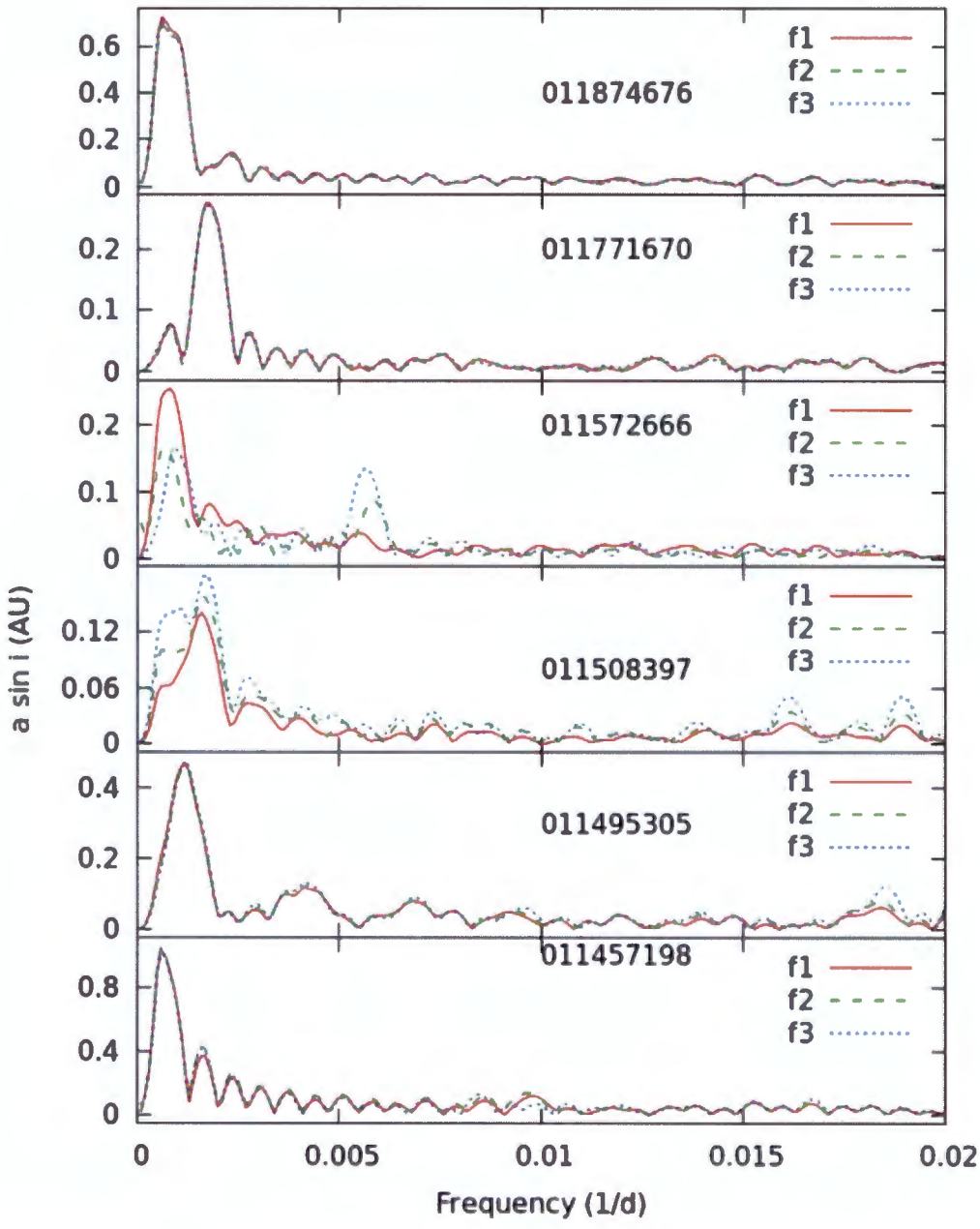

Figure 2.28: The same as Fig.2.7, in this case for KIC numbers 011874676, 011771670, 011572666, 011508397, 011495305 and 011457198.

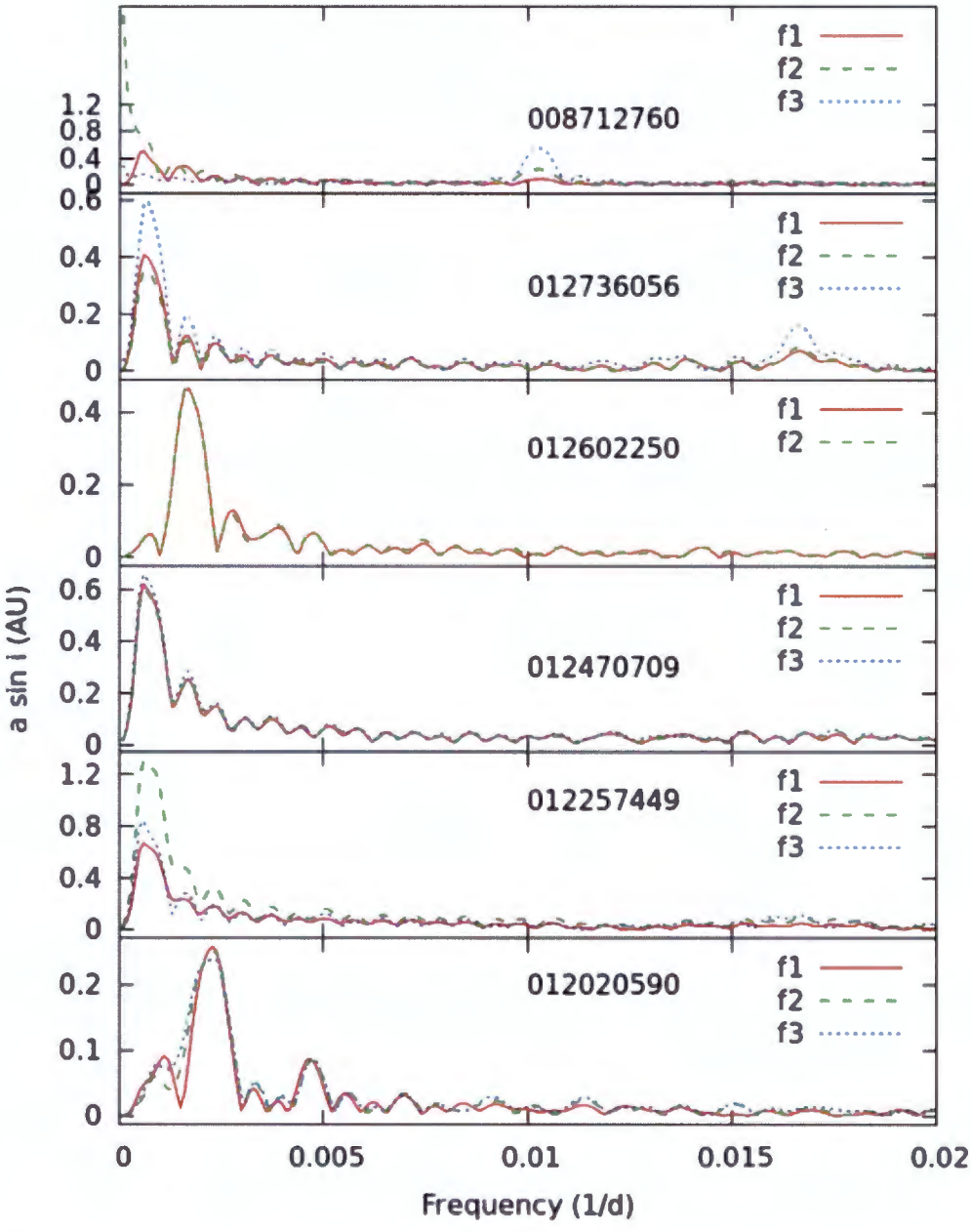

Figure 2.29: The same as Fig.2.7, in this case for KIC numbers 008712760, 012736056, 012602250, 012470709, 012257449 and 012020590.

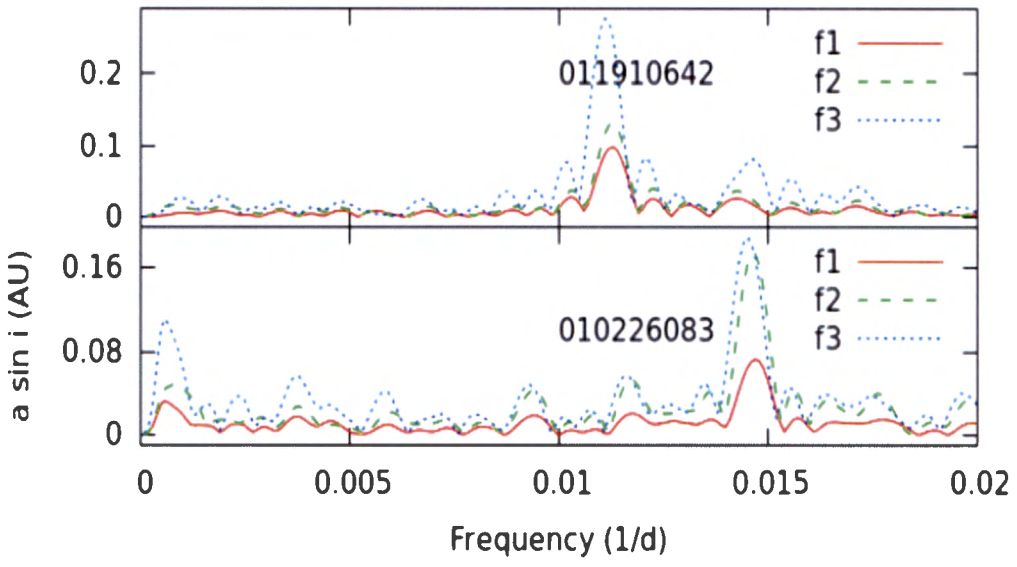

Figure 2.30: The same as Fig.2.7, in this case for KIC numbers 011910642 and 010226083.

2.3 List of Identified Binary Stars

By visual inspection of the binarograms of all 1646 δ Sct stars we eventually identified 141 binary candidates as well as some other systems. These are listed in Table 2.1. In the table, the second column shows the KIC number of the binaries. Effective temperature of the star is given in column three. Column four is the approximate orbital period determined from the binarogram. The fifth column shows the pulsation frequencies and the corresponding amplitudes of the frequencies. True binaries are identified by the fact that two or more pulsation frequencies give rise to the same peak. Only highest amplitude frequency or frequencies are shown in the table. The result is acceptable since only pulsation frequencies of the highest amplitude, free from neighbouring frequency are selected. In addition to this, the binarogram is only a guide to which stars may be binaries. It will be analyzed further using time-delay. The last column shows the type of systems (binary or multiple) and uncategorised systems (named as 'unknown') we identified.

Table 2.1: List of identified binary stars and other types of systems found using binarogram.

	KIC Number	$T_{\rm eff}$ (K)	Orbital period (days)	Frequency (d^{-1}) & Amplitude (ppt)	Type
1	001294670	7076	366	(12.6228, 1.341), (14.9703, 0.934), (16.7269, 0.703)	Triple
2	001577039	6001	2525	(10.3573, 1.264), (10.8032, 0.938), (8.0087, 0.510)	Binary
3	002168333	8137	360	(13.7211, 0.511), (20.5745, 0.478), (16.6584, 0.244)	Binary
4	002168420	7826	1158	(12.51183, 1.423), (8.7043, 1.332), (13.8434, 1.018)	Binary
5	002439660	7991	2527	(42.9670, 0.117), (43.0681, 0.059), (40.2271, 0.031)	Binary
6	002570760	7563	1701	(20.7452, 0.712), (21.4675, 0.604), (27.5957, 0.578)	Binary
7	002571868	7929	157	(27.0597, 0.359), (19.1301, 0.318), (25.5142, 0.203)	Binary
8	002714707	7045	579	(11.5728, 1.710), (11.9498, 1.535), (16.7212, 1.318)	Binary
9	002974815	7632	1201	(13.5001, 3.113), (8.3682, 2.439), (18.8910 0.904)	Binary
10	002994888	7471	1084	(12.6887, 1.444), (21.2028, 1.123), (15.6727, 1.094)	Binary
11	003219256	7292	1263	(17.1530, 0.849), (27.4776, 0.5919), (28.2596, 0.5289)	Binary
12	003223460	7932	1007	(40.8953, 0.0909)	Triple
13	003346195	7508	421	(20.1493, 1.568), (22.5678, 1.241), (24.8477, 1.162)	Binary
14	003425802	8047	1635	(25.1884, 0.174), (36.5718, 0.116), (24.3064, 0.065)	Binary
15	003542566	8121	908	(25.4700, 0.289), (40.4961, 0.182), (23.0733, 0.134)	Binary
16	003546765	8229	514	(21.1142, 0.159), (15.0504, 0.144), (36.1716, 0.139)	Binary
17	003634384	7477	140	(15.1199, 1.103), (9.6915, 0.912), (28.1843, 0.848)	Binary
18	003650057	7124	896	(13.7727, 0.677), (18.366, 0.670), (16.6630, 0.553)	Binary
19	003760002	7032	505	(12.7799, 1.300), (23.3326, 1.2108), (13.3901, 1.1440)	Binary
20	003763579	8336	1281	(12.3371, 3.687), (12.8849, 3.335), (7.5627, 3.319)	Binary

continued ...

...continued

	KIC Number	T_{eff} (K)	Orbital period (days)	Frequency (d^{-1}) & Amplitude (ppt)	Type
21	003975085	7705	972	(7.6375, 0.634)	Binary
22	004048494	7621	1635	(14.8942, 3.481), (13.7093, 2.962), (11.0589, 1.420)	Binary
23	004072582	7750	1659	(9.4834, 0.358), (11.4666, 0.335), (7.1129, 0.298)	Binary
24	004243984	6859	579	(18.0515, 0.813), (17.4119, 0.515), (21.7571, 0.470)	Binary
25	004269337	8003	723	(23.6751, 0.438), (13.7235, 0.417), (16.8638, 0.409)	Binary
26	004283747	7310	940	(24.4051, 0.525), (12.6962, 0.474), (27.4450, 0.380)	Binary
27	004574142	8339	1737	(25.8547, 0.3401), (27.4035, 0.304), (37.5365, 0.296)	Binary
28	004679562	7435	997	(29.8944, 0.723), (28.7796, 0.570), (29.3033, 0.346)	Binary
29	004902475	7172	922	(13.9283, 1.358), (20.6470, 0.898)	Binary
30	004937435	7803	1762	(13.0134, 2.916), (11.7965, 2.214), (13.3238, 1.810)	Binary
31	005034039	7218	624	(8.4694, 0.930), (7.4933, 0.921), (23.0162, 0.861)	Binary
32	005042785	7148	1635	(8.3859, 0.971), (8.6969, 0.686), (28.6420, 0.584)	Binary
33	005209712	8336	1112	(8.6341, 0.419), (31.5446, 0.345), (17.1641, 0.343)	Binary
34	005356349	8294	1566	(7.3262, 0.061), (19.6033, 0.051), (46.4871, 0.046)	Binary
35	005370646	7010	394	(15.4951, 0.2461), (15.9777, 0.172)	Binary
36	005391416	8062	1566	(13.3154, 1.448), (10.0362, 1.411), (7.6963, 0.870)	Binary
37	005394574	6759	339	(15.3718, 0.140)	Binary
38	005440852	8327	854	(29.8442, 0.013)	Binary
39	005459908	8995	427	(8.5969, 0.047), (14.6732, 0.032)	Unknown
40	005466537	6979	993	(19.9703, 0.898), (11.4428, 0.868), (21.1463, 0.856)	Binary
41	005475668	8045	140	(36.0251, 0.093), (25.7862, 0.088), (29.1327, 0.086)	Binary
42	005643103	10225	1567	(43.4094, 0.248), (13.0862, 0.234)	Binary
43	005647514	7178	997	(23.5777, 1.022), (15.0464, 0.986), (14.1576, 0.734)	Binary
44	005723310	7942	1655	(36.2410, 0.131), (37.8963, 0.126), (29.5013, 0.120)	Binary
45	005737687	7033	1658	(27.8330, 0.650), (10.1506, 0.483), (21.3307, 0.469)	Unknown
46	005808231	8181	1544	(45.5737, 0.060), (39.9925, 0.047), (40.3212, 0.041)	Binary
47	005904699	6544	235	(20.2947, 0.529), (24.0341, 0.388), (23.7102, 0.384)	Binary
48	006041680	8291	646	(31.6934, 0.251), (39.3897, 0.228), (35.8864, 0.219)	Binary
49	006115466	7983	742	(32.0717, 0.205), (38.1104, 0.180), (31.3559, 0.168)	Binary
50	006153233	7002	1853	(17.0936, 0.637), (26.3934, 0.539), (16.3116, 0.511)	Binary
51	006229130	7276	512	(8.0254, 1.411), (15.3118, 1.282), (16.3045, 1.254)	Binary
52	006266750	8166	1658	(6.0709, 0.503), (10.7547, 0.469), (11.5891, 0.446)	Binary
53	006280952	7751	1566	(16.4058, 1.091), (17.3545, 0.435), (15.7183, 0.406)	Binary
54	006579643	7059	256	(10.3719, 1.480), (10.4948, 0.787)	Binary
55	006629106	7074	421	(16.9431, 1.867), (12.8616, 1.716), (11.6577, 1.402)	Binary
56	006668729	7767	1128	(10.0544, 0.711), (10.5124, 0.669), (18.1642, 0.499)	Binary
57	006756386	7992	1762	(13.4862, 0.295), (16.9294, 0.283), (10.1655, 0.225)	Binary
58	006762992	7446	695	(12.6064, 4.414), (10.6044, 4.315), (11.4608, 4.070)	Binary
59	006854623	7507	1112	(23.2460, 1.006), (24.5098, 0.852), (18.5818, 0.682)	Binary
60	006865077	7769	512	(9.1701, 0.339), (20.8967, 0.267), (23.0361, 0.261)	Binary
61	006879594	6794	1112	(12.3446, 3.717), (10.4905, 3.694), (8.0692, 3.128)	Binary
62	006939291	7139	881	(14.5862, 0.278), (22.0775, 0.254), (20.9850, 0.164)	Binary
63	007467518	7447	624	(25.0157, 0.315), (21.7570, 0.280), (31.1217, 0.270)	Binary
64	007551993	6693	341	(13.1445, 0.541), (12.6102, 0.341), (13.4479, 0.303)	Binary

continued ...

...continued

	KIC Number	$T_{\rm eff}$ (K)	Orbital period (days)	Frequency (d^{-1}) & Amplitude (ppt)	Type
65	007761855	7140	1658	(16.0166, 0.406), (6.4921, 0.344), (15.4372, 0.283)	Binary
66	007834612	7453	369	(15.8819, 2.735), (15.6986, 1.760), (6.1551, 1.528)	Binary
67	007848288	7384	543	(16.2084, 0.338), (19.0518, 0.246), (34.0988, 0.218)	Binary
68	007977996	7123	1566	(21.4420, 0.360), (21.1943, 0.326), (24.1268, 0.263)	Binary
69	008029546	7123	512	(12.1877, 0.174), (12.5059, 0.172), (12.9048, 0.157)	Binary
70	008082478	7128	2041	(18.8670, 0.180), (40.1267, 0.156), (16.7411, 0.147)	Binary
71	008149341	7537	1029	(14.7037, 0.859), (27.0161, 0.828), (24.0340, 0.585)	Triple
72	008196840	7936	1701	(15.7569, 1.210), (12.2279, 0.921)	Binary
73	008248630	7310	1737	(18.1330, 0.944), (16.3750, 0.858), (14.2623, 0.705)	Binary
74	008264543	7850	314	(12.8387, 0.141), (16.3719, 0.117), (12.5678, 0.084)	Binary
75	008308688	7756	914	(17.5788, 0.470), (20.3124, 0.389), (20.9605, 0.363)	Binary
76	008311110	6959	158	(14.9350, 1.021), (14.7590, 0.919), (21.8590, 0.833)	Binary
77	008346686	7998	780	(31.8055, 0.455), (26.4354, 0.340), (33.5455, 0.233)	Binary
78	008359671	8464	185	(17.0296, 0.239), (20.5755, 0.195), (17.4696, 0.191)	Binary
79	008396062	6837	160	(19.4318, 0.492) (6.7015, 0.485) (16.7226, 0.471)	Binary
80	008397426	7029	1658	(9.1991, 0.342) (11.6264, 0.332) (7.0057, 0.258)	Binary
81	008439566	8218	993	(10.3911, 1.108) (15.7809, 1.090) (17.7732, 1.081)	Binary
82	008443311	7821	1658	(21.4470, 0.084) (32.0946, 0.080) (32.5167, 0.068)	Binary
83	008491816	7393	1112	(24.5337, 0.788) (21.9599, 0.739) (14.66509, 0.657)	Binary
84	008507325	7141	1185	(15.4146, 0.154) (19.1334, 0.141) (13.0573, 0.138)	Binary
85	008516686	8236	172	(21.0924, 0.072) (33.3303, 0.043) (29.0697, 0.042)	Binary
86	008560996	7872	1635	(22.9218, 0.245) (29.1873, 0.201) (28.3947, 0.110)	Binary
87	008565229	7741	1014	(22.5442, 1.760) (21.0106, 1.426) (21.1680, 1.120)	Binary
88	008583770	7659	1044	(22.0286, 0.074) (26.7853, 0.073) (25.1136, 0.070)	Binary
89	008590553	7304	1737	(23.0265, 0.419) (20.6629, 0.280) (28.7230, 0.228)	Binary
90	008630254	7281	1763	(20.9587, 0.517) (24.2788, 0.454) (24.6148, 0.452)	Binary
91	008819284	7801	1690	(32.0257, 0.292) (24.6875, 0.272) (25.7929, 0.222)	Unknown
92	008914322	7117	1763	(21.8324, 2.281) (9.7184, 1.077) (19.4527, 1.019)	Binary
93	008915335	7767	1655	(9.0861, 0.826) (10.7398, 0.661) (7.3642, 0.519)	Binary
94	008974140	6807	302	(12.3671, 1.658) (16.3943, 1.177) (23.0344, 0.913)	Binary
95	009094694	6737	1762	(9.0545, 1.148) (9.7437, 1.063) (7.3111, 1.018)	Binary
96	009108615	6713	1128	(11.3181, 0.274) (7.5860, 0.199) (12.7043, 0.116)	Binary
97	009172981	7435	1112	(21.7456, 0.673) (14.4275, 0.487) (14.9139, 0.393)	Binary
98	009265050	8290	1112	(28.2129, 0.592) (33.9347, 0.376) (30.4122, 0.304)	Binary
99	009369547	7024	958	(11.6353, 2.129) (15.7391, 2.082) (13.6708, 1.575)	Binary
100	009453452	8520	722	(35.5128, 0.026) (32.9828, 0.025) (21.5324, 0.021)	Binary
101	009552758	7530	1484	(10.9467, 0.674) (19.6719, 0.609) (22.1837, 0.607)	Binary
102	009596355	7421	316	(27.0596, 0.629) (22.5002, 0.512) (25.8445, 0.419)	Binary
103	009596469	7543	223	(31.0185, 1.001) (21.1778, 0.721) (11.9314, 0.676)	Binary
104	009598448	7650	1570	(23.3695, 0.509) (17.8673, 0.440) (17.1079, 0.422)	Binary
105	009649801	8461	1281	(31.9075, 0.804) (34.0148, 0.771) (29.6328, 0.675)	Binary
106	009655470	7008	1112	(10.5192, 1.238) (16.5239, 1.150) (12.7080, 0.726)	Binary
107	009655514	7441	1069	(14.6006, 1.266) (11.4661, 1.042) (11.8989, 0.815)	Triple
108	009666465	7032	1029	(22.0896, 1.176) (11.4100, 0.802) (11.2938, 0.725)	Binary

continued ...

...continued

	KIC Number	$T_{\rm eff}$ (K)	Orbital period (days)	Frequency (d^{-1}) & Amplitude (ppt)	Type
109	009667584	7312	1544	(20.0214, 0.980) (15.6881, 0.628) (17.3643, 0.596)	Binary
110	009725543	6809	1175	(9.6311, 2.773) (14.1027, 2.057) (8.6591, 1.731)	Binary
111	009791112	7121	1658	(9.7691, 0.677) (21.0025, 0.592) (23.2518, 0.526)	Binary
112	009823652	7448	1658	(20.4961, 1.184) (18.7550, 1.029) (20.3914, 1.013)	Binary
113	009850393	7140	285	(12.9925, 4.824) (11.3186, 1.937) (10.5849, 1.881)	Binary
114	009963609	7545	908	(17.8797, 1.433) (17.06110, 1.242) (19.2714, 1.236)	Binary
115	010001145	7641	185	(12.9070, 0.988) (16.5888, 0.902) (11.4666, 0.846)	Triple
116	010004660	9181	1484	(13.9804, 0.279)	Binary
117	010130777	8019	1856	(29.5727, 0.551) (15.1188, 0.532) (31.6213, 0.476)	Binary
118	010416779	7548	1633	(22.0404, 0.120) (5.1226, 0.100) (7.8298, 0.099)	Binary
119	010451090	7577	850	(32.8456, 0.472) (34.2358, 0.233) (36.9238, 0.193)	Binary
120	010489783	7802	1738	(16.7564, 0.993) (19.2795, 0.893) (17.9041, 0.874)	Binary
121	010679429	7364	666	(26.6042, 1.038) (15.3233, 0.934) (11.9169, 0.914)	Binary
122	010713398	6990	1158	(18.1957, 1.969) (16.4094, 1.807) (16.2386, 1.739)	Binary
123	010717871	7286	168	(10.8033, 2.498) (9.8769, 1.718) (15.4823, 1.652)	Binary
124	010749793	7634	164	(15.1563, 1.037) (16.8246, 0.955) (19.6155, 0.802)	Triple
125	010977859	8052	394	(11.1950, 0.116) (5.5295, 0.064)	Binary
126	010989032	8620	1684	(32.4212, 0.433) (31.7922, 0.403) (33.4507, 0.401)	Binary
127	011152054	9092	1570	(23.8251, 0.108) (7.6762, 0.082) (18.4422, 0.046)	Binary
128	011457198	7274	1701	(7.6375, 0.438) (24.8263, 0.396) (10.2100, 0.396)	Binary
129	011495305	7259	842	(19.1361, 2.376) (22.0840, 2.351) (12.1396, 1.303)	Binary
130	011508397	7458	598	(22.5274, 0.175) (5.1032, 0.174) (6.1498, 0.172)	Binary
131	011572666	7043	1323	(7.3418, 0.309) (14.1913, 0.298) (15.8458, 0.213)	Binary
132	011771670	8256	585	(38.2319, 0.097) (39.0082, 0.077) (41.5776, 0.067)	Binary
133	011874676	8219	1658	(30.2666, 0.529) (15.9977, 0.492) (11.9008, 0.383)	Binary
134	012020590	8017	434	(23.5319, 0.085) (24.7522, 0.074) (18.8027, 0.044)	Binary
135	012257449	8425	1655	(9.1610, 0.737) (18.1681, 0.384)	Binary
136	012470709	7210	1655	(22.5310, 1.216) (18.4564, 0.904) (21.8526, 0.875)	Binary
137	012602250	6879	590	(14.9742, 7.681)	Binary
138	012736056	9236	1566	(30.3322, 0.122) (26.1479, 0.114) (20.7429, 0.085)	Binary
139	008712760	7173	97	(18.6886, 0.404) (18.9863, 0.302) (20.5525, 0.136)	Binary
140	010226083	7061	70	(14.1612, 0.596) (11.4977, 0.595) (11.0945, 0.536)	Binary
141	011910642	7663	90	(28.9974, 0.433) (22.3314, 0.426) (20.9187, 0.405)	Binary

Chapter 3

Correcting the Time-delay

In Chapter 2 we used binarograms to identify possible binaries from *Kepler* δ Scuti stars. We obtained orbital periods from the peak of the binarograms. In this chapter we identify real binaries from the list of binaries obtained using binarograms. This can be done by plotting graphs of time-delay versus time.

3.1 Time-delay as a Function of Time

We can use different approaches to get plots of time-delay versus time. For example, we can divide the light curve of *Kepler* data into equal short segments (e.g., 20-day segments) and measure the phase of pulsation in each segment. This means that we are folding the light curve into cycles (over the orbital period found using the binarogram). Fitting the particular frequency by the least square method for each segment, we can get the time series for each phase. The choice of the segment size is related for example to the time or frequency resolution we want. Shorter segments might have higher scatter in the time delay curve. We can then calculate phase shifts, subtracting the average phase from each measured phase. We know also that the phase of the observed pulsations varies over the orbit (Paparo et al. 1988; Silvotti et al 2007, 2011; Telting et al 2012). We then obtain a set of phases as a function of time, which could be repeated for each pulsation mode. The amplitude of the phase variations depends on the geometry of the orbit. In general, variations in phase are influenced by neighbouring frequencies which perturb them, thus reducing this effect is necessary.

To perform the above mentioned tasks we used another program. This program reads the time series (time, flux) and also the pulsation frequencies. It fits a multi-frequency Fourier series to part of the data window, moves this window by a given time interval and repeats the process. In other words, for a given pulsation frequency, the time of the mid-point of the window and the amplitude and phase at this time are calculated. Therefore, we can plot the amplitude and phase of a particular pulsation frequency with respect to time. We can calculate the time-delay easily from the phase, so the time delay as a function of time can also be plotted.

To do these calculations, we have to select the pulsation frequency, the window size (in days) and the step in time (in days) between each window. The size of the time window must be carefully chosen. If it is too big (bigger than the orbital period) then there will be no variation because it is averaged out. If the window size is too small, there will be too few data points that can be used to calculate the amplitude and phase, so these values will have large errors and the time delay variation will have a large scatter. Thus about 10 points per orbital period are needed. This means that our window size should be about 0.1 times orbital periods. This implies that in order to select the window size, we need to know the approximate orbital period for each star. Most stars have orbital periods larger than 100 d. Therefore, for most stars, a window size of 10 d is an appropriate choice. We used this size for all stars with orbital period greater than 100 d. For those stars with orbital periods shorter than 100 d, we used a window size of 4 d. Therefore, the stars were divided into two groups - those with periods greater than 100 d and those with periods shorter than 100 d - since the software had to be run separately for the two groups using the two different window sizes mentioned.

The following assumptions and information are also used in our programme. The minimum and maximum pulsation frequencies used are 5.0 and 45.0 d^{-1}. Frequencies outside this range are ignored since they will be outside the δ Sct range. The step size to move between one window and the next (the sampling interval) used is 2 d. The program selects the 10 frequencies of highest amplitude within the specified frequency range. The program will not select frequencies which are too close to each other because this will not give a good phase or amplitude mea-

surement (the frequencies interfere with each other). The minimum acceptable difference between the chosen frequency and any other selected frequency is set to 0.1. Having all this information, the program will read the photometry and the frequencies for the stars in the list. For each frequency, it will calculate the amplitude, phase and time delay as a function of time with their errors. The output also shows the pulsation frequency (d^{-1}), data files corresponding to each pulsation frequency and time corresponding to the mid point of the window (days). Time-delay as a function of time can then be plotted. Fig.3.1 shows the time delay (in d) for KIC 1294670 obtained from the first three modes of highest amplitude: f_1 = 10.0457 d^{-1}, f_2 = 7.4245 d^{-1} and f_3 = 12.6227 d^{-1}. The remaining four modes give similar plots.

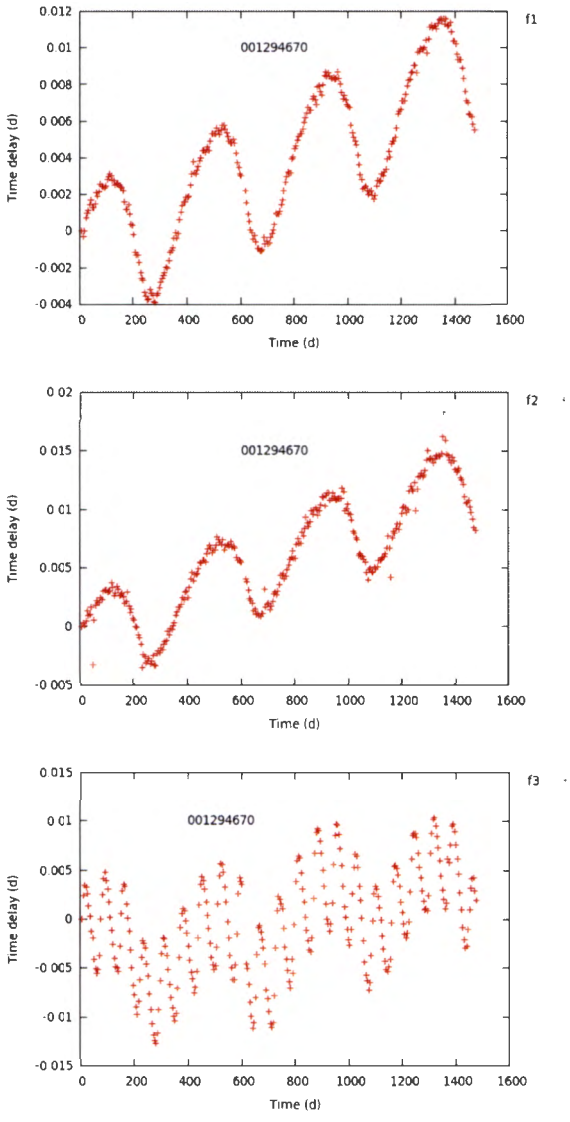

Figure 3.1: Time-delay curve of KIC 1294670 obtained from the first three pulsation modes of highest amplitudes with frequencies 10.0457, 7.4245 and 12.6227 d^{-1}. Note the distortion in the time delay curves.

The time-delay curve is sometimes sinusoidal but more often there is an underlying long-term trend which needs to be removed. A clean time delay curve, including trends, is obtained only for a few pulsation frequencies. Usually most of the selected 10 pulsation frequencies give rise to a random, noisy, variation. This is due to interaction with neighbouring modes. In all cases, we need to remove the underlying trend before the orbital parameters can de deduced. The correction procedure is described below.

3.2 Corrected Time-delay as a Function of Time

3.2.1 Least Squares Fitting on Our *Kepler* Data

In the previous section, we calculated time-delay as a function of time for each of the stars identified as binaries. We have examined time-delay as a function of time in these files and have noted those stars that seem to show periodic variations and have ignored those that do not show anything. We have selected those stars in which at least two frequencies give roughly the same periodic variation. These are the stars which are very likely to be binaries. Other stars are rejected because none of the time-delay curves in the files seem to look right.

Due to close frequencies, most of the time-delay curves are distorted. Fitting the combination of truncated Fourier series and polynomials by least squares, we need to correct this. We assumed that the distortion can be represented by a polynomial of the form:

$$a_0 + a_1 x + a_2 x^2 + a_3 x^3. \tag{3.1}$$

With a period equal to the orbital period, the orbital variation is represented by a Fourier curve of the form:

$$b_1 \sin(\omega t + \phi_1) + b_2 \sin(2\omega t + \phi_2) + b_3 \sin(3\omega t + \phi_3) \tag{3.2}$$

Therefore, the observed time-delay is the sum of these two variations which we

can fit by least squares with a function of the following type:

$$\begin{aligned} \tau &= a_0 + a_1 x + a_2 x^2 + a_3 x^3 + b_1 \sin(\omega t + \phi_1) \\ &+ b_2 \sin(2\omega t + \phi_2) + b_3 \sin(3\omega t + \phi_3) \end{aligned} \tag{3.3}$$

where in this case the distortion is chosen to be a polynomial of degree 3 and the time delay to be a Fourier series of 3rd harmonic. Since time-delay τ is function of time, we have to write this equation in terms of t and we have also to make the equation linear. Therefore, we can write it in compact form as follows:

$$\tau = a_0 + a_1 t + a_2 t^2 + a_3 t^3 + \sum_{k=1}^{m} b_k \sin(k\omega t + \phi_k) \tag{3.4}$$

Expanding the sine function, $\sin(k\omega t + \phi_k)$ we get the following:

$$\begin{aligned} \tau &= a_0 + a_1 t + a_2 t^2 + a_3 t^3 + \sum_{k=1}^{m} (b_k \cos\phi_k \sin(k\omega t) \qquad (3.5) \\ &+ b_k \sin\phi_k \cos(k\omega t)) \\ \tau &= a_0 + a_1 t + a_2 t^2 + a_3 t^3 + \sum_{k=1}^{m} (b_{2k-1} \sin(k\omega t) + b_{2k} \cos(k\omega t)) \qquad (3.6) \end{aligned}$$

Writing the summation part in detail, we can finally have the following equation for time delay, τ:

$$\begin{aligned} \tau &= a_0 + a_1 t + a_2 t^2 + a_3 t^3 + b_1 \sin(\omega t) + b_2 \cos(\omega t) + b_3 \sin(2\omega t) \\ &+ b_4 \cos(2\omega t) + ... + b_{2m-1} \sin(m\omega t) + b_{2m} \cos(m\omega t) \end{aligned} \tag{3.7}$$

By fitting Equation (3.7) to the time-delay data by least squares, we can solve for the coefficients $a_0, a_1, ..., a_i, b_1, b_2, .., b_i, \phi_1, \phi_2, ..., \phi_i$. The value of ω is known since the orbital period is known from its binarogram, i.e, $\omega = 2\pi/P$. We can

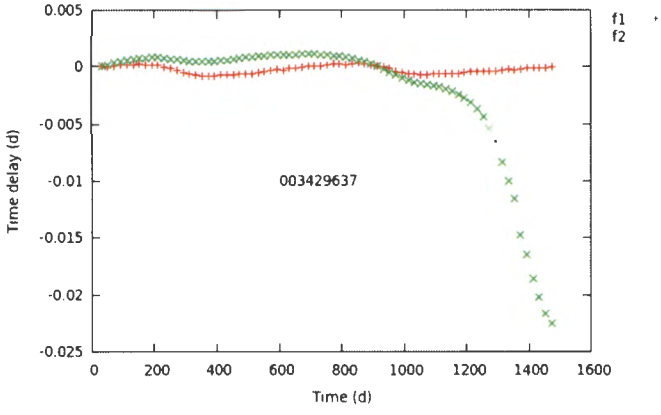

Figure 3.2: Time-delay curve of KIC 3429637 which contains two frequency values with poor agreement between the two plots due to interference.

then subtract the polynomial $a_0 + a_1 t + a_2 t^2 + a_3 t^3$ to get the actual undistorted and corrected time-delay.

As an illustration of the above procedure we use the data for KIC 3429637 and KIC 1294670. In Fig.3.2 the time-delay variation as a function of time for two pulsation frequencies in KIC 3429637 is shown. We notice that for pulsation frequency f_2 there is a sharp drop in phase towards the end of the time series. We presume this may be a result of amplitude or frequency variation of f_2.

In the procedure described above, each of the two time-delay curves is fitted to the function Equation 3.7 by least squares and the polynomial part removed from the data. However, the section containing the sharp drop in phase for f_2 was omitted, though this could possibly be accommodated using a polynomial of higher order. Fig.3.3 shows Equation 3.7 fitted to f_1 and Fig.3.4 shows Equation 3.7 fitted to the good part of f_2. Fig.3.5 shows the result after removing the polynomial part of the fitted function. As can be seen, the corrected time-delay curves are now in very good agreement. The corrected data from f_1 and f_2 can now be used to obtain a mean time-delay curve that is used to determine the orbital parameters. The mean value is found by weighting each data point in inverse proportion to the variance of the residuals calculated by the least squares fit to Equation 3.7. In this example

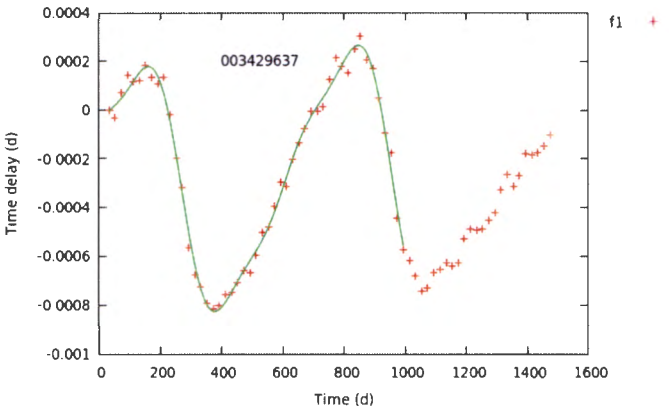

Figure 3.3: Time-delay curve of KIC 3429637 where the polynomial and Fourier curve shows a good fit of data when frequency f1 is used.

both pulsation frequencies have approximately the same residual variance.

In Figures 3.6 and 3.7 we show the phase variation for two pulsation frequencies $f_1 = 10.0457\ \mathrm{d}^{-1}$ and $f_2 = 7.4245\ \mathrm{d}^{-1}$ in KIC 1294670. In this case the assumed pulsation frequencies are both slightly in error, giving rise to a linear trend in both cases. Figure 3.8 shows the time-delay variation for a third pulsation frequency $f_3 = 12.6227\ \mathrm{d}^{-1}$ which shows a similar linear trend but with larger noise level. Similarly, Figures 3.9 to 3.12 show the time-delay curves for $f_4 = 14.9703$, $f_5 = 16.7269$, $f_6 = 18.1998$ and $f_7 = 19.7822\ \mathrm{d}^{-1}$. Figure 3.13 shows the time-delay for all seven pulsation frequencies in one diagram.

After fitting the time-delay for each pulsation frequency using Equation 3.7 and removing the polynomial part, we obtain Fig.3.14. All seven pulsation frequencies give the same time-delay curve, though with varying scatter. As before, the mean time-delay variation is obtained by weighting each point in inverse proportional to the residual variance of the least squares fit to Equation 3.7. Thus the data from f_3 will have little influence in the final value owing to its larger scatter.

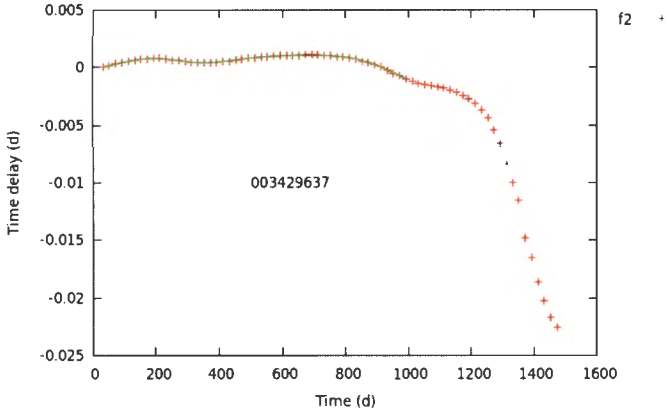

Figure 3.4: Time-delay curve of KIC 3429637 where the polynomial and Fourier curve shows a good fit of data when frequency f2 is used.

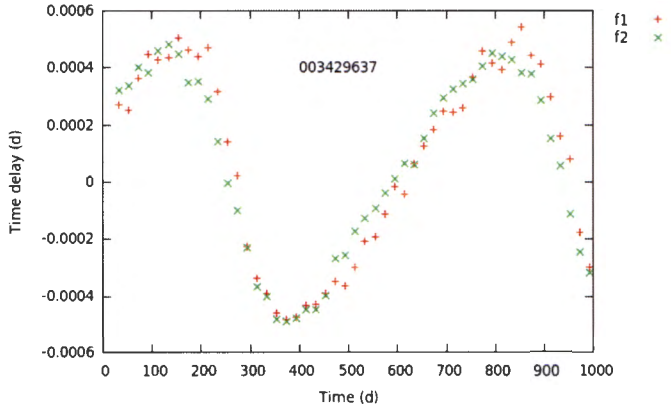

Figure 3.5: Time-delay curve of KIC 3429637 after removing the variation due to interference where the two curves agree well.

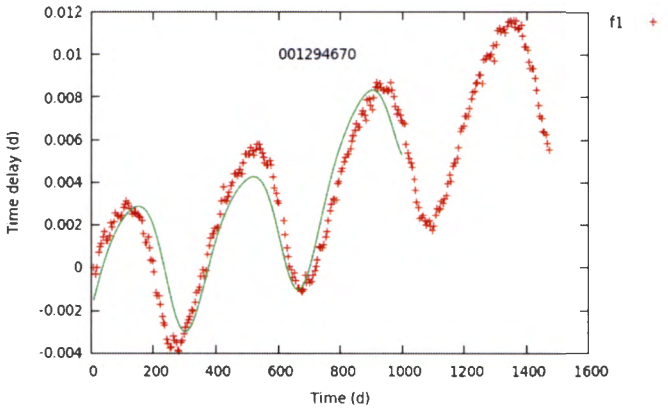

Figure 3.6: Time-delay curve of KIC 1294670 for the first pulsation frequency (f_1 = 10.0457 d^{-1}) where the polynomial and Fourier curve fits properly.

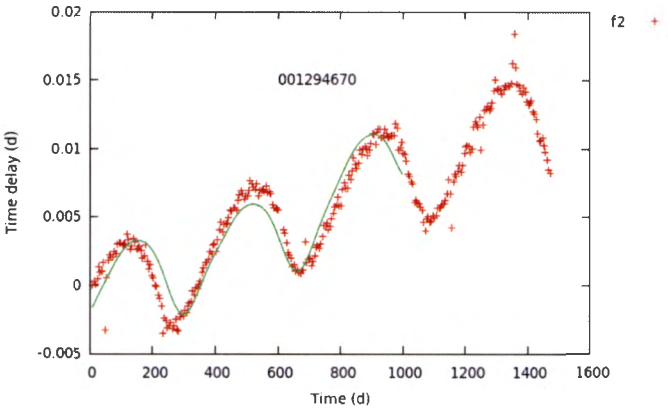

Figure 3.7: Time-delay curve of KIC 1294670 for the second pulsation frequency (f_2 = 7.4245 d^{-1}) where the polynomial and Fourier curve fits properly.

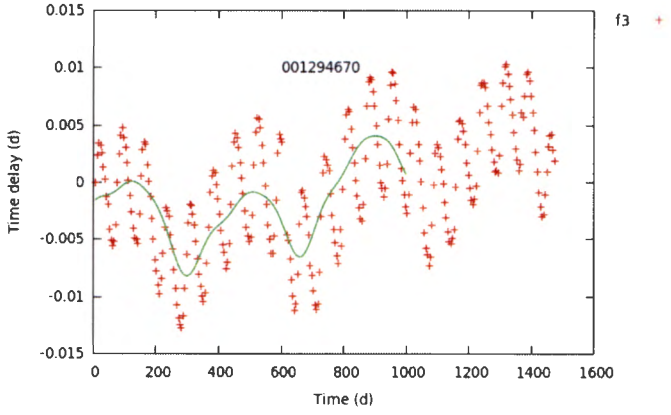

Figure 3.8: Time-delay curve of KIC 1294670 for the third pulsation frequency (f_3 = 12.6227 d^{-1}) where the polynomial and Fourier curve fits properly.

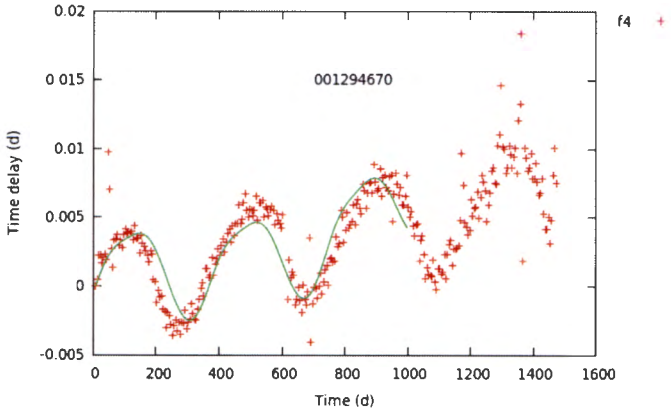

Figure 3.9: Time-delay curve of KIC 1294670 for the fourth pulsation frequency (f_4 = 14.9703 d^{-1}) where the polynomial and Fourier curve fits properly.

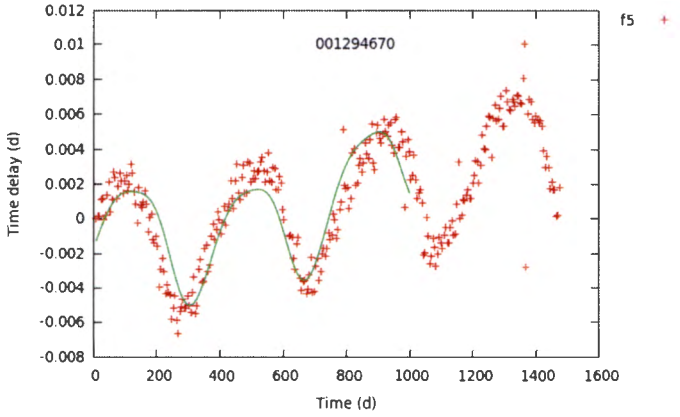

Figure 3.10: Time-delay curve of KIC 1294670 for the fifth pulsation frequency (f_5 = 16.7269 d^{-1}) where the polynomial and Fourier curve fits properly.

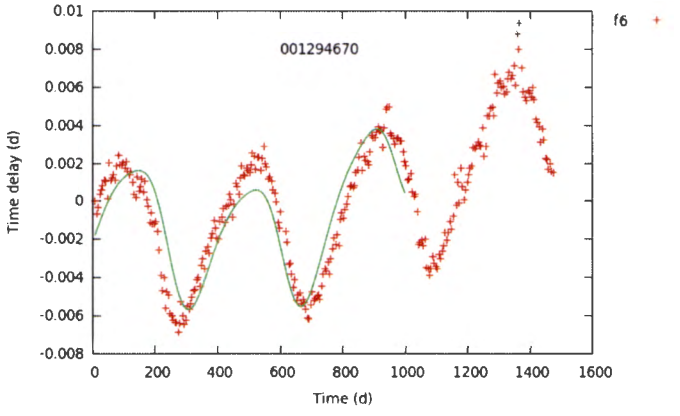

Figure 3.11: Time-delay curve of KIC 1294670 for the sixth pulsation frequency (f_6 = 18.1998 d^{-1}) where the polynomial and Fourier curve fits properly.

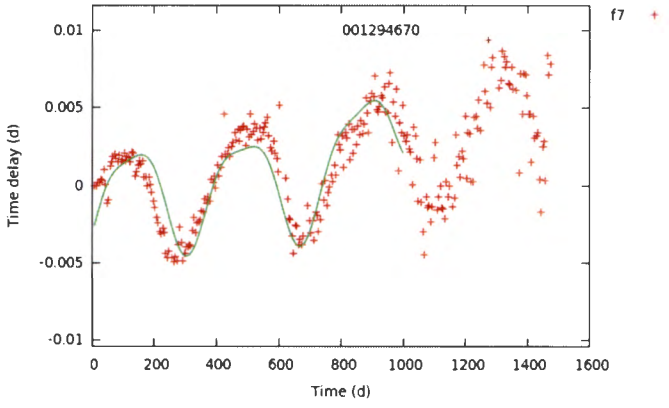

Figure 3.12: Time-delay curve of KIC 1294670 for the seventh pulsation frequency ($f_7 = 19.7822\ \mathrm{d}^{-1}$) where the polynomial and Fourier curve fits properly.

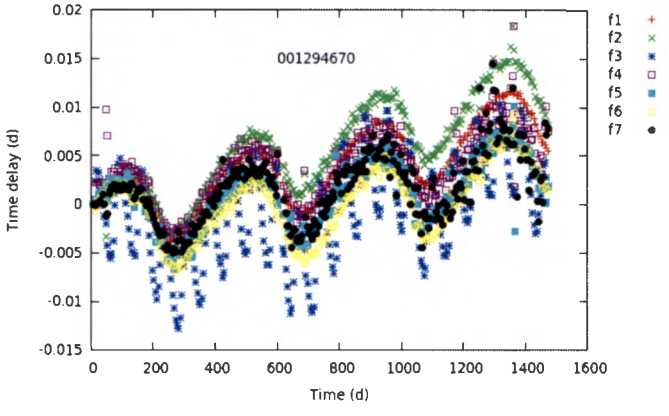

Figure 3.13: Time-delay curve of KIC 1294670 for the highest seven pulsation frequencies with the interference effect not yet removed.

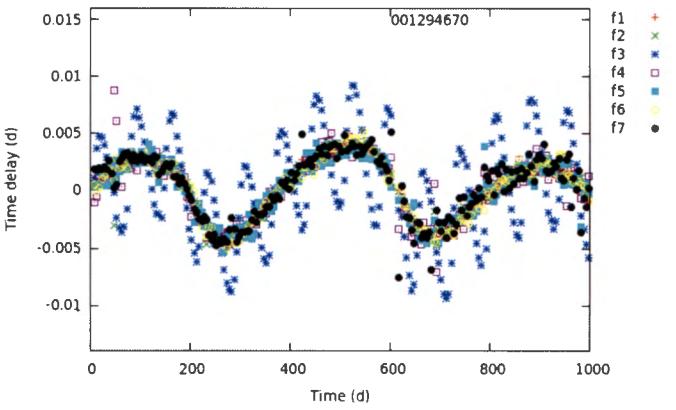

Figure 3.14: The corrected time-delay curve of KIC 1294670 for the highest seven pulsation frequencies after removing the variation due to interference.

The method of least squares mentioned in this section is further explained in detail in Appendix D. Ten of the best samples of the corrected time-delay plots and the corresponding phase diagrams are presented from Fig.3.15 to Fig.3.24. The remaining time-delay plots and the corresponding phase diagrams are shown in Appendix A.

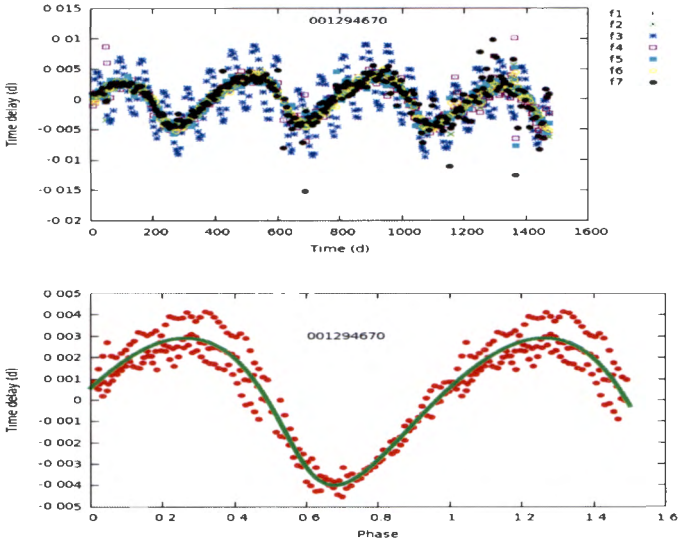

Figure 3.15: Time-delay curve (top panel) of KIC 1294670 for the seven pulsation frequencies of highest amplitudes and the corresponding orbital phase plot (bottom panel). The solid line in the bottom panel is a fit from the orbital solution.

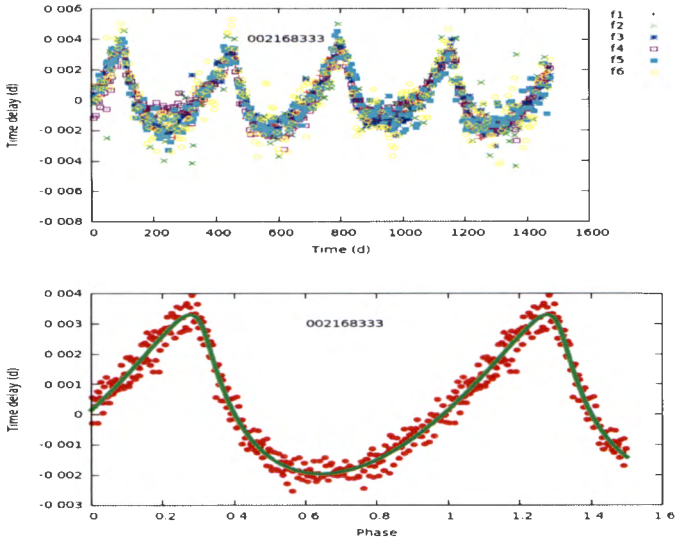

Figure 3.16: Time-delay curve (top panel) of KIC 2168333 for the six pulsation frequencies of highest amplitudes and the corresponding orbital phase plot (bottom panel). The solid line in the bottom panel is a fit from the orbital solution.

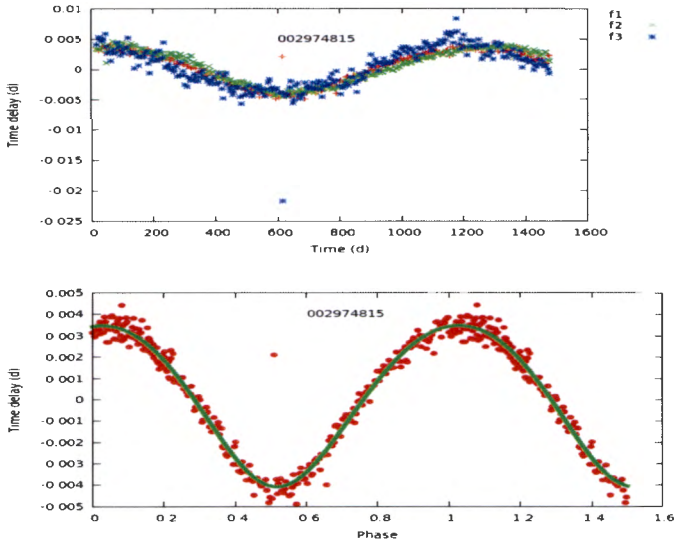

Figure 3.17: Time-delay curve (top panel) of KIC 2974815 for the three pulsation frequencies of highest amplitudes and the corresponding orbital phase plot (bottom panel). The solid line in the bottom panel is a fit from the orbital solution.

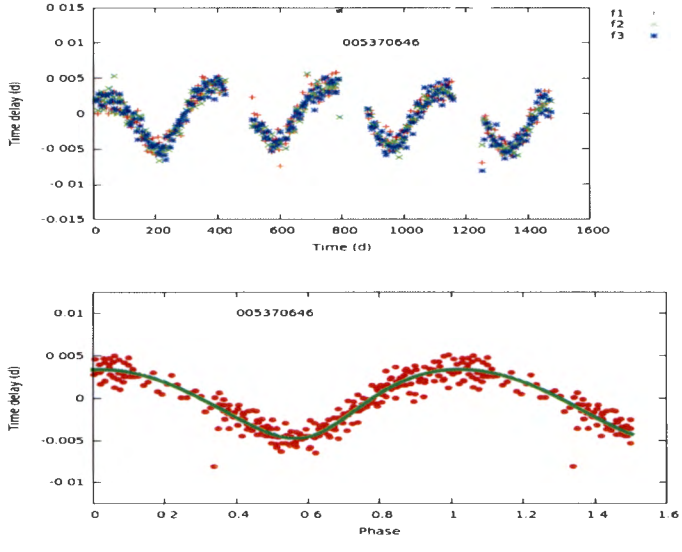

Figure 3.18: Time-delay curve (top panel) of KIC 5370646 for the three pulsation frequencies of highest amplitudes and the corresponding orbital phase plot (bottom panel). The solid line in the bottom panel is a fit from the orbital solution.

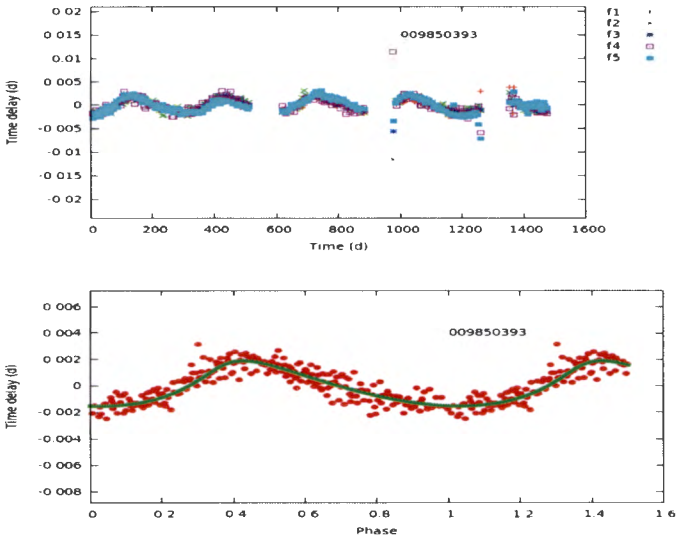

Figure 3.19: Time-delay curve (top panel) of KIC 9850393 for the five pulsation frequencies of highest amplitudes and the corresponding orbital phase plot (bottom panel). The solid line in the bottom panel is a fit from the orbital solution.

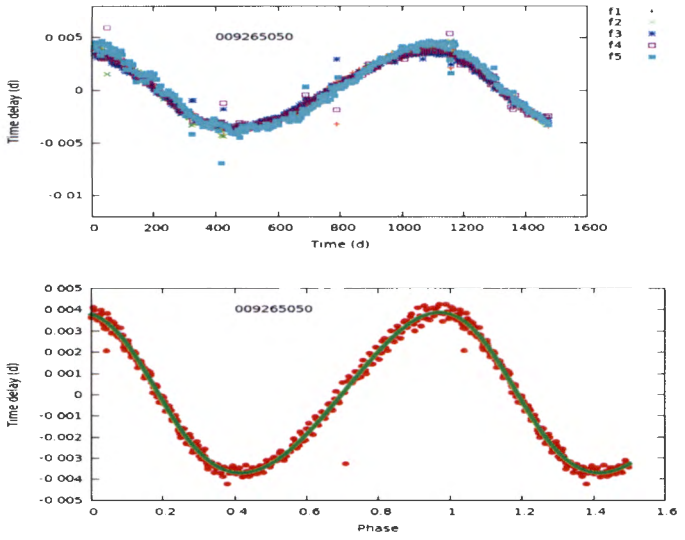

Figure 3.20: Time-delay curve (top panel) of KIC 9265050 for the five pulsation frequencies of highest amplitudes and the corresponding orbital phase plot (bottom panel). The solid line in the bottom panel is a fit from the orbital solution.

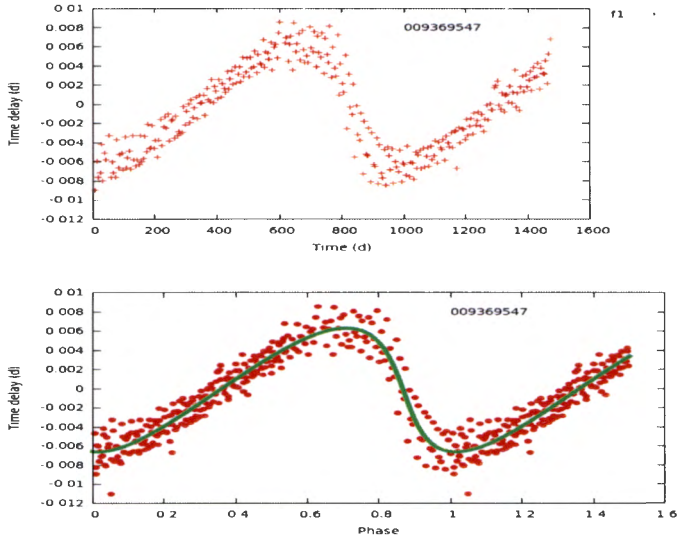

Figure 3.21: Time-delay curve (top panel) of KIC 9369547 for the pulsation frequency of highest amplitude and the corresponding orbital phase plot (bottom panel). The solid line in the bottom panel is a fit from the orbital solution.

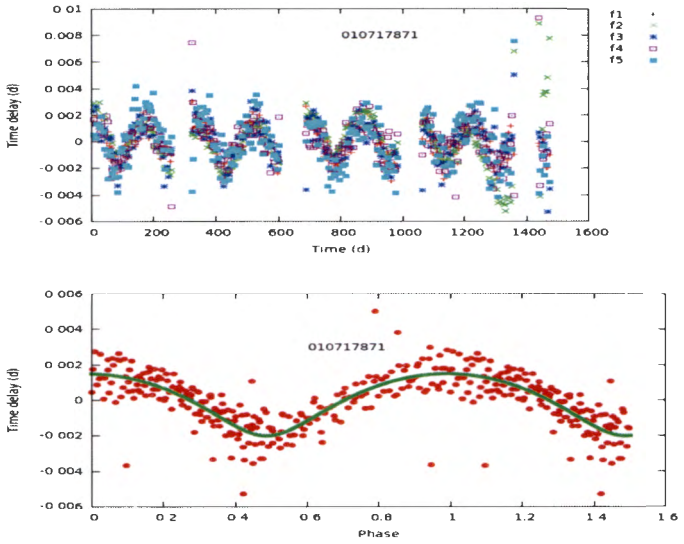

Figure 3.22: Time-delay curve (top panel) of KIC 10717871 for the five pulsation frequencies of highest amplitudes and the corresponding orbital phase plot (bottom panel). The solid line in the bottom panel is a fit from the orbital solution.

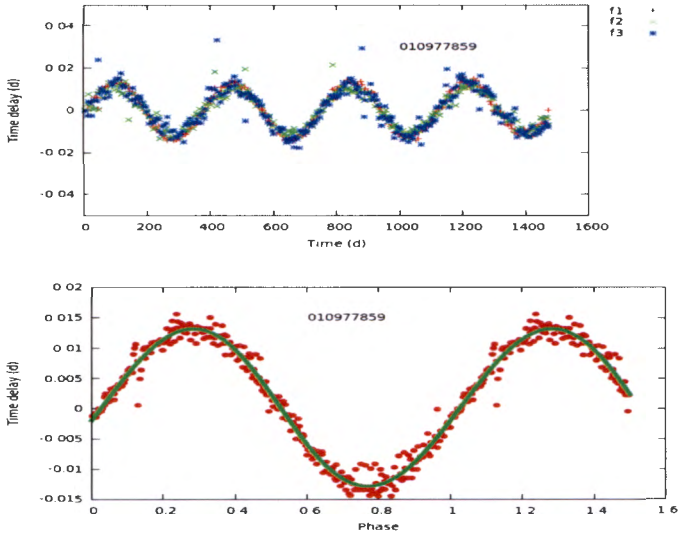

Figure 3.23: Time-delay curve (top panel) of KIC 10977859 for the three pulsation frequencies of highest amplitudes and the corresponding orbital phase plot (bottom panel). The solid line in the bottom panel is a fit from the orbital solution.

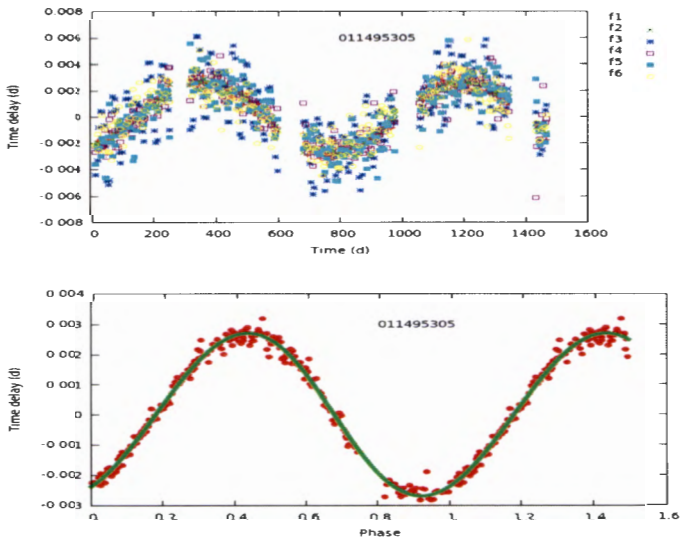

Figure 3.24: Time-delay curve (top panel) of KIC 11495305 for the six pulsation frequencies of highest amplitudes and the corresponding orbital phase plot (bottom panel). The solid line in the bottom panel is a fit from the orbital solution.

Chapter 4

Results and Discussion

In this chapter we present a table of binary orbital parameters. These were obtained by the iterative method described in Section 1.8.3. Some results are discussed. For some stars the orbital parameters have been obtained independently by different methods and these are also discussed.

4.1 Calculation of the Orbital Parameters

Table 4.1 lists the orbital parameters using the code shown in Appendix C. In the table, the KIC number, the projected semi-major axis, $a \sin i$ in AU, the eccentricity, e, the angle of ascending node, ω (radians), the time of periastron passage, $T_{\rm per}$, and the orbital period, P are given. The value of $T_{\rm per}$ is given with respect to JD 2454950.00 which was used as the zero point of the system. The two ancillary parameters: the semi-ampitude of the radial velocity, K (km s^{-1}), and the mass function $f(m)$ (solar mass) are also given. The standard deviations in these quantities are derived from the errors of the corrections obtained in the iterative least-square solution.

When a solution is obtained, it often happens that the eccentricity is not significantly different from zero. In that case, it is best to assume a circular orbit. To do this, we compared the eccentricity in the final solution to its standard deviation. If the value of e is less than two or three standard deviations, we set $e = 0$, i.e. a circular orbit is assumed. In the table, two forms of parameters are included. One

is for elliptical orbits and the other is for circular orbits. For circular orbits, $T_{\rm per}$ and ω are not defined.

Table 4.1: List of binary stars and their orbital parameters determined.

KIC	$a \sin i$ (au)	e	ω (rad)	$T_{\rm per}$ (d)	P (d)	K (km/s)	f(m) ($M_\odot$)
001294670	0.62181 ± 0.00008	0.365 ± 0.038	3.848 ± 0.104	237.9 ± 6.4	404.3 ± 1.9	16.5 ± 0.2	0.196E+00 ± 0.185E-02
001577039	510.1516 ± 0.0005	0.140 ± 0.001	0.040 ± 0.003	2087.8 ± 2.5	2542.1 ± 2.6	2026.8 ± 2.1	0.274E+07 ± 0.558E+04
002168333	0.527 ± 0.0001	0.688 ± 0.021	2.398 ± 0.030	111.3 ± 1.3	351.6 ± 0.4	20.6 ± 0.5	0.158E+00 ± 0.383E-03
002168420	0.41650 ± 0.00003	0.477 ± 0.017	3.113 ± 0.035	152.0 ± 6.3	1160.7 ± 3.2	4.08 ± 0.04	0.715E-02 ± 0.397E-04
002570760	13.9980 ± 0.0002	0.190 ± 0.005	2.926 ± 0.017	1502.7 ± 4.0	1700.8 ± 3.7	83.8 ± 0.2	0.126E+03 ± 0.560E+00
002571868	0.3898 ± 0.0001	0.383 ± 0.053	0.654 ± 0.134	88.4 ± 3.3	158.7 ± 0.2	26.5 ± 0.6	0.313E+00 ± 0.100E-02
002714707	0.6510 ± 0.0001	0.074 ± 0.037	1.706 ± 0.515	17.4 ± 47.9	585.6 ± 2.4	11.14 ± 0.05	0.107E+00 ± 0.906E-03
002974815	0.65335 ± 0.00004	0.167 ± 0.025	4.513 ± 0.153	590.4 ± 28.7	1202.8 ± 9.3	5.50 ± 0.04	0.257E-01 ± 0.401E-03
002994888	0.7755 ± 0.0001	0.236 ± 0.056	3.655 ± 0.227	379.2 ± 38.3	1082.9 ± 10.5	7.3 ± 0.1	0.530E-01 ± 0.103E-02
003219256	0.2828 ± 0.0002	0.783 ± 0.105	5.557 ± 0.130	1044.1 ± 16.7	1330.4 ± 98.3	3.4 ± 0.7	0.170E-02 ± 0.251E-03
003223460	5.9282 ± 0.0063	0.846 ± 0.070	3.633 ± 0.092	969.8 ± 7.2	1008.7 ± 14.3	110.4 ± 23.2	0.273E+02 ± 0.784E+00
003346195	0.48038 ± 0.00003	0.688 ± 0.015	4.990 ± 0.022	359.5 ± 1.0	398.3 ± 0.3	16.6 ±0.3	0.931E-01 ± 0.180E-03
003425802	17.6347 ± 0.0002	0.259 ± 0.003	6.190 ± 0.007	1511.5 ± 1.9	1621.7 ± 2.0	112.5 ± 0.1	0.278E+03 ± 0.698E+00
003542566	0.51510 ± 0.00003	0.170 ± 0.020	5.649 ± 0.121	784.7 ± 17.7	907.5 ± 3.2	5.76 ± 0.02	0.221E-01 ± 0.160E-03
003546765	0.3152 ± 0.0059	0			514.0	6.1 ± 0.1	0.158E-01 0.897E-03
003634384	0.2627 ± 0.0001	0.361 ± 0.083	3.329 ± 0.217	60.4 ± 4.9	141.0 ± 0.2	19.9 ± 0.6	0.121E+00 ± 0.523E-03
003650057	0.44289 ± 0.00004	0.216 ± 0.030	3.109 ± 0.143	843.0 ± 20.7	895.7 ± 5.1	5.06 ± 0.04	0.144E-01 ± 0.167E-03
003760002	0.4017 ± 0.0001	0.810 ± 0.083	1.708 ± 0.115	111.3 ± 4.6	470.3 ± 2.1	14.5 ± 2.8	0.390E-01 ± 0.358E-03
003763579	0.7001 ± 0.0614	0			1281.0	5.4 ± 0.4	0.278E-01 0.734E-02
003975085	1.80437 ± 0.00008	0.103 ± 0.017	3.791 ± 0.161	32.9 ± 24.1	968.2 ± 2.7	18.73 ± 0.06	0.835E+00 ± 0.473E-02
004048494	0.72275 ± 0.00006	0.492 ± 0.019	3.116 ± 0.050	473.8 ± 10.8	1749.7 ± 28.9	4.74 ± 0.09	0.164E-01 ± 0.544E-03
004072582	18.7489 ± 0.0004	0.191 ± 0.011	3.154 ± 0.037	1503.9 ± 8.7	1662.8 ± 7.5	114.8 ± 0.5	0.317E+03 ± 0.288E+01
004243984	0.37716 ± 0.00005	0.241 ± 0.047	6.290 ± 0.197	228.7 ± 17.8	571.8 ± 2.8	6.79 ± 0.08	0.218E-01 ± 0.217E-03
004269337	0.7687 ± 0.0002	0.539 ± 0.065	4.150 ± 0.147	639.3 ± 13.3	700.4 ± 5.7	13.0 ± 0.6	0.123E+00 ± 0.201E-02
004283747	0.5999 ± 0.0001	0.512 ± 0.049	0.729 ± 0.086	662.6 ± 12.4	942.7 ± 9.8	7.4 ± 0.2	0.324E-01 ± 0.675E-03
004574142	26.4701 ± 0.0002	0.191 ± 0.005	6.175 ± 0.018	1663.2 ± 7.4	1732.5 ± 4.4	155.6 ± 0.4	0.824E+03 ± 0.422E+01
004679562	0.88164 ± 0.00009	0.731 ± 0.011	3.015 ± 0.010	919.2 ± 1.7	1000.7 ± 3.5	12.9 ± 0.2	0.912E-01 ± 0.655E-03
004902475	0.43916 ± 0.00001	0.245 ± 0.008	0.432 ± 0.036	183.2 ± 5.1	925.6 ± 1.3	4.89 ± 0.01	0.131E-01 ± 0.377E-04

continued ...

...continued

KIC	$a \sin i$ (au)	e	ω (rad)	$T_{\rm per}$ (d)	P (d)	K (km/s)	f(m) ($M_\odot$)
004937435	10.0483 ± 0.0002	0.198 ± 0.010	3.162 ± 0.048	20.3 ± 10.8	1743.9 ± 10.5	58.7 ± 0.3	0.444E+02 ± 0.537E+00
005034039	3.1891 ± 0.0012	0.658 ± 0.051	6.313 ± 0.065	613.8 ± 5.6	572.8 ± 2.6	73.9 ± 4.4	0.131E+02 ± 0.122E+00
005042785	2.4556 ± 0.0001	0.107 ± 0.018	0.536 ± 0.333	1306.8 ± 85.1	1728.6 ± 31.4	14.2 ± 0.2	0.660E+00 ± 0.240E-01
005209712	1.4954 ± 0.0001	0.356 ± 0.033	3.215 ± 0.094	217.5 ± 16.3	1115.4 ± 6.2	14.3 ± 0.2	0.358E+00 ± 0.404E-02
005356349	13.4371 ± 0.0001	0.217 ± 0.005	3.177 ± 0.014	12.1 ± 3.5	1564.3 ± 2.5	88.0 ± 0.1	0.132E+03 ± 0.430E+00
005370646	0.7107 ± 0.0001	0.271 ± 0.057	11.534 ± 0.244	610.4 ± 13.6	375.5 ± 1.5	19.6 ± 0.3	0.339E+00 ± 0.277E-02
005391416	10.8644 ± 0.0001	0.254 ± 0.005	3.156 ± 0.014	1478.8 ± 3.2	1549.0 ± 2.6	72.5 ± 0.1	0.712E+02 ± 0.240E+00
005394574	0.34324 ± 0.00003	0.467 ± 0.026	5.543 ± 0.056	73.4 ± 2.8	336.3 ± 0.4	11.5 ± 0.1	0.476E-01 ± 0.142E-03
005440852	0.6695 ± 0.0002	0.482 ± 0.099	3.851 ± 0.194	605.6 ± 25.4	851.7 ± 12.1	8.9 ± 0.5	0.551E-01 ± 0.157E-02
005459908	1.6390 ± 0.0003	0.266 ± 0.063	9.947 ± 0.218	598.7 ± 12.6	368.8 ± 1.4	46.1 ± 0.8	0.431E+01 ± 0.337E-01
005466537	1.3197 ± 0.0002	0.134 ± 0.060	5.989 ± 0.438	186.5 ± 68.8	996.1 ± 10.7	13.3 ± 0.1	0.308E+00 ± 0.666E-02
005475668	0.3775 ± 0.0002	0.607 ± 0.155	4.842 ± 0.264	146.5 ± 4.8	137.6 ± 0.4	34.5 ± 5.1	0.379E+00 ± 0.263E-02
005643103	5.3518 ± 0.0002	0.270 ± 0.017	4.715 ± 0.093	335.3 ± 22.1	1737.9 ± 20.9	31.9 ± 0.4	0.676E+01 ± 0.163E+00
005647514	0.32208 ± 0.00001	0.230 ± 0.015	2.436 ± 0.064	801.2 ± 10.2	996.0 ± 3.2	3.32 ± 0.01	0.449E-02 ± 0.293E-04
005723310	1.5025 ± 0.0001	0.088 ± 0.019	1.179 ± 0.112	1553.7 ± 20.8	1708.1 ± 32.0	8.8 ± 0.1	0.155E+00 ± 0.581E-02
005737687	4.69814 ± 0.00008	0.129 ± 0.008	4.351 ± 0.103	1234.6 ± 25.1	1730.6 ± 10.8	27.3 ± 0.1	0.461E+01 ± 0.580E-01
005808231	1.2652 ± 0.0001	0.468 ± 0.026	3.968 ± 0.046	74.0 ± 7.6	1532.1 ± 11.4	9.3 ± 0.1	0.115E+00 ± 0.171E-02
005904699	0.45853 ± 0.00008	0.622 ± 0.038	5.468 ± 0.059	64.8 ± 2.0	233.9 ± 0.3	25.0 ± 0.9	0.234E+00 ± 0.693E-03
006041680	0.3070 ± 0.0072	0			646.0	4.7 ± 0.1	0.925E-02 ± 0.652E-03
006115466	0.57865 ± 0.00002	0.068 ± 0.013	5.337 ± 0.197	495.3 ± 23.1	733.5 ± 1.5	7.90 ± 0.01	0.480E-01 ± 0.201E-03
006153233	72.1931 ± 0.0009	0.199 ± 0.006	6.073 ± 0.012	1640.3 ± 4.9	1844.1 ± 5.9	399.5 ± 1.3	0.147E+05 ± 0.944E+02
006229130	0.5518 ± 0.0001	0.157 ± 0.103	41.733 ± 0.650	4082.0 ± 71.8	591.4 ± 6.7	9.4 ± 0.1	0.640E-01 ± 0.147E-02
006266750	18.8823 ± 0.0004	0.245 ± 0.010	0.036 ± 0.051	1410.7 ± 10.6	1675.9 ± 13.0	116.2 ± 0.9	0.319E+03 ± 0.497E+01
006280952	1.02259 ± 0.00006	0.405 ± 0.017	3.533 ± 0.055	520.1 ± 12.3	1786.4 ± 35.0	6.2 ± 0.1	0.446E-01 ± 0.175E-02
006579643	1.4340 ± 0.0005	0.473 ± 0.081	3.278 ± 0.155	251.7 ± 6.1	244.7 ± 0.8	66.4 ± 3.3	0.656E+01 ± 0.472E-01
006629106	0.33840 ± 0.00006	0.381 ± 0.046	6.215 ± 0.113	249.1 ± 7.4	397.5 ± 1.2	9.2 ± 0.1	0.326E-01 ± 0.208E-03
006668729	0.60046 ± 0.00009	0.400 ± 0.041	3.338 ± 0.095	364.7 ± 17.4	1123.7 ± 9.1	5.8 ± 0.1	0.228E-01 ± 0.373E-03
006756386	14.0845 ± 0.0001	0.169 ± 0.006	6.187 ± 0.017	1604.3 ± 5.9	1772.7 ± 5.1	80.6 ±0.2	0.118E+03 ± 0.691E+00
006762992	0.4457 ± 0.0122	0			695.0	6.4 ± 0.1	0.244E-01 ± 0.201E-02

continued ...

...continued

KIC	$a \sin i$ (au)	e	ω (rad)	$T_{\rm per}$ (d)	P (d)	K (km/s)	f(m) ($M_\odot$)
006854623	0.30074 ± 0.00002	0.293 ± 0.022	3.515 ± 0.075	833.8 ± 13.3	1115.3 ± 5.2	2.82 ± 0.02	0.291E-02 ± 0.274E-04
006865077	0.76302 ± 0.00009	0.212 ± 0.040	3.606 ± 0.187	687.4 ± 13.3	453.4 ± 1.6	17.2 ± 0.1	0.288E+00 ± 0.207E-02
006879594	1.0809 ± 0.0002	0.460 ± 0.066	5.852 ± 0.141	77.5 ± 23.8	1116.8 ± 11.8	10.9 ± 0.4	0.135E+00 ± 0.286E-02
006939291	1.22997 ± 0.00003	0.148 ± 0.008	2.222 ± 0.056	406.8 ± 7.9	886.1 ± 1.1	14.03 ± 0.02	0.316E+00 ± 0.792E-03
007467518	0.45154 ± 0.00001	0.283 ± 0.008	1.700 ± 0.031	244.2 ± 2.9	621.6 ± 0.5	7.57 ± 0.02	0.317E-01 ± 0.606E-04
007551993	0.49895 ± 0.00002	0.617 ± 0.013	4.355 ± 0.022	182.0 ± 0.9	338.2 ± 0.2	18.7 ± 0.2	0.144E+00 ± 0.228E-03
007761855	7.46053 ± 0.00008	0.205 ± 0.004	6.189 ± 0.014	1511.2 ± 3.2	1665.9 ± 3.1	45.76 ± 0.09	0.199E+02 ± 0.743E-01
007834612	0.1808 ± 0.0108	0			369.0	4.9 ± 0.2	0.579E-02 ± 0.104E-02
007848288	0.53517 ± 0.00009	0.484 ± 0.038	0.074 ± 0.073	270.7 ± 6.9	585.6 ± 2.1	10.4 ± 0.2	0.596E-01 ± 0.442E-03
007977996	1.41102 ± 0.00002	0.190 ± 0.006	4.806 ± 0.039	200.9 ± 8.5	1582.8 ± 4.7	9.08 ± 0.02	0.149E+00 ± 0.900E-03
008029546	0.8779 ± 0.0002	0.220 ± 0.082	4.890 ± 0.376	196.6 ± 29.6	507.5 ± 3.9	17.7 ± 0.3	0.350E+00 ± 0.548E-02
008082478	190.4274 ± 0.0008	0.132 ± 0.003	3.276 ± 0.009	1829.0 ± 4.8	2082.4 ± 4.4	922.6 ± 2.0	0.212E+06 ± 0.915E+03
008149341	0.24804 ± 0.00007	0.228 ± 0.079	3.024 ± 0.342	778.6 ± 56.5	1027.4 ± 16.4	2.48 ± 0.06	0.192E-02 ± 0.617E-04
008196840	15.2366 ± 0.0001	0.177 ± 0.004	3.395 ± 0.010	1616.5 ± 3.3	1716.6 ± 2.8	90.1 ± 0.1	0.160E+03 ± 0.530E+00
008248630	0.75355 ± 0.00006	0.221 ± 0.035	5.823 ± 0.104	1501.5 ± 23.0	1743.3 ± 28.0	4.43 ± 0.08	0.187E-01 ± 0.603E-03
008264543	0.5407 ± 0.0003	0.360 ± 0.197	1.899 ± 0.559	220.5 ± 26.6	313.6 ± 3.7	18.4 ± 1.5	0.214E+00 ± 0.509E-02
008308688	0.41581 ± 0.00004	0.087 ± 0.035	5.273 ± 0.417	803.6 ± 60.9	912.4 ± 5.3	4.57 ± 0.03	0.115E-01 ± 0.135E-03
008311110	0.34657 ± 0.00002	0.227 ± 0.024	5.476 ± 0.108	154.6 ± 2.6	156.5 ± 0.1	22.7 ± 0.1	0.226E+00 ± 0.327E-03
008346686	0.38601 ± 0.00004	0.051 ± 0.043	1.165 ± 0.848	796.1 ±105.1	778.4 ± 5.3	4.96 ± 0.03	0.126E-01 ± 0.175E-03
008359671	0.5115 ± 0.0001	0.226 ± 0.106	18.469 ± 0.451	622.7 ± 12.4	174.0 ± 0.5	30.1 ± 0.7	0.589E+00 ± 0.408E-02
008396062	0.14675 ± 0.00003	0.606 ± 0.069	4.669 ± 0.119	56.9 ± 2.5	163.8 ± 0.2	11.2 ± 0.7	0.156E-01 ± 0.567E-04
008397426	2.2926 ± 0.0003	0.243 ± 0.063	3.304 ± 0.144	1523.5 ± 35.2	1612.5 ± 35.1	14.6 ± 0.4	0.618E+00 ± 0.269E-01
008439566	0.53101 ± 0.00009	0.625 ± 0.029	5.793 ± 0.039	907.9 ± 5.9	1002.5 ± 7.9	6.7 ± 0.2	0.198E-01 ± 0.315E-03
008443311	2.44505 ± 0.00009	0.190 ± 0.017	6.265 ± 0.048	1536.0 ± 12.2	1667.4 ± 10.7	14.9 ± 0.1	0.701E+00 ± 0.903E-02
008491816	0.6487 ± 0.0001	0.723 ± 0.049	1.124 ± 0.084	3.4 ± 13.5	1114.7 ± 10.9	8.4 ± 0.6	0.293E-01 ± 0.576E-03
008507325	0.68759 ± 0.00009	0.089 ± 0.046	3.410 ± 0.514	809.2 ± 97.5	1184.2 ± 10.6	5.82 ± 0.05	0.309E-01 ± 0.558E-03
008516686	0.4187 ± 0.0001	0.446 ± 0.060	2.487 ± 0.129	78.3 ± 3.5	171.4 ± 0.3	27.2 ± 0.9	0.333E+00 ± 0.119E-02
008560996	0.32117 ± 0.00001	0.179 ± 0.015	3.237 ± 0.043	1567.2 ± 12.3	636.9 ± 8.4	1.99 ± 0.01	0.164E-02 ± 0.170E-04
008565229	0.2188 ± 0.0002	0.692 ± 0.135	2.775 ± 0.160	685.2 ± 24.6	1055.1 ± 35.9	2.8 ± 0.5	0.125E-02 ± 0.858E-04

continued ...

...continued

KIC	$a \sin i$ (au)	e	ω (rad)	$T_{\rm per}$ (d)	P (d)	K (km/s)	f(m) ($M_\odot$)
008583770	0.63409 ± 0.00006	0.194 ± 0.028	6.113 ± 0.145	782.9 ± 24.4	1044.3 ± 6.0	6.19 ± 0.05	0.311E-01 ± 0.360E-03
008590553	2.92697 ± 0.00003	0.257 ± 0.005	3.504 ± 0.008	1627.4 ± 3.1	1726.7 ± 3.8	17.54 ± 0.04	0.112E+01 ± 0.503E-02
008630254	23.4079 ± 0.0003	0.160 ± 0.006	0.029 ± 0.019	1594.7 ± 5.4	1754.1 ± 5.0	135.1 ± 0.4	0.555E+03 ± 0.317E+01
008712760	0.9603 ± 0.0002	0.554 ± 0.049	6.238 ± 0.078	37.4 ± 1.3	99.18 ± 0.08	116.3 ± 4.6	0.120E+02 ± 0.233E-01
008819284	3.0033 ± 0.0001	0.172 ± 0.017	3.119 ± 0.040	1579.3 ± 11.8	1685.7 ± 11.5	18.0 ± 0.1	0.127E+01 ± 0.174E-01
008914322	3.52720 ± 0.00003	0.144 ± 0.003	2.658 ± 0.057	1371.3 ± 15.1	1899.3 ± 10.4	18.7 ± 0.1	0.162E+01 ± 0.177E-01
008915335	28.7389 ± 0.0002	0.166 ± 0.004	6.243 ± 0.014	1547.5 ± 3.9	1659.8 ± 2.8	175.5 ± 0.3	0.114E+04 ± 0.397E+01
008974140	0.5828 ± 0.0001	0.335 ± 0.074	3.060 ± 0.210	24.9 ± 11.1	313.7 ± 1.4	19.7 ± 0.5	0.268E+00 ± 0.251E-02
009094694	3.0415 ± 0.0002	0.079 ± 0.017	1.896 ± 0.101	35.1 ± 22.4	1718.5 ± 27.6	17.7 ± 0.2	0.127E+01 ± 0.409E-01
009108615	0.93744 ± 0.00006	0.428 ± 0.017	2.931 ± 0.038	283.6 ± 6.6	1127.1 ± 3.3	9.20 ± 0.08	0.864E-01 ± 0.508E-03
009172981	2.2516 ± 0.0001	0.121 ± 0.026	4.353 ± 0.213	372.9 ± 37.4	1115.8 ± 5.1	20.3 ± 0.1	0.122E+01 ± 0.113E-01
009265050	0.66233 ± 0.00002	0.175 ± 0.013	2.883 ± 0.080	168.6 ± 14.0	1112.3 ± 2.6	6.04 ± 0.02	0.313E-01 ± 0.148E-03
009369547	1.4076 ± 0.0003	0.608 ± 0.036	3.195 ± 0.046	835.2 ± 7.2	958.0 ± 8.3	18.5 ± 0.6	0.405E+00 ± 0.709E-02
009453452	0.40898 ± 0.00009	0.524 ± 0.058	4.074 ± 0.113	541.7 ± 11.8	715.6 ± 5.3	6.7 ± 0.2	0.178E-01 ± 0.268E-03
009552758	3.52468 ± 0.00006	0.315 ± 0.006	0.229 ± 0.012	34.7 ± 2.8	1479.2 ± 2.0	25.11 ± 0.06	0.266E+01 ± 0.738E-02
009596355	0.2594 ± 0.0001	0.484 ± 0.114	3.490 ± 0.219	75.8 ± 11.0	314.1 ± 1.9	9.4 ± 0.6	0.235E-01 ± 0.295E-03
009596469	0.12337 ± 0.00003	0.148 ± 0.085	2.394 ± 0.577	31.2 ± 20.0	219.8 ± 0.7	5.67 ± 0.07	0.518E-02 ± 0.368E-04
009598448	1.9995 ± 0.0001	0.208 ± 0.020	0.402 ± 0.163	1151.5 ± 34.5	1570.1 ± 28.4	13.0 ± 0.2	0.432E+00 ± 0.156E-01
009649801	0.57428 ± 0.00003	0.203 ± 0.024	2.628 ± 0.109	220.8 ± 20.9	1274.7 ± 9.6	4.60 ± 0.04	0.155E-01 ± 0.235E-03
009655470	0.4938 ± 0.0002	0.486 ± 0.109	0.430 ± 0.194	649.6 ± 34.0	1130.7 ± 38.4	4.9 ± 0.3	0.125E-01 ± 0.854E-03
009655514	0.4411 ± 0.0001	0.525 ± 0.056	3.332 ± 0.093	715.1 ± 15.4	1038.0 ± 13.8	4.9 ± 0.2	0.106E-01 ± 0.283E-03
009666465	0.16311 ± 0.00002	0.426 ± 0.046	5.139 ± 0.090	438.5 ± 13.9	1035.5 ± 7.9	1.74 ± 0.04	0.539E-03 ± 0.832E-05
009667584	1.33362 ± 0.00009	0.487 ± 0.026	4.417 ± 0.068	285.9 ± 14.0	1782.7 ± 37.0	8.5 ± 0.2	0.995E-01 ± 0.413E-02
009725543	1.6022 ± 0.0003	0.538 ± 0.053	4.045 ± 0.082	1032.6 ± 14.0	1172.0 ± 11.4	16.2 ± 0.6	0.399E+00 ± 0.778E-02
009791112	5.7512 ± 0.0001	0.177 ± 0.009	3.164 ± 0.028	1616.3 ± 9.5	1659.4 ± 5.3	35.2 ± 0.1	0.921E+01 ± 0.598E-01
009823652	3.51125 ± 0.00003	0.067 ± 0.005	0.904 ± 0.060	65.6 ± 15.3	1691.2 ± 4.0	20.80 ±0.04	0.201E+01 ± 0.955E-02
009850393	0.3129 ± 0.0001	0.500 ± 0.107	0.795 ± 0.205	109.3 ± 8.8	298.9 ± 1.8	12.0 ±0.8	0.457E-01 ± 0.557E-03
009963609	0.51569 ± 0.00006	0.113 ± 0.041	5.392 ± 0.372	770.4 ± 54.4	910.6 ± 6.5	5.69 ± 0.04	0.220E-01 ± 0.319E-03
010001145	0.5900 ± 0.0002	0.323 ± 0.101	2.777 ± 0.305	144.3 ± 8.9	181.4 ± 0.6	34.3 ± 1.2	0.831E+00 ± 0.585E-02

continued ...

...continued

KIC	$a \sin i$ (au)	e	ω (rad)	$T_{\rm per}$ (d)	P (d)	K (km/s)	f(m) ($M_\odot$)
010004660	5.7767 ± 0.0003	0.228 ± 0.025	2.461 ± 0.072	1440.8 ± 17.6	1480.9 ± 9.8	40.0 ± 0.3	0.117E+02 ± 0.156E+00
010130777	15.8044 ± 0.0001	0.064 ± 0.010	3.150 ± 0.069	1696.4 ± 20.9	1988.8 ± 11.8	79.6 ± 0.4	0.133E+03 ± 0.158E+01
010226083	0.4340 ± 0.0001	0.178 ± 0.080	9.934 ± 0.450	107.6 ± 4.8	68.33 ± 0.06	64.5 ± 0.9	0.233E+01 ± 0.502E-02
010416779	38.3819 ± 0.0005	0.241 ± 0.005	3.230 ± 0.010	1546.8 ± 2.9	1629.2 ± 2.9	242.7 ± 0.5	0.284E+04 ± 0.104E+02
010451090	0.18448 ± 0.00001	0.229 ± 0.024	5.665 ± 0.103	333.9 ± 13.8	867.5 ± 3.3	2.18 ± 0.01	0.111E-02 ± 0.850E-05
010489783	20.7432 ± 0.0003	0.111 ± 0.011	3.222 ± 0.049	1692.7 ± 17.7	1786.5 ± 8.6	116.8 ± 0.5	0.372E+03 ± 0.359E+01
010679429	0.83613 ± 0.00005	0.143 ± 0.017	3.403 ± 0.131	81.1 ± 13.8	667.0 ± 1.2	12.66 ± 0.04	0.175E+00 ± 0.636E-03
010713398	0.3831 ± 0.0004	0.807 ± 0.081	3.188 ± 0.072	107.9 ± 13.4	1169.2 ± 13.0	5.5 ± 1.0	0.548E-02 ± 0.123E-03
010717871	0.3020 ± 0.0001	0.375 ± 0.105	7.820 ± 0.292	171.3 ± 7.6	174.3 ± 0.5	18.6 ± 0.8	0.120E+00 ± 0.765E-03
010749793	0.6693 ± 0.0001	0.319 ± 0.067	3.930 ± 0.203	106.1 ± 5.2	162.2 ± 0.3	43.5 ± 1.0	0.151E+01 ± 0.578E-02
010977859	2.2510 ± 0.0001	0.048 ± 0.017	3.081 ± 0.345	192.0 ± 20.4	371.5 ± 0.4	60.66 ± 0.08	0.110E+02 ± 0.265E-01
010989032	14.5823 ± 0.0002	0.249 ± 0.007	3.161 ± 0.013	1605.8 ± 5.2	1672.6 ± 4.6	90.0 ± 0.3	0.147E+03 ± 0.822E+00
011152054	0.73964 ± 0.00006	0.207 ± 0.029	5.552 ± 0.191	1310.4 ± 43.0	1570.5 ± 19.3	4.81 ± 0.06	0.218E-01 ± 0.540E-03
011457198	4.3898 ± 0.0001	0.197 ± 0.011	0.043 ± 0.027	1573.0 ± 7.9	1685.4 ± 7.2	26.5 ± 0.1	0.397E+01 ± 0.341E-01
011495305	0.46772 ± 0.00001	0.051 ± 0.013	3.044 ± 0.263	558.7 ± 35.4	841.5 ± 1.8	5.56 ± 0.01	0.192E-01 ± 0.828E-04
011508397	0.20976 ± 0.00006	0.284 ± 0.105	4.390 ± 0.377	27.3 ± 35.6	604.2 ± 6.9	3.6 ± 0.1	0.337E-02 ± 0.781E-04
011572666	0.46613 ± 0.00002	0.438 ± 0.015	4.564 ± 0.040	1204.5 ± 6.9	1324.8 ± 4.5	3.91 ± 0.03	0.769E-02 ± 0.529E-04
011771670	0.2707 ± 0.0001	0.268 ± 0.114	3.214 ± 0.404	468.1 ± 36.9	568.9 ± 7.5	4.9 ± 0.1	0.817E-02 ± 0.216E-03
011874676	12.2946 ± 0.0001	0.179 ± 0.005	2.807 ± 0.015	1523.9 ± 4.0	1679.5 ± 3.3	74.4 ± 0.1	0.878E+02 ± 0.355E+00
011910642	0.7377 ± 0.0002	0.617 ± 0.044	3.086 ± 0.059	52.7 ± 0.9	89.38 ± 0.06	104.9 ± 4.6	0.670E+01 ± 0.112E-01
012020590	0.32254 ± 0.00001	0.485 ± 0.010	5.375 ± 0.021	101.9 ± 1.3	435.0 ± 0.3	8.48 ± 0.05	0.236E-01 ± 0.334E-04
012257449	3.6193 ± 0.0001	0.469 ± 0.010	6.219 ± 0.008	1527.4 ± 3.1	1599.2 ± 5.0	25.6 ± 0.1	0.247E+01 ± 0.155E-01
012470709	1.1728 ± 0.00002	0.160 ± 0.008	2.883 ± 0.058	52.0 ± 12.8	1654.2 ± 9.6	7.18 ± 0.04	0.786E-01 ± 0.920E-03
012602250	0.533174 ± 0.000006	0.425 ± 0.002	2.771 ± 0.005	405.5 ± 0.5	588.7 ± 0.1	10.00 ± 0.01	0.583E-01 ± 0.369E-04
012736056	0.78761 ± 0.00008	0.212 ± 0.041	2.934 ± 0.116	1484.1 ± 27.9	1580.6 ± 20.2	5.09 ± 0.08	0.260E-01 ± 0.668E-03

4.2 Discussion

Table 4.1 contains 141 binaries out of a sample of 1646 δ Sct stars which is 8.5 percent of the sample. Quite clearly, this is a lower limit as the time-delay method cannot be applied to orbits with planes nearly perpendicular to the line of sight. In these cases, the time-delay will be too small to measure. The greatest limitation to the method is interference due to neighbouring pulsation frequencies. We suspect that the time-delay method is not applicable to a considerable fraction of the sample owing to this limitation. The method fails for orbital periods longer than about 4 yrs, which is the duration of the *Kepler* observations.

The method is also not suitable for orbital periods shorter than about 50 d. This is not so much a limitation of the method as a limitation on the applicability to δ Sct stars. For short orbital periods, a short window size (about one-tenth the duration of the orbital period) must be used to calculate the phase. The short duration implies a large frequency spread and a higher probability of including neighbouring frequencies. This is the reason why so few stars with orbital periods less than 100 d are present in the above Table.

Information From Time-delay Curves

Time-delay diagrams are very helpful in giving us information about the orbit of binary systems. For example, deviation of the curve from a sinusoid indicates that the orbit is eccentric. The projected size of the orbit can also be found from the difference in time-delay between the maximum and the minimum. The other information we can get from the time-delay curve is that when the pulsating star is nearest to us, the time-delay curve reaches its minima and when the star is furthest from us, the time-delay curve reaches its maxima. Fast fall and slow rise of the time-delay curve reveal that the star passes the periapsis after reaching the farthest point from us. Fast rise and slow fall also shows that the star passes the periapsis after reaching the nearest point to us.

Triple Systems

In a heirarchical triple star system, two stars orbit each other at close range, and a third, more distant, companion orbits around the first binary. It is possible to identify such systems from the binarogram which will show two peaks corresponding to the two orbital frequencies. Based on this idea, we suggest that the following systems are triple star systems as can be seen from the binarogram plots in Chapter 2: KIC 10001145, 9655514, 3223460, 8149341, 10749793 and KIC 11572666. Their corresponding time-delay plots also support this interpretation. They show two independent variations as can be seen in Figures 4.1, 4.2, 4.3, 4.4, 4.5 and 4.6.

From literature, further information about these stars is given as follows. The Tycho-2 Catalogue is an astrometric reference catalogue of brightest stars in the Milky Way. KIC 8149341, 9655514, 10001145 and 11572666 are listed in this catalogue. In the Simbad astronomical database, KIC 3223460 is described as a variable star of δ Sct type. KIC 8149341 is further mentioned as a star of V-magnitude 10.48. In the database of physical parameters presented by Uytterhoeven et al. (2011), it is mentioned in the list of Kepler A-F type stars with an effective temperature value of 7540 K.

KIC 9655514 is listed as a variable star of δ Sct type, with a V-magnitude of 11.88 in the Simbad astronomical database. KIC 9655514 is also compiled in the database of physical parameters which was presented by Uytterhoeven et al. (2011). According to this catalogue, this star was considered as a binary or multiple system. On the Simbad database, KIC 10001145 is mentioned as a star with a V-magnitude of 10.9 and KIC 10749793 as a variable star of δ Sct type.

Niemczura et al. (2011) mentioned KIC 11572666 as a double-lined spectroscopic binary with 'hybrid' pulsation (where frequencies of γ Dor and δ Sct type respectively are visible in the spectra). This spectroscopic confirmation further shows the binary nature of the star in addition to the photometric result we obtained.

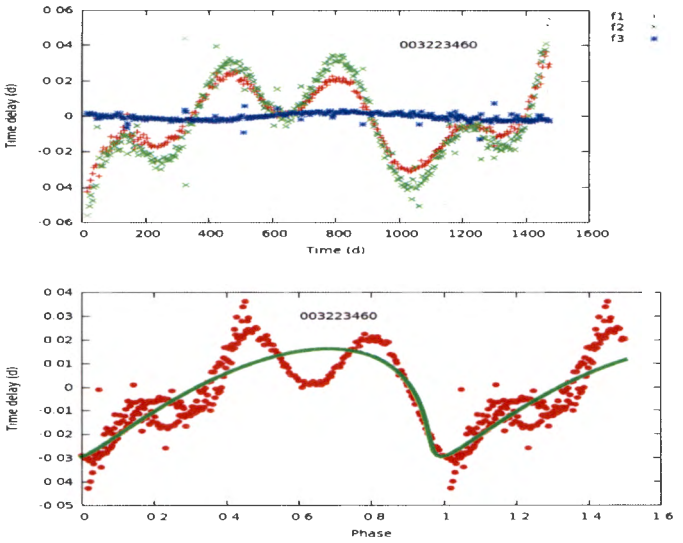

Figure 4.1: Time-delay curve (top panel) of KIC 3223460 for the three pulsation frequencies of highest amplitudes and the corresponding orbital phase plot (bottom panel). The solid line in the bottom panel is a fit from the orbital solution.

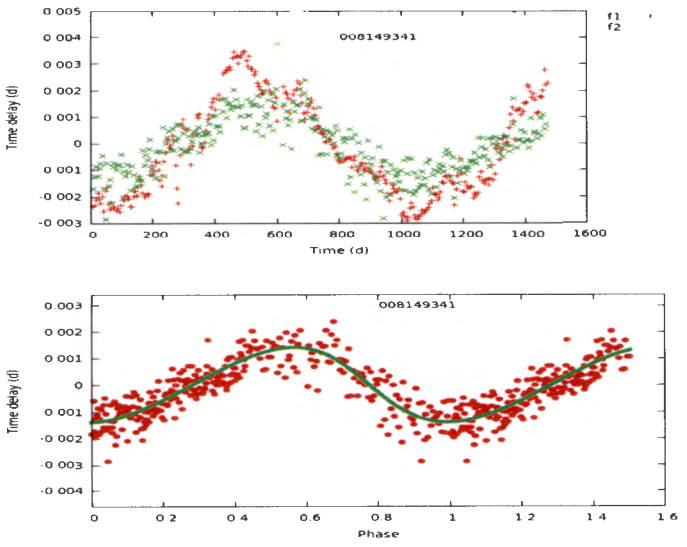

Figure 4.2: Time-delay curve (top panel) of KIC 8149341 for the two pulsation frequencies of highest amplitudes and the corresponding orbital phase plot (bottom panel). The solid line in the bottom panel is a fit from the orbital solution.

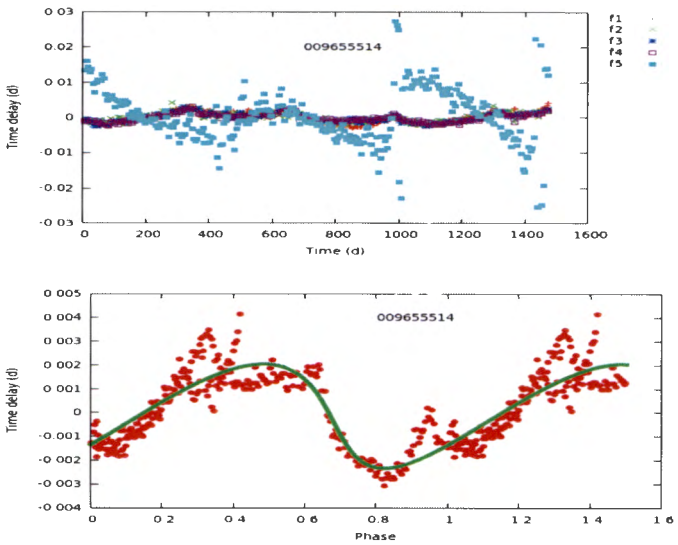

Figure 4.3: Time-delay curve (top panel) of KIC 9655514 for the five pulsation frequencies of highest amplitudes and the corresponding orbital phase plot (bottom panel). The solid line in the bottom panel is a fit from the orbital solution.

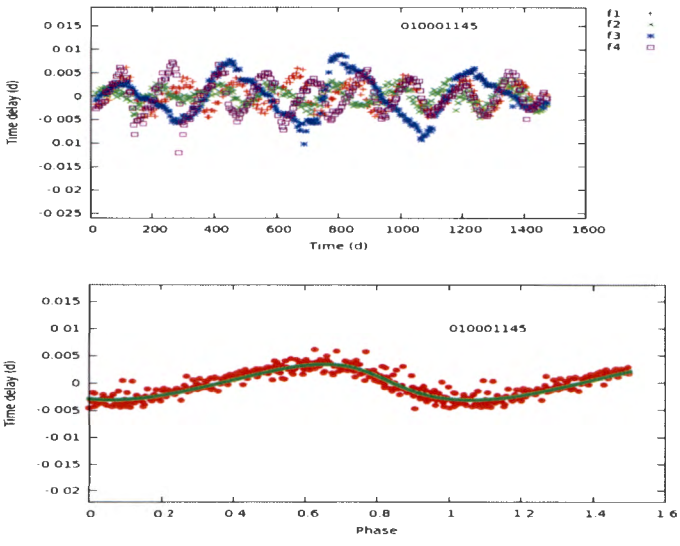

Figure 4.4: Time-delay curve (top panel) of KIC 10001145 for the four pulsation frequencies of highest amplitudes and the corresponding orbital phase plot (bottom panel). The solid line in the bottom panel is a fit from the orbital solution.

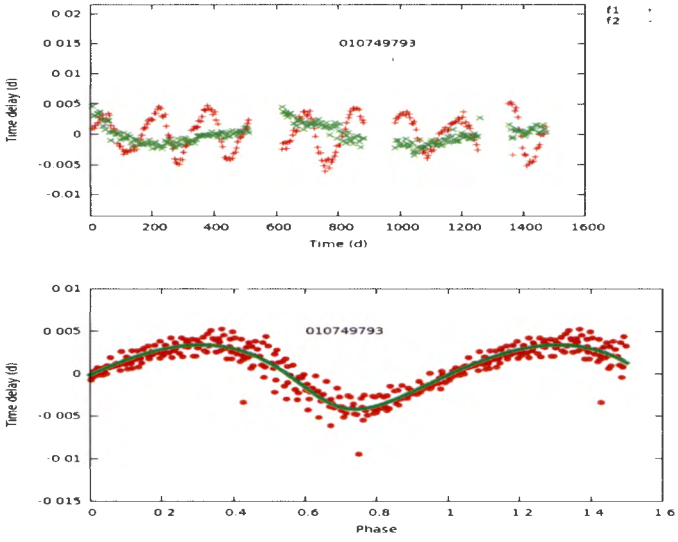

Figure 4.5: Time-delay curve (top panel) of KIC 10749793 for thetwo pulsation frequencies of highest amplitudes and the corresponding orbital phase plot (bottom panel). The solid line in the bottom panel is a fit from the orbital solution.

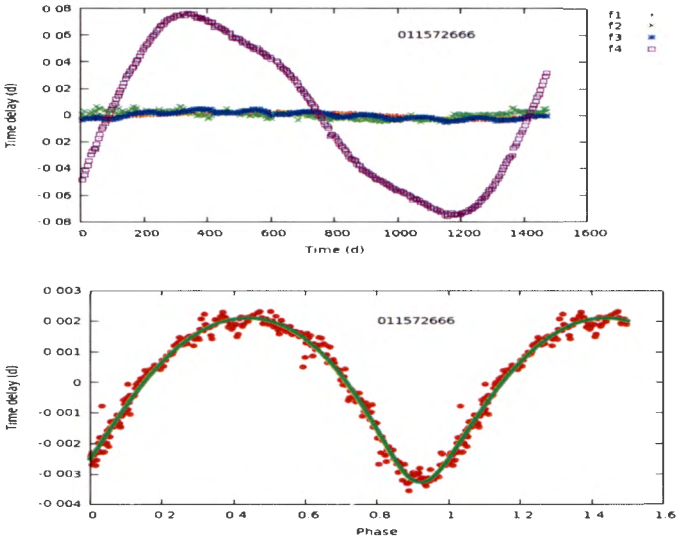

Figure 4.6: Time-delay curve (top panel) of KIC 11572666 for the four pulsation frequencies of highest amplitudes and the corresponding orbital phase plot (bottom panel). The solid line in the bottom panel is a fit from the orbital solution

Systems With Two Pulsating Stars

A binary with resolved spectroscopic companions results in two separate radial velocity curves measured from lines belonging to each companion. These double-lined systems have radial velocity variations of opposite phase: when one star is approaching the other is receding and vice-versa. In the same way, two pulsating stars in a binary system will produce time-delays which are of opposite sign in the two stars. The following stars appear to be binaries in which both stars pulsate; KIC 5042785, 5904699, 8443311 and KIC 7977996. This can be seen from the plots shown in Figures 4.7, 4.8, 4.9 and 4.10.

From literature, information described about these stars is as follows. KIC 5042785, 7977996 and 8443311 are listed in the Tycho-2 astrometric reference catalogue of brightest stars. KIC 5042785 is mentioned as a star with V-magnitude of 11.69 and KIC 5904699 as a rotationally variable star. KIC 7977996 is described as a rotationally variable star with V-magnitude of 11.35 and Uytterhoeven et al. (2011) listed this star in a database of Kepler A-F type stars with an effective temperature value of 7120 K. In the Simbad astronomical database, KIC 8443311 is mentioned as a variable star of δ Sct type and V-magnitude of 11.40.

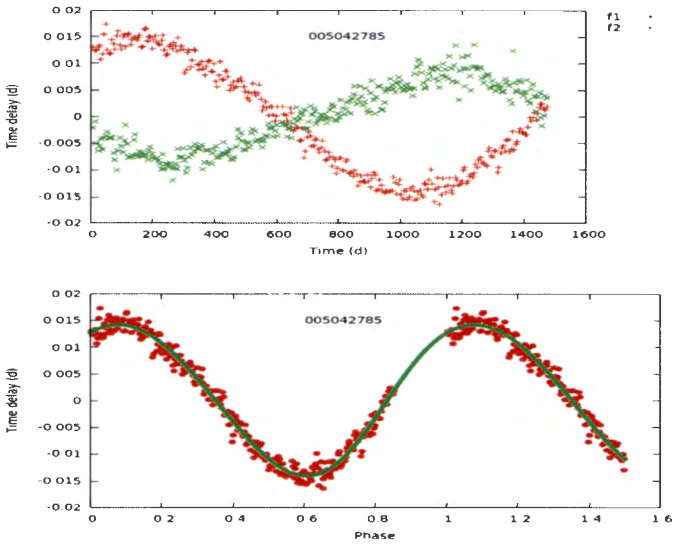

Figure 4.7: Time-delay curve (top panel) of KIC 5042785 for the highest two pulsation frequencies of highest amplitudes and the corresponding orbital phase plot (bottom panel). The solid line in the bottom panel is a fit from the orbital solution.

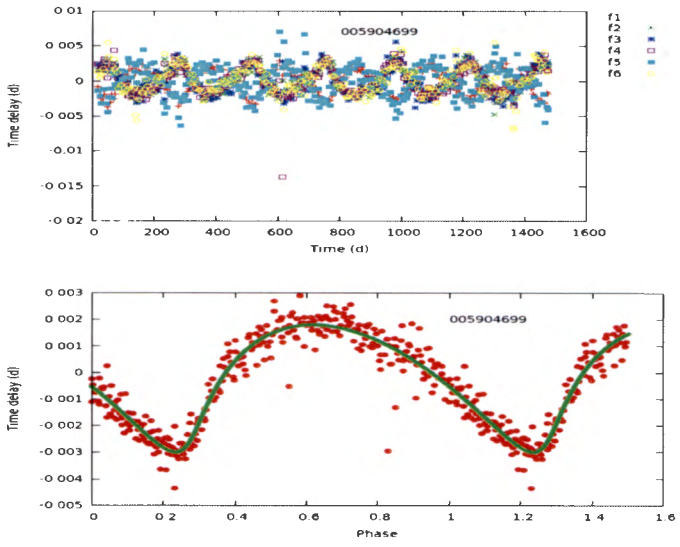

Figure 4.8: Time-delay curve (top panel) of KIC 5904699 for the six pulsation frequencies of highest amplitudes and the corresponding orbital phase plot (bottom panel). The solid line in the bottom panel is a fit from the orbital solution.

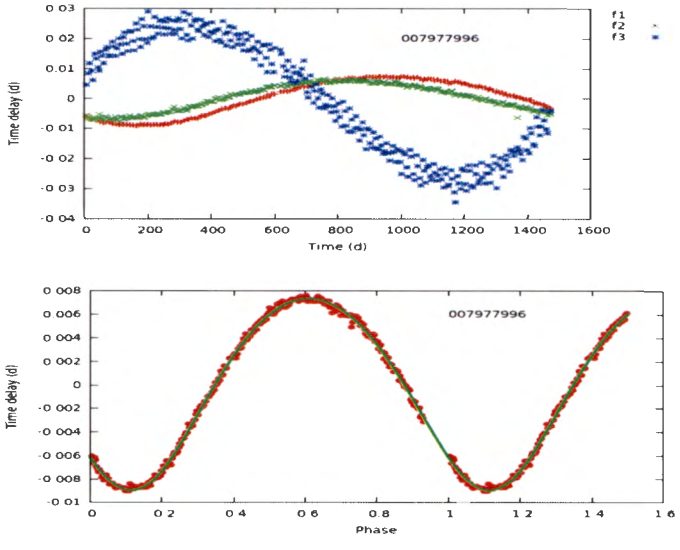

Figure 4.9: Time-delay curve (top panel) of KIC 7977996 for the three pulsation frequencies of highest amplitudes and the corresponding orbital phase plot (bottom panel). The solid line in the bottom panel is a fit from the orbital solution.

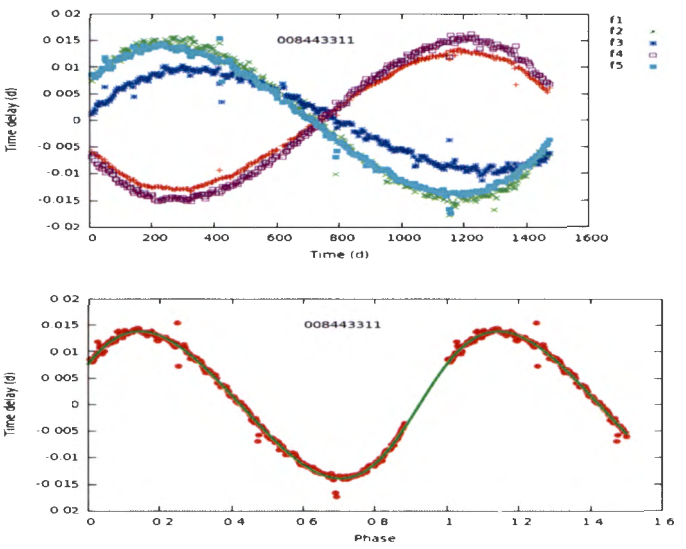

Figure 4.10: Time-delay curve (top panel) of KIC 8443311 for the five pulsation frequencies of highest amplitudes and the corresponding orbital phase plot (bottom panel). The solid line in the bottom panel is a fit from the orbital solution.

Other Kinds of Time-delay Plots

We also observed other new kind of plots (e.g., KIC 5737687, KIC 8819284 and KIC 5459908) on the corrected time-delay curves. These systems might be further hierarchical structures, or different pulsation modes. Additional explanation might be necessary apart from what is mentioned here. The fact that time-delay plots give information on the nature of the orbit of the binary system implies that these plots might also mean something about the structure of the orbit.

Stars from our sample which have also been categorised as binaries in the literature

A literature search was used to confirm that the method we used agrees with previous studies. Through the analysis of the Kepler light curve of each star, Uytterhoeven et al. (2011) compiled a database of physical parameters. Their sample of stars were taken from literature and new ground-based observations. The result of the analysis showed that several stars are considered as binaries or multiple systems, and are also binaries according to the method we used. These stars are the ones with the following KIC number: 1577039, 4048494, 4269337, 5356349, 7848288, 8583770 and 9655514. According to our analysis, KIC 965514 is identified as a triple system. The first two (KIC 1577039, KIC 4048494) are also listed as binaries in Catalogue of the Components of Double and Multiple stars (CCDM). This evidence is confirmation that our method works properly and yields results which are consistent with the results of previous studies.

Independent Confirmations of Our Results

In order to further confirm our results of binary parameters, we sent some of our samples to two individuals for an independent analysis. The two astronomers, S. Murphy and H. Shibahashi have several publications on orbital parameters of *Kepler* binaries, and they confirmed that our results are in good agreement with their method (personal communication). As an example, Table 4.2 shows the comparison between our results and the values given by Murphy for the case of binary system KIC 3346195.

Table 4.2: Comparison of orbital parameters for KIC 3346195 obtained using our method and the one given by independent analysis by Murphy. Our uncertainties on the orbital elements are considerably smaller than the analysis given by Murphy.

Source	$a \sin i$ (au)	e	ω (rad)	$T_{\rm per}$ (d)	P (d)	K (kms)	f(m) ($M_\odot$)
This work	0.480384	0.688379	4.990862	359.5788	398.3405	16.6260	0.0931821
	± 0.00003	± 0.01514	± 0.02210	± 1.0659	± 0.3832	± 0.3298	± 0.00018
Murphy	0.483	0.65	5.06	not calculated	400.3	not calculated	0.094
	± 0.0001	± 0.02	± 0.03	-	± 0.5	-	± 0.005

Chapter 5

Conclusions

The *Kepler* space telescope provides a unique opportunity to investigate stellar variability at a photometric precision which has never been previously attained. One of the results is the detection of large numbers of δ Sct stars which are easily identified by the large number of peaks in the periodogram with frequencies higher than about 5 d^{-1}. The high pulsation frequency implies good time resolution which means that these A-F main sequence and giant stars are good clocks. They can therefore be used to measure the change in time-delay caused by the cyclical change in distance from the observer as a result of binary motion. The time-delay is most easily measured by the changing phase of the pulsational light variation at a given fixed frequency.

The pulsations do not normally vary in amplitude or frequency (although this is not true in some cases), but the multiple close pulsation frequencies in these stars are a major problem. In frequency space, the varying time-delay in a binary system can be represented by the appearance of multiple close peaks surrounding the main pulsation peak in the periodogram (Shibahashi & Kurtz 2012). To measure the time-delay requires that these satellite peaks be distinctly resolved, but this cannot happen if there is another close pulsation mode.

In the time domain, a close pulsation mode results in an interference which modifies the phase and renders the time-delay measurement unreliable. The result is a distortion of the time-delay as a function of time which needs to be corrected in some way. The aim of this work is to examine the 1646 δ Sct stars previously

identified in the *Kepler* data, identify possible cyclic time-delay variations and calculate the orbital parameters.

To this end we used a method first developed by Balona (2014a) to quickly identify binary candidates among the δ Sct stars. The method is similar in concept to the periodogram and produces a plot of time-delay amplitude (or $a \sin i$) as a function of orbital frequency which is called a binarogram. In principle, the method produces just a single peak provided all pulsation frequencies are used in the solution. However, this is not practical and only the first three modes of highest amplitude are used. Interference due to other modes which are not taken into account in the binarogram produces spurious peaks. A true orbital peak is identified if at least two different pulsation frequencies give the same peak in the binarogram. In this way we found 325 possible binary candidates.

Further examination of these candidates requires calculation of the phase as a function of time. To this end a window of a certain duration was chosen and a sinusoid at the pulsation frequency was fitted to this data segment. From this solution, the phase at the mid-point time of the window was obtained. The window was shifted along the time series to obtain the phase as a function of time. Unlike the binarogram, which does not require such a moveable window, a balance between choice of window size and signal-to-noise must be made. Clearly, the window size needs to be shorter than the orbital period, but long enough to lead to a phase of sufficient accuracy. Fortunately, the orbital period is available from the binarogram and a choice can be made. We used a window duration of 10 days for stars with orbital periods greater than 100 days and a window size of 4 days for stars with orbital periods less than 100 days.

The resulting phase variation as a function of time for the ten frequencies of highest amplitude was visually examined. Variations which clearly showed the same period in different pulsation frequencies were selected. Most variations did not show distinct periodicity, most likely because of interference due to close pulsation frequencies. Even those phase variations that are periodic are generally distorted.

To correct for this distortion we fitted a function which is a combination of a poly-

nomial and truncated Fourier series by least squares to individual phase variations from different pulsation frequencies in the same star. The polynomial part models the distortion which can therefore be removed. The least squares fit also provides a measure of the goodness of fit: the standard deviation of the residuals. A poor phase variation leads to a large residual standard deviation, whereas a good phase variation leads to a small residual standard deviation. The final phase or time-delay variation is the mean of the individual corrected time-delays weighted inversely as the variance of the residuals to the model fit.

Using the mean corrected time-delay, we applied an algorithm to deduce the orbital parameters. This algorithm consists of a scan across the full range of eccentricity, $0 < e < 1$. For each chosen eccentricity, a scan across the full range of time of periastron, $0 < T_{\rm per} < P_{\rm orb}$ is made and the residual error, σ, at the given pair $\sigma(e, T_{\rm per})$ is calculated. The best estimates of e and $T_{\rm per}$ are those which lead to a minimum σ. Using this estimate as a starting value, an iterative method was developed which quickly converges on the optimal orbital parameters. At the same time, the least squares solution of the correction terms provides the standard deviation in all the parameters. The calculation of these parameters, as presented in Table 4.1, is the main aim of this work.

As an additional product, we have identified several triple systems and some pairs in which both components of the binary are δ Sct stars. These interesting objects clearly deserve further study.

Appendix A

Corrected Time-delay Plots and Orbital Phase Diagrams

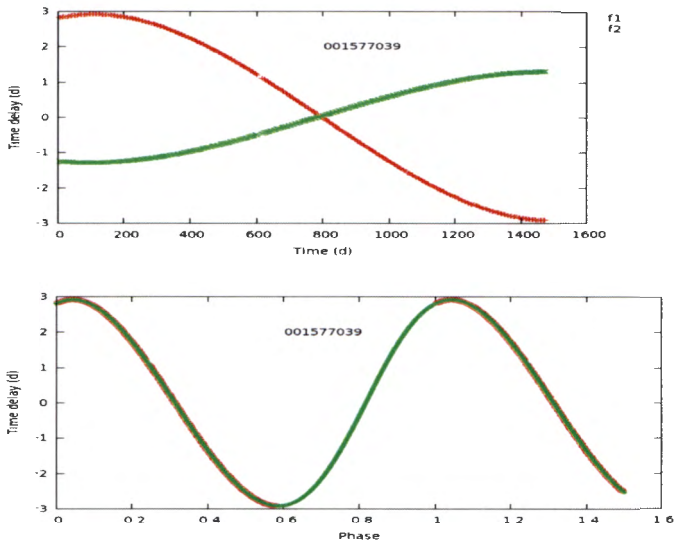

Figure A.1: Time-delay curve (top panel) of KIC 1577039 for the two pulsation frequencies of highest amplitudes and the corresponding orbital phase plot (bottom panel). The solid line in the bottom panel is a fit from the orbital solution.

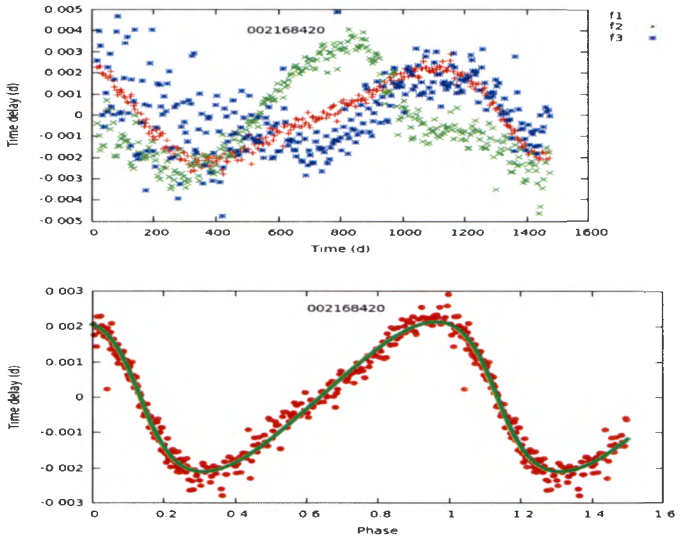

Figure A.2: Time-delay curve (top panel) of KIC 2168420 for the three pulsation frequencies of highest amplitudes and the corresponding orbital phase plot (bottom panel). The solid line in the bottom panel is a fit from the orbital solution.

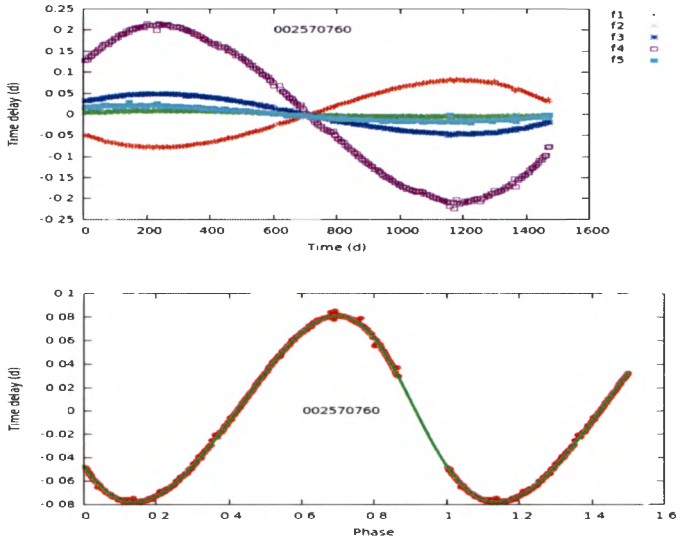

Figure A.3: Time-delay curve (top panel) of KIC 2570760 for the five pulsation frequencies of highest amplitudes and the corresponding orbital phase plot (bottom panel). The solid line in the bottom panel is a fit from the orbital solution.

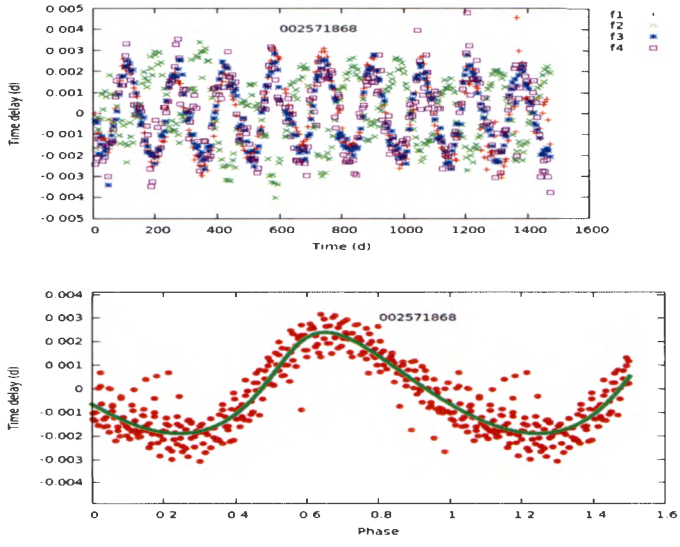

Figure A.4: Time-delay curve (top panel) of KIC 2571868 for the four pulsation frequencies of highest amplitudes and the corresponding orbital phase plot (bottom panel). The solid line in the bottom panel is a fit from the orbital solution.

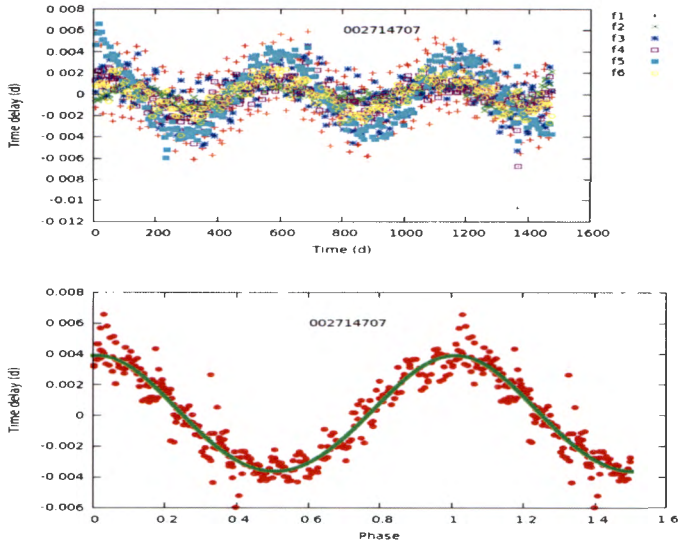

Figure A.5: Time-delay curve (top panel) of KIC 2714707 for the six pulsation frequencies of highest amplitudes and the corresponding orbital phase plot (bottom panel). The solid line in the bottom panel is a fit from the orbital solution.

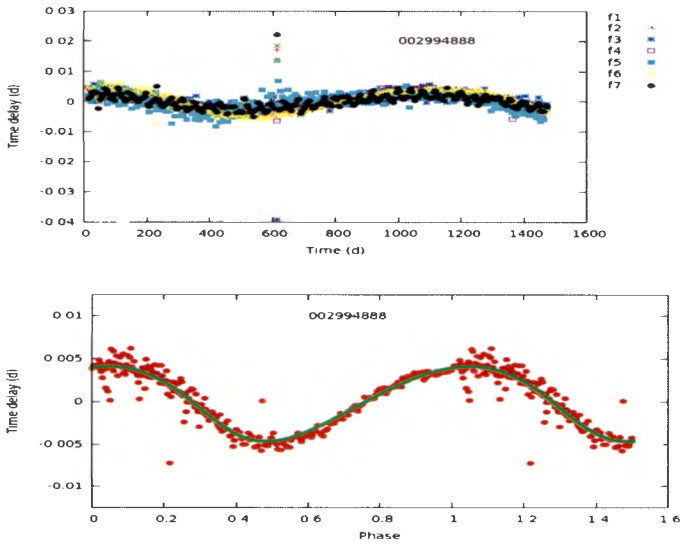

Figure A.6: Time-delay curve (top panel) of KIC 2994888 for the seven pulsation frequencies of highest amplitudes and the corresponding orbital phase plot (bottom panel). The solid line in the bottom panel is a fit from the orbital solution.

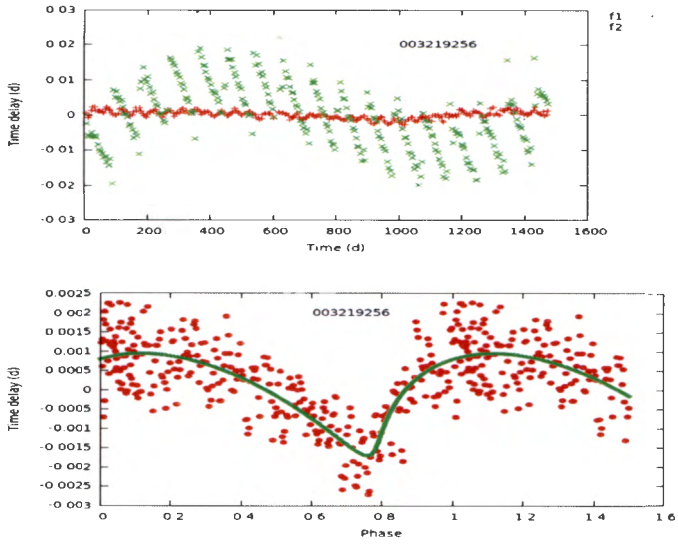

Figure A.7: Time-delay curve (top panel) of KIC 3219256 for the two pulsation frequencies of highest amplitudes and the corresponding orbital phase plot (bottom panel). The solid line in the bottom panel is a fit from the orbital solution.

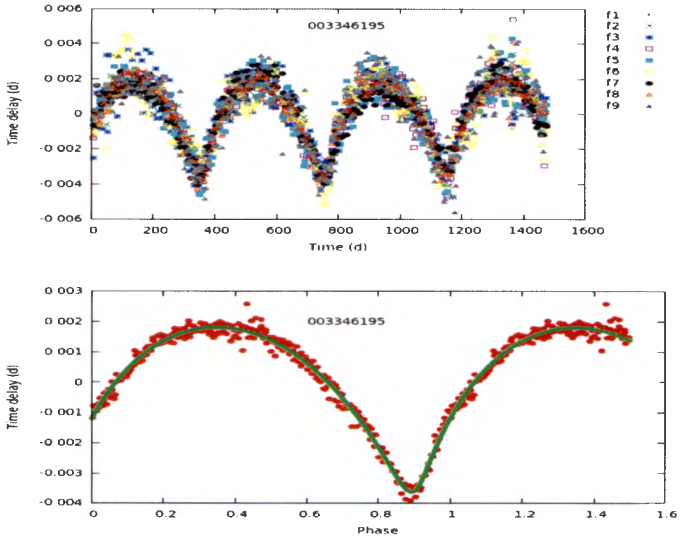

Figure A.8: Time-delay curve (top panel) of KIC 3346195 for the nine pulsation frequencies of highest amplitudes and the corresponding orbital phase plot (bottom panel). The solid line in the bottom panel is a fit from the orbital solution.

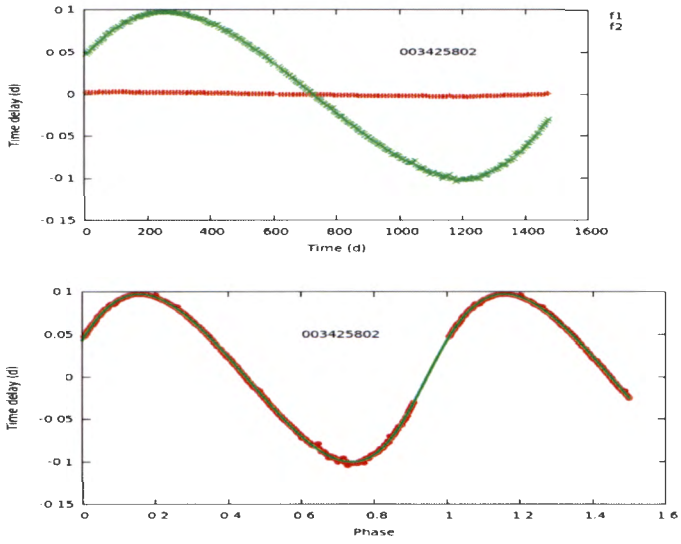

Figure A.9: Time-delay curve (top panel) of KIC 3425802 for the two pulsation frequencies of highest amplitudes and the corresponding orbital phase plot (bottom panel). The solid line in the bottom panel is from the orbital solution.

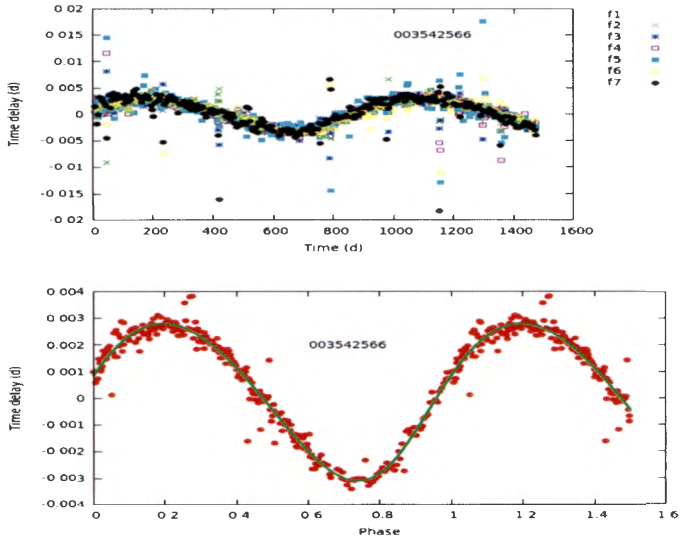

Figure A.10: Time-delay curve (top panel) of KIC 3542566 for the seven pulsation frequencies of highest amplitudes and the corresponding orbital phase plot (bottom panel). The solid line in the bottom panel is a fit from the orbital solution.

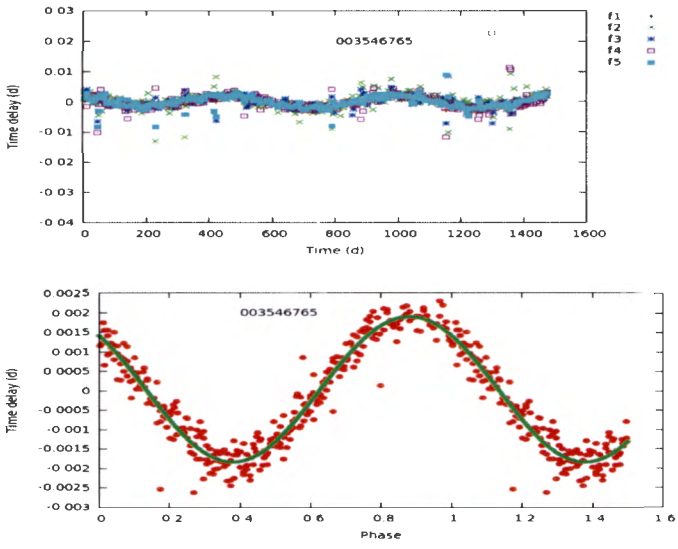

Figure A.11: Time-delay curve (top panel) of KIC 3546765 for the five pulsation frequencies of highest amplitudes and the corresponding orbital phase plot (bottom panel). The solid line in the bottom panel is a fit from the orbital solution.

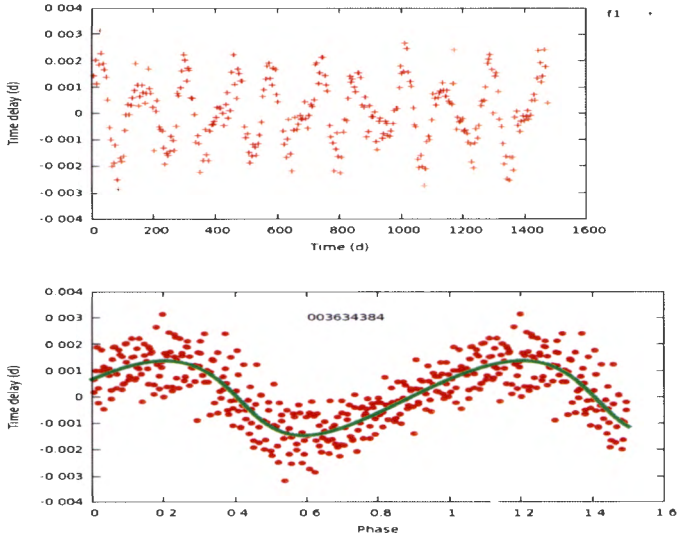

Figure A.12: Time-delay curve (top panel) of KIC 3634384 for the pulsation frequency of highest amplitude and the corresponding orbital phase plot (bottom panel). The solid line in the bottom panel is a fit from the orbital solution.

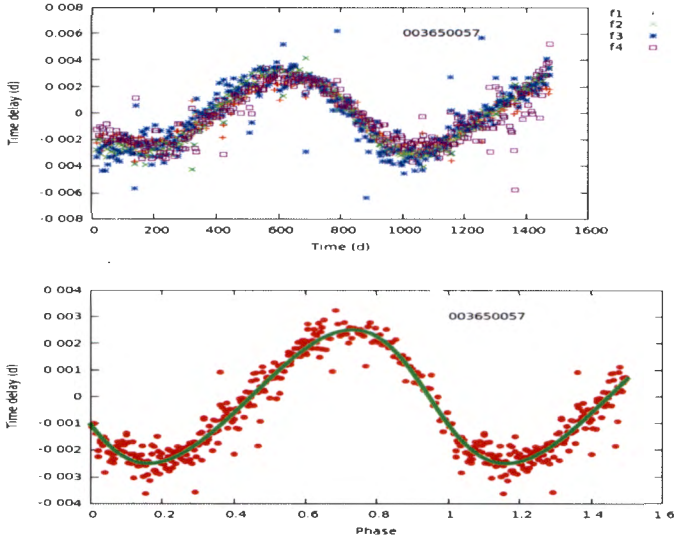

Figure A.13: Time-delay curve (top panel) of KIC 3650057 for the four pulsation frequencies of highest amplitudes and the corresponding orbital phase plot (bottom panel). The solid line in the bottom panel is a fit from the orbital solution.

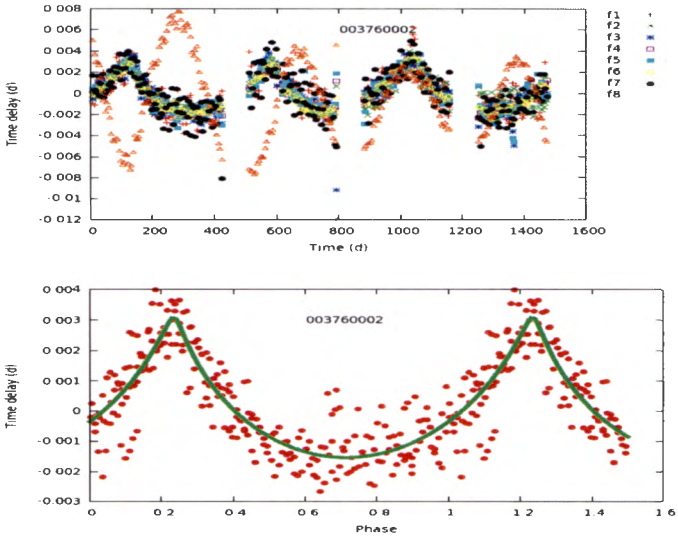

Figure A.14: Time-delay curve (top panel) of KIC 3760002 for the eight pulsation frequencies of highest amplitudes and the corresponding orbital phase plot (bottom panel). The solid line in the bottom panel is a fit from the orbital solution.

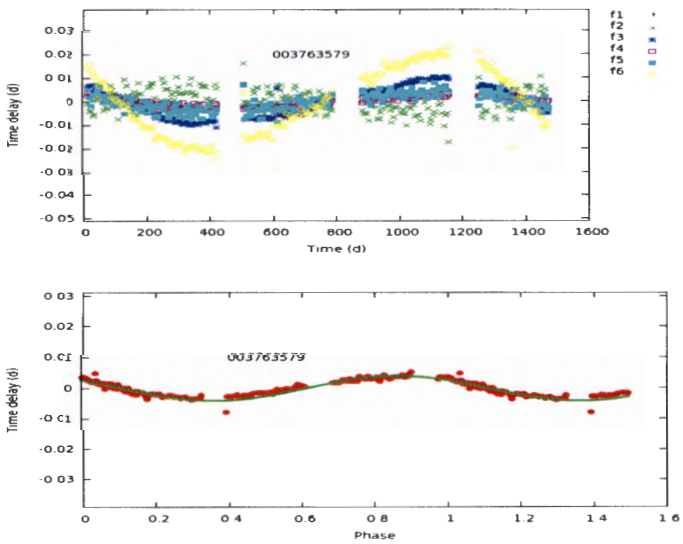

Figure A.15: Time-delay curve (top panel) of KIC 3763579 for the six pulsation frequencies of highest amplitudes and the corresponding orbital phase plot (bottom panel). The solid line in the bottom panel is a fit from the orbital solution.

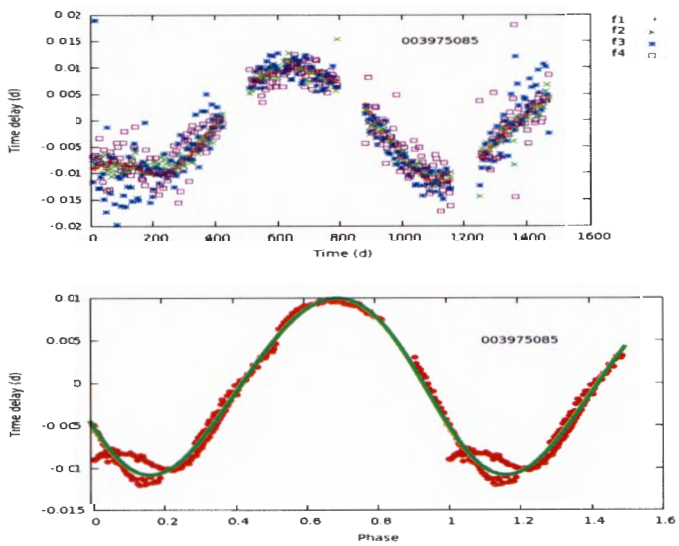

Figure A.16: Time-delay curve (top panel) of KIC 3975085 for the four pulsation frequencies of highest amplitudes and the corresponding orbital phase plot (bottom panel). The solid line in the bottom panel is a fit from the orbital solution.

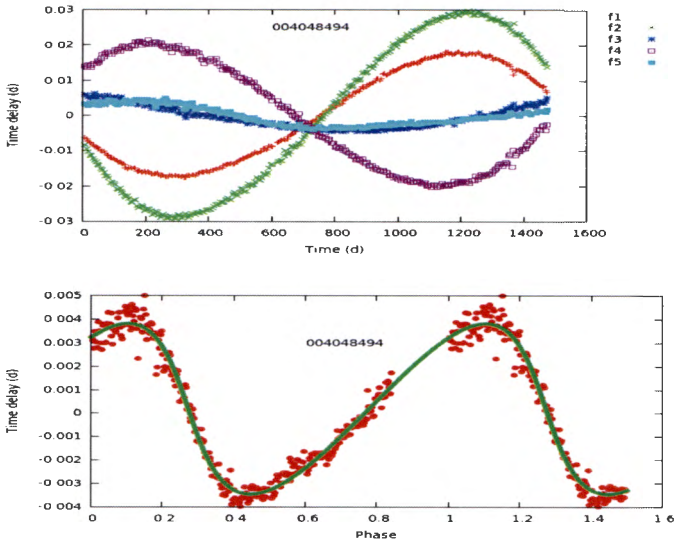

Figure A.17: Time-delay curve (top panel) of KIC 4048494 for the five pulsation frequencies of highest amplitudes and the corresponding orbital phase plot (bottom panel). The solid line in the bottom panel is a fit from the orbital solution.

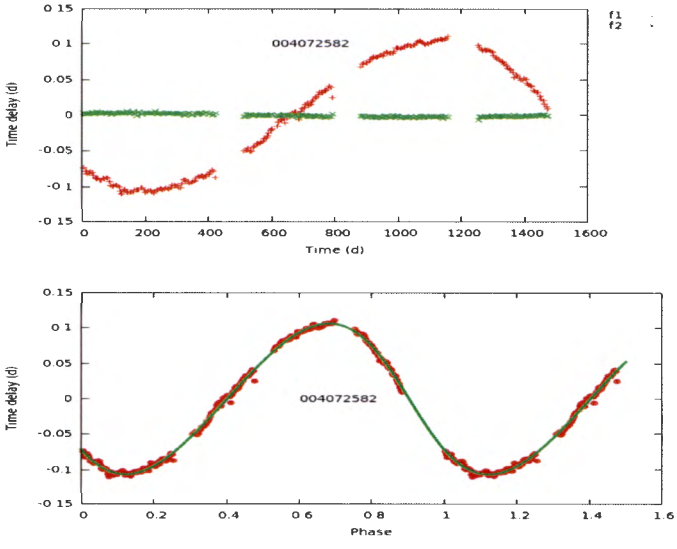

Figure A.18: Time-delay curve (top panel) of KIC 4072582 for the two pulsation frequencies of highest amplitudes and the corresponding orbital phase plot (bottom panel). The solid line in the bottom panel is a fit from the orbital solution.

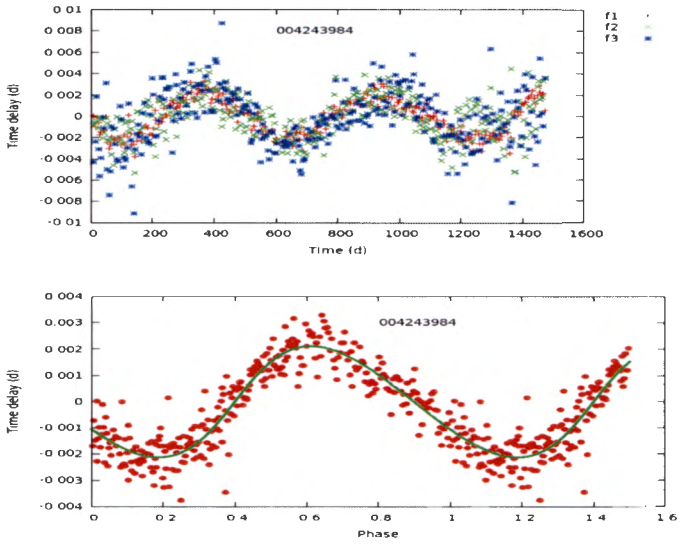

Figure A.19: Time-delay curve (top panel) of KIC 4243984 for the three pulsation frequencies of highest amplitudes and the corresponding orbital phase plot (bottom panel). The solid line in the bottom panel is a fit from the orbital solution.

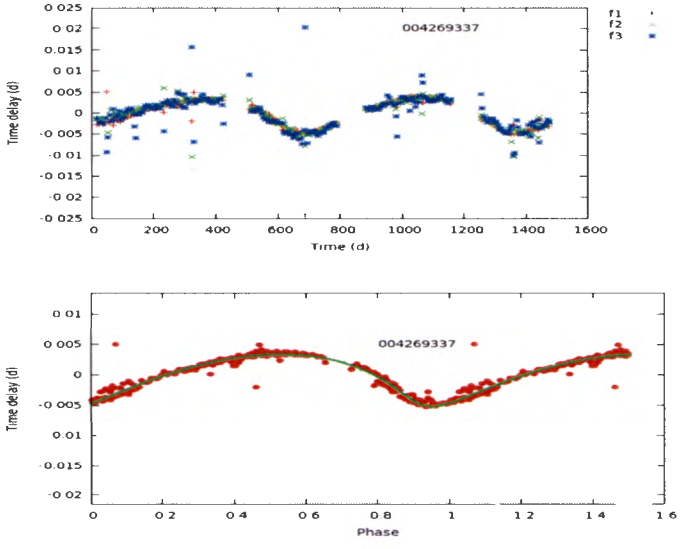

Figure A.20: Time-delay curve (top panel) of KIC 4269337 for the three pulsation frequencies of highest amplitudes and the corresponding orbital phase plot (bottom panel). The solid line in the bottom panel is a fit from the orbital solution.

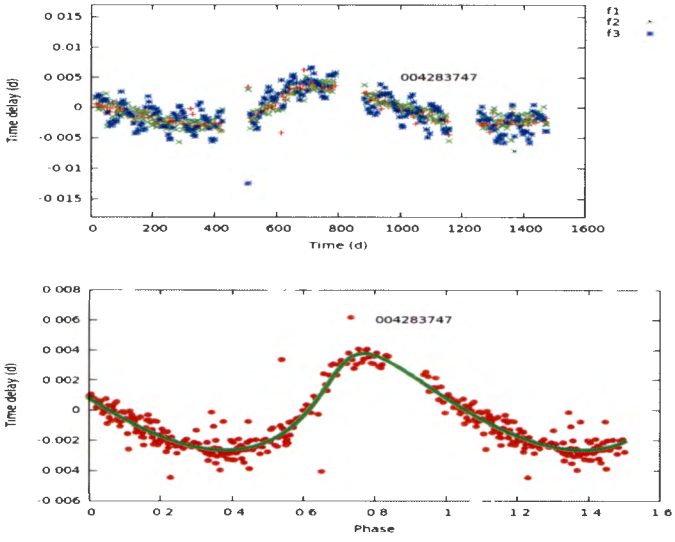

Figure A.21: Time-delay curve (top panel) of KIC 4283747 for the three pulsation frequencies of highest amplitudes and the corresponding orbital phase plot (bottom panel). The solid line in the bottom panel is a fit from the orbital solution.

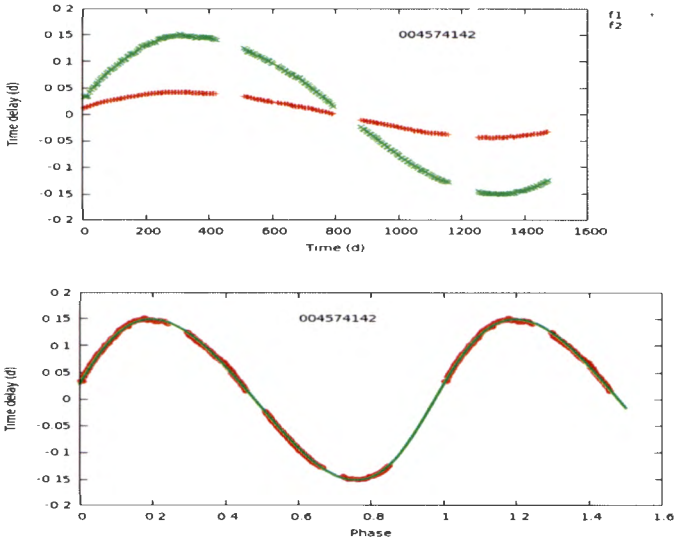

Figure A.22: Time-delay curve (top panel) of KIC 4574142 for the two pulsation frequencies of highest amplitudes and the corresponding orbital phase plot (bottom panel). The solid line in the bottom panel is a fit from the orbital solution.

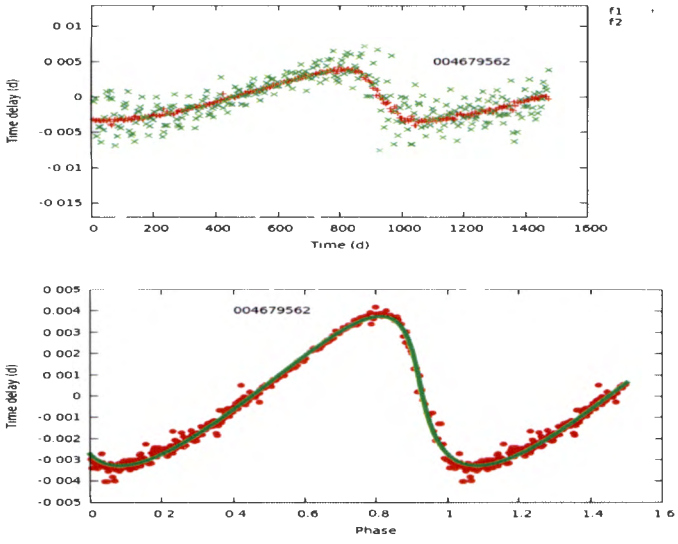

Figure A.23: Time-delay curve (top panel) of KIC 4679562 for the two pulsation frequencies of highest amplitudes and the corresponding orbital phase plot (bottom panel). The solid line in the bottom panel is a fit from the orbital solution.

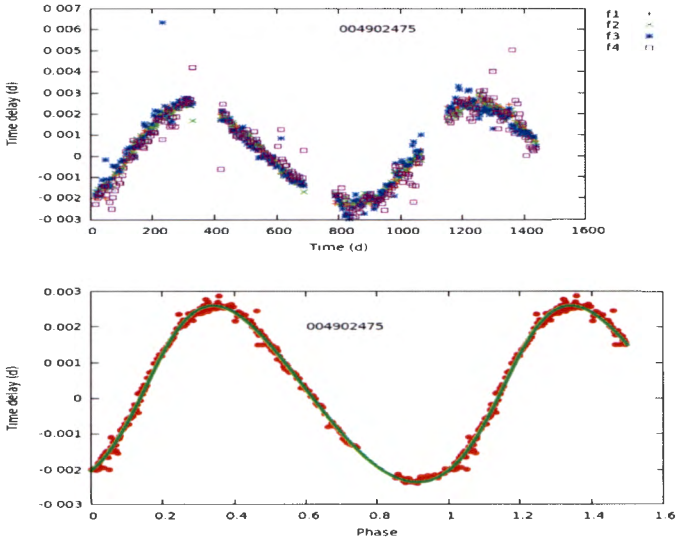

Figure A.24: Time-delay curve (top panel) of KIC 4902475 for the four pulsation frequencies of highest amplitudes and the corresponding orbital phase plot (bottom panel). The solid line in the bottom panel is a fit from the orbital solution.

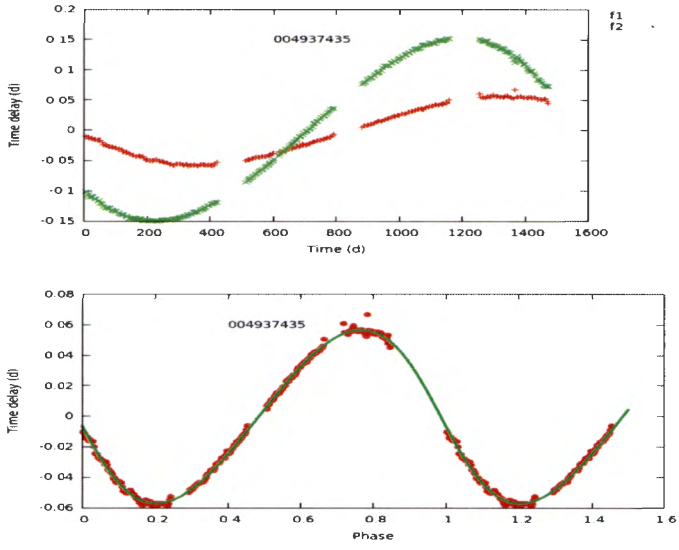

Figure A.25: Time-delay curve (top panel) of KIC 493735 for the two pulsation frequencies of highest amplitudes and the corresponding orbital phase plot (bottom panel). The solid line in the bottom panel is a fit from the orbital solution.

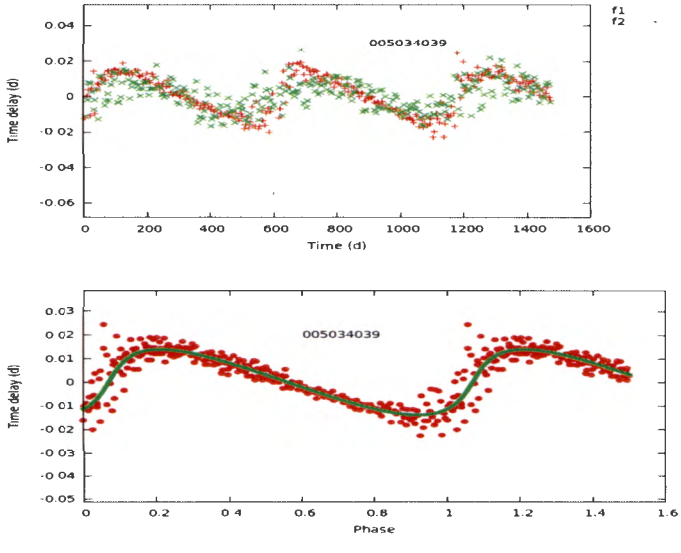

Figure A.26: Time-delay curve (top panel) of KIC 5034039 for the two pulsation frequencies of highest amplitudes and the corresponding orbital phase plot (bottom panel). The solid line in the bottom panel is a fit from the orbital solution.

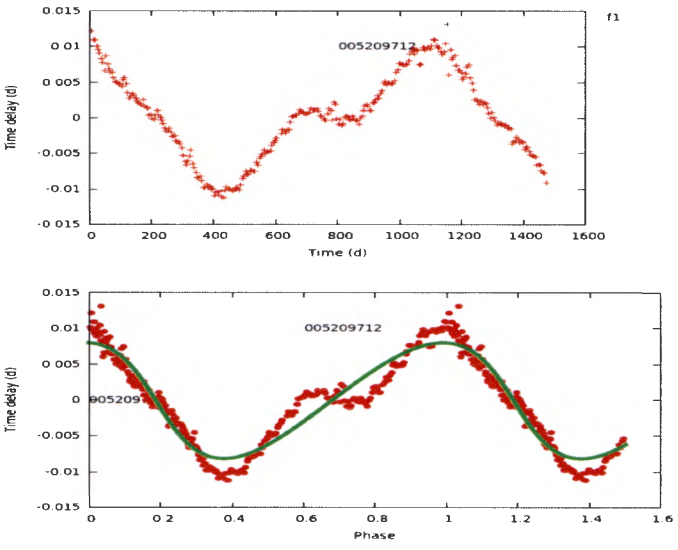

Figure A.27: Time-delay curve (top panel) of KIC 5209712 for the pulsation frequency of highest amplitude and the corresponding orbital phase plot (bottom panel). The solid line in the bottom panel is a fit from the orbital solution.

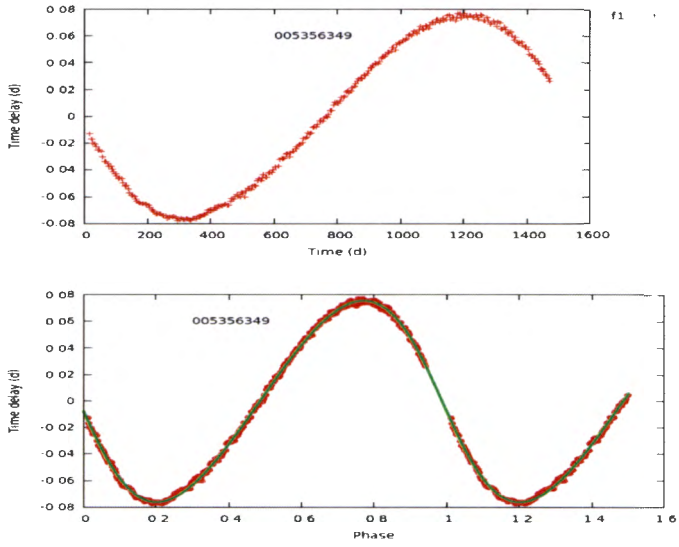

Figure A.28: Time-delay curve (top panel) of KIC 5356349 for the pulsation frequency of highest amplitude and the corresponding orbital phase plot (bottom panel). The solid line in the bottom panel is a fit from the orbital solution.

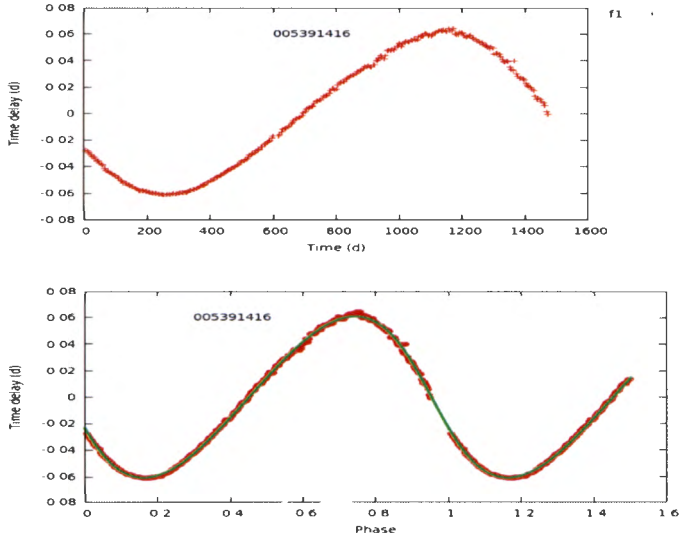

Figure A.29: Time-delay curve (top panel) of KIC 5391416 for the pulsation frequency of highest amplitude and the corresponding orbital phase plot (bottom panel). The solid line in the bottom panel is a fit from the orbital solution.

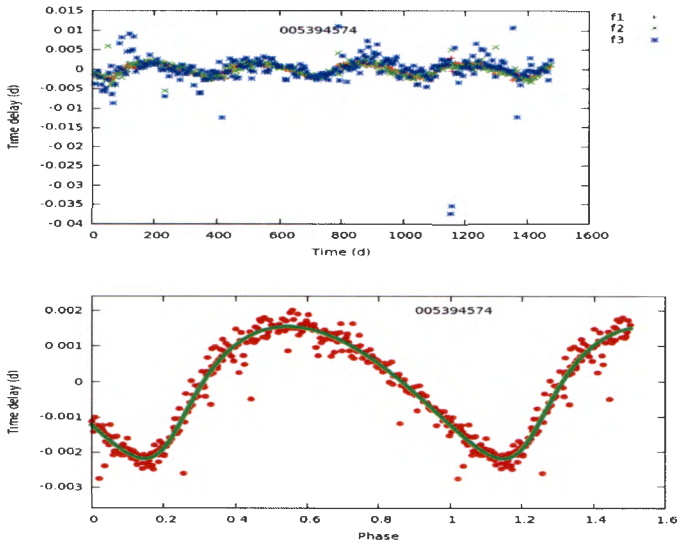

Figure A.30: Time-delay curve (top panel) of KIC 5394574 for the three pulsation frequencies of highest amplitudes and the corresponding orbital phase plot (bottom panel). The solid line in the bottom panel is a fit from the orbital solution.

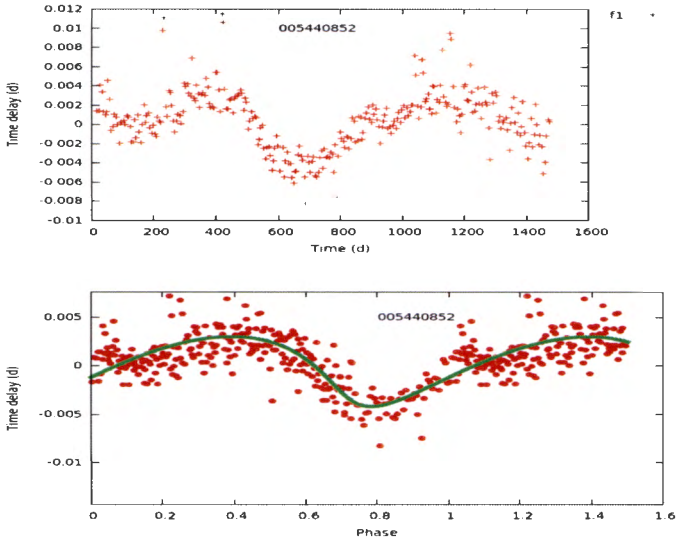

Figure A.31: Time-delay curve (top panel) of KIC 5440852 for the pulsation frequency of highest amplitude and the corresponding orbital phase plot (bottom panel). The solid line in the bottom panel is a fit from the orbital solution.

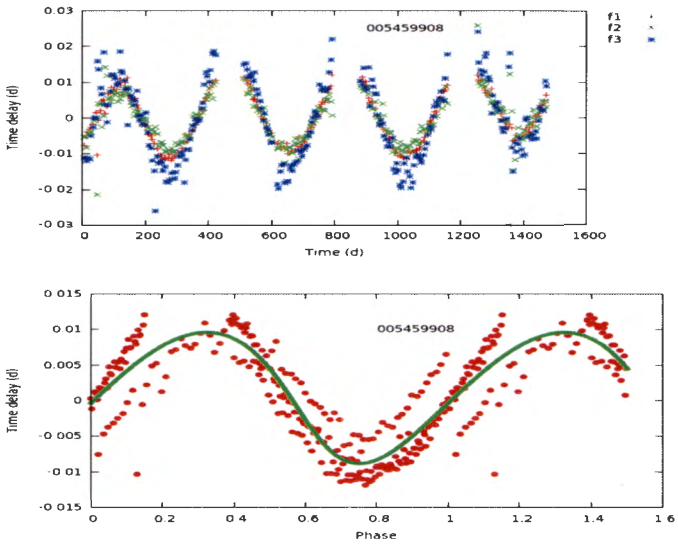

Figure A.32: Time-delay curve (top panel) of KIC 5459908 for the three pulsation frequencies of highest amplitudes and the corresponding orbital phase plot (bottom panel). The solid line in the bottom panel is from the orbital solution.

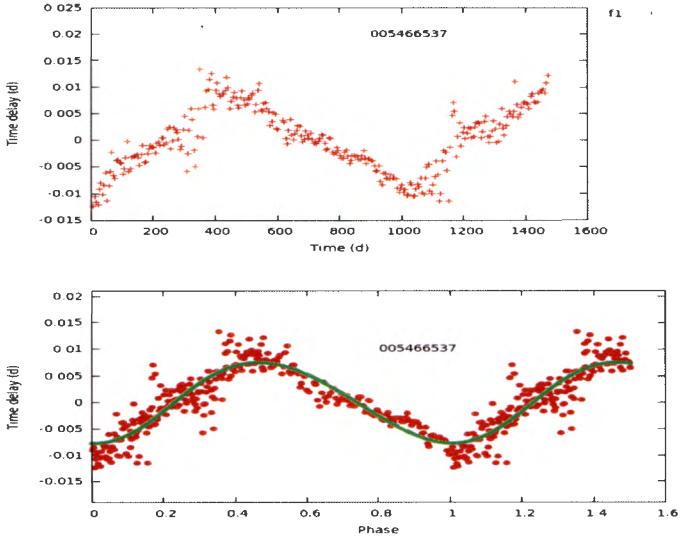

Figure A.33: Time-delay curve (top panel) of KIC 5466537 for the pulsation frequency of highest amplitude and the corresponding orbital phase plot (bottom panel). The solid line in the bottom panel is a fit from the orbital solution.

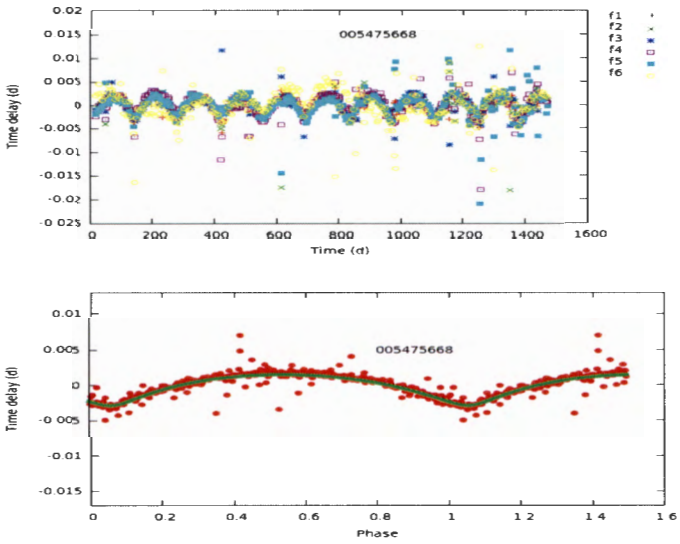

Figure A.34: Time-delay curve (top panel) of KIC 5475668 for the six pulsation frequencies of highest amplitudes and the corresponding orbital phase plot (bottom panel). The solid line in the bottom panel is a fit from the orbital solution.

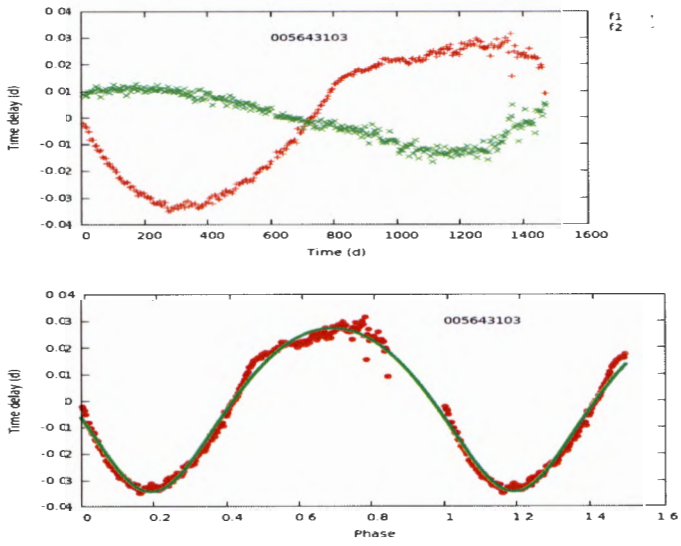

Figure A.35: Time-delay curve (top panel) of KIC 5643103 for the two pulsation frequencies of highest amplitudes and the corresponding orbital phase plot (bottom panel). The solid line in the bottom panel is a fit from the orbital solution.

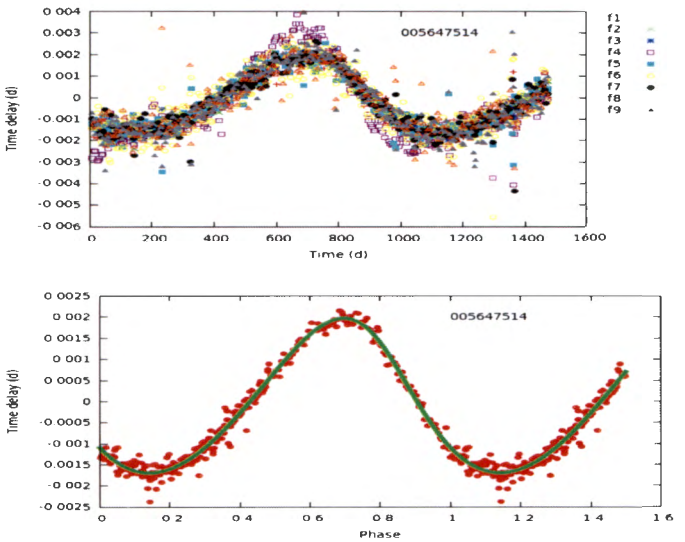

Figure A.36: Time-delay curve (top panel) of KIC 5647514 for the nine pulsation frequencies of highest amplitudes and the corresponding orbital phase plot (bottom panel). The solid line in the bottom panel is a fit from the orbital solution.

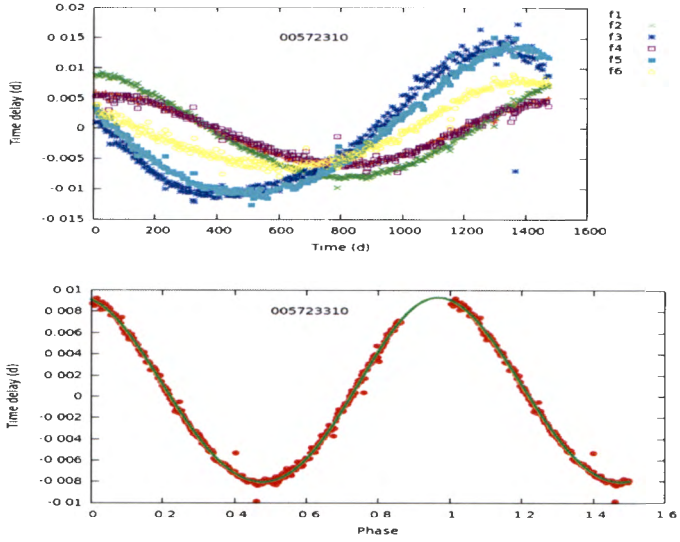

Figure A.37: Time-delay curve (top panel) of KIC 5723310 for the six pulsation frequencies of highest amplitudes and the corresponding orbital phase plot (bottom panel). The solid line in the bottom panel is a fit from the orbital solution.

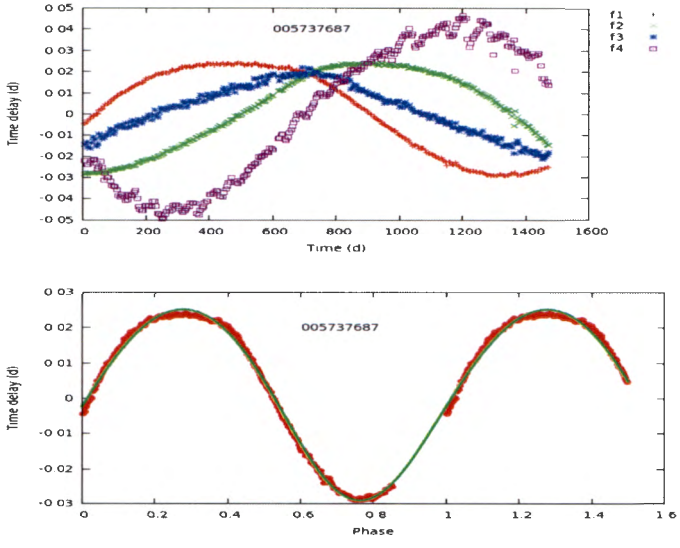

Figure A.38: Time-delay curve (top panel) of KIC 5737687 for the four pulsation frequencies of highest amplitudes and the corresponding orbital phase plot (bottom panel). The solid line in the bottom panel is a fit from the orbital solution.

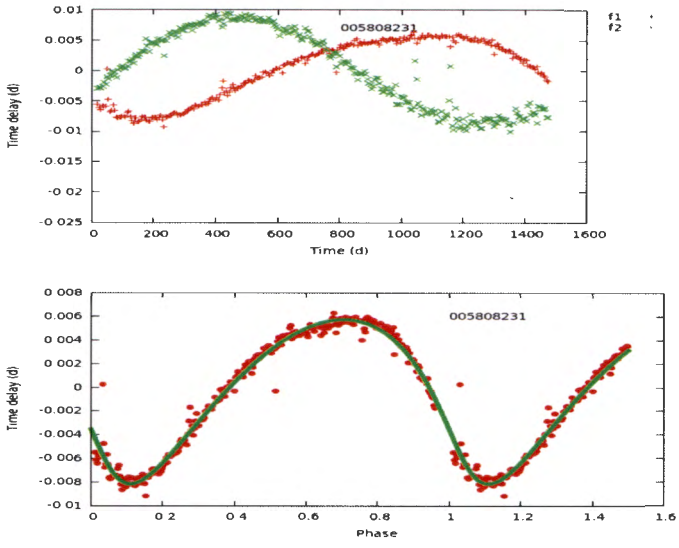

Figure A.39: Time-delay curve (top panel) of KIC 5808231 for the two pulsation frequencies of highest amplitudes and the corresponding orbital phase plot (bottom panel). The solid line in the bottom panel is a fit from the orbital solution.

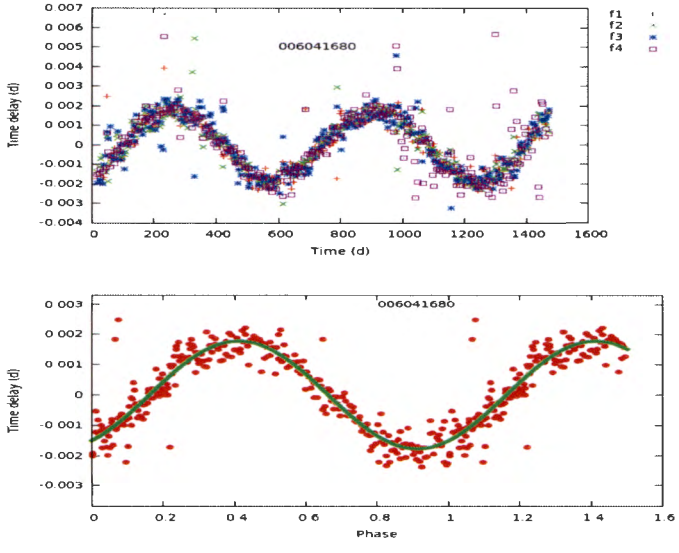

Figure A.40: Time-delay curve (top panel) of KIC 6041680 for the four pulsation frequencies of highest amplitudes and the corresponding orbital phase plot (bottom panel). The solid line in the bottom panel is a fit from the orbital solution.

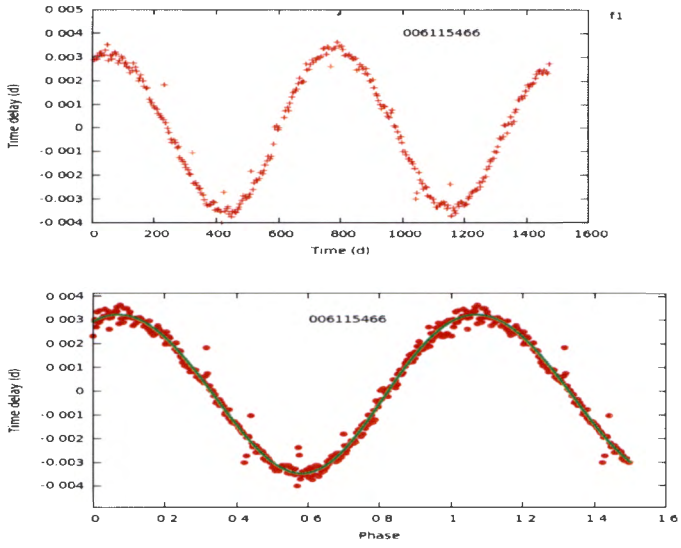

Figure A.41: Time-delay curve (top panel) of KIC 6115466 for the pulsation frequency of highest amplitude and the corresponding orbital phase plot (bottom panel). The solid line in the bottom panel is a fit from the orbital solution.

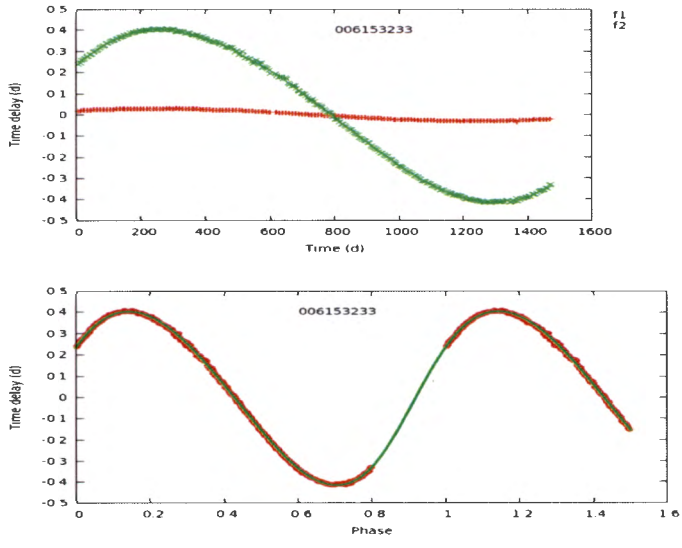

Figure A.42: Time-delay curve (top panel) of KIC 6153233 for the two pulsation frequencies of highest amplitudes and the corresponding orbital phase plot (bottom panel). The solid line in the bottom panel is a fit from the orbital solution.

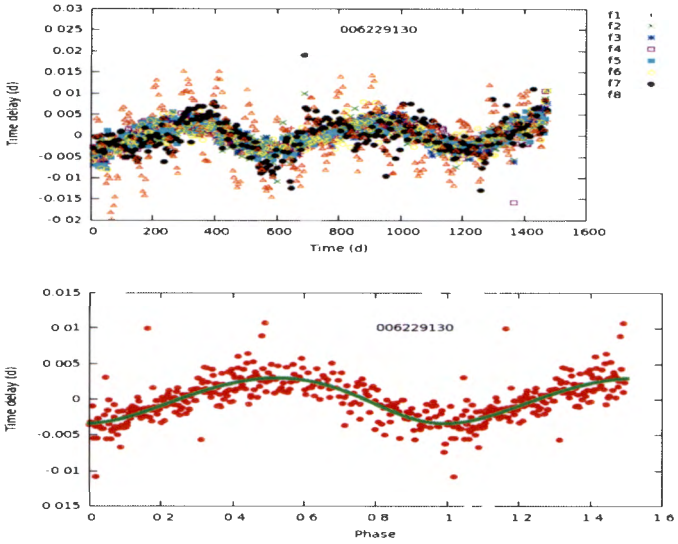

Figure A.43: Time-delay curve (top panel) of KIC 6229130 for the eight pulsation frequencies of highest amplitudes and the corresponding orbital phase plot (bottom panel). The solid line in the bottom panel is a fit from the orbital solution.

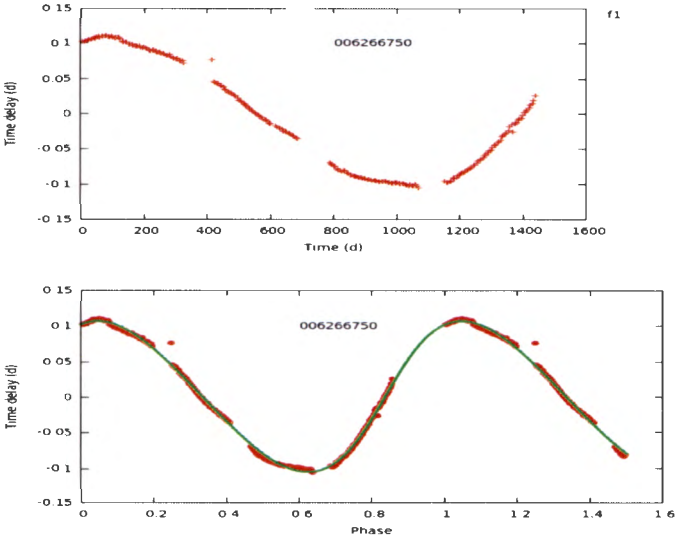

Figure A.44: Time-delay curve (top panel) of KIC 6266750 for the pulsation frequency of highest amplitude and the corresponding orbital phase plot (bottom panel). The solid line in the bottom panel is a fit from the orbital solution.

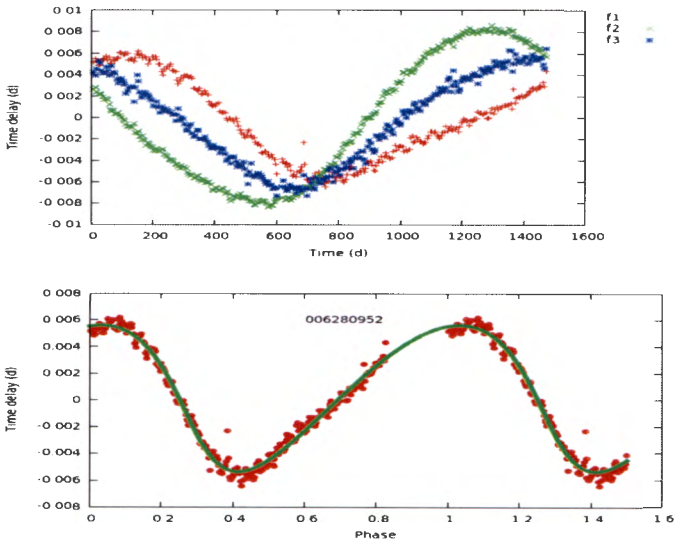

Figure A.45: Time-delay curve (top panel) of KIC 6280952 for the three pulsation frequencies of highest amplitudes and the corresponding orbital phase plot (bottom panel). The solid line in the bottom panel is a fit from the orbital solution.

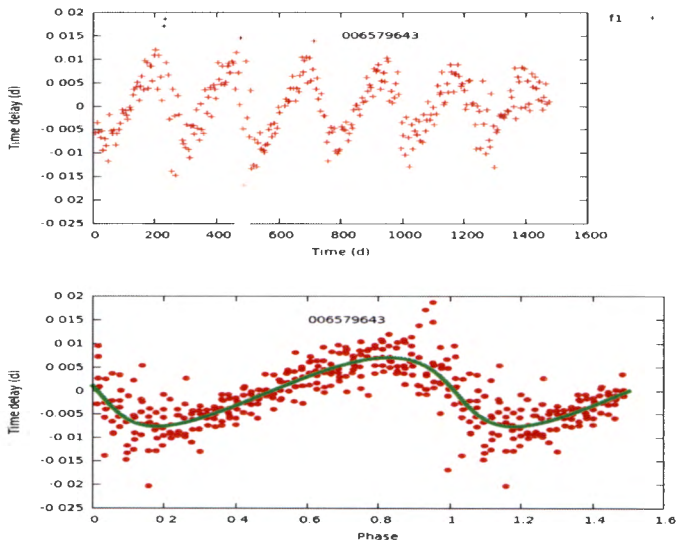

Figure A.46: Time-delay curve (top panel) of KIC 6579643 for the pulsation frequency of highest amplitude and the corresponding orbital phase plot (bottom panel). The solid line in the bottom panel is a fit from the orbital solution.

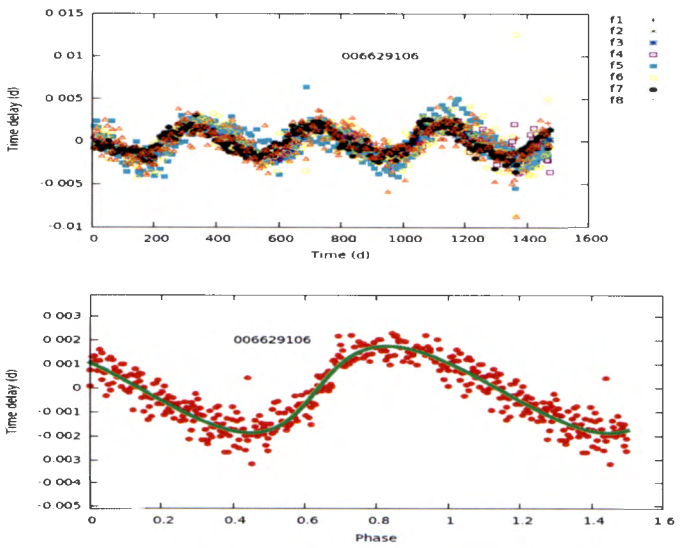

Figure A.47: Time-delay curve (top panel) of KIC 6629106 for the eight pulsation frequencies of highest amplitudes and the corresponding orbital phase plot (bottom panel). The solid line in the bottom panel is a fit from the orbital solution.

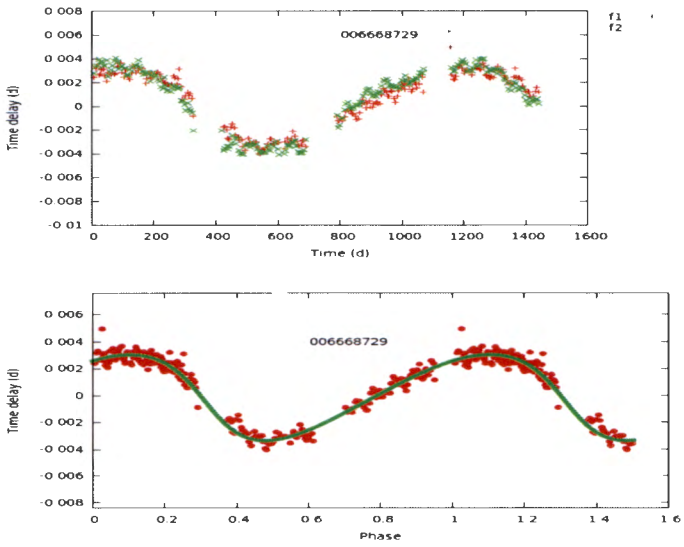

Figure A.48: Time-delay curve (top panel) of KIC 6668729 for the two pulsation frequencies of highest amplitudes and the corresponding orbital phase plot (bottom panel). The solid line in the bottom panel is a fit from the orbital solution.

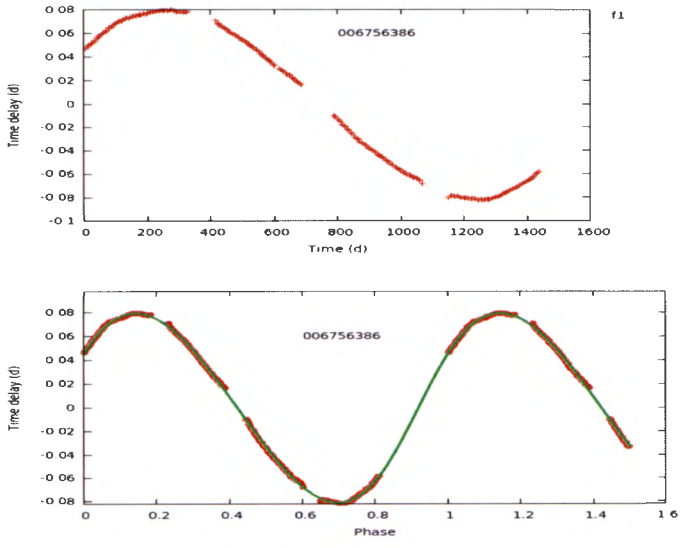

Figure A.49: Time-delay curve (top panel) of KIC 6756386 for the pulsation frequency of highest amplitude and the corresponding orbital phase plot (bottom panel). The solid line in the bottom panel is a fit from the orbital solution.

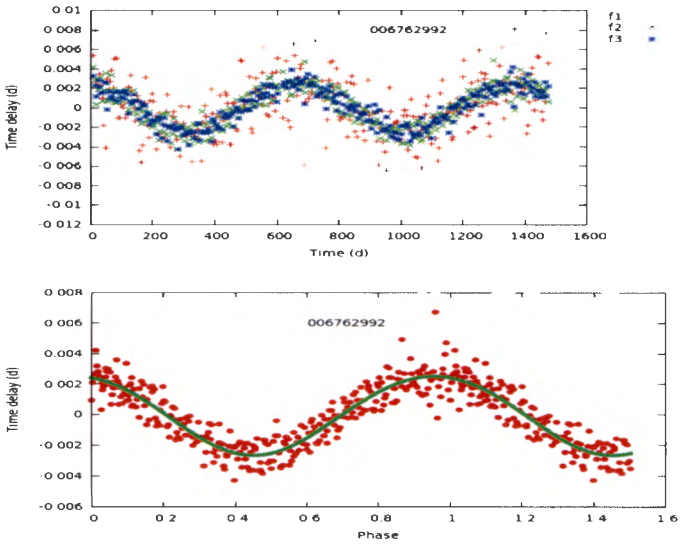

Figure A.50: Time-delay curve (top panel) of KIC 6762992 for the three pulsation frequencies of highest amplitudes and the corresponding orbital phase plot (bottom panel). The solid line in the bottom panel is a fit from the orbital solution.

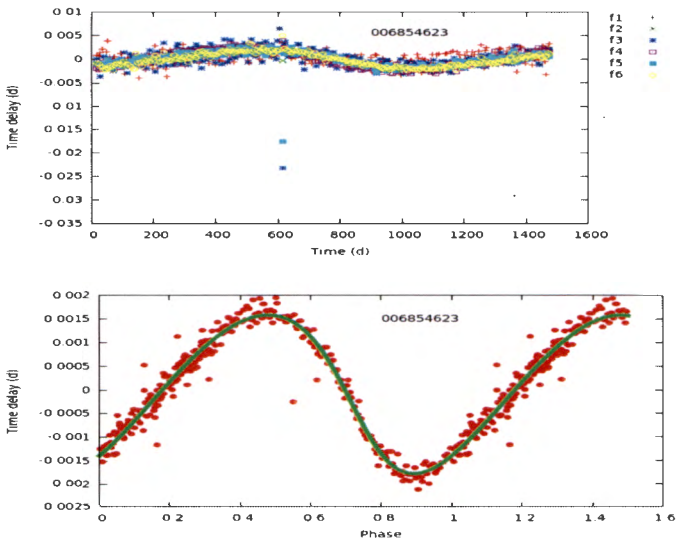

Figure A.51: Time-delay curve (top panel) of KIC 6854623 for the six pulsation frequencies of highest amplitudes and the corresponding orbital phase plot (bottom panel). The solid line in the bottom panel is a fit from the orbital solution.

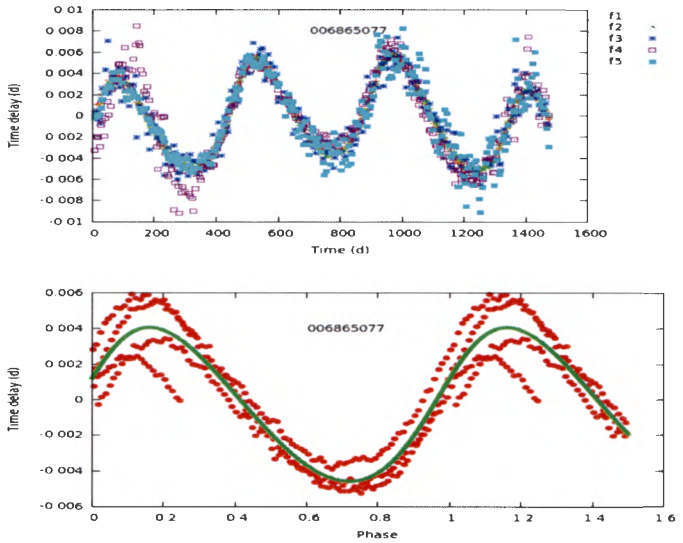

Figure A.52: Time-delay curve (top panel) of KIC 6865077 for the five pulsation frequencies of highest amplitudes and the corresponding orbital phase plot (bottom panel). The solid line in the bottom panel is a fit from the orbital solution.

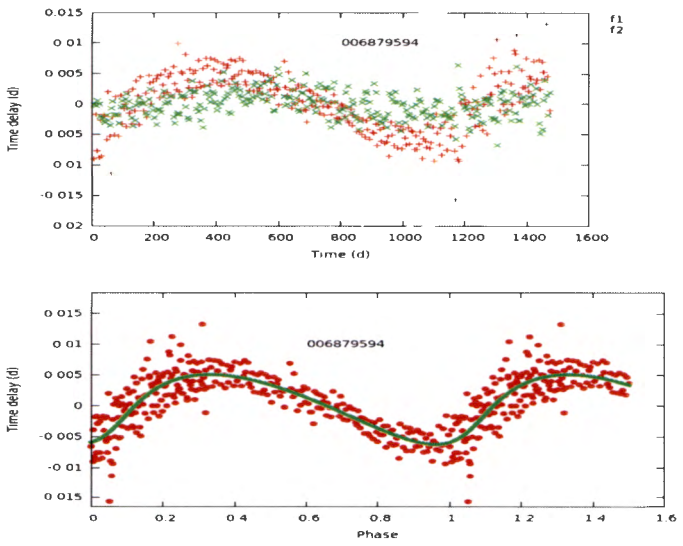

Figure A.53: Time-delay curve (top panel) of KIC 6879594 for the two pulsation frequencies of highest amplitudes and the corresponding orbital phase plot (bottom panel). The solid line in the bottom panel is a fit from the orbital solution.

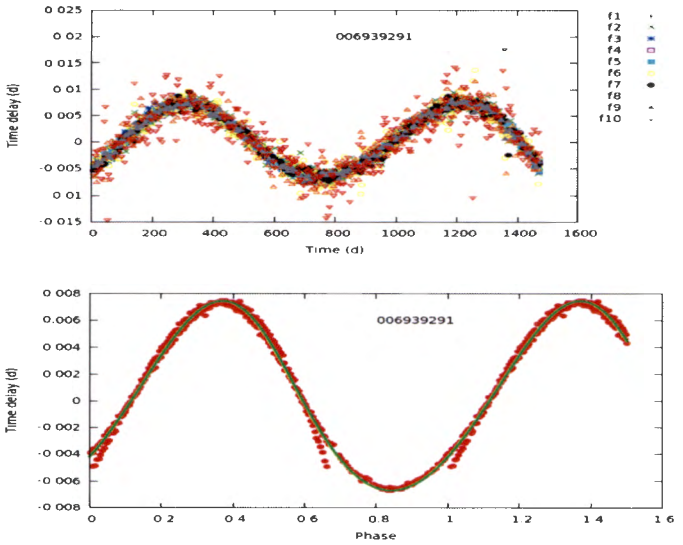

Figure A.54: Time-delay curve (top panel) of KIC 6939291 for the ten pulsation frequencies of highest amplitudes and the corresponding orbital phase plot (bottom panel). The solid line in the bottom panel is a fit from the orbital solution.

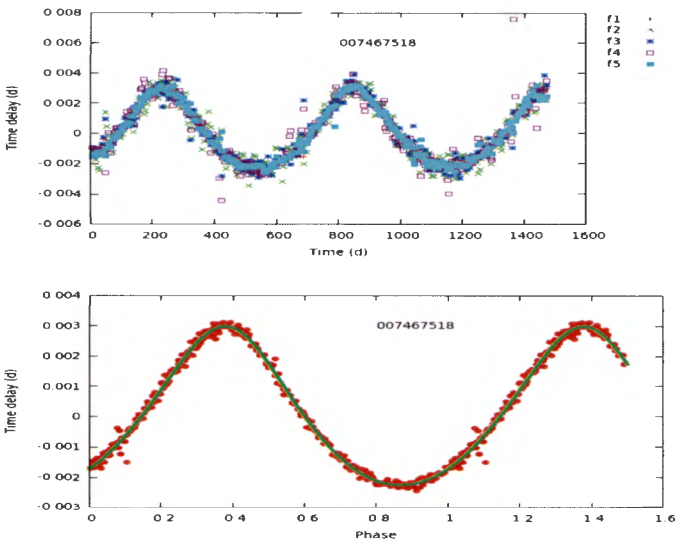

Figure A.55: Time-delay curve (top panel) of KIC 7465518 for the five pulsation frequencies of highest amplitudes and the corresponding orbital phase plot (bottom panel). The solid line in the bottom panel is a fit from the orbital solution.

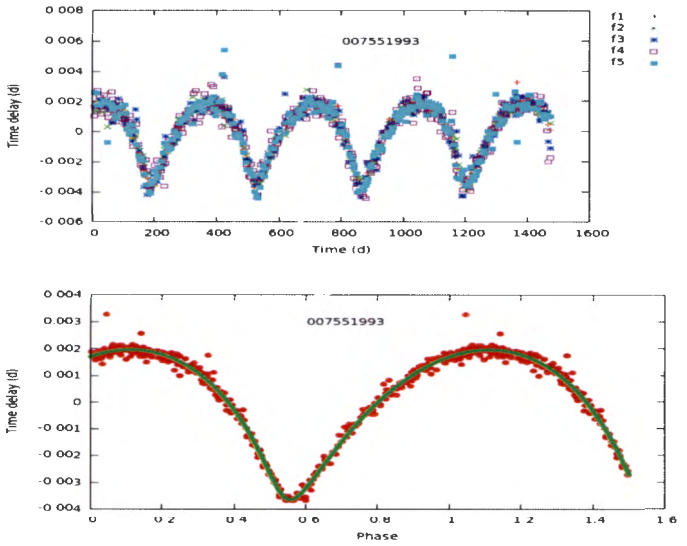

Figure A.56: Time-delay curve (top panel) of KIC 7551993 for the five pulsation frequencies of highest amplitudes and the corresponding orbital phase plot (bottom panel). The solid line in the bottom panel is a fit from the orbital solution.

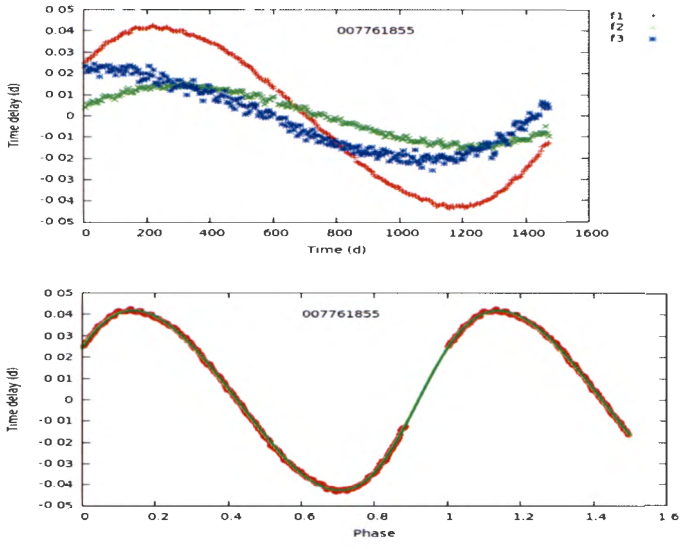

Figure A.57: Time-delay curve (top panel) of KIC 7761855 for the three pulsation frequencies of highest amplitudes and the corresponding orbital phase plot (bottom panel). The solid line in the bottom panel is from the orbital solution.

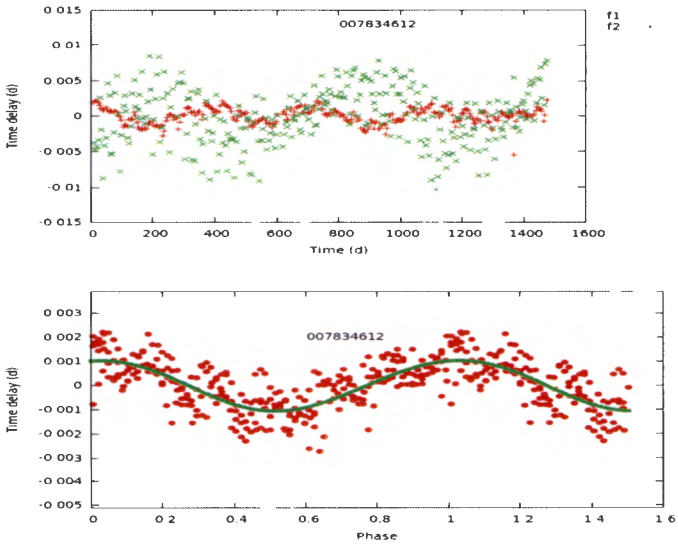

Figure A.58: Time-delay curve (top panel) of KIC 7834612 for the two pulsation frequencies of highest amplitudes and the corresponding orbital phase plot (bottom panel). The solid line in the bottom panel is a fit from the orbital solution.

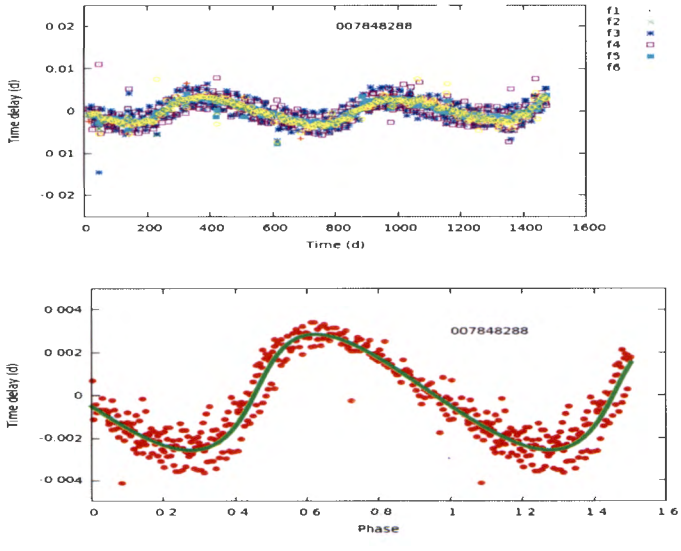

Figure A.59: Time-delay curve (top panel) of KIC 7848288 for the six pulsation frequencies of highest amplitudes and the corresponding orbital phase plot (bottom panel). The solid line in the bottom panel is a fit from the orbital solution.

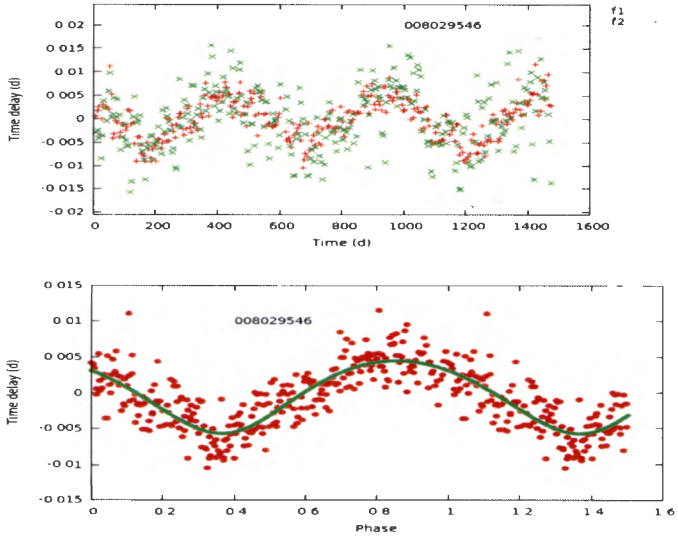

Figure A.60: Time-delay curve (top panel) of KIC 8029546 for the two pulsation frequencies of highest amplitudes and the corresponding orbital phase plot (bottom panel). The solid line in the bottom panel is a fit from the orbital solution.

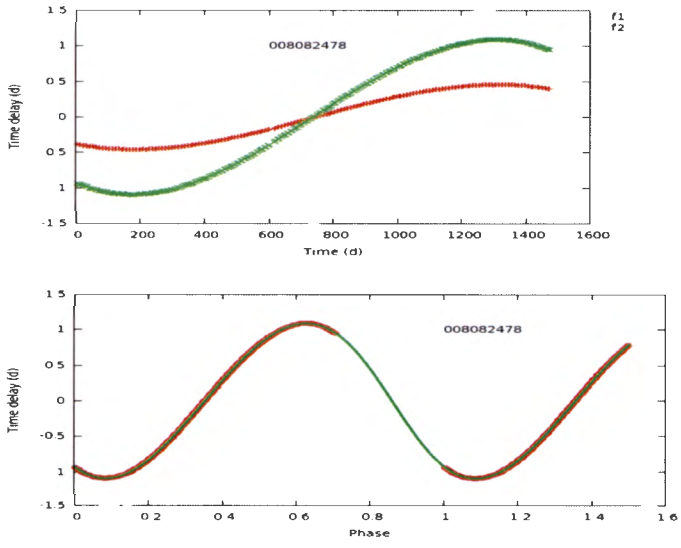

Figure A.61: Time-delay curve (top panel) of KIC 8082478 for the two pulsation frequencies of highest amplitudes and the corresponding orbital phase plot (bottom panel). The solid line in the bottom panel is a fit from the orbital solution.

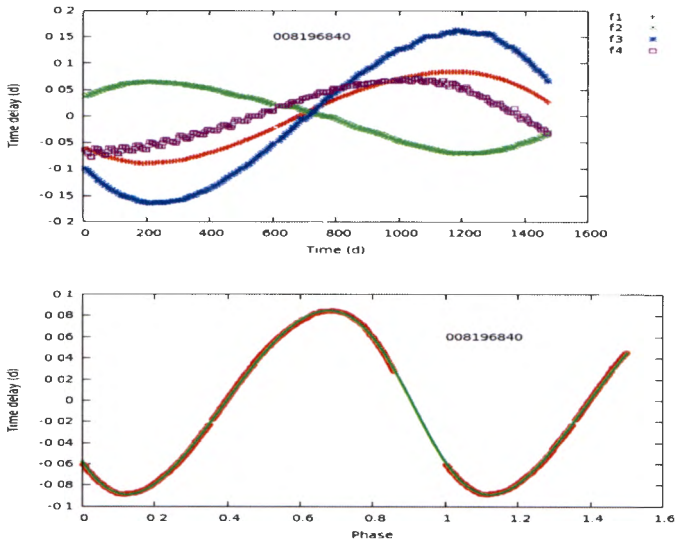

Figure A.62: Time-delay curve (top panel) of KIC 8196840 for the four pulsation frequencies of highest amplitudes and the corresponding orbital phase plot (bottom panel). The solid line in the bottom panel is a fit from the orbital solution.

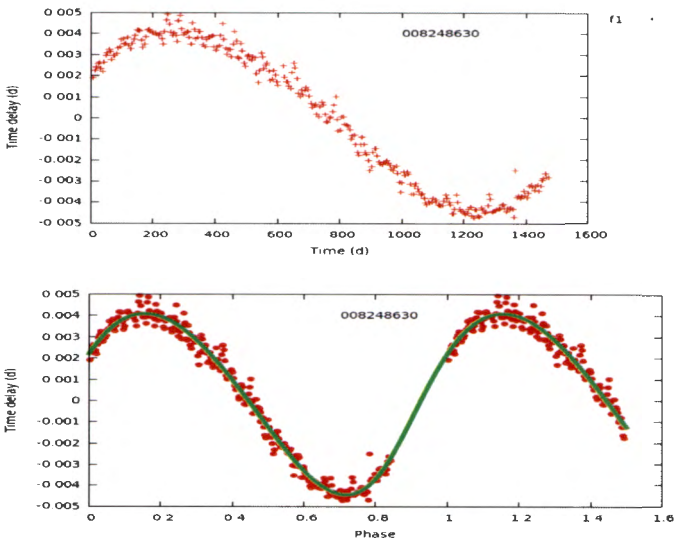

Figure A.63: Time-delay curve (top panel) of KIC 8248630 for the pulsation frequency of highest amplitude and the corresponding orbital phase plot (bottom panel). The solid line in the bottom panel is a fit from the orbital solution.

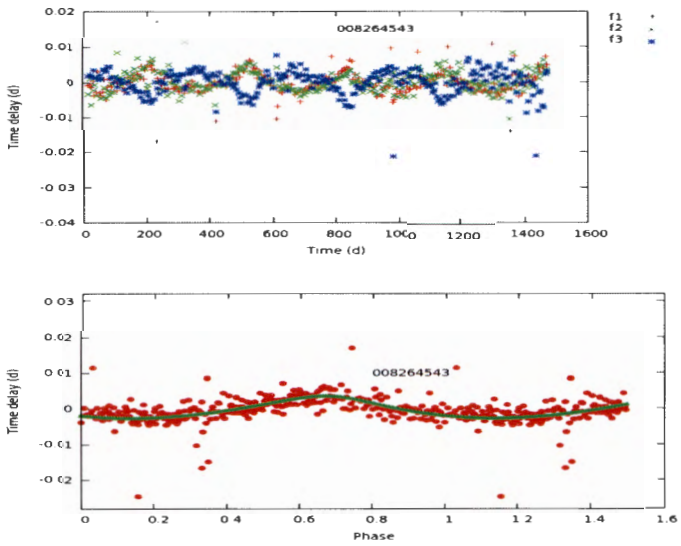

Figure A.64: Time-delay curve (top panel) of KIC 8264543 for the three pulsation frequencies of highest amplitudes and the corresponding orbital phase plot (bottom panel). The solid line in the bottom panel is a fit from the orbital solution.

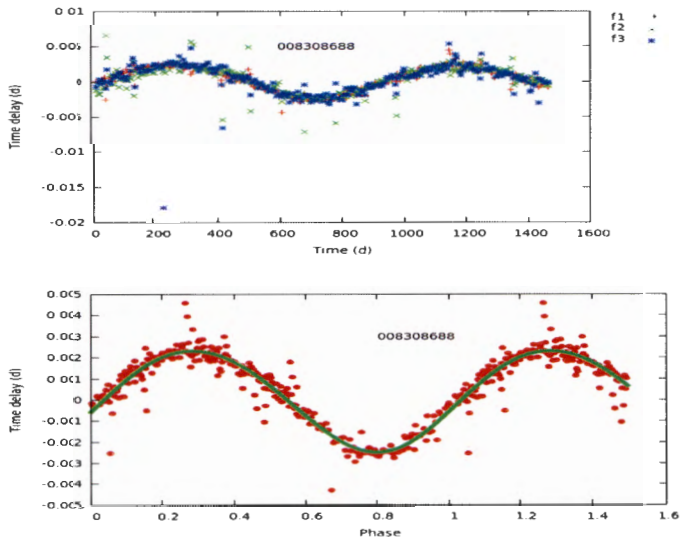

Figure A.65: Time-delay curve (top panel) of KIC 8308688 for the three pulsation frequencies of highest amplitudes and the corresponding orbital phase plot (bottom panel). The solid line in the bottom panel is a fit from the orbital solution.

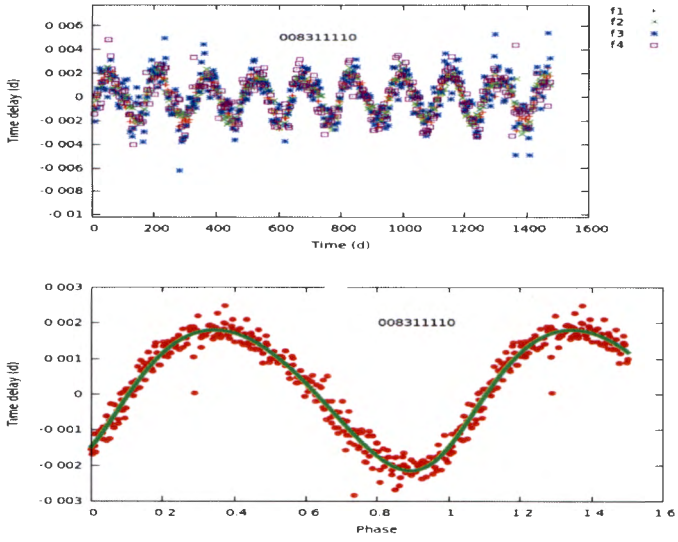

Figure A.66: Time-delay curve (top panel) of KIC 8311110 for the four pulsation frequencies of highest amplitudes and the corresponding orbital phase plot (bottom panel). The solid line in the bottom panel is a fit from the orbital solution.

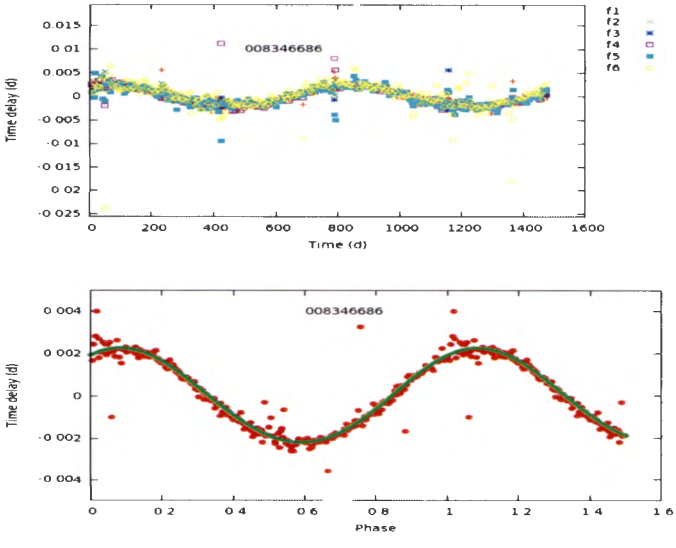

Figure A.67: Time-delay curve (top panel) of KIC 8346686 for the six pulsation frequencies of highest amplitudes and the corresponding orbital phase plot (bottom panel). The solid line in the bottom panel is a fit from the orbital solution.

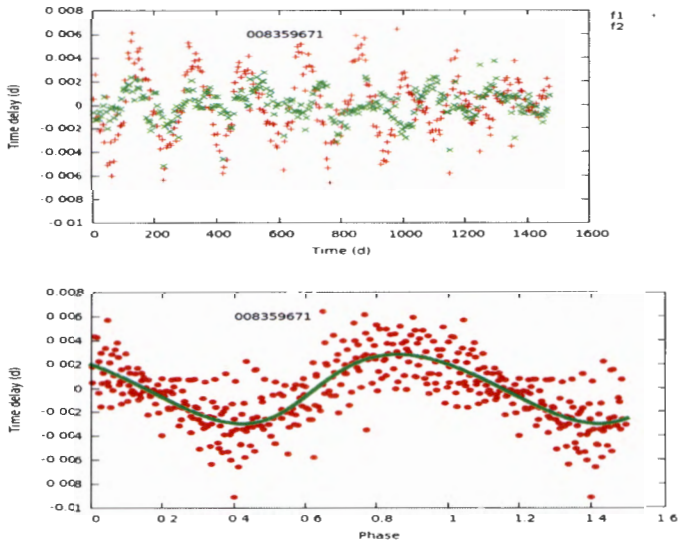

Figure A.68: Time-delay curve (top panel) of KIC 8359671 for the two pulsation frequencies of highest amplitudes and the corresponding orbital phase plot (bottom panel). The solid line in the bottom panel is a fit from the orbital solution.

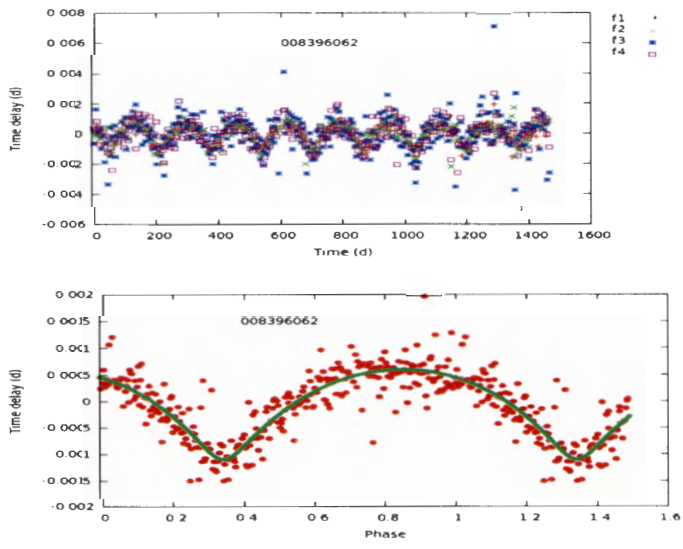

Figure A.69: Time-delay curve (top panel) of KIC 8396062 for the four pulsation frequencies of highest amplitudes and the corresponding orbital phase plot (bottom panel). The solid line in the bottom panel is a fit from the orbital solution.

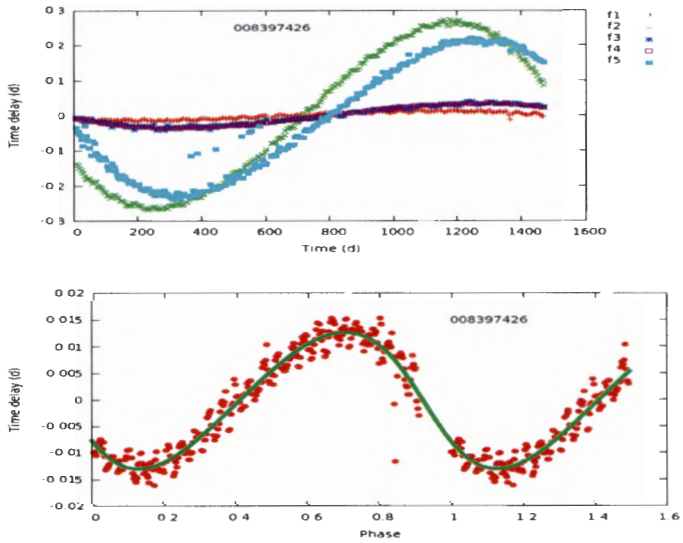

Figure A.70: Time-delay curve (top panel) of KIC 8397426 for the five pulsation frequencies of highest amplitudes and the corresponding orbital phase plot (bottom panel). The solid line in the bottom panel is a fit from the orbital solution.

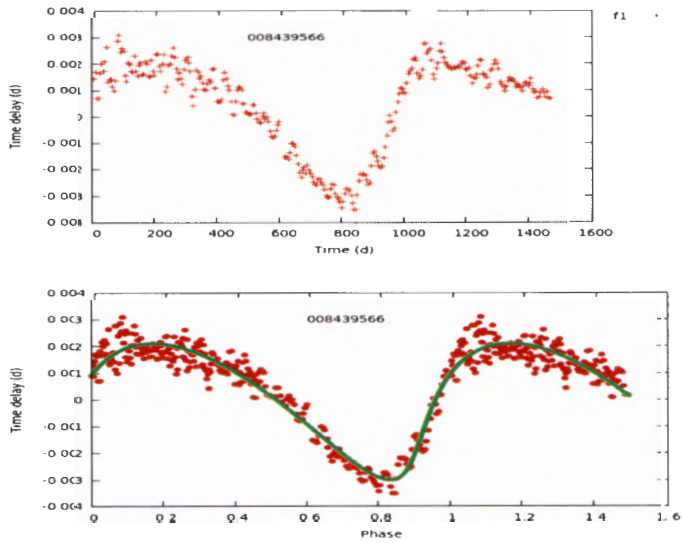

Figure A.71: Time-delay curve (top panel) of KIC 8439566 for the pulsation frequency of highest amplitude and the corresponding orbital phase plot (bottom panel). The solid line in the bottom panel is a fit from the orbital solution.

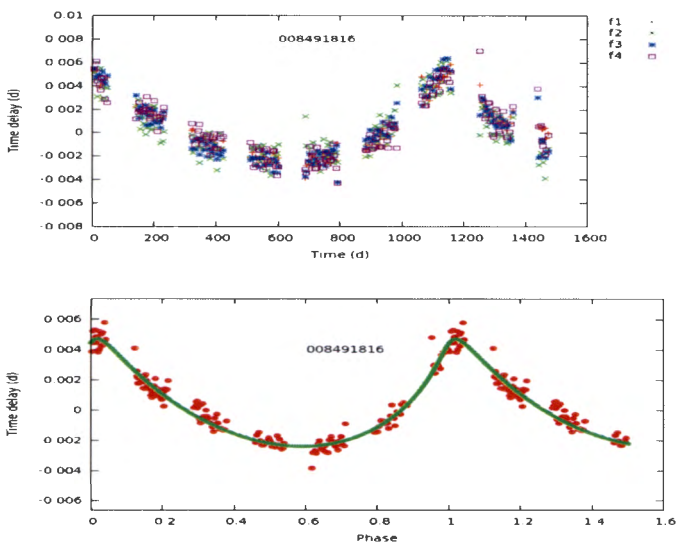

Figure A.72: Time-delay curve (top panel) of KIC 8491816 for the four pulsation frequencies of highest amplitude and the corresponding orbital phase plot (bottom panel). The solid line in the bottom panel is a fit from the orbital solution.

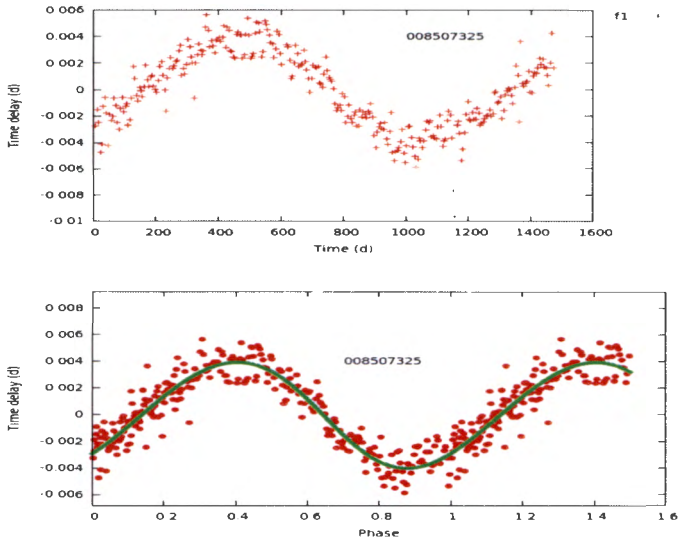

Figure A.73: Time-delay curve (top panel) of KIC 8507325 for the pulsation frequency of highest amplitude and the corresponding orbital phase plot (bottom panel). The solid line in the bottom panel is a fit from the orbital solution.

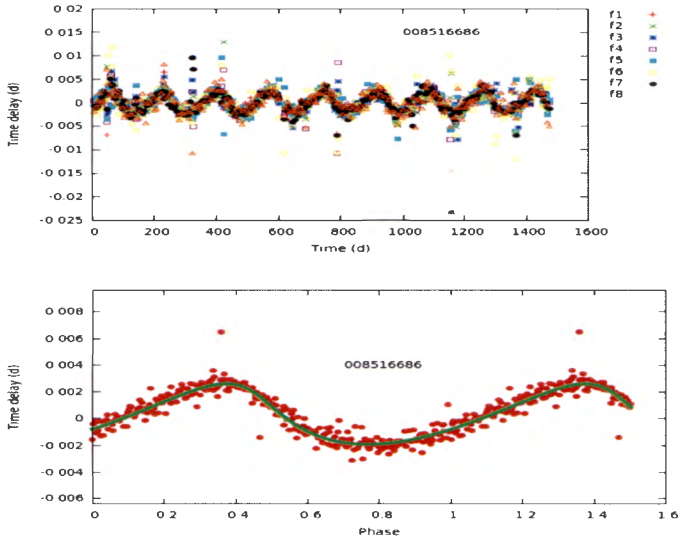

Figure A.74: Time-delay curve (top panel) of KIC 8516686 for the eight pulsation frequencies of highest amplitudes and the corresponding orbital phase plot (bottom panel). The solid line in the bottom panel is a fit from the orbital solution.

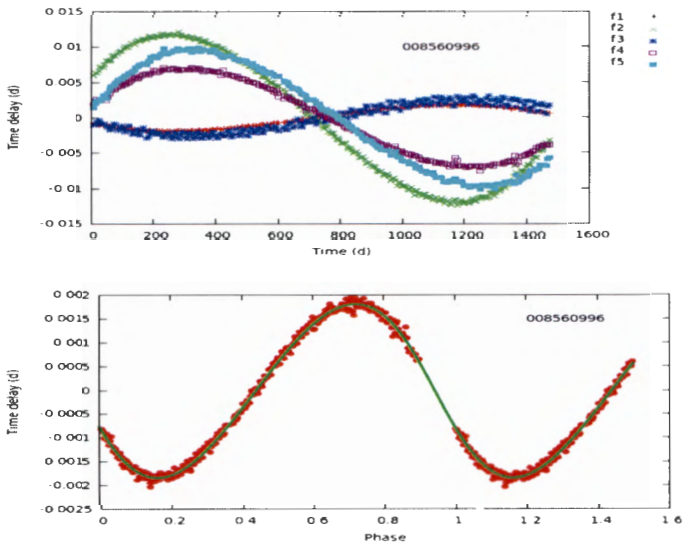

Figure A.75: Time-delay curve (top panel) of KIC 8560996 for the five pulsation frequencies of highest amplitudes and the corresponding orbital phase plot (bottom panel). The solid line in the bottom panel is a fit from the orbital solution.

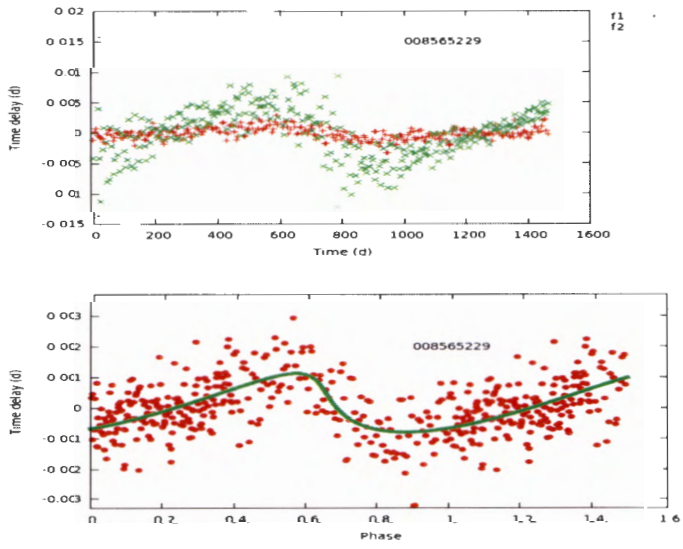

Figure A.76: Time-delay curve (top panel) of KIC 8565229 for the two pulsation frequencies of highest amplitudes and the corresponding orbital phase plot (bottom panel). The solid line in the bottom panel is a fit from the orbital solution.

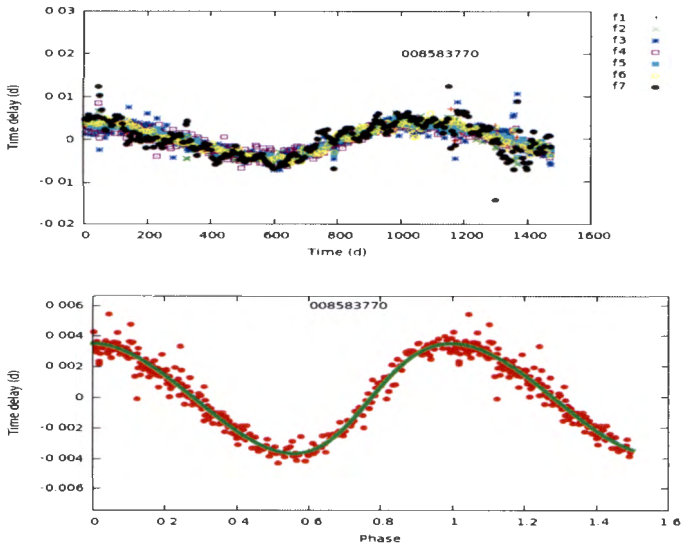

Figure A.77: Time-delay curve (top panel) of KIC 8583770 for the seven pulsation frequencies of highest amplitudes and the corresponding orbital phase plot (bottom panel). The solid line in the bottom panel is a fit from the orbital solution.

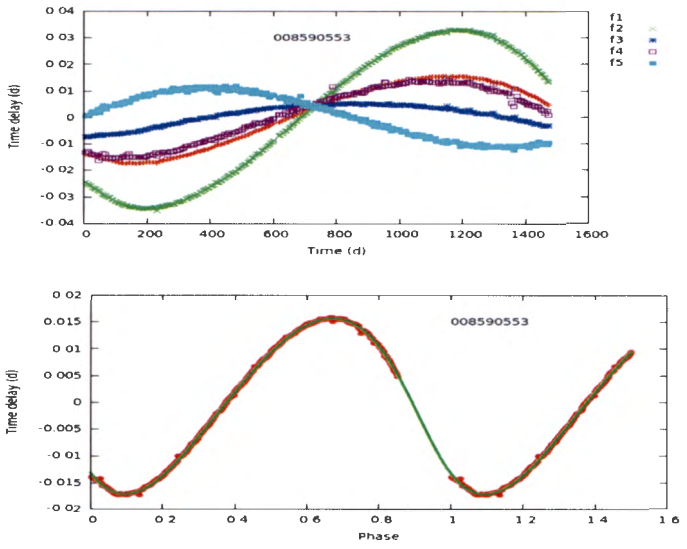

Figure A.78: Time-delay curve (top panel) of KIC 8590553 for the five pulsation frequencies of highest amplitudes and the corresponding orbital phase plot (bottom panel). The solid line in the bottom panel is a fit from the orbital solution.

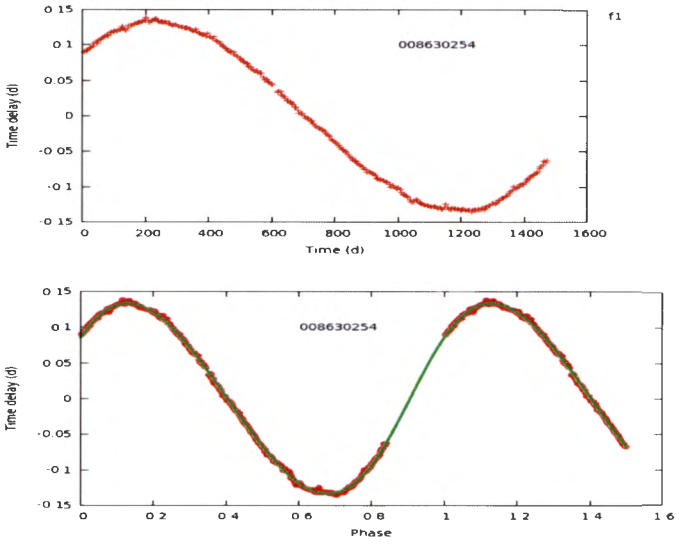

Figure A.79: Time-delay curve (top panel) of KIC 8630254 for the pulsation frequency of highest amplitude and the corresponding orbital phase plot (bottom panel). The solid line in the bottom panel is a fit from the orbital solution.

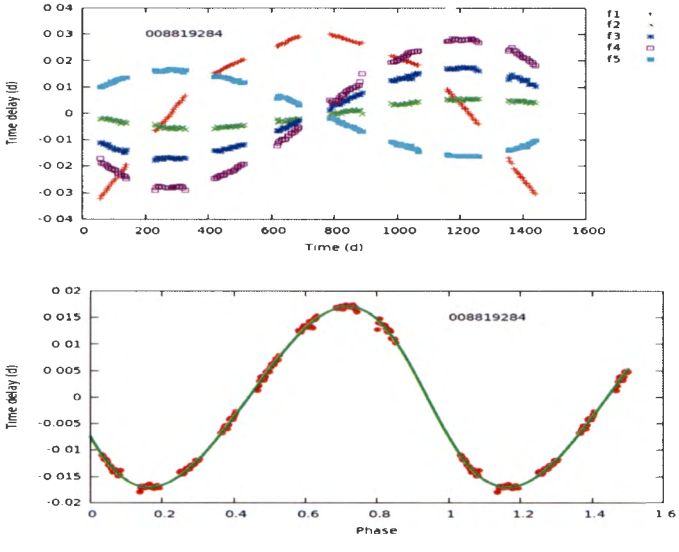

Figure A.80: Time-delay curve (top panel) of KIC 8819284 for the five pulsation frequencies of highest amplitudes and the corresponding orbital phase plot (bottom panel). The solid line in the bottom panel is a fit from the orbital solution.

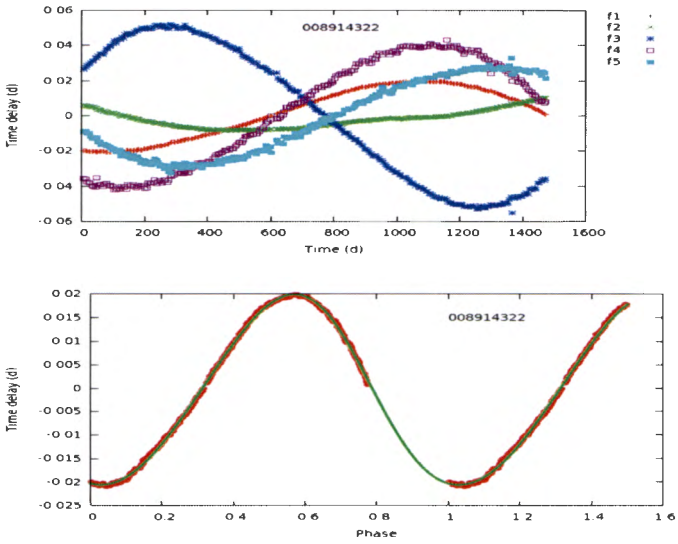

Figure A.81: Time-delay curve (top panel) of KIC 8914322 for the five pulsation frequencies of highest amplitudes and the corresponding orbital phase plot (bottom panel). The solid line in the bottom panel is a fit from the orbital solution.

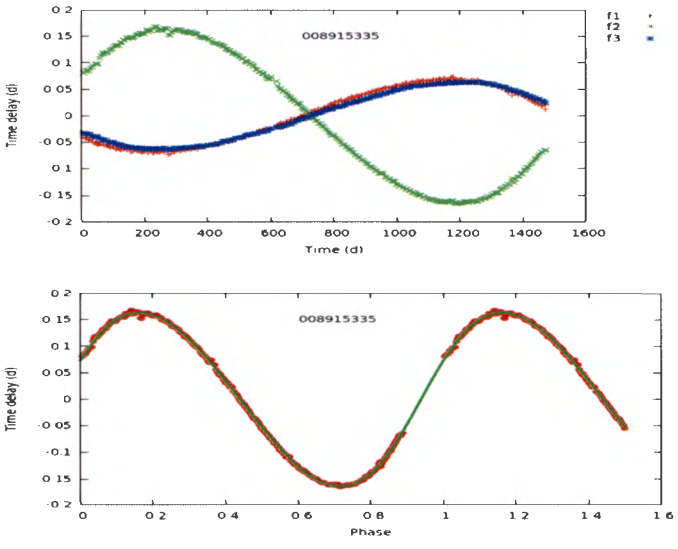

Figure A.82: Time-delay curve (top panel) of KIC 8915335 for the three pulsation frequencies of highest amplitudes and the corresponding orbital phase plot (bottom panel). The solid line in the bottom panel is a fit from the orbital solution.

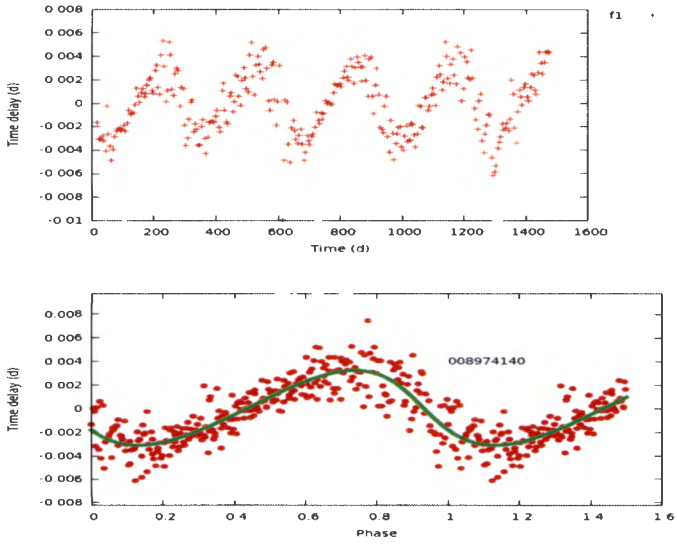

Figure A.83: Time-delay curve (top panel) of KIC 8974140 for the pulsation frequency of highest amplitude and the corresponding orbital phase plot (bottom panel). The solid line in the bottom panel is a fit from the orbital solution.

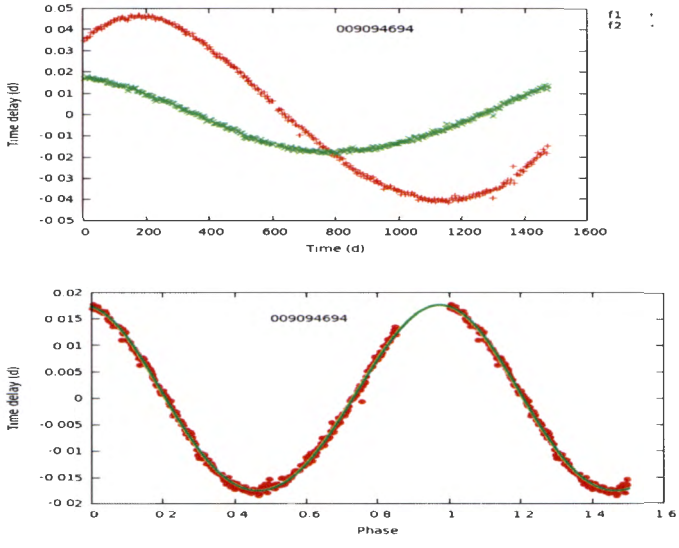

Figure A.84: Time-delay curve (top panel) of KIC 9094694 for the two pulsation frequencies of highest amplitudes and the corresponding orbital phase plot (bottom panel). The solid line in the bottom panel is a fit from the orbital solution.

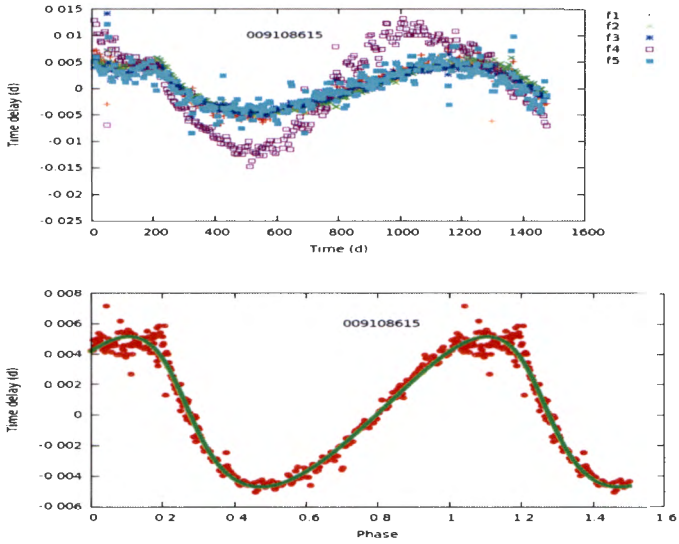

Figure A.85: Time-delay curve (top panel) of KIC 9108615 for the five pulsation frequencies of highest amplitudes and the corresponding orbital phase plot (bottom panel). The solid line in the bottom panel is a fit from the orbital solution.

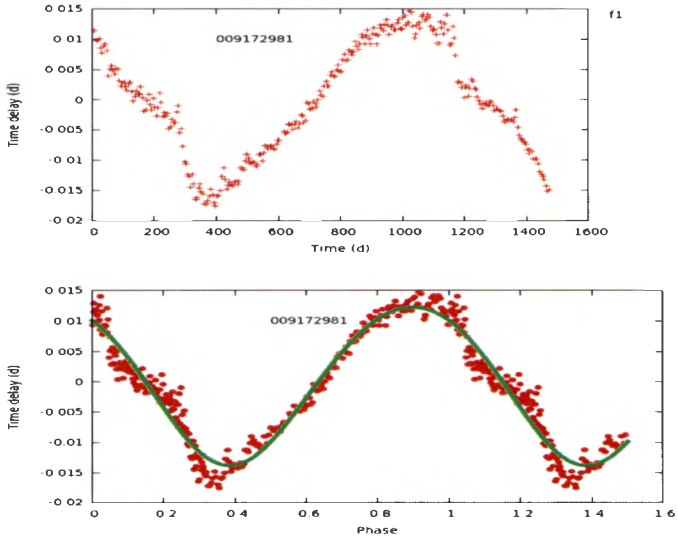

Figure A.86: Time-delay curve (top panel) of KIC 9172981 for the pulsation frequency of highest amplitude and the corresponding orbital phase plot (bottom panel). The solid line in the bottom panel is a fit from the orbital solution.

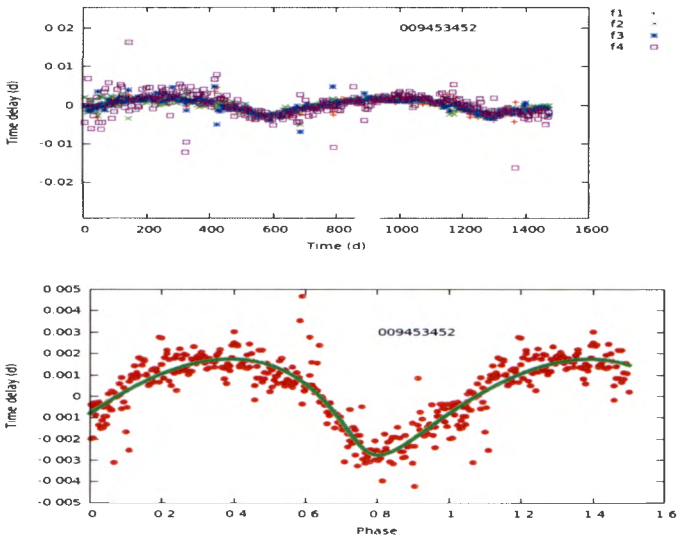

Figure A.87: Time-delay curve (top panel) of KIC 9453452 for the four pulsation frequencies of highest amplitudes and the corresponding orbital phase plot (bottom panel). The solid line in the bottom panel is a fit from the orbital solution.

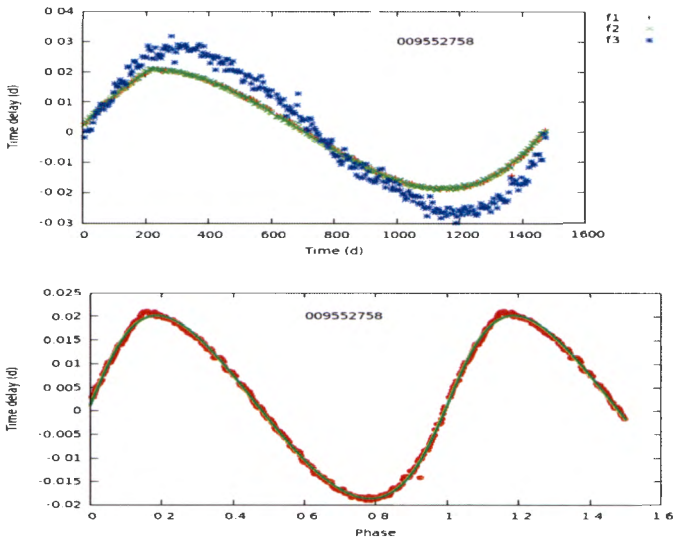

Figure A.88: Time-delay curve (top panel) of KIC 9552758 for the three pulsation frequencies of highest amplitudes and the corresponding orbital phase plot (bottom panel). The solid line in the bottom panel is a fit from the orbital solution.

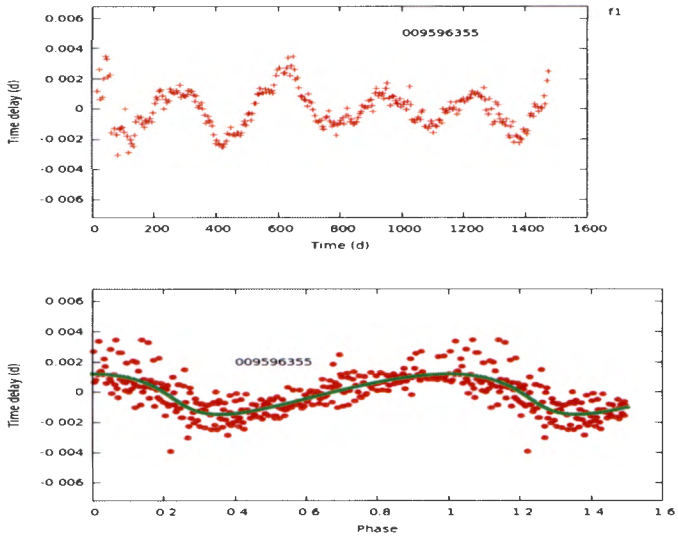

Figure A.89: Time-delay curve (top panel) of KIC 9596355 for the pulsation frequency of highest amplitude and the corresponding orbital phase plot (bottom panel). The solid line in the bottom panel is a fit from the orbital solution.

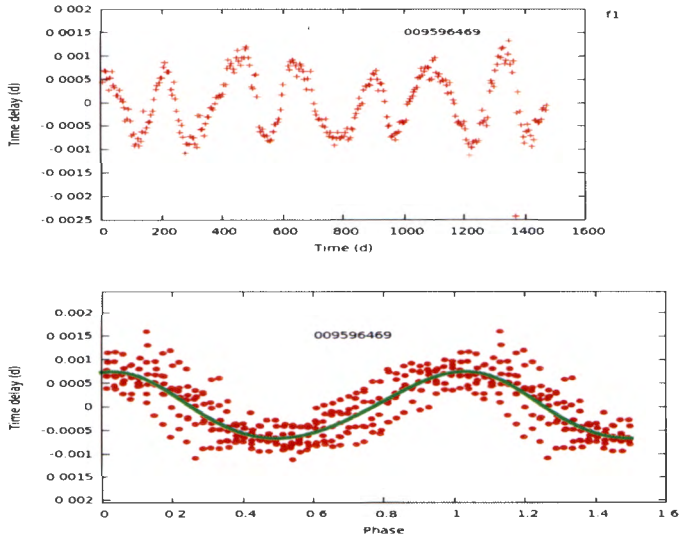

Figure A.90: Time-delay curve (top panel) of KIC 9596469 for the pulsation frequency of highest amplitude and the corresponding orbital phase plot (bottom panel). The solid line in the bottom panel is a fit from the orbital solution.

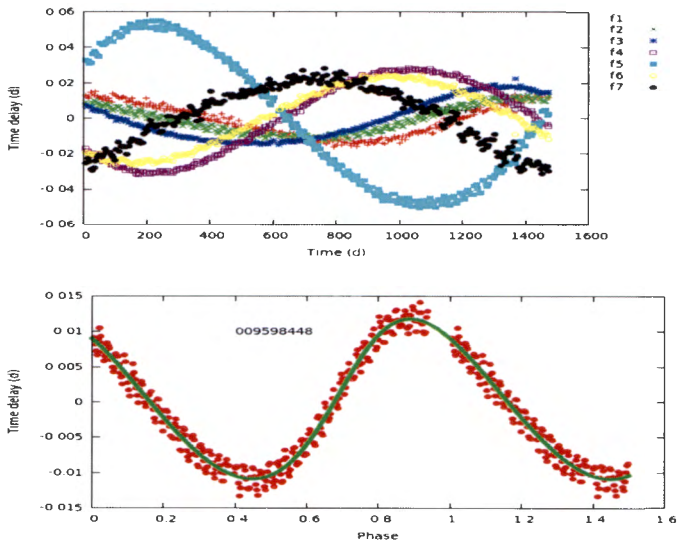

Figure A.91: Time-delay curve (top panel) of KIC 9598448 for the seven pulsation frequencies of highest amplitudes and the corresponding orbital phase plot (bottom panel). The solid line in the bottom panel is a fit from the orbital solution.

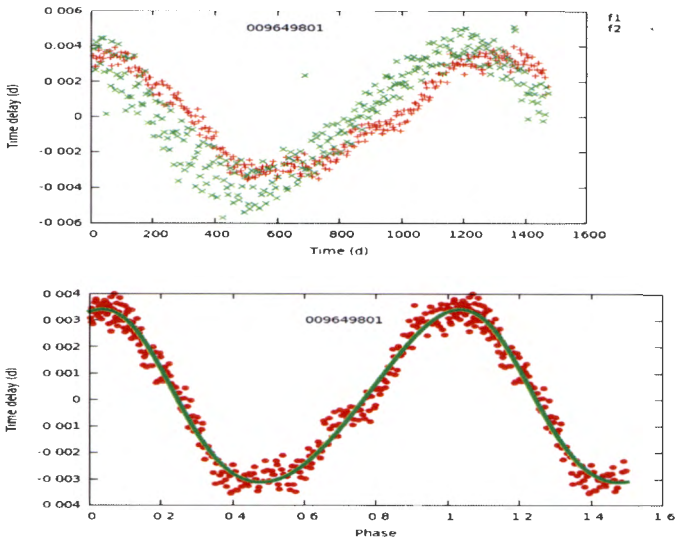

Figure A.92: Time-delay curve (top panel) of KIC 9649801 for the two pulsation frequencies of highest amplitudes and the corresponding orbital phase plot (bottom panel). The solid line in the bottom panel is a fit from the orbital solution.

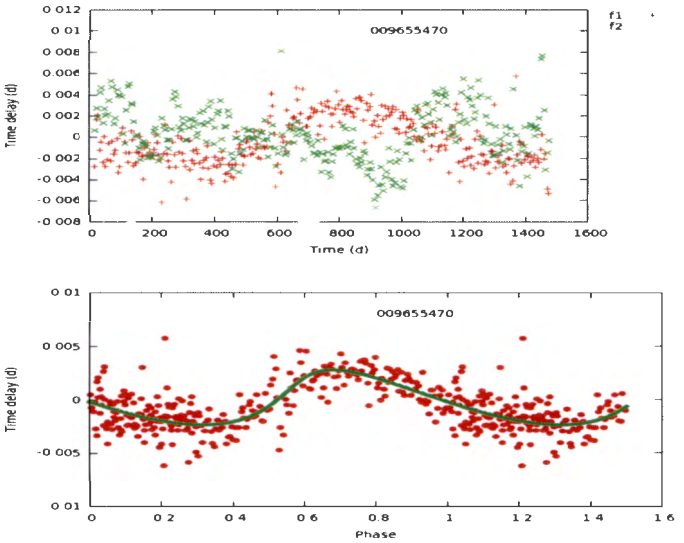

Figure A.93: Time-delay curve (top panel) of KIC 9655470 for the two pulsation frequencies of highest amplitudes and the corresponding orbital phase plot (bottom panel). The solid line in the bottom panel is a fit from the orbital solution.

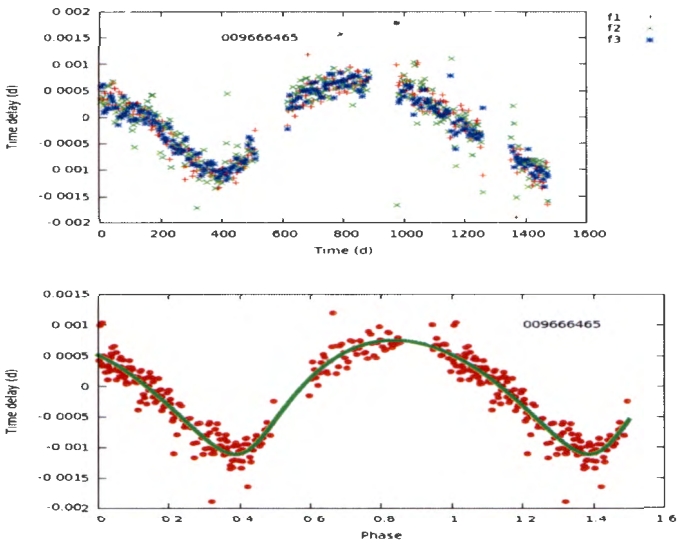

Figure A.94: Time-delay curve (top panel) of KIC 9666465 for the three pulsation frequencies of highest amplitudes and the corresponding orbital phase plot (bottom panel). The solid line in the bottom panel is a fit from the orbital solution.

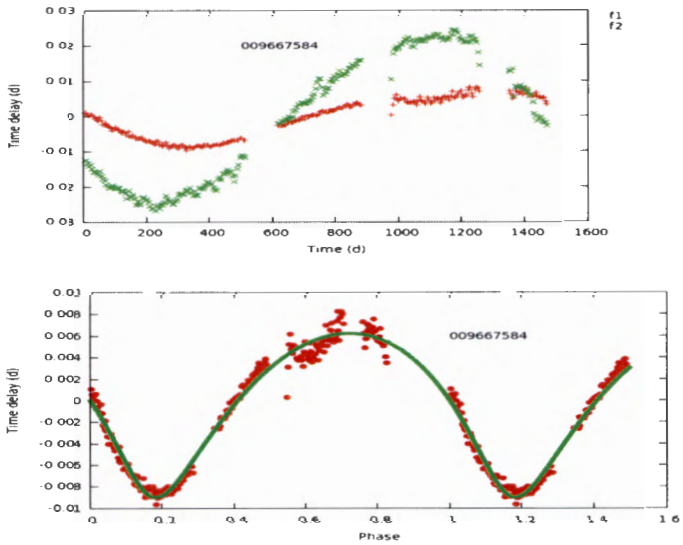

Figure A.95: Time-delay curve (top panel) of KIC 9667584 for the two pulsation frequencies of highest amplitudes and the corresponding orbital phase plot (bottom panel). The solid line in the bottom panel is a fit from the orbital solution.

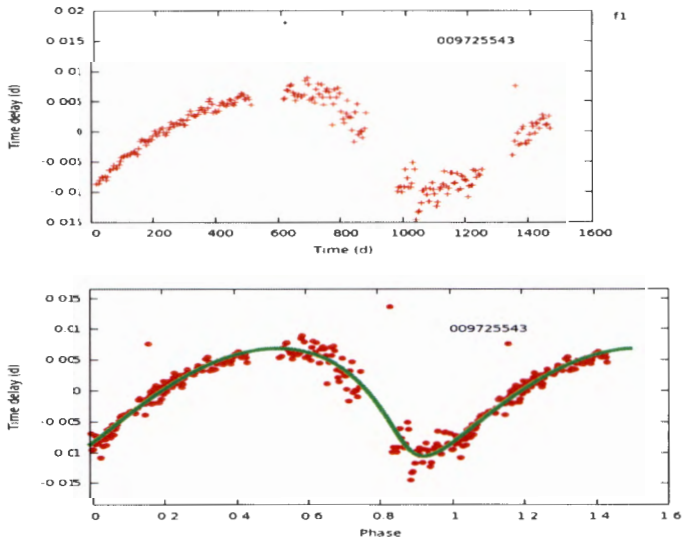

Figure A.96: Time-delay curve (top panel) of KIC 9725543 for the pulsation frequency of highest amplitude and the corresponding orbital phase plot (bottom panel). The solid line in the bottom panel is a fit from the orbital solution.

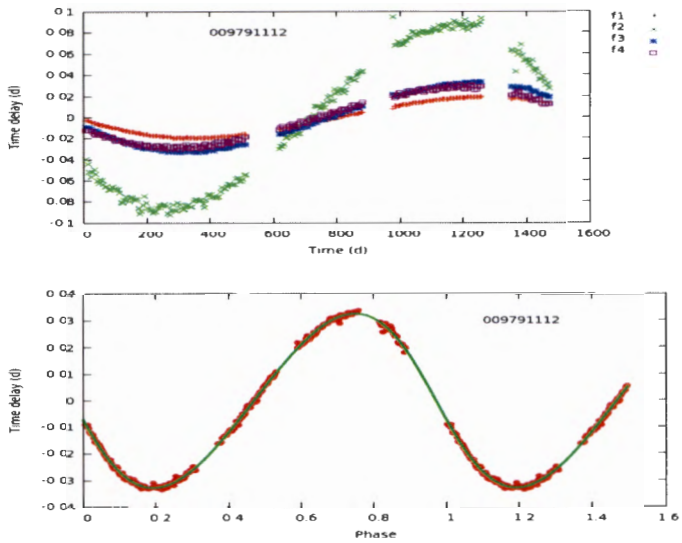

Figure A.97: Time-delay curve (top panel) of KIC 9791112 for the four pulsation frequencies of highest amplitudes and the corresponding orbital phase plot (bottom panel). The solid line in the bottom panel is a fit from the orbital solution.

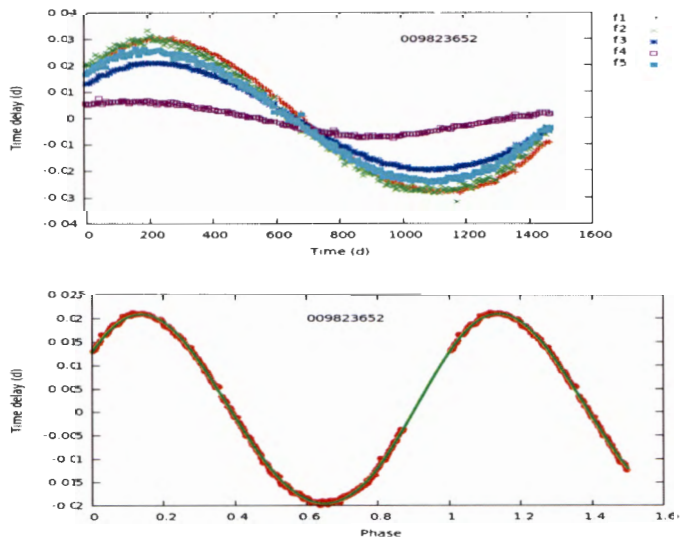

Figure A.98: Time-delay curve (top panel) of KIC 9823652 for the five pulsation frequencies of highest amplitudes and the corresponding orbital phase plot (bottom panel). The solid line in the bottom panel is a fit from the orbital solution.

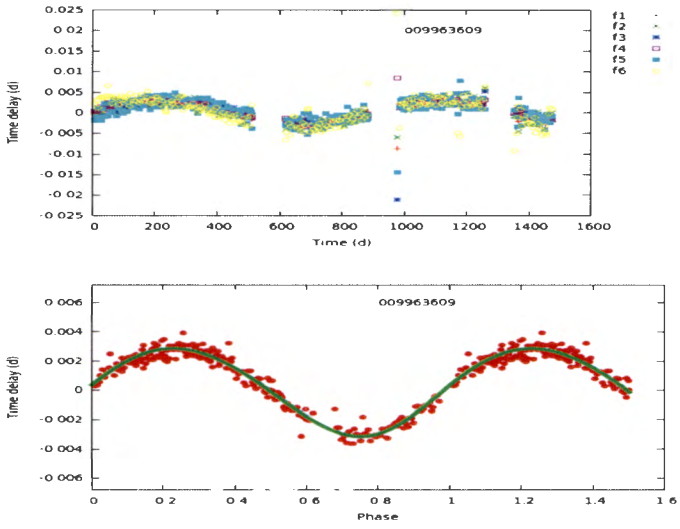

Figure A.99: Time-delay curve (top panel) of KIC 9963609 for the six pulsation frequencies of highest amplitudes and the corresponding orbital phase plot (bottom panel). The solid line in the bottom panel is a fit from the orbital solution.

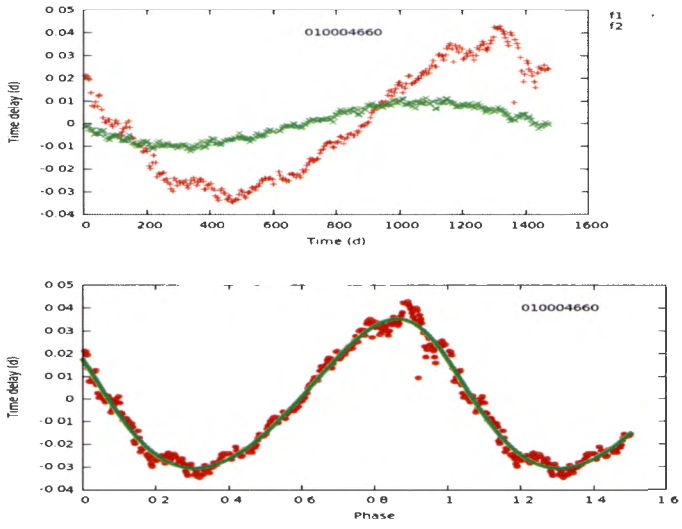

Figure A.100: Time-delay curve (top panel) of KIC 10004660 for the two pulsation frequencies of highest amplitudes and the corresponding orbital phase plot (bottom panel). The solid line in the bottom panel is a fit from the orbital solution.

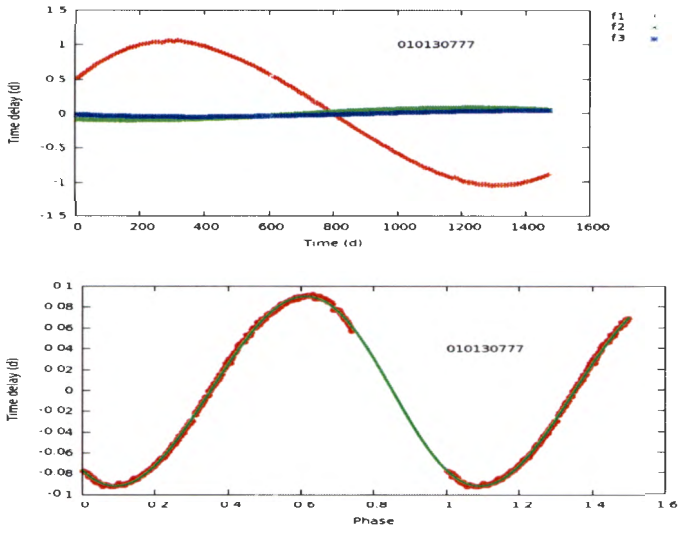

Figure A.101: Time-delay curve (top panel) of KIC 10130777 for the three pulsation frequencies of highest amplitudes and the corresponding orbital phase plot (bottom panel). The solid line in the bottom panel is a fit from the orbital solution.

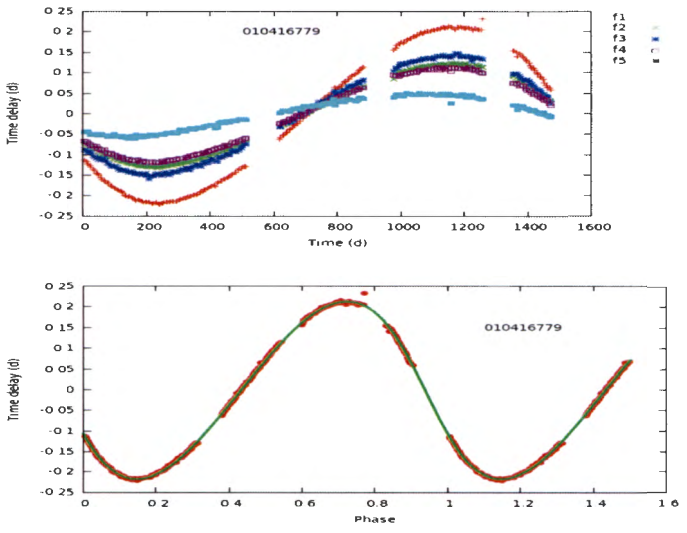

Figure A.102: Time-delay curve (top panel) of KIC 10416779 for the five pulsation frequencies of highest amplitudes and the corresponding orbital phase plot (bottom panel). The solid line in the bottom panel is a fit from the orbital solution.

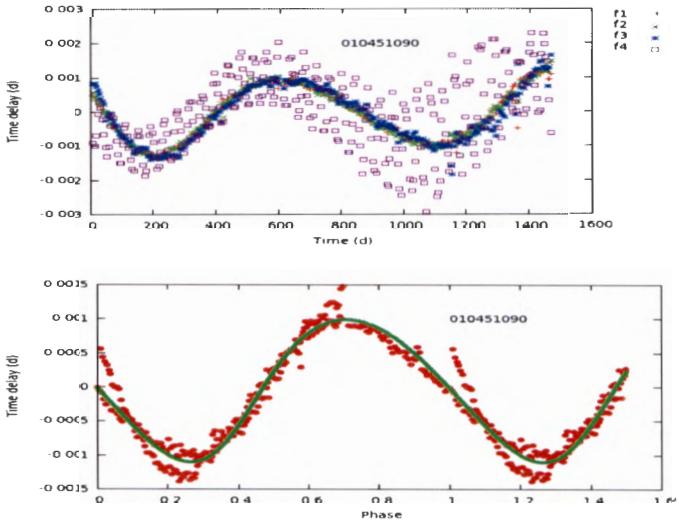

Figure A.103: Time-delay curve (top panel) of KIC 10451090 for the four pulsation frequencies of highest amplitudes and the corresponding orbital phase plot (bottom panel). The solid line in the bottom panel is a fit from the orbital solution.

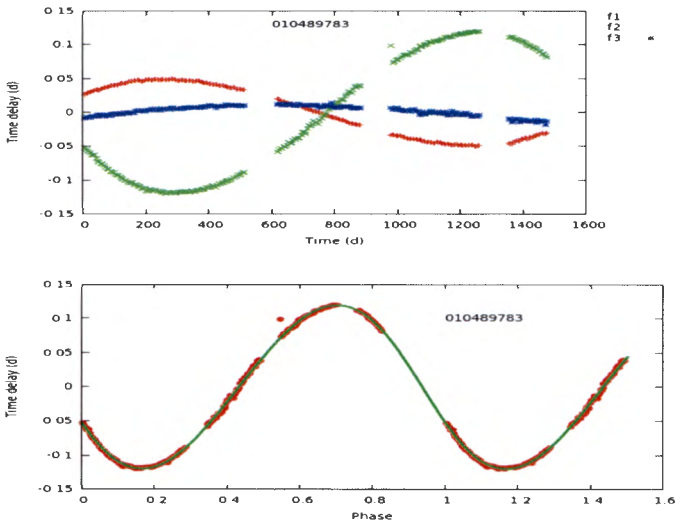

Figure A.104: Time-delay curve (top panel) of KIC 10489783 for the three pulsation frequencies of highest amplitudes and the corresponding orbital phase plot (bottom panel). The solid line in the bottom panel is a fit from the orbital solution.

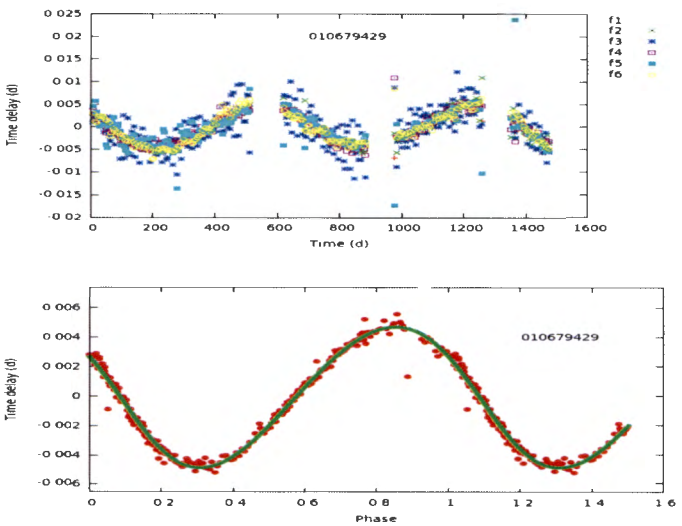

Figure A.105: Time-delay curve (top panel) of KIC 10679429 for the six pulsation frequencies of highest amplitudes and the corresponding orbital phase plot (bottom panel). The solid line in the bottom panel is a fit from the orbital solution.

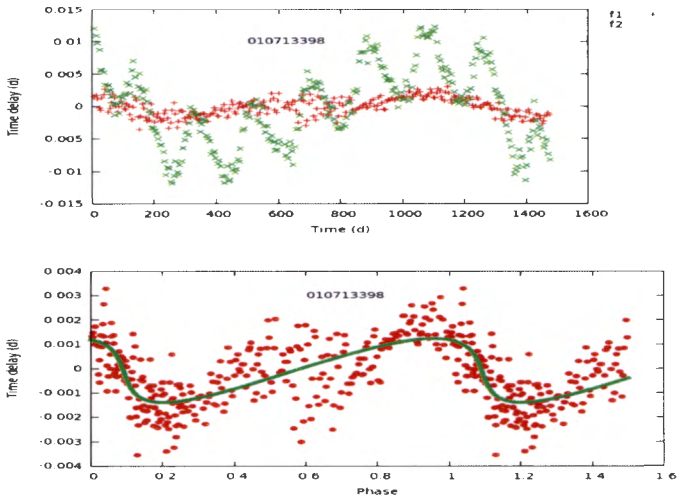

Figure A.106: Time-delay curve (top panel) of KIC 10713398 for the two pulsation frequencies of highest amplitudes and the corresponding orbital phase plot (bottom panel). The solid line in the bottom panel is a fit from the orbital solution.

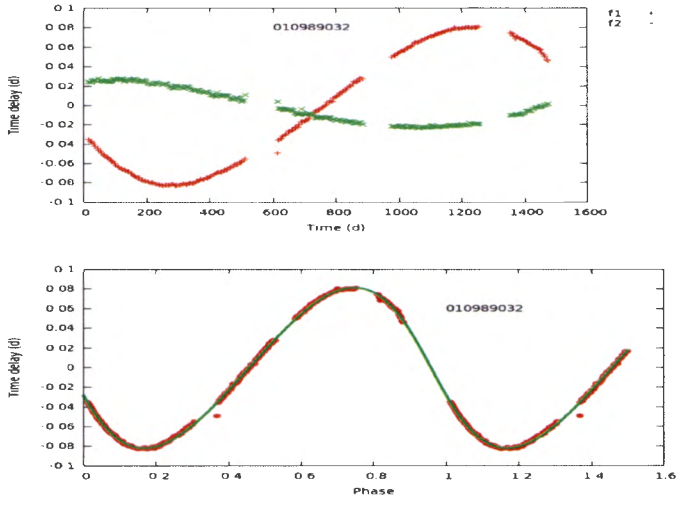

Figure A.107: Time-delay curve (top panel) of KIC 10989032 for the two pulsation frequencies of highest amplitudes and the corresponding orbital phase plot (bottom panel). The solid line in the bottom panel is a fit from the orbital solution.

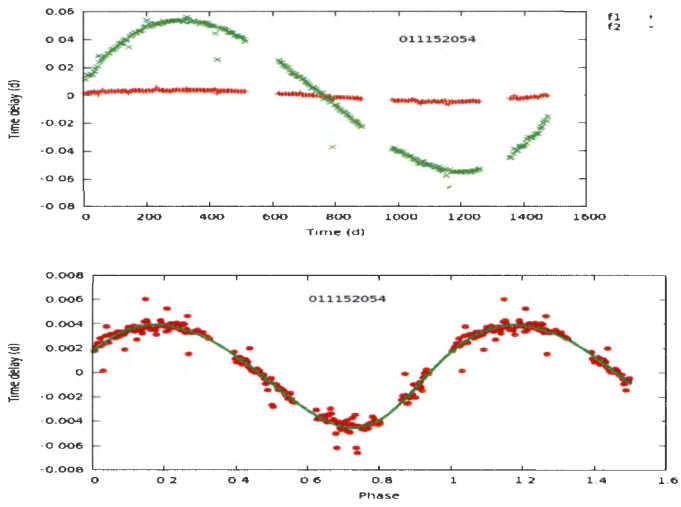

Figure A.108: Time-delay curve (top panel) of KIC 11152054 for the two pulsation frequencies of highest amplitudes and the corresponding orbital phase plot (bottom panel). The solid line in the bottom panel is a fit from the orbital solution.

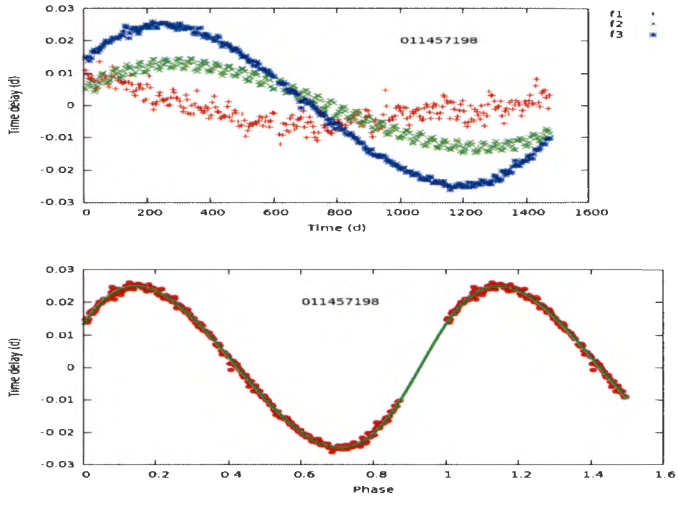

Figure A.109: Time-delay curve (top panel) of KIC 11457198 for the three pulsation frequencies of highest amplitudes and the corresponding orbital phase plot (bottom panel). The solid line in the bottom panel is a fit from the orbital solution.

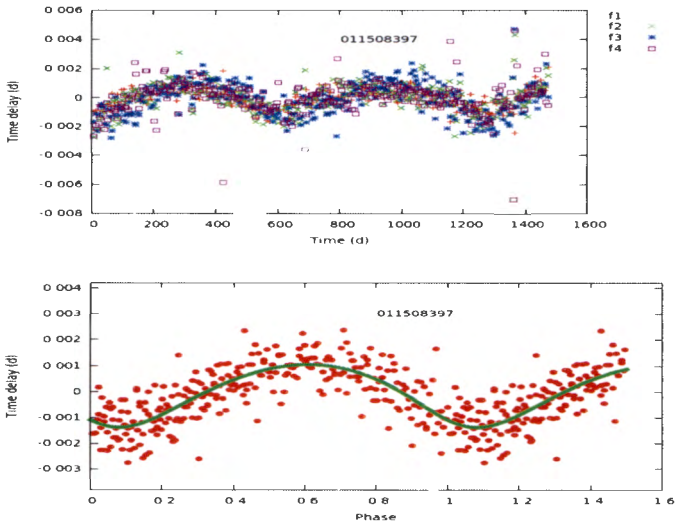

Figure A.110: Time-delay curve (top panel) of KIC 11508397 for the four pulsation frequencies of highest amplitudes and the corresponding orbital phase plot (bottom panel). The solid line in the bottom panel is a fit from the orbital solution.

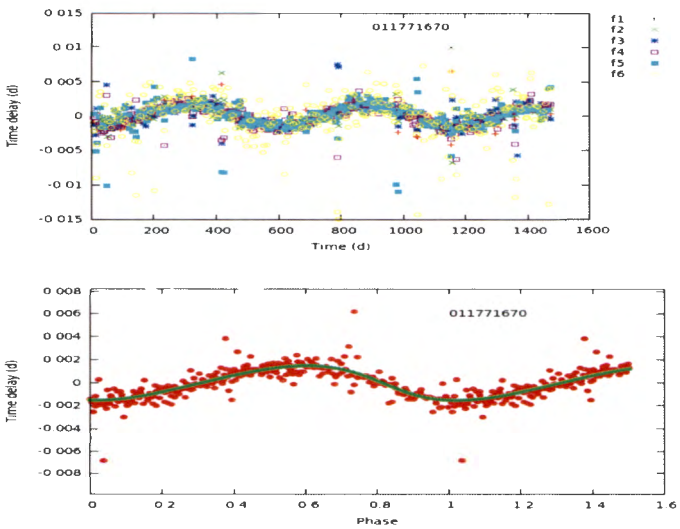

Figure A.111: Time-delay curve (top panel) of KIC 11771670 for the six pulsation frequencies of highest amplitudes and the corresponding orbital phase plot (bottom panel). The solid line in the bottom panel is a fit from the orbital solution.

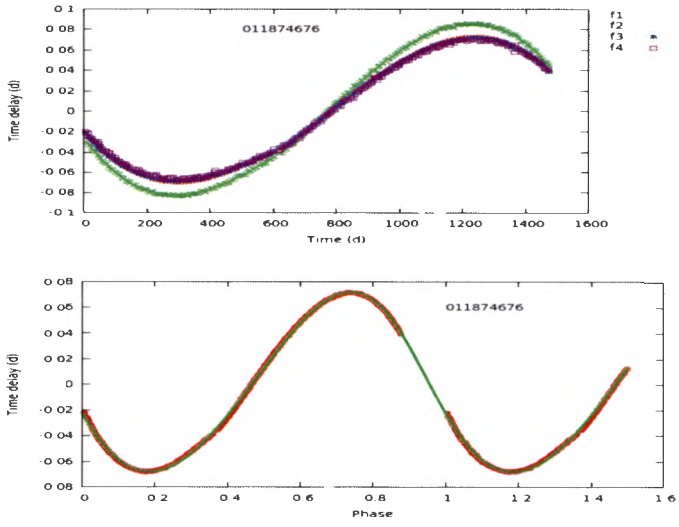

Figure A.112: Time-delay curve (top panel) of KIC 11874676 for the four pulsation frequencies of highest amplitudes and the corresponding orbital phase plot (bottom panel). The solid line in the bottom panel is a fit from the orbital solution.

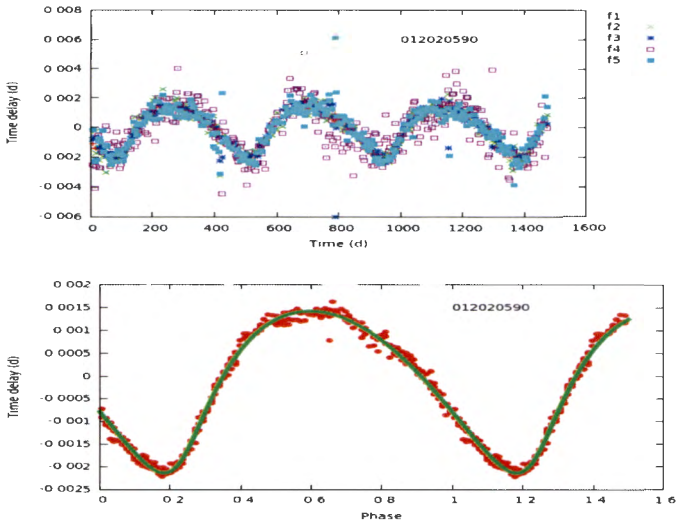

Figure A.113: Time-delay curve (top panel) of KIC 12020590 for the five pulsation frequencies of highest amplitudes and the corresponding orbital phase plot (bottom panel). The solid line in the bottom panel is a fit from the orbital solution.

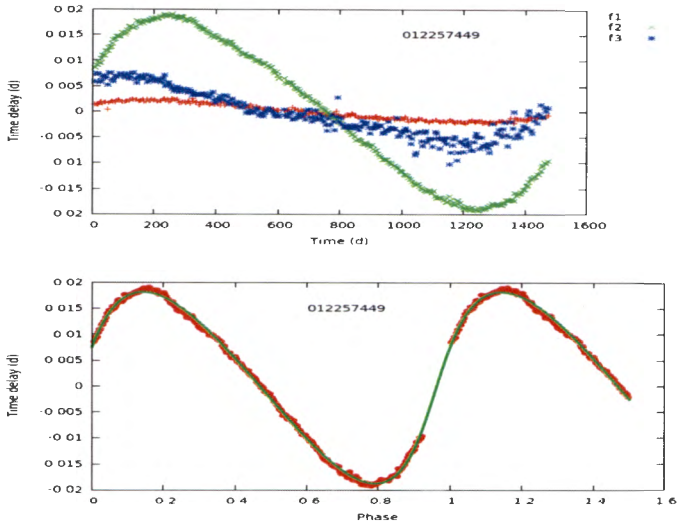

Figure A.114: Time-delay curve (top panel) of KIC 12257449 for the three pulsation frequencies of highest amplitudes and the corresponding orbital phase plot (bottom panel). The solid line in the bottom panel is a fit from the orbital solution.

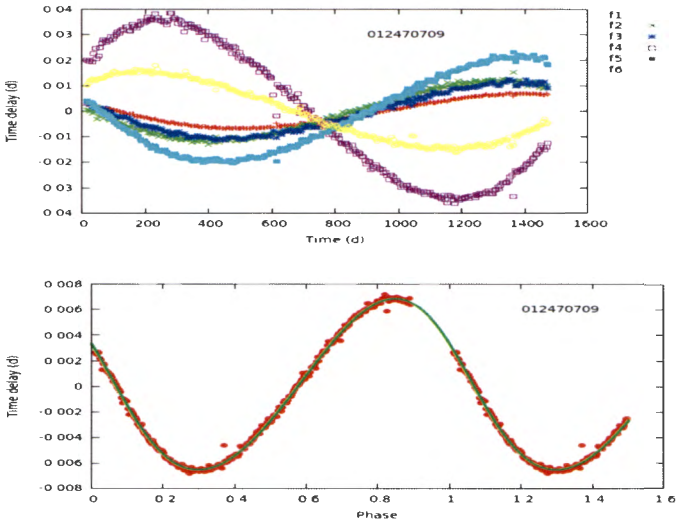

Figure A.115: Time-delay curve (top panel) of KIC 12470709 for the six pulsation frequencies of highest amplitudes and the corresponding orbital phase plot (bottom panel). The solid line in the bottom panel is a fit from the orbital solution.

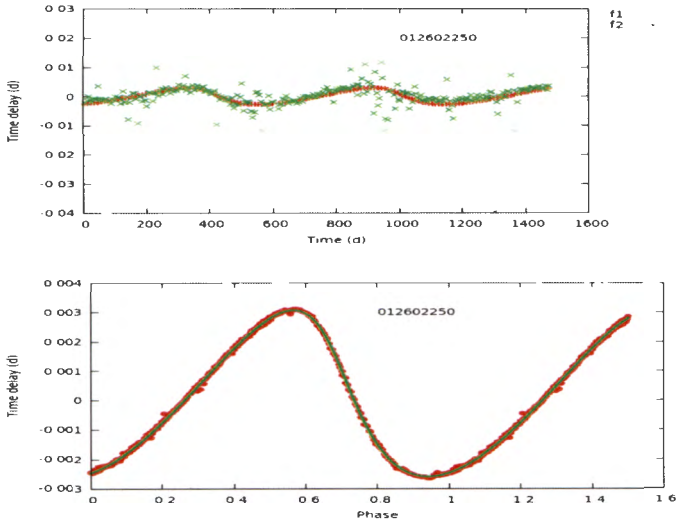

Figure A.116: Time-delay curve (top panel) of KIC 12602250 for the two pulsation frequencies of highest amplitudes and the corresponding orbital phase plot (bottom panel). The solid line in the bottom panel is a fit from the orbital solution.

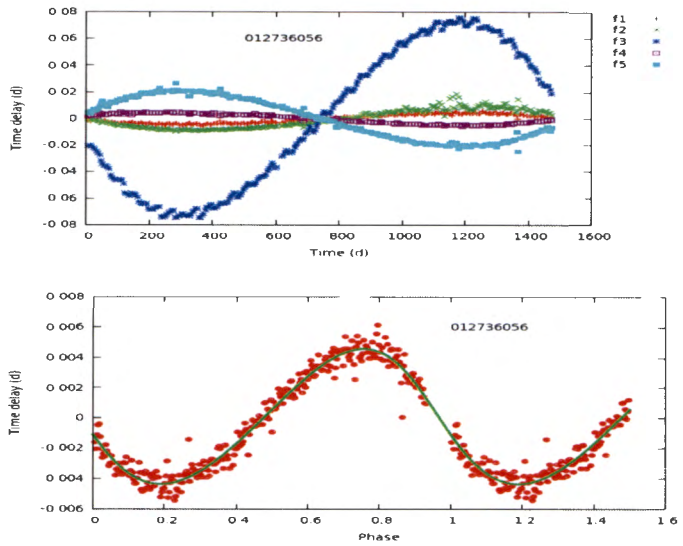

Figure A.117: Time-delay curve (top panel) of KIC 12736056 for the five pulsation frequencies of highest amplitudes and the corresponding orbital phase plot (bottom panel). The solid line in the bottom panel is a fit from the orbital solution.

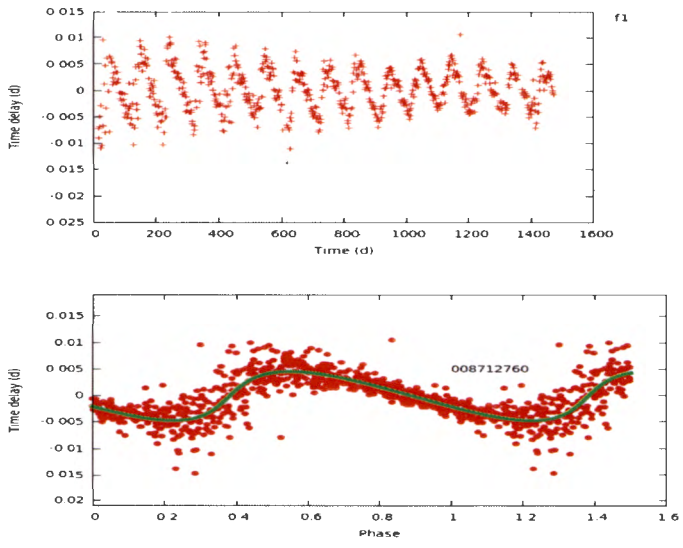

Figure A.118: Time-delay curve (top panel) of KIC 8712760 for the pulsation frequency of highest amplitude and the corresponding orbital phase plot (bottom panel). The solid line in the bottom panel is a fit from the orbital solution.

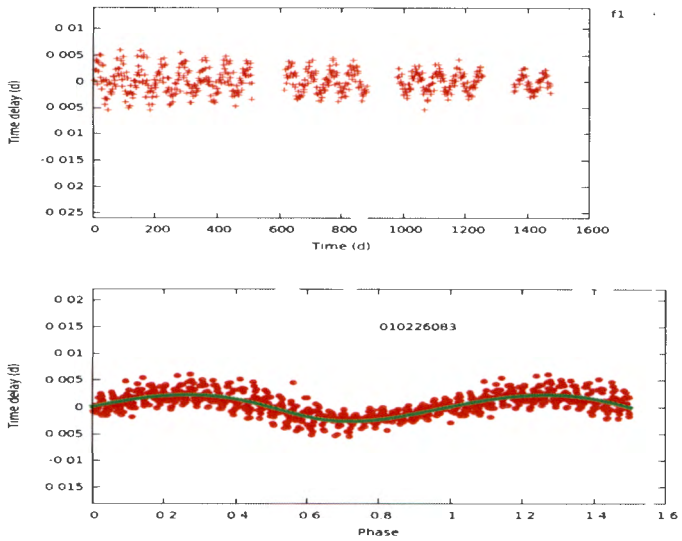

Figure A.119: Time-delay curve (top panel) of KIC 10226083 for the pulsation frequency of highest amplitude and the corresponding orbital phase plot (bottom panel). The solid line in the bottom panel is a fit from the orbital solution.

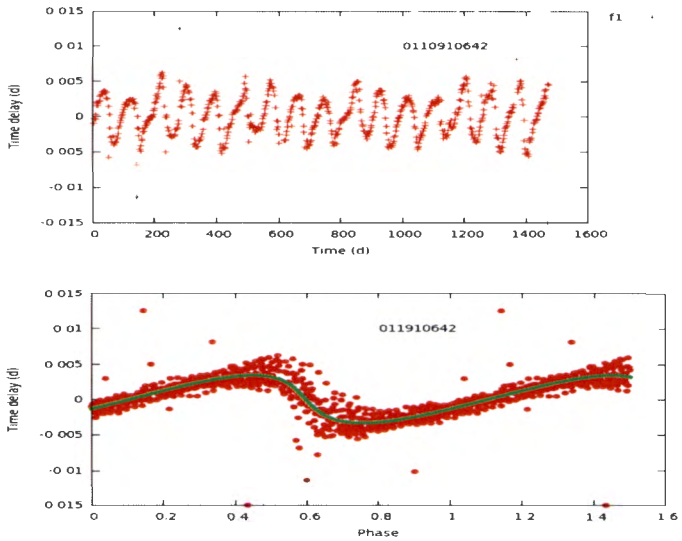

Figure A.120: Time-delay curve (top panel) of KIC 11910642 for the pulsation frequency of highest amplitude and the corresponding orbital phase plot (bottom panel). The solid line in the bottom panel is a fit from the orbital solution.

Appendix B

The Partial Derivatives Used to Find Corrections in Parameters

In order to calculate the corrections to the starting values of the orbital parameters using non-linear least squares, we need to know the partial derivatives of time delay as a function of the parameters. The values of the derivatives were used in the Fortran program developed which calculates orbital parameters.

$\frac{\partial \tau}{\partial \tau_0}$:

$$\frac{\partial \tau}{\partial \tau_0} = 1 \tag{B.1}$$

$\frac{\partial \tau}{\partial A}$:

$$\frac{\partial \tau}{\partial A} = \sqrt{1 - e^2}\cos\omega \sin E + \sin\omega \cos E - e\sin\omega \tag{B.2}$$

$\frac{\partial \tau}{\partial \omega}$:

$$\frac{\partial \tau}{\partial \omega} = -A\sqrt{1-e^2}\sin E \sin\omega + A\cos\omega\cos E - Ae\cos\omega \tag{B.3}$$

$\frac{\partial \tau}{\partial P}$:

$$\frac{\partial \tau}{\partial P} = \frac{\partial \tau}{\partial E}\frac{\partial E}{\partial P} \tag{B.4}$$

$$\frac{\partial \tau}{\partial P} = [A\sqrt{1-e^2}(\cos\omega)(\cos E) + A\sin\omega(-\sin E)]\frac{\partial E}{\partial P} \tag{B.5}$$

But,

$$E - e\sin E = \frac{2\pi}{P}(t - T_{per}) \tag{B.6}$$

$$\frac{\partial E}{\partial P} - e\cos E\frac{\partial E}{\partial P} = 2\pi(t - T_{per})(-1/p^2) \tag{B.7}$$

$$\frac{\partial E}{\partial P}(1 - e\cos E) = \frac{-2\pi(t - T_{per})}{P^2} \tag{B.8}$$

$$\frac{\partial E}{\partial P} = \frac{-2\pi(t - T_{per})}{P^2(1 - e\cos E)} \tag{B.9}$$

$$\frac{\partial \tau}{\partial P} = [A\sqrt{1-e^2}(\cos\omega)(\cos E) - A\sin\omega(\sin E)]\frac{-2\pi(t - T_{per})}{P^2(1 - e\cos E)} \tag{B.10}$$

$\frac{\partial \tau}{\partial T_{per}}$:

$$\frac{\partial \tau}{\partial T_{per}} = \frac{\partial \tau}{\partial E}\frac{\partial E}{\partial T_{per}} \tag{B.11}$$

$$= [A\sqrt{1-e^2}(\cos\omega)(\cos E) - A\sin\omega(\sin E)]\frac{\partial E}{\partial T_{per}} \tag{B.12}$$

But,

$$E - e\sin E = \frac{2\pi}{P}(t - T_{per}) \tag{B.13}$$

$$\frac{\partial E}{\partial T_{per}} - e\cos E\frac{\partial E}{\partial T_{per}} = \frac{-2\pi}{P} \tag{B.14}$$

$$\frac{\partial E}{\partial T_{per}}(1 - e\cos E) = \frac{-2\pi}{P} \tag{B.15}$$

$$\frac{\partial E}{\partial T_{per}} = \frac{-2\pi}{P}(1 - e\cos E)^{-1} \tag{B.16}$$

$$\frac{\partial \tau}{\partial T_{per}} = [A\sqrt{1-e^2}(\cos\omega)(\cos E) - A\sin\omega(\sin E)][\frac{-2\pi}{P}(1 - e\cos E)^{-1}] \tag{B.17}$$

$$\frac{\partial \tau}{\partial T_{per}} = \frac{-2\pi}{P}\frac{1}{(1 - e\cos E)}[A\sqrt{1-e^2}(\cos\omega)(\cos E) - A\sin\omega(\sin E)] \tag{B.18}$$

$\frac{\partial \tau}{\partial e}$:

$$\frac{\partial \tau}{\partial e} = (A\cos\omega)\frac{\partial[\sqrt{1-e^2}\sin E]}{\partial e} + A\sin\omega(-\sin E)\frac{\partial E}{\partial e} - A\sin\omega \tag{B.19}$$

$$\frac{\partial \tau}{\partial e} = (A\cos\omega)[\frac{-e}{\sqrt{1-e^2}}(\sin E)+\sqrt{1-e^2}(\cos E)\frac{\partial E}{\partial e}]-A\sin\omega(\sin E)\frac{\partial E}{\partial e}-A\sin\omega \tag{B.20}$$

But from

$$E - e\sin E = \frac{2\pi}{P}(t - T_{per}) \tag{B.21}$$

and taking partial derivatives with respect to e,

$$\frac{\partial E}{\partial e} - \sin E - e\cos E\frac{\partial E}{\partial e} = 0 \tag{B.22}$$

$$\frac{\partial E}{\partial e} = \frac{\sin E}{(1 - e\cos E)} \tag{B.23}$$

$$\frac{\partial \tau}{\partial e} = (A\cos\omega)[\frac{-e}{\sqrt{1-e^2}}(\sin E) + \sqrt{1-e^2}(\cos E)\frac{\sin E}{(1 - e\cos E)}] - (A\sin\omega\sin E)\frac{\sin E}{(1 - e\cos E)} - A\sin\omega \tag{B.24}$$

$$\frac{\partial \tau}{\partial e} = (A\cos\omega)(\sin E)[\frac{-e}{\sqrt{1-e^2}} + \frac{\sqrt{1-e^2}\cos E}{(1 - e\cos E)}] - A\sin\omega[\frac{\sin^2 E}{1 - e\cos E} + 1] \tag{B.25}$$

Appendix C

The Fortran Program Used to Calculate Orbital Parameters

```
++++++++++++++++++++++++++++++++++++++++

                    LSQUARE

This program fits tau=a(1) + a(2)*sin(E) + a(3)*sin(E)
to a data (observations) by least squares and solves
coefficients a(1), a(2) \& a(3) with their standared
deviations of each coefficent b(1), b(2), b(3). The
least square is solved for each value of ecn. The best
value of ecn is the one which gives the smallest value
of standared deviation of the fit, r0.
++++++++++++++++++++++++++++++++++++++++
        implicit real*8 (a-h,o-z)\\
        parameter(NPTS=15000)! m1=3,NMAT=20,
        parameter(pi=3.14159265358979d0,
            SLAU=173.1446323270202d0)
        dimension t(NPTS),tau\_o(NPTS),y(NPTS),dp(10),
            dy(NPTS)
```

```
      dimension x(8,NPTS),a(10),b(10),c(10),par(10)
      dimension df(10)
      character*8 npar(6),npar2(6)
      character yn*1
      data npar /'Aa','e','omega','Tper','P','tau\_0'/
      data npar2 /'a(1)=','a(2)=','a(3)=','a(4)=','a(5)=',
     'a(6)='/
      NCOF=4
      m1=3


      twopi = 2.*pi
      write(*,1006)
1006  format('Enter Per (days):',\$)
      read(*,*) Per
      open(11,file='tau.out',status='old')
      i=1
10    read(11,*,end=12) t(i),tau\_o(i)
      i = i + 1
      if(i.gt.NPTS) then
        write(*,*) "Too many data points!"
        stop
      endif
      goto 10
12    close(11)
      k = i - 1
      write(*,1007) k
1007 format('Number of data points:', i8)
      tn = twopi/Per
      de = 0.05!Step in ecn
      dt = 0.05!Step in Tper
      emin = 0.0 !Starting ecn
```

```
        emax = 0.95 !Ending ecn
        Tmin = 0.0 !Starting Tper
        Tmax = Per !Ending Tper

        rmin = 1.0e+30
15      do ecn = emin,emax,de
         do T\_per = Tmin,Tmax,dt
          r0 = 0.0d0
          do i = 1, k

            aM = tn*(t(i) \- T\_per)
            eE = eanom(aM,ecn)
            x(1,i) = 1
            x(2,i) = sin(eE)
            x(3,i) = cos(eE)
            x(4,i) = tau\_o(i)
          enddo
          n=k
          call mlstsq(x,n,m1,a,b,r0,NCOF)

          if(r0.lt.rmin) then
            rmin = r0
            ebest = ecn
            a1=a(1)
            b1=b(1)
            a2=a(2)
            b2=b(2)
            a3=a(3)
            b3=b(3)
            Tbest=T\_per
          endif
         enddo
```

```
        enddo

        Ask to repeat by typing in 'y' or 'Y':
        write(*,1025)
        write(*,1026) r0
1026    format('Standared deviation =', E14.7)
1025    format('Repeat? ',\$)
        read(*,1000) yn
1000 format(a)
        if((yn.eq.'y').or.(yn.eq.'Y') ) then
         if(yn.eq.'y') then
          Tmin = Tbest - dt
          if(Tmin.lt.0.0) Tmin = 0.0
          Tmax = Tbest + dt
          if(Tmax.gt.Per) Tmax = Per
          emin = ebest - de
          if(emin.lt.0.0) emin = 0.0
          emax = ebest + de
          if(emax.gt.0.99) emax = 0.99
          goto 15
         endif
         endif

        write(*,1010) ebest
        print*, 'Time of periastron passage,', Tbest
1010    format('Eccentricity at minimum r0 is:', f10.6)

        write(*,1020) a1, b1
1020    format('a(1) = ', E14.7, '+/-', E14.7)
        write(*,1030) a2, b2
1030    format('a(2) = ', E14.7, '+/-', E14.7)
        write(*,1040) a3, b3\\
```

```
1040    format('a(3) = ', E14.7, '+/-', E14.7)

        write(*,1050) r0
1050    format('Standared deviation =', E14.7)

        Calculating time delay using eccentricity, ebest.
        open(unit=1,file='taucal.dat',status='unknown')
        do i = 1, k
          aM = tn*(t(i) - Tbest)
          eE = eanom(aM,ebest)
          tau\_c = a1 + a2*sin(eE) + a3*cos(eE)
          write(1,108) t(i),tau\_c
108       format(f20.12, f20.12)
        enddo
        close(1)


        ecn=ebest
        alpha2 = a2/(sqrt(1.0-ecn*ecn))
        Aa = sqrt(alpha2*alpha2 + a3*a3)
        som = a3/Aa
        com = alpha2/Aa
        omega = atan2(som,com)
        tau\_0 = a1+Aa*ecn*sin(omega)

        print*, 'Aa=' , Aa
        print*, 'omega=', omega
        print*, 'asini=', Aa*SLAU

        write(*,1060)
1060 format('Approximate parameters'/
     +  'Aa ecn omega Tbest Period tau\_0')
```

```
        write(*,1070) Aa, ecn, omega, Tbest, Per, tau\_0
1070    format(5f10.4)


        ------NOW WE CAN IMPROVE THE APPROXIMATE
        PARAMETERS-------

        par(1) = Aa
        par(2) = ecn
        par(3) = omega
        par(4) = Tbest
        par(5) = Per
        par(6) = tau\_0
        These are maximum error on all 6 parameters.
        do i = 1,6
          dp(i) = 1.0e-4
        enddo

13      continue
        Create matrix for LS fit.
        do i = 1,n
          call dfdx(t(i),par,df)
          do j = 1,6
            x(j,i) = df(j)
          enddo
          Obtain residuals, DY= Yobs - Ycal, from calculated
          binary time delay.
          x(7,i) = y(i) - td(t(i),par
        enddo
        Fit least squares
        call mlstsq(x,n,6,b,c,r0,7)
        Test if corrections small enough.
```

```
        ko = 1
        do i = 1,5
          if(abs(b(i)).gt.dp(i)) ko = 0
          par(i) = par(i) + b(i)
        enddo
        write(*,*)
        write(*,*)
        write(*,1089) (npar2(i),par(i),b(i),i=1,6)
        Test if corrections are below tolerance.
        if(ko.eq.0) goto 13

        Write out final parameters.
        write(*,*)
        write(*,1089) (npar(i),par(i),c(i),i=1,6)
1080    format(a,f10.4,' +/-',f10.4)
1089    format(a, E14.7, '+/-', E14.7)


        call writetd('tdfit.tdc',par,75)
        stop
        end


++++++++++++++++++++++++++++++++++++++++++++

      DFDX(t,A,ecn,omega,Tper,per,df)

 Given time t and approximate parameters,
 (A,ecn,omega,Tper,per),
 this routine calculates corrections to
 these parameters in array DF(*)
```

```
++++++++++++++++++++++++++++++++++++++++++++++++

        subroutine dfdx(t,par,df)
        implicit real*8 (a-h,o-z)
        parameter (TWOPI=6.283185308)!,
                    SLAU=173.1446323270202d0
        dimension par(*),df(*)

        asini = par(1)
        Aa = par(1)
        ecn = par(2)
        omega = par(3)
        Tper = par(4)
        Tbest = par(4)
        Per = par(5)
        tau\_0 = par(6)
        Mean anomaly, M:
        tn = TWOPI/per
        tn = TWOPI/Per
        aM = tn*(t - Tper)
        aM = tn*(t - Tbest)
        Solve for eccentric anomaly, E:
        eE = eanom(aM,ecn)

        se = sin(eE)
        ce = cos(eE)
        so = sin(omega)
        co = cos(omega)
        e1 = sqrt(1.0-ecn*ecn)
        e2 = 1.0 - ecn*cos(eE)

        dtau/dA
```

```
        df(1) = e1*co*se + so*ce - ecn*so
        dtau/de
        df(2) = Aa*co*se*((-ecn/e1) + (e1*ce/e2)) -
     +  Aa*so*((se*se/e2)+1)
        dtau/domega
        df(3) = -Aa*e1*se*so + Aa*co*ce -
     +  Aa*ecn*co
        dtau/dTper
        df(4) = ((-TWOPI)/(Per*e2)) * (Aa*e1*co*ce -
     +  Aa*so*se)
        dtau/dPer
        df(5) = (Aa*e1*co*ce-Aa*so*se)*
     +  (-TWOPI*(t-Tbest)/(Per*Per*e2))
        dtau/dtau\_0
        df(6) = 1

        return
        end
```

```
++++++++++++++++++++++++++++++++++++++++++++++++++++++
```

TD(t, par)

Returns time-delay at time T, using binary parameters in array PAR().

```
++++++++++++++++++++++++++++++++++++++++++++++++++++++
```

```
        function td(t,par)
        implicit real*8 (a-h,o-z)
        parameter (TWOPI=6.283185308)!,
            SLAU=173.1446323270202d0
```

```
      dimension par(*)

      a1=a(1)!-0.00005561
      tn = TWOPI/par(5)
      Mean anomaly, M:
      aM = tn*(t - par(4))
      Solve for eccentric anomaly, E:
      eE = eanom(aM, par(2))
      The time-delay
      td = par(1)*sqrt(1.0-par(2)**2)*cos(par(3))*sin(eE)
     +  + par(1)
     +  *sin(par(3))*cos(eE)-par(1)*par(2)*sin(par(3))
     +  + a1+par(1)*par(2)*sin(par(3))
     +  + tau\_0

      return
      end

++++++++++++++++++++++++++++++++++++++++++++++++

            WRITETD(filn,t,par)

  Read (time, time-delay) data from the first
  two columns in file FILN. Stores the time in
  array T(*) and time-delay in Y(*) and returns
  number of data points, N, which must
  be less than NPTS.

++++++++++++++++++++++++++++++++++++++++++++++++

      subroutine writetd(filn,par,num)
      implicit real*8 (a-h,o-z)
```

```
        parameter (TWOPI=6.283185308)
        character*(*) filn
        dimension par(*)

        open(unit=1,file=filn,status='unknown')
        dt = par(5)/num
        t = -dt
        do i = 1,num
          t = t + dt
          write(1,1030) t,td(t,par)
1030    format(2f20.12)
        enddo
        close(1)

        return
        end
++++++++++++++++++++++++++++++++++++++++++++++
```

EANOM(aM,ecn)

This function solves the equation E - e sin E = M when M and e are given.

```
++++++++++++++++++++++++++++++++++++++++++++++

        function eanom(aM, ecn)
        implicit real*8 (a-h,o-z)


        epsilon = 1.0e-5
        eE1 = aM
20      eE = aM + ecn*sin(eE1)
```

```
        de = abs(eE-eE1)
        eE1 = eE
        if(de.gt.epsilon) goto 20

        eanom = eE
        return
        end

++++++++++++++++++++++++++++++++++++++++++++++++++++++++

           MLSTSQ(x,n,m1,a,b,r0,NCOF)

  Least squares fitting of multivariable

        x(NCOF,*) = Matrix of input values
        n    = No of points
        m1   = No of independent variables
        a(*) = Coefficients a(1)=const term etc.
        b(*) = Std error of a
        r0   = Std error of one observation

++++++++++++++++++++++++++++++++++++++++++++++++++++++++

        subroutine mlstsq(x,n,m1,a,b,r0,NCOF)
        parameter (NPTS=100000)
        implicit real*8 (a-h,o-z)
        dimension x(NCOF,*),a(*),b(*),c(NCOF,NCOF),
           d(NCOF,NCOF)

        m2 = m1 + 1
        do i = 1,m2
          do j = 1,m2
```

```
    c(i,j) = 0.0
  enddo
enddo

do i=1,n
  do j=1,m2
    do k=1,m2
      c(j,k) = c(j,k) + x(j,i)*x(k,i)
    enddo
  enddo
enddo

call matinv(c,d,m1,NCOF)

do j=1,m1
  a(j)=0.0
  do i=1,m1
    a(j) = a(j) + c(i,m2)*d(i,j)
  enddo
enddo

u = c(m2,m2)
do i = 1,m1
  u = u - a(i)*c(i,m2)
enddo

p = float(n-m1)
w = u/p
r0 = sqrt(w)

do i = 1,m1
  u = w*d(i,i)
```

```
          b(i) = sqrt(u)
        enddo

        return
        end

++++++++++++++++++++++++++++++++++++++++++++++++

                MATINV(a,b,n,nmat)

  Inverts matrix A(1:n,1:n) by elimination with
  partial pivoting.  The inverted matrix is returned
  in B(1:n,1:n); NMAT is the physical dimension
  of A and B.  On return A is destroyed.

++++++++++++++++++++++++++++++++++++++++++++++++

        subroutine matinv(a,b,n,nmat)
        implicit real*8 (a-h,o-z)
        dimension a(nmat,*),b(nmat,*)

        set threshold value eps
        eps=1.0e-20

        construct identity matrix
        do 1 i=1,n
         do 1 j=1,n
          b(i,j)=0.
          if(i.eq.j) b(i,j)=1.0
1       continue

        locate maximum of a(i,j) on or below diagonal
```

```
      do 8 k=1,n
       if(k.eq.n) goto 4
       l=k
       t=abs(a(k,k))
       k1=k+1
       do 2 i=k1,n
        z=abs(a(i,k))
        if(t.ge.z) goto 2
        l=i
        t=z
2      continue

      interchange rows l and k if l is not equal to k
       if(l.eq.k) goto 4
       do 3 j=1,n
        t=a(l,j)
        a(l,j)=a(k,j)
        a(k,j)=t
        t=b(l,j)
        b(l,j)=b(k,j)
3      b(k,j)=t

      test for non-singular matrix
4      if(abs(a(k,k)).le.eps) goto 9

      divide pivot row by its main diagonal element
       t=a(k,k)

       do 5 j=1,n
        a(k,j)=a(k,j)/t
        b(k,j)=b(k,j)/t
5      continue
```

```
        replace each row by linear combinations with pivot row
         do 7 i=1,n
          t=a(i,k)
          if(i.eq.k) goto 7
          do 6 j=1,n
           a(i,j)=a(i,j)-t*a(k,j)
6         b(i,j)=b(i,j)-t*b(k,j)
7        continue
8       continue
        return

        if matrix is singular put n=0 and exit
9       n=0
        write(*,'(''SINGULAR MATRIX - INVERSE IMOSSIBLE!'')')
        return
        end
```

Appendix D

The Method of Least Squares

Linear Least Squares

In many situations, there is a single response variable y, also called the *dependent variable*, which depends on the value of a set of input, also called *independent variables*, $x_1, ..., x_m$. The simplest type of relationship between the dependent variable y and the input variables $x_1, ..., x_m$ is a *linear relationship*. Now we are interested in constructing the best fitting straight line such that, for each observed response x_i, the corresponding value of y on the straight line will be as close as possible to the actual response y_i.

Fitting a Linear Function of Two Variables

Let us consider an arbitrary straight line:

$$y = a_0 + a_1 x \tag{D.1}$$

in which the values of the constants a_0 and a_1 are to be determined. Therefore, it would be possible to exactly predict the dependent variable for any set of imput values. However, in practice, such precision is almost never attainable and the most that one expects is that this equation would be valid subject to random error ϵ_i. By this means that the explicit relationship is

$$y_i + \epsilon_i = a_0 + a_1 x_i \tag{D.2}$$

where ϵ_i, represents the random error.

$$\epsilon_i = a_0 + a_1 x_i - y_i \tag{D.3}$$

$$\epsilon_i^2 = (a_0 + a_1 x_i - y_i)^2 \tag{D.4}$$

The height of the line is $a_0 + a_1 x_i$. Therefore, the vertical distance between the points (x_i, y_i) and the line is $a_0 + a_1 x_i - y_i$. Suppose that the line is to be fitted to n points, and let S denote the sum of the squares of the vertical distance at the n points. Then

$$S = \sum_{i=1}^{n} \epsilon_i^2 = \sum_{i=1}^{n} (a_0 + a_1 x_i - y_i)^2 \tag{D.5}$$

The method of least squares specifies that the values of a_0 and a_1 must be chosen so that the value of S is minimized. It is not difficult to minimize the value of S with respect to a_0 and a_1. We take the partial derivatives and set these values to zero:

$$\frac{\partial S}{\partial a_0} = 2 \sum_{i=1}^{n} (a_0 + a_1 x_i - y_i) = 0 \tag{D.6}$$

$$\frac{\partial S}{\partial a_1} = 2 \sum_{i=1}^{n} (a_0 + a_1 x_i - y_i) x_i = 0 \tag{D.7}$$

This gives

$$\sum_{i=1}^{n} (a_0 + a_1 x_i - y_i) = 0 \tag{D.8}$$

$$\sum_{i=1}^{n} (a_0 x_i + a_1 x_i^2 - x_i y_i) = 0 \tag{D.9}$$

Re-writing these equations, we obtain the following pair of equations:

$$\begin{aligned} n a_0 + a_1 \sum_{i=1}^{n} x_i - \sum_{i=1}^{n} y_i &= 0 \\ a_0 \sum_{i=1}^{n} x_i + a_1 \sum_{i=1}^{n} x_i^2 - \sum_{i=1}^{n} x_i y_i &= 0 \end{aligned} \tag{D.10}$$

Thses two equations are called *normal equations* for a_0 and a_1. We can determine the following sums easily: $\sum x_i, \sum y_i, \sum x_i y_i$ *and* $\sum x_i^2$. The above notation is clumsy, so let us represent the average of any quantity as follows:

$$< x >= \frac{1}{n} \sum_{i=1}^{n} x_i \tag{D.11}$$

and

$$< y >= \frac{1}{n} \sum_{i=1}^{n} y_i \tag{D.12}$$

This notation allows us to write the above equation as

$$a_0 + a_1 < x >=< y > \tag{D.13}$$

$$a_0 < x > + a_1 < x^2 >=< xy > \tag{D.14}$$

In matrix notation we can write these two simultanious equations as

$$\begin{pmatrix} 1 & < x > \\ < x > & < x^2 > \end{pmatrix} \begin{pmatrix} a_0 \\ a_1 \end{pmatrix} = \begin{pmatrix} < y > \\ < xy > \end{pmatrix} \tag{D.15}$$

or simply as

$$XA = Y \tag{D.16}$$

from which the unknown coefficient matrix, A, can be obtained:

$$A = (X^{-1})Y \tag{D.17}$$

where X^{-1} is the *inverse of the matrix* X. In this simple case we do not need direct matrix inversion. Algebric manipulation of the normal equations easily leads to the solution

$$a_0 = \frac{< y >< x^2 > - < xy >< x >}{< x^2 > - < x >^2} \tag{D.18}$$

$$a_1 = \frac{< xy > - < x >< y >}{< x^2 > - < x >^2} \tag{D.19}$$

Fitting a Linear Function of Several Variables

In the majority of applications, functional relationships can be predicted more adequately not on the basis of a single independent input variable but on a collection of such variables. A typical situation is one in which there are a set of, say, m input variables and the response y is related to them by the relation

$$y_i + \epsilon_i = a_0 + a_1 x_{1i} + a_2 x_{2i} + a_3 x_{3i} + ... + a_m x_{mi} \tag{D.20}$$

where $x_j, j = 1, 2..., m$ is the level of the jth input variable, m is the number of independent variables and ϵ_i is a random error. The parameters $a_0, a_1, ..., a_m$ are assumed to be unknown and must be estimated from the data by the method of least squares. As before, it is required to minimize the sum of the squares of the differences between the y_i and their estimated expected values as follows:

$$S = \sum_{i=1}^{n} (a_0 + a_1 x_{i1} + a_2 x_{i2} + ... + a_m x_{im} - y_i)^2 \tag{D.21}$$

We then repeatedly take partial derivatives of the sum of squares. On equating equations to 0, we obtain the following set of equations:

$$\begin{gathered}
\sum_{i=1}^{n} (a_0 + a_1 x_{i1} + a_2 x_{i2} + ... + a_m x_{im} - y_i) = 0 \\
\sum_{i=1}^{n} (a_0 + a_1 x_{i1} + a_2 x_{i2} + ... + a_m x_{im} - y_i) x_{i1} = 0 \\
\sum_{i=1}^{n} (a_0 + a_1 x_{i1} + a_2 x_{i2} + ... + a_m x_{im} - y_i) x_{i2} = 0 \\
\ldots \ldots \ldots \ldots \\
\sum_{i=1}^{n} (a_0 + a_1 x_{i1} + a_2 x_{i2} + ... + a_m x_{im} - y_i) x_{im} = 0
\end{gathered} \tag{D.22}$$

Re-writing these equations yields the following set of linear equations called the *normal equations*:

$$
\begin{aligned}
na_0 + a_1 \sum_{i=1}^{n} x_{i1} + a_2 \sum_{i=1}^{n} x_{i2} + ... + a_m \sum_{i=1}^{n} x_{im} &= \sum_{i=1}^{n} y_i \\
a_0 \sum_{i=1}^{n} x_{i1} + a_1 \sum_{i=1}^{n} x_{i1}^2 + a_2 \sum_{i=1}^{n} x_{i1}x_{i2} + ... + a_m \sum_{i=1}^{n} x_{i1}x_{im} &= \sum_{i=1}^{n} x_{i1}y_i \\
&\cdots\cdots\cdots\cdots \\
&\cdots\cdots\cdots\cdots \\
a_0 \sum_{i=1}^{n} x_{im} + a_1 \sum_{i=1}^{n} x_{im}x_{i1} + a_2 \sum_{i=1}^{n} x_{im}x_{i2} + ... + a_m \sum_{i=1}^{n} x_{im}^2 &= \sum_{i=1}^{m} x_{imyi}
\end{aligned}
\tag{D.23}
$$

Now the simple algebraic solution is more laborious and it is best to use matrix methods. Therefore, the solutions can be found by matrix inversion using computer programs. Thus this equation can be written in matrix formalism: $Y = AX$, where Y and A are column vectors $[(n+1) \times 1]$ and X is a matrix of dimensions $[(n+1) \times (n+1)]$. The elements of the vector A are the required coefficients. Multiplying $Y = AX$ by the inverse matrix of X^{-1}, $(XX^{-1} = I)$, where I is the unit matrix, leads to $A = YX^{-1}$. Finding X^{-1} and YX^{-1} are simple operations using a computer program where we also used the matrix solution approach to find the coefficients (orbital parameters in).

Finally, we can get the following two matrices X and Y:

$$
X = \begin{pmatrix}
1 & < x_1 > & < x_2 > & \cdots & < x_m > \\
< x_1 > & < x_1^2 > & < x_1x_2 > & \cdots & < x_1x_m > \\
< x_2 > & < x_1x_2 > & < x_2^2 > & \cdots & < x_2x_m > \\
\vdots & \vdots & \vdots & \ddots & \vdots \\
< x_m > & < x_1x_m > & < x_2x^m > & \cdots & < x_mx_m >
\end{pmatrix}
\tag{D.24}
$$

$$
Y = \begin{pmatrix}
< y > \\
< x_1y > \\
< x_2y > \\
\cdots \\
< x_my >
\end{pmatrix}
\tag{D.25}
$$

Fitting a Polynomial Equation by Least Squares Method

In situations where the functional relationship between the response Y and the independent variable x cannot be adequately approximated by a linear relationship, it is sometimes possible to obtain a reasonable fit by considering a polynomial (degree m) relationship. Most curved calibration lines are fitted to a quadratic equation $y = a_0 + a_1x + a_2x^2$ or to a third-power (cubic) equation $y = a_0 + a_1x + a_2x^2 + a_3x^3$. The principle of least squares fitting to these polynomials is the same as for the linear function. For instance in the case of a quadratic equation, we want to minimize the S: $S = \sum_{i=1}^{n}(a_0+a_1x+a_2x^2-y_i)^2$. In the more general case of a polynomial of degree m, we might try to fit to the data set a functional relationship of the form

$$y_i + \epsilon_i = a_0 + a_1x_i + a_2x_i^2 + a_3x_i^3 + ... + a_mx_i^m. \tag{D.26}$$

where the method of least squares specifies that the constants $a_0, a_1, a_2, ..., a_m$ should be chosen so that the sum S of the squares of the vertical deviations of the points from the curve is a minimum. In other words, these constants should be chosen so as to minimize the following expression for S:

$$S = \sum_{i=1}^{n}(a_0 + a_1x_i + a_2x_i^2 + ... + a_mx_i^m - y_i)^2 \tag{D.27}$$

To minimize S, we take partial derivatives with respect to $a_0, a_1, ..., a_n$ of the forgoing sum of squares, and then set these equations to 0. On doing so and re-arranging the resulting equations, we obtain the following linear equations called the normal equations.

$$
\begin{aligned}
a_0 n + a_1 \sum_{i=1}^{n} x_i + a_2 \sum_{i=1}^{n} x_i^2 + ... + a_m \sum_{i=1}^{n} x_i^m &= \sum_{i=1}^{n} y_i \\
a_0 \sum_{i=1}^{n} x_i + a_1 \sum_{i=1}^{n} x_i^2 + a_2 \sum_{i=1}^{n} x_i^3 + ... + a_m \sum_{i=1}^{n} x_i^{m+1} &= \sum_{i=1}^{n} x_i y_i \\
a_0 \sum_{i=1}^{n} x_i^2 + a_1 \sum_{i=1}^{n} x_i^3 + ... + a_m \sum_{i=1}^{n} x_i^{m+2} &= \sum_{i=1}^{n} x_i^2 y_i \\
\cdots\cdots \quad \cdots\cdots \quad \cdots\cdots & \\
\cdots\cdots \quad \cdots\cdots \quad \cdots\cdots & \\
a_0 \sum_{i=1}^{n} x_i^m + a_1 \sum_{i=1}^{n} x_i^{m+1} + ... + a_m \sum_{i=1}^{n} x_i^{2m} &= \sum_{i=1}^{n} x_i^m y_i
\end{aligned}
\tag{D.28}
$$

Fourier Fitting

We can still apply the method of least squares further for a different kind of function. One of the most interesting is for Fourier fitting where we also used it to represent the variation of time-delay as one star orbits its companion about their center of mass. For example, periodic functions can be described by a sum of Fourier components of the following type using sine function:

$$Y = a_0 + A_1 \sin(\omega t + \phi_1) + A_2 \sin(2\omega t + o_2) + A_3 \sin(3\omega t + \phi_3) + ... + A_m \sin(m\omega t + \phi_m) \tag{D.29}$$

where $\omega = 2\pi/P$, P is the period, ϕ is the phase in radians and $a_0, A_1, A_2, ...A_m, \phi_1, \phi_2, ..., \phi_m$ are unknown coefficients to be determined. We can further write this equation more compactly in the form

$$
\begin{aligned}
Y &= a_0 + \sum_{k=1}^{m} A_k \sin(k\omega t + \phi_k) \\
&= a_0 + \sum_{k=1}^{m} (A_k \cos\phi_k \sin(k\omega t) + A_k \sin\phi_k \cos(k\omega t)) \\
&= a_0 + \sum_{k=1}^{m} (a_{2k-1} \sin(k\omega t) + a_{2k} \cos(k\omega t))
\end{aligned}
\tag{D.30}
$$

This equation finally gives the following:

$$Y = a_0 + a_1 \sin(\omega t) + a_2 \cos(\omega t) + a_3 \sin(2\omega t) + a_4 \cos(2\omega t) + ... + a_{2m-1} \sin(m\omega t) + a_{2m} \cos(m\omega t) \quad \text{(D.31)}$$

If we have some kind of periodic data of n observations, we can put $x_{1i} = \sin(\omega t_i)$, $x_{2i} = \cos(\omega t_i)$, $x_{3i} = \sin(2\omega t_i)$, $x_{4i} = \cos(2\omega t_i)$,....,etc. These values are the same as the expressions we got before:

$$Y_i = y_i + \epsilon_i = a_0 + a_1 x_{1i} + a_2 x_{2i} + a_3 x_{3i} + ... + a_{2m-1} x_{(2m-1)i} + a_{2m} x_{2mi} \quad \text{(D.32)}$$

As usual, to detrmine the the unknown coefficients, $a_0, a_1, ..., a_{2m}$, we can use least squares method.

Non-linear Least Squares

Most of the time functional relationships are neither linear nor polynomial but rather a kind of exponential type. In this case the least squares fitting can be done iteratively as will be seen in the next section, or in some cases the equation can be transformed into a linear one, usually by taking the logarithm of the whole equation.

Suppose we are asked to find the least squares solution to fit the following equations:

$$y_i + \epsilon_i = a_0 \sin(\omega t + a_1), or \quad \text{(D.33)}$$

$$y_i + \epsilon_i = a_0 e^{-a_1 t} + a_2 e^{-a_3 t}, or \quad \text{(D.34)}$$

$$y_i + \epsilon_i = a_0 + a_1 e^{-a_3 (x - a_2)^2} \quad \text{(D.35)}$$

Such a non-linear case is very common and it is often very difficult to find the minimum analytically. This is because equating of the partial derivatives to zero does not lead to explicit equations for the adjustable parameters. However, it can often be handled with the aid of a computer program which can find the minimum

of a function in multidimensional space. Given trial values for the parameters, the different methods give a procedure that improves the trial solution.

Therefore, the best technique of solving such a problem is to start with approximate values of the unknown constants and to apply an algorithm which will iteratively improve the solution. In the above example of the third expression, y is a function of the constants a_0, a_1, a_2 and a_3 i.e., $y = y(a_0, a_1, a_2, a_3)$. Suppose we know approximate values for these constants. Then to first order, we can write as follows,

$$\Delta y = \frac{\partial y}{\partial a_0}\Delta a_0 + \frac{\partial y}{\partial a_1}\Delta a_1 + \frac{\partial y}{\partial a_2}\Delta a_2 + \frac{\partial y}{\partial a_3}\Delta a_3 \qquad \text{(D.36)}$$

with

$\Delta y_i = y_i - y_c$,

where y_c is the value of y at x_i calculated using the approximate values. If the function we are fitting is an analytical function, we can determine the partial derivatives at x_i. The above equation is linear and we can solve for the corrections, $\Delta a_0, \Delta a_1, \Delta a_2, and\, \Delta a_3$ using least squares. This gives us better approximations:

$a_0 + \Delta a_0$, $a_1 + \Delta a_1$, $a_2 + \Delta a_2$ and $a_3 + \Delta a_3$.

We can continue in this way until the corrections are sufficiently smaller than the predefined value. To solve this problem we need to calculate the derivatives:

$\frac{\partial y}{\partial a_0}$, $\frac{\partial y}{\partial a_1}$, $\frac{\partial y}{\partial a_2}$ and $\frac{\partial y}{\partial a_3}$.

As was said in the introduction, there is no closed form solution to a non-linear least squares problem. Instead, numerical algorithms are used to find the values of the parameters. Most algorithms involve choosing initial values for the parameters and then refining the parameters. We also used such procedures and methods in the programs we wrote.

References

Abt, H. A. 1965, ApJS, 11, 429

Abt, H. A. & Hunter, Jr., J. H. 1962, ApJ, 136, 381

Abt, H. A. & Levy, S. G. 1985, ApJS, 59, 229

Abt, H. A. & Snowden, M. S. 1964, ApJ, 139, 1139

Aerts, C., Christensen-Dalsgaard, J., & Kurtz, D. W. 2010, Asteroseismology

Aitken, R. G. 1964, The binary stars

Ambartsumian, V. A. 1956, Vistas in Astronomy, 2, 1708

Andersen, J. 1991, A&A Rev., 3, 91

Argyle, B. 2004, Observing and Measuring Visual Double Stars

Auvergne, M., Bodin, P., Boisnard, L., et al. 2009, A&A, 506, 411

Baglin, A., Auvergne, M., Barge, P., et al. 2006, in ESA Special Publication, Vol. 1306, The CoRoT Mission Pre-Launch Status - Stellar Seismology and Planet Finding, ed. M. Fridlund, A. Baglin, J. Lochard, & L. Conroy, 33

Balona, L. A. 2011, MNRAS, 415, 1691

Balona, L. A. 2013, MNRAS, 436, 1415

Balona, L. A. 2014a, MNRAS, 443, 1946

Balona, L. A. 2014b, MNRAS, 437, 1476

Balona, L. A., Catanzaro, G., Abedigamba, O. P., Ripepi, V., & Smalley, B. 2015, MNRAS, 448, 1378

Balona, L. A., Medupe, T., Abedigamba, O. P., et al. 2013, MNRAS, 430, 3472

Balona, L. A. & Nemec, J. M. 2012, MNRAS, 426, 2413

Batalha, N. M., Borucki, W. J., Koch, D. G., et al. 2010, ApJ, 713, L109

Bate, M. R. 2009, MNRAS, 392, 590

Bate, M. R. & Bonnell, I. A. 1997, MNRAS, 285, 33

Bate, M. R., Bonnell, I. A., & Bromm, V. 2002, MNRAS, 336, 705

Batten, A. H. 1968, JRASC, 62, 344

Batten, A. H. 1973, Binary and multiple systems of stars

Bazarghan, M., Safari, H., Innes, D. E., Karami, E., & Solanki, S. K. 2008, A&A, 492, L13

Beck, T. L., Simon, M., & Close, L. M. 2003, ApJ, 583, 358

Benacquista, M. 2013, An Introduction to the Evolution of Single and Binary Stars

Bhattacharya, D. & van den Heuvel, E. P. J. 1991, Phys. Rep., 203, 1

Blaauw, A. & van Albada, T. S. 1967, in IAU Symposium, Vol. 30, Determination of Radial Velocities and their Applications, ed. A. H. Batten & J. F. Heard, 215

Bleksley, A. E. H. 1934, Nature, 133, 613

Bodenheimer, P., Burkert, A., Klein, R. I., & Boss, A. P. 2000, Protostars and Planets IV, 675

Bonnell, I. A., Bate, M. R., & Vine, S. G. 2003, MNRAS, 343, 413

Borkovits, T., Derekas, A., Kiss, L. L., et al. 2013, MNRAS, 428, 1656

Borucki, W. J., Koch, D., Basri, G., et al. 2010, Science, 327, 977

Boss, A. P. 1991, Nature, 351, 298

Boss, A. P. 1995, Ap&SS, 223, 140

Bozkurt, Z. & Değirmenci, Ö. L. 2007, MNRAS, 379, 370

Breger, M. 2000, in Astronomical Society of the Pacific Conference Series, Vol. 210, Delta Scuti and Related Stars, ed. M. Breger & M. Montgomery, 3

Bryson, S. T., Tenenbaum, P., Jenkins, J. M., et al. 2010, ApJ, 713, L97

Cagaš, P. & Pejcha, O. 2012, A&A, 544, L3

Caldwell, D. A., Kolodziejczak, J. J., Van Cleve, J. E., et al. 2010, ApJ, 713, L92

Carquillat, J.-M. & Prieur, J.-L. 2007, MNRAS, 380, 1064

Carroll, B. W. & Ostlie, D. A. 1996, An Introduction to Modern Astrophysics

Carter, J. A., Fabrycky, D. C., Ragozzine, D., et al. 2011a, Science, 331, 562

Carter, J. A., Rappaport, S., & Fabrycky, D. 2011b, ApJ, 728, 139

Chandrasekhar, S. 1944, ApJ, 99, 54

Chaplin, W. J., Appourchaux, T., Elsworth, Y., et al. 2010, ApJ, 713, L169

Chini, R., Hoffmeister, V. H., Nasseri, A., Stahl, O., & Zinnecker, H. 2012, MNRAS, 424, 1925

Christiansen, J., Science Office, K., & Science Operations Center, K. 2012, in AAS/Division for Planetary Sciences Meeting Abstracts, Vol. 44, AAS/Division for Planetary Sciences Meeting Abstracts, 113.01

Clarke, C. J. 2001, in IAU Symposium, Vol. 200, The Formation of Binary Stars, ed. H. Zinnecker & R. Mathieu, 346

Clarke, C. J., Bonnell, I. A., & Hillenbrand, L. A. 2000, Protostars and Planets IV, 151

Conroy, K. E., Prša, A., Stassun, K. G., et al. 2014, AJ, 147, 45

Curtiss, R. H. 1916, Publications of Michigan Observatory, 2

D'Angelo, C., van Kerkwijk, M. H., & Rucinski, S. M. 2006, AJ, 132, 650

De Loore, C. W. H. & Doom, C., eds. 1992, Astrophysics and Space Science Library, Vol. 179, Structure and evolution of single and binary stars

Debosscher, J., Aerts, C., Tkachenko, A., et al. 2013, A&A, 556, A56

Derekas, A., Kiss, L. L., Borkovits, T., et al. 2011, Science, 332, 216

Dhital, S., West, A. A., Stassun, K. G., & Bochanski, J. J. 2010, AJ, 139, 2566

Docobo, J. A. 1985, Celestial Mechanics, 36, 143

Doyle, L. R., Carter, J. A., Fabrycky, D. C., et al. 2011, Science, 333, 1602

Duchêne, G., Delgado-Donate, E., Haisch, Jr., K. E., Loinard, L., & Rodríguez, L. F. 2007, Protostars and Planets V, 379

Dunham, E. W., Borucki, W. J., Koch, D. G., et al. 2010, ApJ, 713, L136

Duquennoy, A. & Mayor, M. 1991, A&A, 248, 485

Dvorak, S. 2009, Communications in Asteroseismology, 160, 64

Eggleton, P. 2006, Evolutionary Processes in Binary and Multiple Stars

Eggleton, P. P. & Kisseleva-Eggleton, L. 2006, Ap&SS, 304, 75

Fabrycky, D. & Tremaine, S. 2007, ApJ, 669, 1298

Fabrycky, D. C., Ford, E. B., Steffen, J. H., et al. 2012, ApJ, 750, 114

Faigler, S. & Mazeh, T. 2011, MNRAS, 415, 3921

Faigler, S., Tal-Or, L., Mazeh, T., Latham, D. W., & Buchhave, L. A. 2013, ApJ, 771, 26

Ferraz-Mello, S. 1981, AJ, 86, 619

Fitzpatrick, R. 2012, An Introduction to Celestial Mechanics

Ford, E. B., Ragozzine, D., Rowe, J. F., et al. 2012, ApJ, 756, 185

Geary, J. C. & Abt, H. A. 1970, AJ, 75, 718

Ghaderi, K., Pirkhedri, A., Rostami, T., Khodamoradi, S., & Fatahi, H. 2012, Journal of Korean Astronomical Society, 45, 1

Ghez, A. M., Neugebauer, G., & Matthews, K. 1993, AJ, 106, 2005

Gies, D. R., Williams, S. J., Matson, R. A., et al. 2012, AJ, 143, 137

Gilliland, R. L., Brown, T. M., Christensen-Dalsgaard, J., et al. 2010, PASP, 122, 131

Goodricke, J. 1783, Philosophical Transactions of the Royal Society of London Series I, 73, 474

Graczyk, D., Soszyński, I., Poleski, R., et al. 2011, , 61, 103

Grigahcène, A., Antoci, V., Balona, L., et al. 2010, ApJ, 713, L192

Guinan, E. F., Ribas, I., Fitzpatrick, E. L., et al. 2000, ApJ, 544, 409

Haas, M. R., Batalha, N. M., Bryson, S. T., et al. 2010, ApJ, 713, L115

Haghighipour, N., ed. 2010, Astrophysics and Space Science Library, Vol. 366, Planets in Binary Star Systems

Halbwachs, J. L., Arenou, F., Mayor, M., Udry, S., & Queloz, D. 2000, A&A, 355, 581

Heintz, W. D. 1967, , 17, 311

Heintz, W. D. 1969, JRASC, 63, 275

Herschel, W. 1802, Philosophical Transactions of the Royal Society of London Series I, 92, 477

Horton, A. J., Bate, M. R., & Bonnell, I. A. 2001, MNRAS, 321, 585

Huang, S.-S. 1957, PASP, 69, 427

Hulse, R. A. & Taylor, J. H. 1975, ApJ, 195, L51

Irwin, J. B. 1952, ApJ, 116, 211

Jackson, B. K., Lewis, N. K., Barnes, J. W., et al. 2012, ApJ, 751, 112

Jaschek, C. & Jaschek, M. 1957, PASP, 69, 546

Jenkins, J. M., Caldwell, D. A., Chandrasekaran, H., et al. 2010a, ApJ, 713, L87

Jenkins, J. M., Caldwell, D. A., Chandrasekaran, H., et al. 2010b, ApJ, 713, L120

Johnson, D. O. 2004, Journal of Astronomical Data, 10

Karami, K. & Mohebi, R. 2007a, , 7, 558

Karami, K. & Mohebi, R. 2007b, Journal of Astrophysics and Astronomy, 28, 217

Karami, K. & Mohebi, R. 2009, Journal of Astrophysics and Astronomy, 30, 153

Karami, K., Mohebi, R., & Soltanzadeh, M. M. 2008, Ap&SS, 318, 69

Karami, K. & Teimoorinia, H. 2007, Ap&SS, 311, 435

Karttunen, H., Kroeger, P., Oja, H., Poutanen, M., & Donner, K. J. 2003, Fundamental astronomy

Kim, S.-L., Lee, J. W., Youn, J.-H., Kwon, S.-G., & Kim, C. 2002, A&A, 391, 213

Kiseleva, L. G., Eggleton, P. P., & Mikkola, S. 1998, MNRAS, 300, 292

Klaus, T. C., Cote, M. T., McCauliff, S., et al. 2010a, in Proc. SPIE, Vol. 7740, Software and Cyberinfrastructure for Astronomy, 774018

Klaus, T. C., McCauliff, S., Cote, M. T., et al. 2010b, in Proc. SPIE, Vol. 7740, Software and Cyberinfrastructure for Astronomy, 774017

Kobulnicky, H. A. & Fryer, C. L. 2007, ApJ, 670, 747

Koch, D. G., Borucki, W. J., Basri, G., et al. 2010, ApJ, 713, L79

Koen, C. 2014, MNRAS, 444, 1486

Kopal, Z. 1947, Harvard College Observatory Circular, 450, 1

Kopal, Z. 1955, Annales d'Astrophysique, 18, 379

Kopal, Z. 1959, in Liege International Astrophysical Colloquia, Vol. 9, Liege International Astrophysical Colloquia, 74–75

Kouwenhoven, M. B. N., Brown, A. G. A., Portegies Zwart, S. F., & Kaper, L. 2007, A&A, 474, 77

Kozai, Y. 1962, AJ, 67, 591

Lada, C. J. 2006, ApJ, 640, L63

Lampens, P. 2006, in Astronomical Society of the Pacific Conference Series, Vol. 349, Astrophysics of Variable Stars, ed. C. Aerts & C. Sterken, 153

Law, N. M., Dhital, S., Kraus, A., Stassun, K. G., & West, A. A. 2010, ApJ, 720, 1727

Lee, C.-U., Kim, S.-L., Lee, J. W., et al. 2008, MNRAS, 389, 1630

Lehmann, H., Zechmeister, M., Dreizler, S., Schuh, S., & Kanzler, R. 2012, A&A, 541, A105

Lehmann-Filhés, R. 1894, Astronomische Nachrichten, 136, 17

Leinert, C., Zinnecker, H., Weitzel, N., et al. 1993, A&A, 278, 129

Liakos, A. & Niarchos, P. 2009, Communications in Asteroseismology, 160, 2

Loeb, A. & Gaudi, B. S. 2003, ApJ, 588, L117

Lohr, M. E., Norton, A. J., Kolb, U. C., et al. 2012, A&A, 542, A124

Lomb, N. R. 1976, Ap&SS, 39, 447

Lowrance, P. J., Kirkpatrick, J. D., & Beichman, C. A. 2002, ApJ, 572, L79

Lucy, L. B. & Sweeney, M. A. 1971, AJ, 76, 544

Maceroni, C., Lehmann, H., da Silva, R., et al. 2014, A&A, 563, A59

Maceroni, C., Montalbán, J., Gandolfi, D., Pavlovski, K., & Rainer, M. 2013, A&A, 552, A60

Mahy, L., Rauw, G., De Becker, M., Eenens, P., & Flores, C. A. 2013, A&A, 550, A27

Mason, B. D., Gies, D. R., Hartkopf, W. I., et al. 1998, AJ, 115, 821

Mason, B. D., Hartkopf, W. I., Gies, D. R., Henry, T. J., & Helsel, J. W. 2009, AJ, 137, 3358

Mason, B. D., Wycoff, G. L., Hartkopf, W. I., Douglass, G. G., & Worley, C. E. 2001, AJ, 122, 3466

Mayor, M. & Mazeh, T. 1987, A&A, 171, 157

Mazeh, T. 1990, AJ, 99, 675

Mazeh, T. 2008, in EAS Publications Series, Vol. 29, EAS Publications Series, ed. M.-J. Goupil & J.-P. Zahn, 1–65

Mazeh, T. & Faigler, S. 2010, A&A, 521, L59

Mazeh, T., Nachmani, G., Sokol, G., Faigler, S., & Zucker, S. 2012, A&A, 541, A56

Mazeh, T. & Shaham, J. 1979, A&A, 77, 145

Mazeh, T., Simon, M., Prato, L., Markus, B., & Zucker, S. 2003, ApJ, 599, 1344

Middour, C., Klaus, T. C., Jenkins, J., et al. 2010, in Proc. SPIE, Vol. 7740, Software and Cyberinfrastructure for Astronomy, 77401A

Miglio, A., Montalbán, J., Baudin, F., et al. 2009, A&A, 503, L21

Mislis, D., Heller, R., Schmitt, J. H. M. M., & Hodgkin, S. 2012, A&A, 538, A4

Mkrtichian, D. E., Kusakin, A. V., Gamarova, A. Y., & Nazarenko, V. 2002, in Astronomical Society of the Pacific Conference Series, Vol. 259, IAU Colloq. 185: Radial and Nonradial Pulsationsn as Probes of Stellar Physics, ed. C. Aerts, T. R. Bedding, & J. Christensen-Dalsgaard, 96

Murphy, S. J. 2012, MNRAS, 422, 665

Murphy, S. J., Bedding, T. R., Shibahashi, H., Kurtz, D. W., & Kjeldsen, H. 2014, MNRAS, 441, 2515

Murphy, S. J., Pigulski, A., Kurtz, D. W., et al. 2013a, MNRAS, 432, 2284

Murphy, S. J. & Shibahashi, H. 2015, MNRAS, 450, 4475

Murphy, S. J., Shibahashi, H., & Kurtz, D. W. 2013b, MNRAS, 430, 2986

Ostriker, J. P. 1970, in IAU Colloq. 4: Stellar Rotation, ed. A. Slettebak, 147

Paddock, G. F. 1915, Lick Observatory Bulletin, 8, 153

Paparo, M., Szeidl, B., & Mahdy, H. A. 1988, Ap&SS, 149, 73

Patience, J., Ghez, A. M., Reid, I. N., & Matthews, K. 2002, AJ, 123, 1570

Percy, J. R. 2007, Understanding Variable Stars

Perryman, M. A. C., Lindegren, L., Kovalevsky, J., et al. 1997, A&A, 323

Petr, M. G., Coudé du Foresto, V., Beckwith, S. V. W., Richichi, A., & McCaughrean, M. J. 1998, ApJ, 500, 825

Petrie, R. M. 1960, JRASC, 54, 29

Petrie, R. M. 1962, AJ, 67, 279

Pigulski, A. 2006, in Astronomical Society of the Pacific Conference Series, Vol. 349, Astrophysics of Variable Stars, ed. C. Aerts & C. Sterken, 137

Pigulski, A. & Michalska, G. 2007, , 57, 61

Plavec, M. 1964, Bulletin of the Astronomical Institutes of Czechoslovakia, 15, 156

Plummer, H. C. 1908, ApJ, 28, 212

Pribulla, T. & Rucinski, S. M. 2006, AJ, 131, 2986

Prosser, C. F., Stauffer, J. R., Hartmann, L., et al. 1994, ApJ, 421, 517

Prša, A., Batalha, N., Slawson, R. W., et al. 2011, AJ, 141, 83

Rabe, W. 1951, Astronomische Nachrichten, 280, 1

Raghavan, D., McAlister, H. A., Henry, T. J., et al. 2010, ApJS, 190, 1

Rappaport, S., Deck, K., Levine, A., et al. 2013, ApJ, 768, 33

Reipurth, B. & Mikkola, S. 2012, Nature, 492, 221

Rucinski, S. M., Pribulla, T., & van Kerkwijk, M. H. 2007, AJ, 134, 2353

Russell, H. N. 1902, ApJ, 15, 252

Sahade, J. 1960, in Stellar Atmospheres, ed. J. L. Greenstein, 466

Sana, H., de Mink, S. E., de Koter, A., et al. 2012, Science, 337, 444

Sana, H., James, G., & Gosset, E. 2011, MNRAS, 416, 817

Scargle, J. D. 1982, ApJ, 263, 835

Schlesinger, F. 1910, Publications of the Allegheny Observatory of the University of Pittsburgh, 1, 123

Schlesinger, F. 1915, ApJ, 41, 162

Schroder, K.-P., Pols, O. R., & Eggleton, P. P. 1997, MNRAS, 285, 696

Schwarz, R., Haghighipour, N., Eggl, S., Pilat-Lohinger, E., & Funk, B. 2011, MNRAS, 414, 2763

Shibahashi, H. & Kurtz, D. W. 2012, MNRAS, 422, 738

Shporer, A., Jenkins, J. M., Rowe, J. F., et al. 2011, AJ, 142, 195

Silvotti, R., Schuh, S., Janulis, R., et al. 2007, Nature, 449, 189

Silvotti, R., Szabó, R., Degroote, P., Østensen, R. H., & Schuh, S. 2011, in American Institute of Physics Conference Series, Vol. 1331, American Institute of Physics Conference Series, ed. S. Schuh, H. Drechsel, & U. Heber, 133–146

Simon, M., Ghez, A. M., & Leinert, C. 1993, ApJ, 408, L33

Singh, M. 1984, Ap&SS, 100, 13

Skuljan, J., Ramm, D. J., & Hearnshaw, J. B. 2004, MNRAS, 352, 975

Smalley, B., Southworth, J., Pintado, O. I., et al. 2014, A&A, 564, A69

Smart, W. M. & Green, E. b. R. M. 1977, Textbook on Spherical Astronomy

Smullen, R. A. & Kobulnicky, H. A. 2015, ApJ, 808, 166

Soydugan, E., İbanoğlu, C., Soydugan, F., Akan, M. C., & Demircan, O. 2006a, MNRAS, 366, 1289

Soydugan, E., Soydugan, F., Demircan, O., & İbanoğlu, C. 2006b, MNRAS, 370, 2013

Steffen, J. H., Ford, E. B., Rowe, J. F., et al. 2012, ApJ, 756, 186

Steffen, J. H., Quinn, S. N., Borucki, W. J., et al. 2011, MNRAS, 417, L31

Steinitz, R. & Pyper, D. M. 1970, in IAU Colloq. 4: Stellar Rotation, ed. A. Slettebak, 165

Stello, D., Chaplin, W. J., Bruntt, H., et al. 2009, ApJ, 700, 1589

Sterne, T. E. 1941, Proceedings of the National Academy of Science, 27, 175

Sterzik, M. F., Tokovinin, A. A., & Shatsky, N. I. 2003, in Astronomical Society of the Pacific Conference Series, Vol. 287, Galactic Star Formation Across the Stellar Mass Spectrum, ed. J. M. De Buizer & N. S. van der Bliek, 403–408

Stumpe, M. C., Smith, J. C., Van Cleve, J. E., et al. 2012, PASP, 124, 985

Szebehely, V. 1969, in BAAS, Vol. 1, Bulletin of the American Astronomical Society, 263

Tal-Or, L., Faigler, S., & Mazeh, T. 2015, A&A, 580, A21

Tauris, T. M. & van den Heuvel, E. P. J. 2006, Formation and evolution of compact stellar X-ray sources, ed. W. H. G. Lewin & M. van der Klis, 623–665

Telting, J. H., Østensen, R. H., Baran, A. S., et al. 2012, A&A, 544, A1

Terebizh, V. I. 1992, Analiz vremennykh riadov v astrofizike

Tohline, J. E. 2002, ARA&A, 40, 349

Tokovinin, A., Thomas, S., Sterzik, M., & Udry, S. 2006, A&A, 450, 681

Tokovinin, A. A. 1997, Astronomy Letters, 23, 727

Torres, G. & Ribas, I. 2002, ApJ, 567, 1140

Tsvetkov, T. G. & Petrova, T. C. 1993, Ap&SS, 203, 257

Turcu, V., Pop, A., & Moldovan, D. 2008, Information Bulletin on Variable Stars, 5826

Unno, W., Osaki, Y., Ando, H., Saio, H., & Shibahashi, H. 1989, Nonradial oscillations of stars

Uytterhoeven, K., Moya, A., Grigahcène, A., et al. 2011, A&A, 534, A125

van Albada, T. S. 1968, Bull. Astron. Inst. Netherlands, 20, 57

van den Bos, W. H. 1937, Circular of the Union Observatory Johannesburg, 98, 337

van den Bos, W. H. 1962, AJ, 67, 552

van den Heuvel, E. P. J. 1983, in Accretion-Driven Stellar X-ray Sources, ed. W. H. G. Lewin & E. P. J. van den Heuvel, 303–341

van den Heuvel, E. P. J. 2011, Bulletin of the Astronomical Society of India, 39, 1

van Kerkwijk, M. H., Rappaport, S. A., Breton, R. P., et al. 2010, ApJ, 715, 51

Walker, G., Matthews, J., Kuschnig, R., et al. 2003, PASP, 115, 1023

Welsh, W. F., Orosz, J. A., Carter, J. A., et al. 2012, Nature, 481, 475

Wilsing, J. 1893, Astronomische Nachrichten, 134, 89

Wilson, R. E. 1953, Carnegie Institute Washington D.C. Publication

Wolszczan, A. & Frail, D. A. 1992, Nature, 355, 145

Woltjer, Jr., J. 1922, Bull. Astron. Inst. Netherlands, 1, 93

Worley, C. E. 1967, in On the Evolution of Double Stars, ed. J. Dommanget, Vol. 17, 221

Worrall, G. 1967, in Liege International Astrophysical Colloquia, Vol. 14, Liege International Astrophysical Colloquia, 365–366

Wyse, A. B. & Kron, G. E. 1939, Lick Observatory Bulletin, 19, 17

Yabushita, S. 1966, MNRAS, 133, 133

Zasche, P. & Uhlař, R. 2013, MNRAS, 429, 3472

Zucker, S., Mazeh, T., & Alexander, T. 2007, ApJ, 670, 1326

Zucker, S., Torres, G., & Mazeh, T. 1995, ApJ, 452, 863

Zurhellen, W. 1907, Astronomische Nachrichten, 173, 353

Zwintz, K., Fossati, L., Ryabchikova, T., et al. 2014, Science, 345, 550